International Cotutelle

THESE
pour obtenir le grade de Docteur
Délivré par : *l'Université Montpellier II*

DISSERTATION
zur Erlangung des akademischen Grades "Doctor rerum naturalium" (Dr. rer. nat.)
Eingereicht an: *der Universität Potsdam*

Sessile Droplets of Salt Solutions on Inert and Metallic Surfaces:
Influence of Salt Concentration Gradients on Evaporation and Corrosion Behaviour

Virginie Soulié

JURY

Prof. Dr. DUFRÊCHE Jean-François	ICSM	Chairman
Dr. RIEGLER Hans	MPIKG	Examiner
Dr. LEQUIEN Florence	CEA Saclay	Examiner

Doctoral Schools and specialities:
Sciences Chimiques Balard ED 469: Chimie et Physico-Chimie des Matériaux
Mathematisch-Naturwissenschaftlichen Fakultät: Physikalische Chemie

Research Units:
Commissariat à l'Energie Atomique et aux Energies Alternatives (Saclay, France)
Max-Planck-Institut für Kolloid- und Grenzflächenforschung (Potsdam, Germany)
in partnership with *L.I.A "RECYCLING" CNRS - MPG*

PhD Supervisors:

Prof. Dr. ZEMB Thomas	ICSM
Prof. Dr. Dr. h.c. MÖHWALD Helmuth	MPIKG

Reviewers:

Prof. Dr. BREZESINSKI Gerald	MPIKG
Prof. Dr. LEVITZ Pierre	UPMC - CNRS

Paris, September 2015

A Jacqueline, ma grand-mère adorée

”Le chemin importe peu, la volonté d’arriver suffit à tout”
Albert Camus

ACKNOWLEDGEMENTS

First of all I would like to thank Prof. Helmuth Möhwald for the opportunity to take and develop the first steps of this thesis at the Max Planck Institute of Colloids and Interfaces. It was a wonderful and challenging experience in an environment conducive to scientific freedom and cultural exchanges. I really enjoyed your dedication to research and your PhD students which made the PhD experience productive and stimulating.

I would like to express my sincere gratitude to Prof. Thomas Zemb. Since we have known each other, I deeply appreciate your trust in me and my scientific skills. Thank you for offering me this rewarding research project under your supervision. I have always been able to count on you, at any time, to guide me, give me advice or just reassure me. You have always kept an eye on me while allowing me to explore my own ideas. The numerous opportunities that I had to meet and interact with experienced researchers, and extend my knowledge are owed to him. My truly thanks.

I am particularly grateful to Hans Riegler for his enthusiastic, inspirational and fruitful discussions. Especially I would like to acknowledge his patience and the trust that he gave me from the beginning to the end. Thank you for showing me how to become and think as a scientist: *"the obvious is not trivial!"*

I cannot imagine a better Mummy-guide into the world of corrosion science than Florence Lequien. Florence, you have taught me how to survive scientifically: from the very basic principles of corrosion to how to improve talks, how to conduct effectively meetings and how to deal with scientists. You were always there to help me or give me confidence whenever I needed it. You really supported me whatever I decided to do. *"There are no right or wrong choices in life, but rather decisions we make towards achieving right ones"* (Tim J. Wooster). Many thanks for all of that.

I am very thankful to Stefan Karpitschka for his numerous contributions that led to many investigations and interesting results. Thank you for sharing your knowledge on droplet science. It was great that, even though you were extremely busy, you always found time to discuss, gave feedbacks on data interpretation and papers, and provided support.

I would like to thank Damien Féron for the helpful and enlightening scientific discussions that have led to a profound understanding of the corrosion phenomena. I enjoyed your support and your kindness.

Philippe Prené, thank you very much for all your advice, suggestions and help. It was great that you were always available to collaborate and discuss about any problem I encountered. I will remember your alphabetical classification of the solutions: there is always a suitable plan Z solution! I have good memories of our short trips to Marcoule and Berlin.

It is a great pleasure to thank my colleagues from the Interfaces department for the friendly atmosphere that I enjoyed from the first moment at the summer school in Lecce. My special thanks are to Marie Jehannin, with whom I shared all the (mis)adventures of a PhD student, Sebastian Podszus, for our numerous discussions about the political and social system in France and Germany, Stephan Eickelmann, Hubert Gojzewski and Chenyu Jiu, for the uncountable little assistances in the daily lab work, Stefanie Riedel, for the great deal of help with administration. Amy Peterson and Hideh Asanuma, it was always great fun to share office with you! I would like to thank Rodrigo Pérez-García for his experimental contributions in AFM characterization.

I was really fortunate to be also a PhD fellow in the Non-Aqueous Corrosion Laboratory (LECNA). It is a nice and social group, in which the working atmosphere would not be as cooperative and friendly as it is now without Mylène Belgome, Marie Benoit, Marion Bigot, Marie-Christine Demizieux, Stéphane Heurtault, Barbara Laurent, Anthony Muccioli and Matthieu Rivollier. Many thanks to Marie Benoit for everything! Marie, you have been a wonderful friend, my confidante and my USB keys saviour, you never doubted me. I also want to thank everyone in LECNA for immediate support. In particular, I would like to mention Jean-Louis Courouau, Brigitte Duprey, Sidonie Pasquier-Tilliette, Raphaël Robin and Fabien Rouillard.

I would like to acknowledge Gervaise Moine who has taken care of me so well: you comforted me, supported me and even fed on sweets! I had a real pleasure to be your office mate for two years.

A special thanks to Franck Ferreira-Gomes for his great experimental (and cleaning!) skills and contributions to the third part of this thesis and ongoing studies. I really enjoyed your optimism, your joie de vivre without a hitch: *"Think like a proton, stay positive!"*.

I gratefully acknowledge the funding sources that made my PhD work possible. I was honored to be a Max Planck Institute PhD fellow for my first one year and was funded by the French Alternative Energies and Atomic Energy Commission (CEA) Saclay for the last two years. My work was also supported by LIA (Laboratoire International Associé) Recycling between CNRS/INC and MPG/MPIKG. Special thanks goes to Aurélie Menasria for her unconditional help to prepare my last minute missions. I also wish to thank the LabEx CheMISyst.

Je tiens à remercier mes parents et mes soeurs pour leur inconditionnel soutien, pour tout l'amour et toute la force qu'ils m'ont donnés et inspirés ... Vous me permettez de vivre mes rêves mais surtout de continuer à rêver ! Merci pour tout !

Je remercie très sincèrement ma famille et mes amis qui m'ont encouragée et ont toujours cru en moi.

Merci à toi, Yannick, qui a supporté et partagé mes joies, mes tristesses et mes caprices. Merci pour tout ton amour et ton fidèle soutien aux quatre coins de l'Europe.

Virginie Soulié
June 2015

CONTENTS

SYMBOLS AND ABBREVIATIONS

Abbreviations

FoV	Field of View
PTV	Particle Tracking Velocimetry
SEM	Scanning Electron Microscopy
EDS	Energy Dispersive X-ray Spectroscopy

Chemicals

NaCl	Sodium chloride
$MgCl_2$	Magnesium chloride
LiCl	Lithium chloride
KCl	Potassium chloride
KNO_3	Potassium nitrate
K_2SO_4	Potassium sulfate

Mathematical Symbols and Operators

∇	Nabla operator
∇^2	Laplace operator

Constant

R	Gas constant

Material Parameters

θ_e	Equilibrium three-phase contact angle
γ	Surface tension
γ_{lv}	Liquid-vapour surface tension
γ_{lv}°	Liquid-vapour surface tension of pure water
γ_{sl}	Solid-liquid surface tension
γ_{sv}	Solid-vapour surface tension
$\Delta\gamma$	Surface tension difference between a salt solution and pure water
σ	Surface tension increment
η_0	Dynamic viscosity
c_0	Initial salt concentration
P_{sat}	Saturated vapour pressure

RH_{eq}	Equilibrium relative humidity
D	Diffusion coefficient
M	Molecular weight
ρ	Volumetric mass density

Dimensionless Fluid-Mechanical Numbers

Bo	Bond number
Ca	Capillary number

Variables

c	Salt concentration
c_0^*	Critical initial salt concentration

Environment Variables

P	Vapour pressure
RH	Relative humidity
T	Temperature

Droplet Variables

θ	Three-phase contact angle
θ_{adv}	Advancing contact angle
θ_{rec}	Receding contact angle
β, $f(\theta)$	Functions of the contact angle
R_S	Radius of the sphere forming the spherical cap
r	Radius of the spherical-cap shaped droplet
$\tilde{r}$	Droplet size factor
h	Height of the sessile droplet
V	Volume of the sessile droplet
V_0	Initial volume of the sessile droplet
$\tilde{v}$	Normalized volume

Time Variables

t	Time
t_D	Diffusion time
t_F	Total evaporation time
$\tilde{t}_F$	Time scaled to t_F
$\tilde{t}_{RH}$	Time scaled with the normalized relative vapour pressure (see I.3.2)
$\tilde{t}$	Scaled time

Evaporation Variables

J	Evaporative flux
c	vapour concentration
$\tilde{Q}_i$	Normalized evaporation rate

Corrosion Variables

m_0	Initial weight of the iron sample
m_F	Weight of the iron sample after corrosion experiment
Δm	Weight loss of the iron sample
S_{drop}	Surface area of the initially deposited sessile droplet on the iron substrate
S_C	Surface area of the cathode
V_{corr}	Corrosion rate
W	Width of the peripheral film
e	Thickness of the peripheral film
D_p	Growth diffusion coefficient
c^*	Critical global salt concentration

INTRODUCTION

When you spill a droplet of coffee or tea on a table and let it dry, it leaves behind a distinct stain. All the coffee particles, which were initially uniformly distributed over the sessile droplet, have collected into a dark ring at the edge of the droplet. This is the so-called *"coffee-ring effect"* firstly investigated by Deegan and coworkers [1] in 1997. They discovered how particles are transported towards the droplet edge, towards the contact line pinned to the underlying substrate (e.g. the table top), where the water evaporates. Drying stains are not specific to our daily life but are also encountered with any type of liquid mixture with (non-volatile) particles such as salty water, our model solution system. Inside such an evaporating sessile droplet, the challenge for engineering application is to predict and control beforehand the pattern formation by understanding the evaporation- and solute-driven flows within the drying droplet and their feedback on stain formation.

Evaporation of sessile droplets in ambient atmosphere is a well-known yet not completely solved problem of classical physics. Past decades were marked by significant advance in experiment and theoretical progress in understanding several key aspects of the evaporation process, in particular the vapour diffusion from the sessile droplet surface [2–6] and the hydrodynamics within the evaporating droplets [1, 7–10]. It was found, in particular that the evaporative flux density is inhomogeneous along the surface and diverges on approach to the three-phase contact line [1, 7, 8, 11]. The resulting mass flow modifies the composition distribution of the fluid constituents within the droplet. The compositional evolution as well as the evaporation-driven flow inside the evaporating sessile droplet have been studied almost exclusively and qualitatively with the resulting properties of the deposit [12–16]. The evaporation behaviour itself has been rarely investigated theoretically and experimentally [17], although this is needed for a quantitative understanding and control of the process.

In the particular model case the sessile droplet of salt solutions is deposited on metallic surfaces under atmospheric conditions, the electrolyte solution inside the droplet reacts with the surface, leading to differential aeration corrosion. This is the so-called *"Evans droplet"* experiment firstly described by Evans [18] in 1926. He discovered how the variation in electrolyte thickness and hence in diffusion of oxygen to the saline solution-metal interface between the droplet edge and its center induces spatially separated cathodic and anodic activities under the droplet. The Evans droplet model is specific for "static" macroscopic sessile droplets, which is not so ubiquitous in nature and also in industry.

The under-droplet corrosion behaviour is commonly studied in the context of stationary conditions [19–25] and more recently in evaporating conditions [26, 27]. These reports focus on the characterization of the induced corrosion process, essentially with electrochemical methods [19, 24, 25] or microscopy characterization [28–30]. The contact of salty droplets on metallic surfaces involves inevitably interfacial and hydrodynamic issues: apart from the anode-cathode areas under the droplet, the corrosion behaviour itself and/or the evaporation process would influence the concentration profiles of all species (ionic and neutral) and the shape and size of the droplet that in turn affect the contact angle. The interplay of these phenomena under these complex conditions may change the anode-cathode area separation and evolution.

Most of the work presented in this thesis deals with the consequences of salt concentration gradients within sessile droplets from aqueous saline solutions on inert and metallic surfaces on the evaporation and corrosion behaviour. As a simple model system, we use macroscopic sessile droplets of salt solutions deposited on either inert silicon wafers or pure iron corrosive surfaces.

Part I provides the scientific and basic concepts of wetting, evaporation of sessile droplets from pure and complex liquids as well as the corrosion phenomenon in atmospheric conditions and under sessile droplets. In Chapters 1 and 4 we describe the experimental methods used in this thesis and then present the material and sample preparation in addition to the data analysis of the evaporation and corrosion experiments.

Part II is devoted to the evaporation of sessile droplets of aqueous saline solutions on inert surfaces. In Chapter 2 we investigate the evaporation behaviour of a water droplet. We show that the evaporation rate of such a sessile droplet is indeed entirely determined by diffusive transport of water vapour in the surrounding environment and depends on the relative humidity, the droplet size and shape. In Chapter 3 we extend this experimental investigation to sessile droplets evaporating from sodium chloride solutions on inert surfaces. We demonstrate that evaporation does not occur in an universal way with increasing the salt concentration and decreasing the droplet contact angle. We show that a spectacular change in the nature of the flow field within the drying droplet alters the evaporation behaviour and the patterns of the salty stains.

The classical under-droplet corrosion experiment is discussed in Part III. Our experimental study with sodium chloride solutions presented in Chapter 5 shows surprisingly that the classical Evans droplet experiment results in the formation of a peripheral film ahead of the macroscopic contact line. In Chapter 6 the formation of this peripheral film and the corrosion behaviour have been investigated for various salt concentrations and ion species. We obtain detailed information on the peripheral film phenomenon.

Part IV describes the observed corrosion process induced by evaporating sessile droplets from sodium chloride solutions on iron. In that case once the flow inside the evaporating droplet is identified and known, we can understand the salt-induced corrosion mechanism and the subsequent anode/cathode localisation at the saline solution-metal interface.

I

Scientific Background

1 PREREQUISITES

1.1 Wetting Phenomenon

When a droplet of liquid is placed on a flat and solid surface, there exist two different types of wetting [31]: *partial wetting* (the liquid contracts into a sessile droplet with a macroscopic contact angle θ as illustrated in Figure 1) and *total wetting* (the liquid spreads completely on the surface resulting in $\theta = 0°$[1]). The equilibrium configuration is defined by a minimization of the global surface energy.

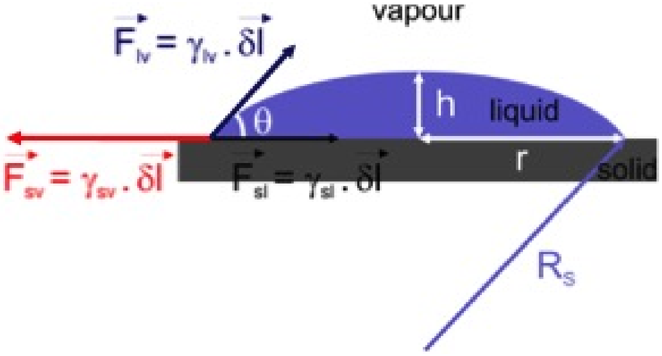

Figure 1 – *Schematic illustration of a liquid droplet on a flat and solid surface in a vapour phase environment. The geometry of the resulting spherical-cap shaped sessile droplet is characterized by: the contact angle θ, the droplet radius r, the radius of the sphere forming the spherical cap R_S and the droplet height h.*

The wetting phenomenon of a liquid droplet on a flat and solid surface in a vapour phase environment, with a contact angle θ_E, depends on the capillary forces acting along the three interfaces towards the direction that the latter shrink (Figure 1). Normalized to a unit vector length $\boldsymbol{\delta l}$, these forces $\boldsymbol{F_{ij}}$ represent the interfacial (surface) energies γ_{ij} between the three phases: solid s, liquid l and vapour v. The Young-Dupré equation describes a local balance of the projecting equilibrium forces acting at the three-phase contact line, the intersection of the solid, liquid and vapour phases [33]:

$$\gamma_{lv} \cdot cos(\theta_e) = \gamma_{sv} - \gamma_{sl} \tag{1}$$

Note that at microscopic scale, in *partial wetting*, ahead of the macroscopic contact line the solid surface is covered by a molecularly thin liquid film called *"precursor film"* [31, 34–36]. It exists because of forces acting on thin layers of a material with different electronic properties such as charge or polarizability, together with forces arising from the molecular structure of the film material. These intermolecular forces are commonly described by the disjoining pressure [37, 38].

In this thesis we focus on macroscopic sessile droplets from aqueous saline solutions. The surface tension γ_{lv} depends on the salt concentration c at the free surface of the sessile droplet [39–43]. The simplest dependency is linear:

$$\gamma_{lv} = \gamma_{lv}^{o} + \sigma\ c \tag{2}$$

with γ_{lv}^{o} as the surface tension of pure water (72.8 mN.m^{-1} at $T = 20°$C) and σ as the surface tension increment, a constant characteristic of each aqueous saline solution [42, 44]. An increase in salt concentration may either raise the surface tension ($\sigma > 0$) resulting in a *salting-out effect* or

---

[1] The final outcome is a very thick film resulting from the competition between molecular and capillary forces [32].

decrease γ_{lv} ($\sigma < 0$) leading to a *salting-in effect* [45]. Divalent chloride salts such as magnesium chloride $MgCl_2$ have been described as exceptions [46, 47]: they are salting-in agents, while they have a positive surface tension increment[2]. as salting-out agents such as sodium chloride NaCl. For instance, these two salts (NaCl and $MgCl_2$) are characterized by a depletion from the liquid-air interface, i.e., both anions and cations move away from this interface and these ions are removed from the surface, so water will be enriched there. This phenomenon is usually explained by the magnitude of the hydration free energy which dominates the free energy required for a partially bare ion to exist at the liquid-air interface [41, 43]. They have been ordered in the well-known Hofmeister series [41–43] on the basis of the magnitude of the specific salt ions from enhancing to disrupting local water structure: e.g., NaCl > $MgCl_2$ and therefore $\sigma_{MgCl_2} > \sigma_{NaCl}$. The salt-induced alteration in the structure of the nearby water molecules has led to a famous but controversial classification of ions as either *kosmotropes*, structure-makers, or *chaotropes*, structure-breakers depending on their ability to enhance or interrupt, respectively, the water structural character [41, 49–51]. The use of these terms for ions is unfortunate and very misleading, since the actual changes in the structure between the water molecules induced by the ions are opposite to what the name of these terms implies [52]. For instance, NaCl exhibits salting-out behaviour, but is normally referred to as chaotrope.

1.2 Spherical-cap shaped Sessile Droplet

Equivalent to the Young-Dupré equation (Equation 1), the equilibrium shape of a liquid sessile droplet on a flat and solid surface must be minimal of energy. In the absence of gravity, it must be a spherical-cap shaped sessile droplet. The nondimensional Bond number $Bo = (\rho\ g\ r_0\ h_0)/(\gamma_{lv})$ (with ρ as the liquid density and g as the gravitational constant), represents the effect of gravity relative to the surface tension. For a water droplet in air with an initial radius r_0 of 6.5 mm and an initial height h_0 of 150 μm, Bo is about 10^{-4}. Therefore capillary forces dominate over gravity. The small value of Bo ensures that a millimeter-sized sessile droplet deposited onto a solid surface in air can be regarded as a spherical cap.

A spherical-cap shaped sessile droplet can be characterized by four different parameters: the contact angle θ, the droplet radius r, the droplet height h and the radius of the sphere forming the spherical cap R_S (Figure 1). By geometry, the relationships between the two radii, the contact angle and the volume of the spherical cap V are:

$$r = R_S \cdot sin(\theta) \text{ and } R_S = \left(\frac{3\ V}{\pi\ \beta}\right)^{\frac{1}{3}} \tag{3}$$

with

$$V = \frac{1}{2}\ \pi\ h \left(\frac{h^2}{3} + r^2\right) \text{ and } \beta = (1 - cos(\theta))^2 \cdot (2 + cos(\theta))$$

---

[2] In most cases, because σ is usually positive, the salting-out behavior is expected. The addition of salt raises the the surface free energy of the protein. Therefore, the protein-salt interaction is classified as unfavorable indicating that the protein-protein attraction increases, the excess amount of salt is excluded from the domain of the protein. This leads to a reduction in protein solubility [48]. In the particular case of magnesium chloride, the unexpected and experimentally observed salting-in behaviour is attributed to preferential interactions between the magnesium ion and the protein surface, i.e., favorable weak ion-binding interactions between the salt and either the charged surface groups of the protein. These preferential interactions compensate the preferential exclusion of the magnesium ion from the non polar surface of the protein molecule [46–48]

2 EVAPORATION OF SESSILE DROPLETS FROM PURE LIQUIDS

2.1 Evaporation from a Spherical to a Sessile Droplet on a Solid Surface

In 1877, Maxwell was the first to derive the basic droplet evaporation equations by considering the simplest case where a pure liquid evaporates uniformly from a spherical (droplet) bulb surface [2]. Maxwell's model assumes that the evaporation depends on the diffusion relaxation of the saturated vapour layer immediately above the droplet, and not on the transfer rate across the liquid-vapour interface[3]. The time-dependent vapour concentration c in the air surrounding the droplet is governed by the unsteady diffusion equation

$$\frac{\partial c}{\partial t} = D\ \nabla^2 c \tag{4}$$

with D as the diffusion coefficient of vapour in air. However the evaporation-induced motion of the droplet surface (i.e., the liquid-vapour interface slowly moves as the droplet volume decreases) is typically much slower than the diffusion time for the vapour transport [56], so that the time-dependent term in Equation 4 can be neglected and the quasi-steady concentration field is given by

$$\nabla^2 c = 0 \tag{5}$$

The evaporation rate from the spherical droplet surface S_{sphere} is determined by the gradient in the vapour concentration ∇c according to Equation 6. Equation 5 is solved subject to the boundary conditions that the vapour concentration at the spherical droplet surface equals the saturated vapour concentration c_{sat} at the temperature of the droplet surface (there is a local concentration equilibrium at the liquid droplet/air interface), and c_∞ far away.

$$\frac{dV}{dt} = -S_{sphere}\ \frac{D}{\rho}\ \nabla c = -4\pi\ R_S\ \frac{D}{\rho}\ (c_{sat} - c_\infty) \tag{6}$$

The rate of volume change for a spherical droplet is found from Equation 6 and is proportional to the droplet perimeter R_S, and not to its surface area.

In this thesis, we focus on macroscopic sessile droplets under atmospheric conditions. In this case, the presence of a horizontal and solid surface below the evaporating sessile droplet hinders the vapour to diffuse downward. As a result, the evaporation rate is usually determined by the effective diffusion area $f(\theta)$ through which vapour molecules are transported away from the droplet [3, 4, 57–59]. The factor $f(\theta)$ can be totally ignored [4, 60–63], or mathematically approximated [3, 4, 57–59]. On the one hand, the evaporation rate of the sessile droplet is expressed as function of the droplet height h and a droplet evaporation constant λ, mainly determined by the intrinsic properties of the evaporating liquid (e.g., the diffusion coefficient and the heat of vaporization) [61–63]:

$$\frac{dV}{dt} = -\lambda\ h \tag{7}$$

On the other hand, analytical expressions of the factor $f(\theta)$ were determined by considering

---

[3] There are two physical mechanisms that can influence the drying rate of a sessile droplet. The first mechanism is the phase change from liquid to vapour: the rate at which molecules can cross the liquid-vapour interface [53, 54]. The latter is characterized by a time scale of 10^{-10} s [55]. The second rate-limiting step is the transport of the vapour molecules away from the droplet in the surrounding air [1, 7, 9, 10, 53]. This mechanism is valid for times longer than the diffusion time $t_D = r^2/D$, with D the diffusion coefficient of vapour in air. For a 5-millimeter-sized droplet of water, t_D is about 0.1 s.

that the vapour molecules diffused from a curved surface only in a radial direction [4, 58] (as depicted by the solid arc of a radius R_c in Figure 2, the evaporative flux at the droplet edge is neglected), or in a purely radial direction [57] (the effective diffusion area entirely includes the sessile droplet surface area as represented by the dashed and solid arc in Figure 2), or by evaluating the diffusion problem as an equivalent electrostatic problem: the capacitance of an isolated conductor formed by the sessile droplet and its mirror-image in the solid surface [3] as shown in Figure 2.

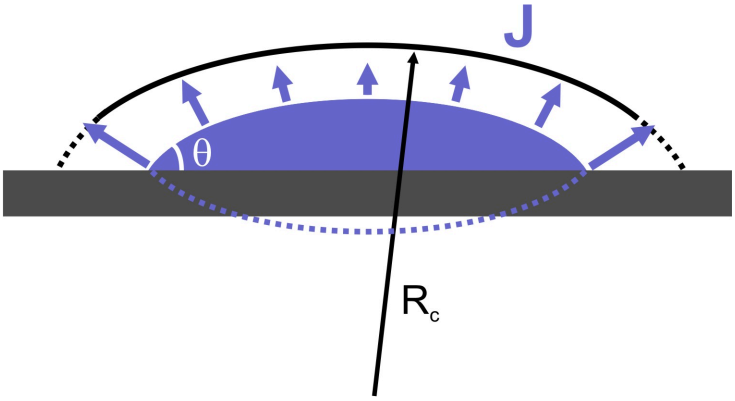

Figure 2 – *Geometry of the effective diffusion area of a sessile droplet deposited on a solid and horizontal surface: the solid line at the distance* R_c *from the center of the curvature represents the diffusion area modeled by Rowan and coworkers [4, 58] while the diffusion region modeled by Shanahan and coworkers [57] is represented by the dashed lines and the solid line. The sessile droplet and its reflection in the solid substrate illustrates the electrostatic equivalent conducting body used to determine the analytical expression of the factor* $f(\theta)$ *(Equation 8) in the Picknett and Bexon evaporation model [3], and the vapour concentration field around a sharp edge that appears when* $\theta < 90°$ *(Equation 10). The arrows indicate the non-uniform evaporative flux* J *(Equation 10) from the surface of the droplet.*

The latter model purposed by Picknett and Bexon [3] was experimentally considered in the literature as the best approximation for predicting accurately the evaporation rate of sessile droplets from pure liquids [64–66]. Therefore, in this thesis, we will consider, according to the Picknett and Bexon model [3], that the change of the volume V with time t of a spherical cap shaped sessile droplet (Equation 3) with a contact angle θ in the quasi steady-state with diffusion-driven evaporation (Equation 6) is given by

$$\frac{dV}{dt} = -4\pi \left(\frac{3}{\pi}\right)^{\frac{1}{3}} \frac{D}{\rho} \left(\frac{V}{\beta}\right)^{\frac{1}{3}} (c_{sat} - c_{\infty})\ f(\theta) \tag{8}$$

To describe the atmospheric conditions in which sessile droplet evaporation occurs, it is convenient to use the vapour pressure P of the liquid at constant temperature as vapour concentration variable c (since the vapour obeys the ideal gas law). The vapour pressure then depends on the relative humidity RH in the surrounding environment:

$$(c_{sat} - c_{\infty}) = \frac{M}{R\,T}\,(P_{sat} - P) = \frac{M}{R\,T}\,P_{sat}\,(1 - RH) \tag{9}$$

with M as molecular weight, R as gas constant, T as temperature, P_{sat} as saturated water vapour pressure at/above the droplet surface and P as the water vapour pressure in the background environment. However, one must be careful with the application of Equations 8 and 9 to real experimental conditions, since some physical parameters such as D, P_{sat} or ρ are temperature-dependent. The evaporative cooling and heat transfer to the liquid-air interface can influence the evaporation rate of a sessile droplet [6, 54, 67, 68].

2.2 Divergence of the Evaporative flux at the Droplet Edge

The strength of the evaporative flux J from the droplet surface is determined by the vapour concentration gradient according to

$$J = -D\ \nabla c \tag{10}$$

The evaporative flux is derived from Equation 5, which fulfills the same boundary conditions as described in the previous section: the vapour concentration c equals c_{sat} at/above the droplet surface and converges to c_∞ far away. When $c_\infty < c_{sat}$, a diffusive outflux arises and the droplet evaporates. A third boundary condition is that the solid surface, onto which the sessile droplet is deposited, is impermeable to the vapour. Mathematically the impermeability condition is equivalent to mirror-imaging of the sessile droplet as illustrated in Figure 2. The sessile droplet and its reflection has a pointy, singular shape near the contact line, as a charged conductor with a sharp tip (e.g., a lightning rod). The mathematical problem of finding the vapour concentration field around a sharp edge has an electrostatic equivalent: the electrostatic potential around a charged conductor. The shape of the droplet (and its reflection) near the contact line can be approximated by a wedge geometry, and a self-similar solution to the evaporative flux can be obtained, which scales as [1, 7, 10]

$$J \sim D\ \frac{(c_{sat} - c_\infty)}{r}\ \left(\frac{R}{r}\right)^{\lambda(\theta)-1} \tag{11}$$

with R as the radial distance to the contact line and

$$\lambda(\theta) = \frac{\pi}{2(\pi - \theta)}. \tag{12}$$

Hence for contact angles below 90° ($\lambda < 1$, Equation 12), the evaporative flux J diverges as the contact line is approached (Equation 11). The sharper the droplet edge, the stronger this divergence. For very flat sessile droplets ($\theta \ll 90°$), a square-root divergence of the evaporative flux is found (Equations 11 and 12). Hu and Larson [7] numerically showed that similarly at the sharp tip of a charged conductor, all the iso-concentration (equipotential) lines come close together at the contact line of an evaporating sessile droplet with $\theta < 90°$, so that the evaporative flux (electric field) diverges.

2.3 Evaporation Modes of a Sessile Droplet on a Solid Surface

The way the liquid-vapour interface moves as the sessile droplet volume decreases depends on the mode along which the evaporation takes place. Droplet evaporation can occur along two basic modes [3, 10, 57, 60, 65]. The first mode is the *constant contact angle mode*, in which the contact line is free to move and hence the contact area of the sessile droplet with the substrate decreases while the contact angle remains constant as depicted in Figure 3.a. For a constant contact angle mode, the time-dependent droplet radius can be estimated from dimensional arguments. Since the typical droplet volume V scales as $V \sim r^3$, the rate of volume change scales as

$$\frac{dV}{dt} \sim r^2\ \frac{dr}{dt} \tag{13}$$

Combining Equation 13 with Equation 6, which implies that the evaporation rate scales as $\frac{dV}{dt} \sim -D\, r$, one obtains the linear decrease of the droplet radius with the square root of time [65, 69, 70]

$$r(t) \sim \sqrt{D(t_F - t)} \tag{14}$$

with t_F the total evaporation time. Moreover if the contact line is free to move, we can obtain the temporal volume change of the sessile droplet by integrating Equation 8.

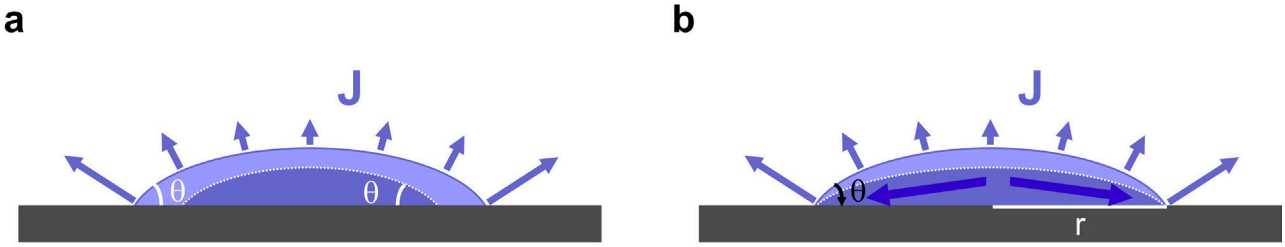

Figure 3 – ***a.*** *A droplet evaporating in constant contact angle mode: the contact area decreases, while the contact angle θ remains constant. The flow in the droplet has an outward contribution that comes from the evaporative flux J from the droplet surface and an inward contribution that arises from the receding motion of the three-phase contact line.* ***b.*** *A droplet evaporating in constant contact area mode: the contact angle decreases while the contact area remains constant. The evaporative flux from the droplet surfaces induces a radially outward flow.*

The second mode is the *constant contact area mode*, in which the contact area remains constant, since the contact line is pinned and the contact angle of the droplet slowly decreases, as shown in Figure 3.b. In case the contact line is pinned, the rate of volume change (Equation 8) and the evolution of the contact angle have to be obtained from the droplet geometry and the exact solution to the evaporative flux from the droplet surface. In the limit of small contact angles ($\theta \ll 90°$) simple analytical expressions for this evaporative flux were determined [5].

3 EVAPORATION OF SESSILE DROPLETS FROM COMPLEX FLUIDS

The consequences of the spatially non-uniform evaporative flux of sessile droplets are particularly interesting in the case of complex fluids. It has been investigated for colloid particle suspensions [1, 8, 16], solutions containing non-volatile species such as polymers [15, 71], surfactants [13, 14, 17] or salts [12].

3.1 Coffee-ring effect

When the three-phase contact line of the sessile droplet is pinned, as in Figure 3.b, the liquid that evaporates from the droplet edge region must be replenished by liquid from the interior of the droplet [1, 10]. A capillary mechanism drives the flow: in order to maintain the droplet's spherical-cap shape dictated by surface tension, a compensating flow is required to refill the evaporative losses from the pinned contact line region (Figure 3.b).

Contact line pinning and the non-uniform evaporative flux are the main ingredients of the so-called *"coffee-ring effect"*, firstly investigated by Deegan and coworkers [1, 10]. They discovered how the strong radially outward flow drags the coffee particles towards the pinned contact line, where the water evaporates while coffee particles are left behind and form the ring stain. The coffee-stain effect is not specific for coffee and tea, but is a robust theory describing the volume flow inside a droplet containing any type of colloidal suspension such as blood [72] or solutions with (non-volatile) particles such as salty water. Pinning of the contact line can occur by pre-existing roughness of the substrate. On top of this, suspended particles that arrive at the contact line due to the coffee-stain effect create or enforce the pinning and thereby generate a self-pinning mechanism [73]. Recently, it has been shown that the ring-stain formation can be suppressed by using non-spherical particles [74] or by shaking the evaporating droplets with strong electric fields [75].

3.2 Marangoni effect

The locally non-uniform evaporative flux of the free surface sessile droplets can lead to surface tension/energy gradients, that induce a flow because of the non-equilibrium character of the situation. The total energy can be lowered by replacing a high-energy surface with a low-energy surface. This phenomenon is commonly known as Marangoni effect [76]. It was first qualitatively and correctly explained by James Thomson in 1855 [77] who described the famous "tears of wine", appearing along the side walls of the glass, out of the wine. The Marangoni effect is either thermal [8, 78–80] or solutal [12, 13, 81] in nature.

On the one hand, surface tension gradients may arise from spatial variations of temperature originating from the difference in temperature between the substrate and the liquid-air interface [82] or more generally from the non-uniform cooling along the free surface of the sessile droplet induced by the singularity of the evaporative flux at the contact line [8, 78–80]. Thermally induced Marangoni flows in evaporating water-based sessile droplets are predicted [78], but up to now they are not observed unambiguously (most likely surface-active contaminants [8] may have spoiled the measurements).

On the other hand, with complex fluids surface tension gradients may result from local variations of the composition [12, 13, 81]. In the case of evaporating sessile droplets from complex fluids, the locally non-uniform evaporation will usually lead to a locally inhomogeneous distribution of the fluid constituents inside the droplet, that then in turn induce solutal Marangoni flows. Solutal Marangoni flows may be directed either towards or away from the three-phase contact line [13, 14, 83] depending on the properties of the liquid constituents. The Marangoni flows may lead to advancing [84, 85] or receding contact lines, or to repeated pinning/depinning with concentric ring-like deposits [13]. Complex internal flow patterns are also considered with Marangoni vortices near the droplet edge, which supposedly promote uniform deposits with receding contact lines [13–15, 81].

Hence, controlling and predicting beforehand the pattern formation by evaporating sessile droplets from complex fluids is not yet fully understood. In particular, it is not yet known, how the internal fluid flow looks like, how it evolves over time and how this affects the dynamics of the stain formation. Although the volume flow inside the evaporating sessile droplet can be found from mass conservation [9], the exact velocity profile within the droplet remains unknown. In the small contact angle regime, the lubrication approximation is often used to describe the velocity field inside the droplet [5]. However, even for relatively flat droplets ($\theta \ll 90^\circ$) the validity of this approximation near the pinned contact line, where the evaporative flux diverges, has been questioned [8]. On top of that, Marangoni stresses originating from surface tension gradients could lead to additional contributions to the velocity field [78, 86] as the motion of the contact line, in case it is free to move [5]. The purpose of the work described in this thesis is therefore to address the fundamental physics of evaporation of sessile droplets from aqueous saline solutions, evaporation-driven flow inside the drying droplet, and the subsequent salt deposition/precipitation and the relation with corrosion.

4 CORROSION PHENOMENON UNDER SESSILE DROPLETS

4.1 Atmospheric Corrosion

Atmospheric corrosion is a chemical and electrochemical phenomenon leading to the deterioration of metals exposed to natural ambient environments. With the large number of outdoor structures such as buildings, bridges and automobiles, atmospheric corrosion is subject of global concern because of its considerable economical importance to the service life of equipment and durability of structured materials. As opposed to metal immersed in a liquid, atmospheric corrosion is a relatively complicated practical process consisting of a base metal and its corrosion products, a non-permanent surface electrolyte (i.e., a thin wet film), and the atmosphere (more or less polluted by contaminants) [87].

Many variables influence the corrosion characteristics of the atmosphere. Atmospheric contaminant content, e.g., gaseous (sulfur dioxide), liquid (chlorine) or solid (dust) pollutants, temperature, relative humidity, and even the geographic location of the exposed metal exhibit a marked influence on corrosion behaviour. Marine and coastal environments are among the more severe atmospheres for corrosion, due to the combination of humidity and atmospheric salts [88]. In marine atmospheres chlorides are deposited mainly as droplets or as crystals formed by evaporation of spray carried by the wind from the sea [89]. Atmospheric sea salts such as magnesium chloride $MgCl_2$ or sodium chloride NaCl concentrated in the surface electrolyte film distincly influence the corrosion behaviour [90, 91].

Atmospheric corrosion depends on the presence of an electrolyte on the metal surface. Electrolyte's composition depends on the air pollutant deposition rate, and changes as its thickness with the humidity conditions of the atmosphere. Depending on the electrolyte thickness e, the atmospheric corrosion process is either anodically controlled (a decrease in the thickness e from 1 μm to 10 nm limits the hydration of the metal ions) or under cathodic control (as e increases from 1 μm to 1 mm, the oxygen diffusion through the electrolyte layer is the rate-determining step) [92, 93]. Sources of surface electrolyte include direct moisture precipitation (e.g., rain, fog, dew formed by condensation on cold metallic surfaces), chemical condensation (by the hygroscopic atmospheric salts and/or corrosion products) and adsorbed water layers on clean metal surfaces resulting from high humidity environment [94, 95]. For such adsorption to occur, the relative humidity must be above a certain moisture content value, known as the critical relative humidity [96, 97]. This value depends on the metal and on the chemical and physical properties of the corrosion products and/or the atmospheric salts, which usually lower the critical humidity level and thereby increase sharply the corrosion process [87, 98, 99]. However, the critical humidity is not simply a threshold value, above which adsorbed water layers on metallic surfaces activate the atmospheric corrosion, but a more complex function of changing humidity in wet/dry (diurnal) cycles [100].

4.2 The Evans Droplet Model

One of the classical experiments in corrosion, the Evans droplet, provides insight into the atmospheric corrosion by illustrating the effect of the three-phase air/electrolyte/metal interface as well as the variation in electrolyte film thickness on the corrosion process [101]. The original experiment, published in 1926 by Evans [18], was conducted by placing a droplet of 3%wt. NaCl solution with agar-agar on a finely abraded iron surface. The solution also contained small amounts of two indicators: potassium ferricyanide, which exhibits a blue coloration in the presence of ferrous ions Fe^{2+}, and phenolphthalein, which exhibits a pink coloration in the presence of alkali environment (i.e., pH > 8.5). After several minutes a central blue region surrounded by a peripheral pink area, and the formation of a rust ring in between is observed [18, 101].

The changes in color of indicators inside the macroscopic and stationary sessile droplet from a jelly electrolyte solution demonstrate the formation of a localized electrochemical cell and in particular, the natural distribution of the anodic and cathodic reactions inside the droplet as shown in Figure 4. The oxygen O_2 reduction, which results in the production of hydroxyl ions OH^-, occurs at the droplet edge at the metal-electrolyte interface, because the diffusion path length of oxygen from the environmental vapour phase to the metallic substrate-solution is shortest at the contact line region. Thus at the perimeter of the droplet the alkaline cathode is formed as depicted in Figure 4.

$$O_{2(dis)} + 4\,e^- + 2\,H_2O \rightarrow 4\,OH^-_{(aq)} \tag{15}$$

The alkalinity developed provides protection for the iron surface in the droplet edge region, since any ferrous ion was detected with the indicator [18, 19].

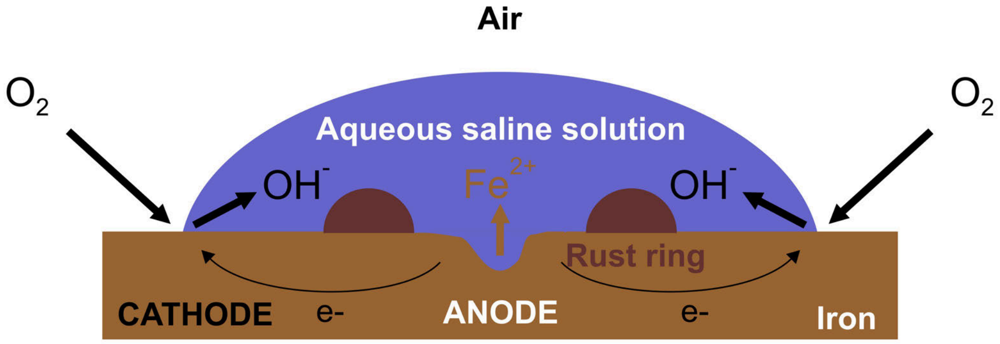

Figure 4 – *The classical Evans droplet model under a sessile droplet from aqueous saline (electrolyte) solution: the oxygen is reduced at the droplet edge, acting as the cathode, whereas the iron dissolution occurs in the droplet center acting as the anode. A rust ring is formed from the reaction between anodic and cathodic products within the sessile droplet, in the region midway between the anodic and cathodic areas.*

The corresponding anode is established at the metal surface-electrolyte interface, where oxygen is deficient (i.e., away from the three-phase contact line). Close(r) to the droplet center, ferrous ions Fe^{2+}, generated from the metal, are released into the droplet solution.

$$Fe_{(s)} \rightarrow Fe^{2+}_{(aq)} + 2\,e^- \tag{16}$$

The anodic reaction leads to localized pitting corrosion (i.e., a localized penetration of the metal surface) somewhere close(r) to the sessile droplet center as depicted in Figure 4.

Where the inner anodic ferrous ion-containing and outer-edged cathodic alkaline liquids impinge upon each other, precipitation of hydrated ferrous hydroxide $Fe(OH)_2$ occurs, which is highly insoluble and forms an annulus within the droplet as illustrated in Figure 4. The ring rust comes from the oxidation of the initially precipitated ferrous hydroxide, leading to the formation of lepidocrocite γ-$FeOOH$ [102, 103]. This reaction, in addition to the cathodic reaction, also reduces the level of dissolved oxygen in the solution.

The Evans droplet experiment illustrates the differential aeration phenomenon, generally observed in semi-immersed conditions (i.e., the iron is partly immersed in a neutral solution): anodic areas are separated from the cathodic regions, appearing near to the waterline where there is a ready availability of oxygen. It is important to note that neither the anodic nor cathodic reaction in the Evans droplet experiment involve the participation of sodium chloride.

The electrolyte function is to provide paths of high conductivity for the ionic current.

The Evans droplet has been performed more recently in stationary or dynamic (evaporating) conditions in order to determine the influence of the chloride concentration, the relative humidity and the droplet size on the occurrence of pitting corrosion under chloride solution droplets deposited onto stainless steels [20, 21, 90, 91]. No single critical chloride concentration or critical relative humidity for pit initiation was found [20, 91]. The increase of the chloride concentration during drying and the initial chloride concentration within the sessile droplet influence sharply the onset of pitting [20]. Tsutsumi *et al.* [21, 90] suggest that there is a decreased likelihood of pitting under small evaporating sessile droplets (with a diameter < 5 mm), because the smaller exposed area supports a less cathodic current. Hence despite a general agreement on the relative roles of the different controlling factors in the Evans droplet model, there is a lack of studies demonstrating how to control and predict the material damages under sessile droplets in environmental conditions. The purpose of the work developed in this thesis is therefore to investigate the corrosion phenomenon under sessile droplets from aqueous saline solutions, the salt-induced corrosion mechanism and the subsequent anodic/cathodic localisation inside stationary or evaporating sessile droplets.

II

Evaporation of Sessile Droplets from Aqueous Saline Solutions*

---

*Oral contributions containing main results of this PhD part have been presented at international conferences as:

- Virginie Soulié, Stefan Karpitschka, Florence Lequien, Philippe Prené, Thomas Zemb, Helmuth Moehwald and Hans Riegler. *Concentration Dependence of Coffee-Ring Formation in Sessile Droplets of Saline Solutions*. **The 1st International Workshop on Wetting and Evaporation: Droplets of Pure and Complex Fluids**, Marseilles, France, June 2013.
- Virginie Soulié, Stefan Karpitschka, Florence Lequien, Philippe Prené, Thomas Zemb, Helmuth Moehwald and Hans Riegler. *Evaporation Behavior of Sessile Droplets from Complex Fluids: Aqueous Saline Solutions*. **The 4th International Workshop on Crystallization in Porous Media**, Amsterdam, The Netherlands, June 2014.
- Virginie Soulié, Stefan Karpitschka, Florence Lequien, Philippe Prené, Thomas Zemb, Helmuth Moehwald and Hans Riegler. *Salt-Induced Marangoni Flows in Evaporating Sessile Droplets*. **The 7th Conference of the International Marangoni Association**, Vienna, Austria, June 2014.

1

EXPERIMENTAL METHODS AND EQUIPMENT

1.1 EXPERIMENTAL SETUP

Setup for evaporation experiments

In this thesis the evaporation experiments were performed with a new experimental setup designed and built by Karpitschka S. and Riegler H. (Max Planck Institute of Colloids and Interfaces, Potsdam) for the study of sessile droplets coalescence [104–107]. The main purpose of the setup is the real-time observation of sessile droplets from the top and the side simultaneously, with a few-micron scale resolutions.

Figure 1.1 shows a schematic illustration of the experimental setup for observing the evaporation process of sessile droplets. The evaporation behaviour was optically imaged from the top and the side. From above the sample one camera imaged the sessile droplets through a macro lens with extension tubes. Therefore the imaging scale or the field of view (FoV) from the top was improved. The sample area was homogeneously illuminated with a coaxial light system. In line with the camera and the sample, a flat mirror at a 45-degree angle to the optical axis was illuminated sidewards and casted light downwards on the sample area. This lighting design enhanced the contrast of the droplet contour. As a result, the local brightness of the droplet image can be translated into the local surface inclination. Simultaneously a second camera with an object-space telecentric lens inspected the side of the sessile droplets. Therefore the imaging scale or FoV remained constant over the whole sample depth (i.e., 2 cm): the apparent size and shape of the sessile droplets did not change with distance from the camera and across the entire FoV. The samples were illuminated from the opposite site with a telecentric illumination, i.e., a collimated light with very good uniformity and low divergence. The two insets in Figure 1.1 show as an example images of a sessile droplet few seconds after its deposition from the top and the side.

The evaporation experiments were performed in an environmental chamber under controlled temperature T and relative humidity RH. The relative humidity was adjusted with a constant gaseous flux (2000 ml.min^{-1}) of an appropriate mixture of dry and wet nitrogen (purity 5.0, Messer) through the environmental chamber. The gas flux was weak enough to avoid convective flows effects on the evaporation behaviour of the sessile droplets. The temperature was controlled by adjusting the temperature of the flow of moist nitrogen diffusing through the sample chamber with a high-precision temperature-controlled heating and cooling bath. Additionally the temperature and the relative humidity were also directly measured in the environmental chamber. All the evaporation experiments were carried out at T = (23.0 $\pm$ 0.5°).

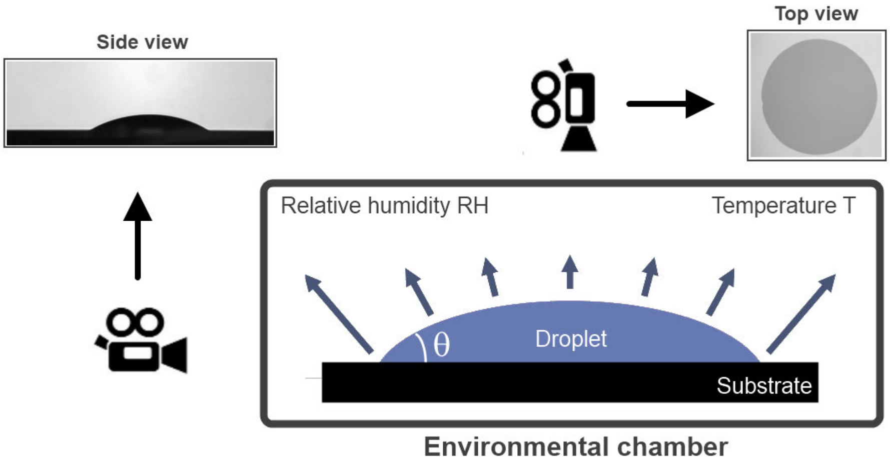

Figure 1.1 – *Schematic illustration of the experimental setup for observing the evaporation process of sessile droplets. The evaporation behaviour was optically imaged from the top and the side. The two insets show simultaneous top and side view images taken from a real experiment. The evaporation experiments were performed in an environmental chamber under controlled temperature T and relative humidity RH.*

Besides the experimental setup allows the "in-situ" visualization of the flow field inside the droplet with particle tracking velocimetry (PTV). For this purpose, the top view illumination is replaced by a monochromatic laser beam allowing the illumination of the fluid motion in a restricted observational area. A specific amount of fluorescent particles with a certain diameter is added in the droplet liquid (see next section for more detailed information). The observation of the particles movement within the droplet fluid reveals the direction of the liquid flow inside the droplet.

Data analysis of evaporation experiments

In a typical evaporation experiment, the dynamics of the sessile droplets' free surface topology were measured. Most relevant were the time evolution of the droplets contact angle $\theta(t)$ and their shape: the droplets radius $r(t)$ and height $h(t)$. The main droplet geometry parameters were derived from the optical imaging in the simultaneous top and side views. A specialized analysis software developed by Karpitschka S. (Max Planck Institute of Colloids and Interfaces, Potsdam) was used for the data analysis of the evaporation experiments.

From the top view, the contact area of sessile droplets with the substrate and their contact line motion could be observed on-line. The radii of the droplet footprint were measured from the top view images by taking the circle with an optimum match to the droplet perimeter (contact) line. The experimentally observed three-phase contact lines were in most cases quite circular, as depicted for instance in the top view inset of the Figure 1.1.

The droplet contact angles and heights were derived from the side aspect. Contours of the sessile droplets were extracted from the side view imaging and circle, ellipse or polynomial fitting methods were used to determine the droplet heights and contact angles. The most widely used method to measure, with accuracy, the droplet heights was the fitting of the droplet shape as a circular contour. This reconstruction is valid since sessile droplets were spherical cap-shaped. The usual dimensions (heights) of the sessile droplets in evaporation experiments were always below the capillary length. Therefore gravitation influences were negligible (see I.1.2). Thus sessile droplets kept a spherical cap shape over the evaporation process.

However to perform accurate contact angle measurements, the side contour aspect of sessile droplets was extrapolated with ellipses or polynomial equations[1]. Advancing (θ_{adv}) and receding (θ_{rec}) contact angles were determined by inflating and deflating the droplet, by adding/pumping liquid with the needle of the syringe embedded in the sessile droplet. The contact angles (left and right, as measured from the side view) at which the triple contact line started or stopped moving were averaged in order to measure θ_{adv} or θ_{rec}, respectively. The repeatability was determined by the substrate and not by the measurement method, since the contact angle hysteresis (i.e., the difference between the advancing and receding contact angles) arises in general from surface roughness and/or heterogeneity [65]. It was typically within $\pm 1^\circ$ for advancing and receding contact angles.

The volume of sessile droplets was determined by combining their top and side aspects: the time evolution of the radius of the contact area was measured from the top aspect and the droplet height from the side aspect. The top and side aspects of sessile droplets were correlated at the moment of the liquid disconnected from the tip of the syringe and changed its shape from a pendant droplet at the tip of the syringe to a sessile droplet on the substrate. The time difference between both images was calculated to correctly extrapolate both sessile droplets radius and height at each time t. Since the sessile droplet had a spherical cap shape, its volume was calculated from the measured heights $h(t)$ and radii $r(t)$ by:

$$V(t) = \frac{1}{2}\,\pi\,h(t)\left(\frac{h^2(t)}{3} + r^2(t)\right) \tag{1.1}$$

The droplet volume determined from the observed heights and radii was consistent with the volume adjusted with the syringe upon its deposition, V_0 (see II.2.1 for more detailed information). The main uncertainties for the droplet volume determination came from the vertical offset of the substrate baseline used in the droplet height measurements and the volume error upon deposition from the syringe. The substrate baseline uncertainty can be eliminated by determining its true position. For this purpose, the time correlation between top and side aspects of sessile droplets can be used to extrapolate the side aspect profile to the positions of the three-phase contact lines known from the top aspects. Typical corrections to the measured droplet heights were 40 μm, resulting in fluctuations of the calculated volumes smaller than 1%. The volume error from the syringe itself and from the manipulator was the main remaining uncertainty. This induced volume variations smaller than 5%.

1.2 MATERIAL AND SAMPLE PREPARATION

Sessile droplets from aqueous saline solutions, with different initial volumes ranging from 1 to 10 μl, were deposited with a syringe onto solid, planar and inert substrates.

Saline solutions and substrate

Two different saline solutions have been chosen for the evaporation experiments: sodium chloride NaCl (Sigma Aldrich) and magnesium chloride $MgCl_2$ (magnesium chloride hexahydrate, VWR Chemicals) solutions. The aqueous saline solutions were prepared with Millipore^{TM} water (resistivity 18 MΩ.cm^{-1}) with salt concentrations ranging from 10^{-7}M NaCl or 10^{-3}M $MgCl_2$ to the saturation limit, i.e., 6.1M NaCl or 5.7M $MgCl_2$ [108, 109]. Surface tension γ of the aqueous saline solutions increased with salt concentration c as presented in Figure 1.2

---

[1] The circular-like profile of the droplet shape under-predicts the contact angle values higher than 30°. The two other fitting methods allow the calculation over a wider range of contact angle values.

[39, 40, 42]. The magnesium chloride solutions were selected in comparison with sodium chloride solutions since their surface tension increment $\frac{\delta\gamma}{\delta c}$ is two times bigger for a similar salt concentration range (i.e., from pure water to saturated salt solution of about 6M) at (20-25)°C [44].

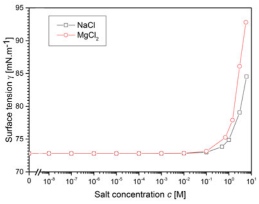

Figure 1.2 – *Surface tensions of aqueous NaCl and* $MgCl_2$ *solutions at* T = 20-25°C *[44].*

As substrates served pieces of single-sided polished silicon wafers (Si(100), p) either with a naturally oxidized surface (the oxide layer thickness was about 15 nm) or with an artificial (thermal) oxide layer. All wafers were supplied by Silchem, Freiberg, Germany. In both cases, the surface roughness was measured about less than 1 nm, as determined by non-contact atomic force microscopy (experimental analysis done by Stefan Karpitschka, Max Planck Institute of Colloids and Interfaces, Potsdam) and optical interferometry (experimental analysis done by Jean-Luc Lacour, DEN/DANS/DPC/SEARS/LANIE, French Atlernative Energies and Atomic Energy Commission, Gif-sur-Yvette). The wafers were cut into pieces of approximately 2 cm x 2 cm.

For PTV experiments, fluorescent polystyrene microspheres (Duke Scientific) with diameters of 2 μm were used. A concentrated solution of fluorescent particles was firstly prepared: they were diluted by a factor of 100 into milli-q water. Then 40 μl of this aqueous fluorescent particles solution was added in 2 ml of the measured aqueous saline solutions. The concentration of fluorescent particles within the sessile droplet from aqueous saline solutions was sufficiently high to correctly perform PTV experiments and sufficiently low to not interact with salt and modify the flow field (and the evaporation behaviour) inside the droplet. Great care was taken for the preparation and the storage of the salt-fluorescent particles solutions. Each solution was carefully agitated before use in order to obtain an homogeneous dispersion of particles within the liquid. The solutions containing fluorescent particles were stored in a dark place.

Cleaning procedure

To avoid/minimize the contamination by dust or any remaining chemical product, a precise and conscientious cleaning was done for the substrates, the syringe/needle and also the vessel. The stainless steel syringe needles were cleaned sequentially with milli-q water, ethanol (purity > 99.8%, Sigma Aldrich), two times with acetone (purity > 99.5%, Baker Analyzed), ethanol and water, each three times. Before use the syringe was cleaned three times with the measured aqueous saline solutions.

The cleaning procedure of the syringe was used as pre-cleaning for the wafers and the glassware. They were sonicated sequentially in each solution (milli-q water, ethanol and acetone) for 10 minutes. After pre-cleaning the substrates and the glassware were cleaned with piranha solution, i.e., a mixed solution of hydrogen peroxide (30%, Fluka) and concentrated sulfuric acid (98%, Sigma Aldrich) at a volume fraction of 1:3, respectively, for 30 minutes. After flushing five times with copious amounts of milli-q water, the samples were sonicated in milli-q water for 15 minutes in order to remove traces of acid and dust. The piranha treatment was concluded by another milli-q water rinse and sonication of about 15 minutes.

After cleaning the glassware were dried by blowing with nitrogen (purity 5.0, Messer) and dried over a night in a drying oven at 150°C. After the complete piranha treatment, the substrates were stored under milli-q water in a closed vessel to prevent contamination. All experiments were performed with freshly prepared substrates, i.e., no more than 8 hours after cleaning. Immediately before further usage, they were dried in a flow of pure nitrogen.

Thermal oxidation procedure

The equilibrium contact angles[2] θ_e of sessile water droplets on the freshly prepared substrates were about 1° with a very small hysteresis ($\leq 0.5°$). The contact angles did not change over the samples storage in milli-q water for up to 8 hours.

The wetting behaviour of sessile droplets from pure water (and also from aqueous saline solutions) is quite sensitive to the temperature treatment of the silicon wafers. This is attributed to the number of OH groups on the wafers surfaces [110]. In support of this hypothesis, the wettabilities of the wafers surfaces were changed by thermal oxidation.

Thermal oxidation was performed in ambient air at different elevated temperatures ranging from 250 to 1000°C. After cleaning and drying, the samples were annealed in an oven for about one hour in normal atmosphere at three different temperatures: 250, 500 and 1000°C. As a last step, the substrates were cooled down for about one hour in the oven. Residual dust was blown off with pure nitrogen before usage. One inconvenient of the thermal treatment was the short-term stability of the samples. 4 hours after the thermal treatment, the contact angle value decreased by at least 10%. For this reason, the samples were used within few hours after the final drying step.

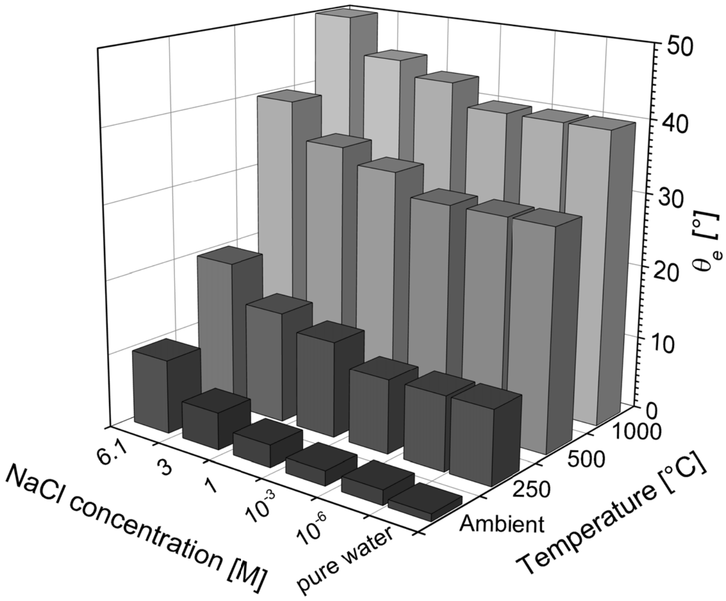

Figure 1.3 – *Contact angles measurements on thermally oxidized silica surfaces for pure (milli-q) water and different aqueous sodium chloride solutions.*

---

[2] Upon contact with the substrate, the sessile droplets spread towards their equilibrium shape. From a macroscopic point of view, the sessile droplets reached a quasi steady-state condition. Within seconds, the liquid-vapour interface hit on the solid substrate a (macroscopic) three-phase equilibrium contact angle θ_e.

Figure 1.3 shows the obtained contact angles with different thermal treatments for different aqueous sodium chloride solutions. Depending on the thermal treatment and on the sodium chloride concentration, the equilibrium contact angle varies between 1 and 50°.

EVAPORATION OF PURE WATER SESSILE DROPLETS

2

In this chapter we investigated the evaporation of sessile droplets from pure water. The aim of this chapter was to apprehend the issues of the evaporation process of sessile droplets from a simple and single liquid. Sessile droplets of pure water on planar, horizontal and inert solid substrates stood for the ideal evaporating case. But how did "ideal" sessile droplets from pure liquid evaporate?

The evaporation behaviour was optically imaged and measured from top and side aspects of the sessile droplet. The temporal study of the droplet volume and shape revealed the signature of the (expected) constant contact angle evaporation mode [3].

Quantitative evaporation experiments were performed at different relative humidities in the surrounding air, with various droplet contact angles and volumes. The main objective was to understand what is the influence of experimental parameters such as the relative humidity on the evaporation process and how important are the geometrical droplet contributions on the evaporation behaviour?

In particular we focused our study on the evaporation rate of the drying sessile droplets from pure water. We found that the evaporation rate was affected and related to the ambient hygrometry and on the droplet size and contact angle. The obtained relations were discussed and theoretically confirmed by analytically solving the evaporation process.

2.1 EVAPORATION BEHAVIOUR: NO-PINNING OF THE CONTACT LINE

Figure 2.1 shows the time evolution of the droplet volume calculated from the measured heights $h(t)$ and radii $r(t)$ (Eq.1.1) during the evaporation of a sessile droplet containing pure water at a relative humidity RH of 0%.

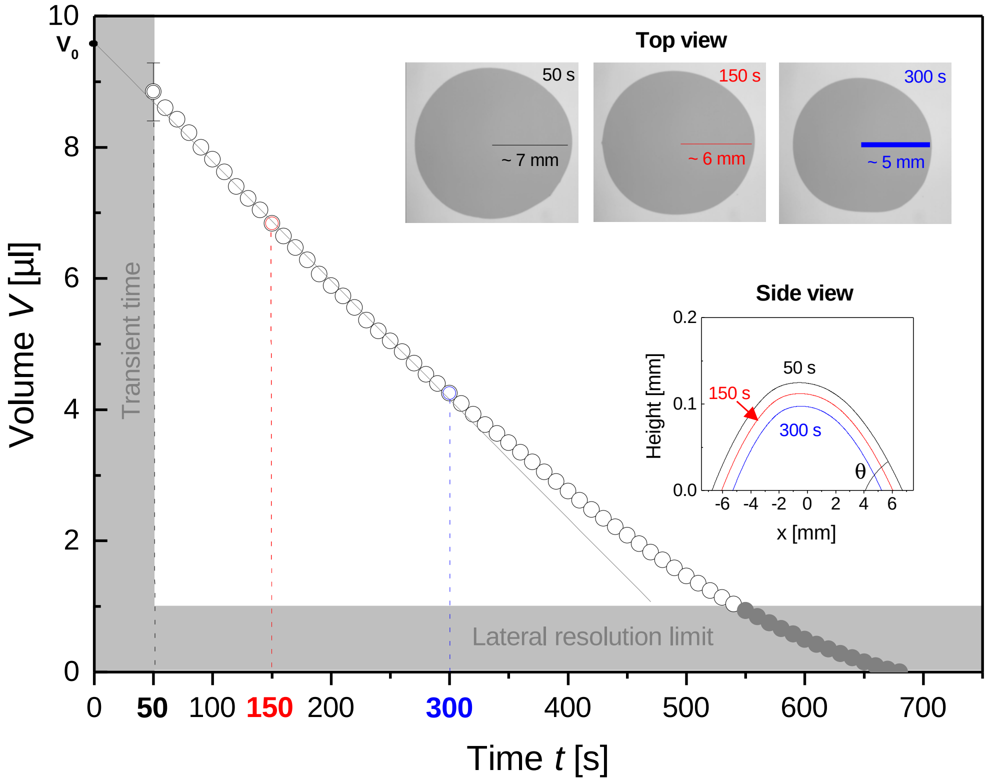

Figure 2.1 – *Evaporation of a sessile droplet from pure water at a relative humidity RH of* 0%. *The insets show the simultaneous height profile and top view images at three different evaporation times:* 50, 150 *and* 300 *s. The straight line depicts the linear decrease of the droplet volume with time experimentally observed at the initial stage of the evaporation (i.e., between* $t = 50$ *and* 300 *s). The extrapolation of this linear volume change yielded at* $t = 0$ *s the initially deposited volume* V_0.

At $t = 0$ s, the sessile droplet was deposited. This was the moment when the liquid (in the present case, pure water) disconnected from the tip of the needle and changed its shape from a pendant droplet at the needle tip to a sessile droplet on the substrate. Upon contact with the substrate, the sessile droplet spread towards its equilibrium shape. Typically the spreading took few seconds, slowing down rapidly. Empirically we found that this transient (spreading) time last less than 50 s. After this transient time, the sessile droplet reached from a macroscopic view point a quasi-steady state condition. The liquid-vapour interface hit on the solid substrate a (macroscopic) three-phase equilibrium contact angle θ_e of about 1°.

Depending on the size and contact angle of the sessile droplet and on the experimental conditions (relative humidity), there was a certain time window, where the sessile droplet shape and its temporal change can be measured quite accurately from the side view of the experimental setup. Accurate height values were obtained before the height of the sessile droplet became smaller than about 50 μm. Thus for all cases presented in this thesis, we can determine with accuracy the evaporation behaviour (i.e., the time evolution of the sessile droplet shape) after the transient time until the experimentally time observed at the lateral resolution limit (the lateral time).

In particular the loss of the sessile droplet volume was quantitatively and accurately calculated in this time window. Figure 2.1 presents the measured volume from the top and side imagings as a function of time. For sessile droplets from pure water, it was possible to measure it approximately after the lateral time and until the droplet totally evaporated (i.e., the sessile droplet volume reached a zero value). The corresponding volume data points are presented in Figure 2.1 as grey closed symbols after the lateral time.

The volume of the sessile droplet containing pure water decreased over the whole evaporation process. Between t = 50 and 300 s, the volume decrease was linear with time as depicted by the straight line in Figure 2.1. A linear extrapolation of the sessile droplet volume change (between t = 50 and 300 s) to t = 0 s yielded the initially deposited volume V_0, which was about 9.6 μl. As explained in the previous chapter (see II.1.1), the syringe manipulation resulted in fluctuations of its indicated volume (i.e., 10 μl) smaller than 5%. Therefore all droplets volume data presented in this thesis were scaled to their initial volume V_0, which was derived from the linear extrapolation of the evaporation curve, as presented in Figure 2.1, to t = 0 s:

$$\tilde{v} = \frac{V}{V_0} \tag{2.1}$$

For times much longer than 300 s, the droplet volume decreased more slowly with time: its change deviated from the linear decrease.

The two insets in Figure 2.1 show the sessile droplet height profile and the simultaneous top view images at three different evaporation times: t = 50, 150 and 300 s, as indicated in the main plot of the time evolution of the sessile droplet volume. The top view images confirm that the contact sessile droplet area with the substrate is reasonably circular in shape. Thus the sessile droplet radii were measured with confidence. Otherwise the top view images correlated with the height profiles show that the sessile droplet keeps its spherical-cap shape over the evaporation process. Therefore the hypothesis of a spherical cap-shaped sessile droplet to determine the droplet volume (Equation 1.1) was consistent and valid during the whole evaporation experiment.

In addition the top view images show that the sessile droplet radius decreases from about 7 to 5 mm between t = 50 and 300 s. Meanwhile the contact angle θ of the sessile droplet remains constant (about 1°), as depicted by the height profiles in the same time interval. As a consequence, after deposition and spreading, the sessile droplet of pure water retains a constant shape (i.e., a constant contact angle) with a decreasing footprint area during its evaporation. Sessile droplets of pure water evaporate in the unpinned, constant contact angle mode[1].

A linear decrease of the droplet volume is observed between t = 50 and 300 s as indicated in Figure 2.1 with a straight line. Thus an evaporation rate (i.e., a droplet volume change per time unit: $\frac{dV}{dt}$) is rather well defined and can be measured in this time interval. For times much longer (t > 300 s), the evaporation rate diminishes over the lifetime of the droplet. The deviation of the evaporation rate at further times was expected for the evaporation of sessile droplets in constant contact angle mode [3]. This will be explained in detail in the discussion section (see II.2.5).

---

[1] Minor deficiencies on the contact line pinning occurred during the evaporation of sessile droplets from pure water. They can be glimpsed in the lower right corner of the droplet footprint area in the top view image at t = 50 or 300 s (as depicted in the inset of Figure 2.1). They were induced by the very small contact angle observed when sessile droplets of pure water were deposited on silicon wafers.

2.2 Effect of Relative Humidity on Evaporation

Figure 2.2 shows the time evolution of the normalized droplet volume $\tilde{v}$ (Equation 2.1) during the evaporation of sessile droplets containing pure water at different relative humidities *RHs* of 0, 20, 40, 60 and 80%.

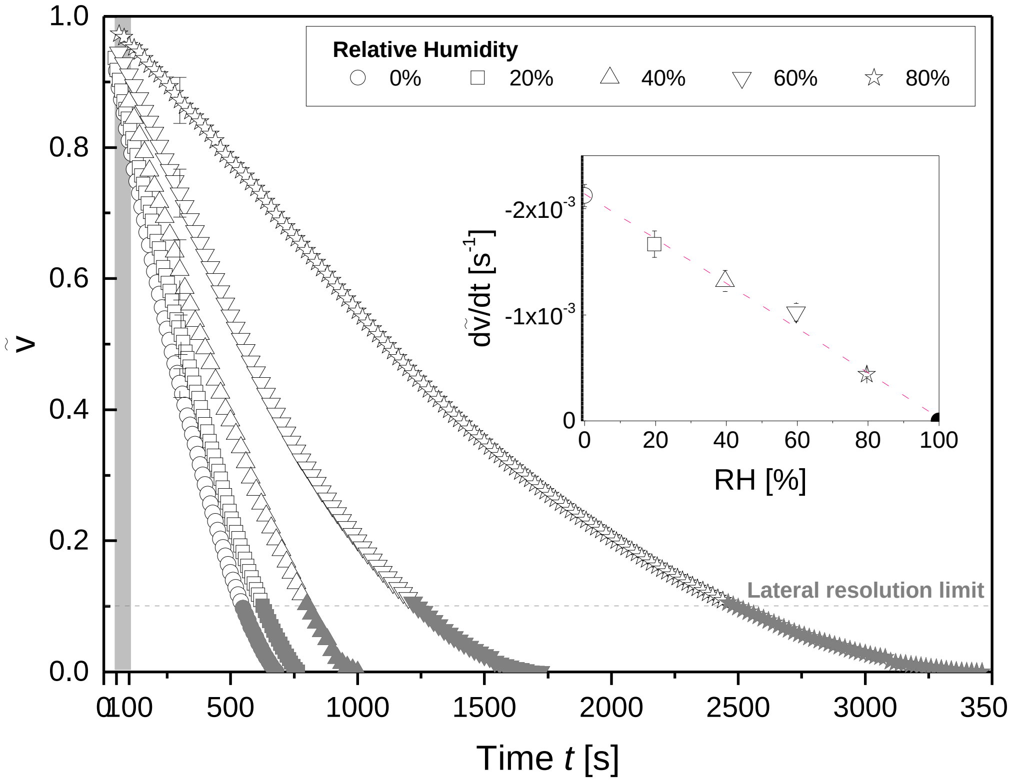

Figure 2.2 – *Evaporation of sessile droplets from pure water at different relative humidities RHs of* 0, 20, 40, 60 *and* 80% *(V_0* 10 *µl, $\theta \approx 1°$). The decrease of the normalized volume $\tilde{v}$ between t = 50 and 100 s after the sessile droplet deposition (marked in grey) was used to derive the evaporation rate $\frac{d\tilde{v}}{dt}$. The inset shows the variation of the evaporation rate $\frac{d\tilde{v}}{dt}$ as a function of the relative humidity RH.*

After droplets deposition at $t = 0$ s, their volume decrease linearly with time and then diminish more slowly (i.e., deviated from the temporal linear diminution) until the sessile droplets evaporate entirely. As explained in the previous section, there was a certain time window where the sessile droplet volume (in particular, the droplet height) can be measured accurately. After lateral time, the droplet height became too small to be determined with confidence. Thus the very end of the evaporation experiment showing the decrease of the droplet volume towards 0 μl is marked in Figure 2.2 with grey closed symbols.

Figure 2.2 shows that the relative humidity has no influence on the general form of the droplet volume-versus-time curve. The typical evaporation curve of a sessile droplet from pure water, as presented in Figure 2.1, was retained at higher relative humidity. In fact the entire evaporation behaviour was unchanged when the relative humidity of the sessile water droplet environment was modified. The characteristic temporal patterns of unpinned evaporating sessile droplets were observed: the droplet footprint area shrunk with time while their contact angle remained constant during the whole evaporation process. An example of the time evolution of the sessile droplet volume and shape (from top and side views) at higher relative humidity is shown in detail in Appendix A.1. It is interesting to notice that the constant contact angle adopted by the sessile water droplet with the silicon wafer kept the same value for all evaporation experiments, i.e., $\theta \simeq 1°$. Sessile droplets containing pure water evaporated in unpinned, constant contact angle mode irrespective of the relative humidity.

Nevertheless the relative humidity had an influence on the evaporation kinetics of sessile water droplets. At the initial stage of the evaporation process, the droplet volume decreased linearly with time. The time window, where the linear diminution of the droplet volume was observed, changed according to the relative humidity. Generally the evaporation curves evolved from a linear to a non-linear slope when the sessile droplet volume reached 4-5 μl. As a result an evaporation rate $\frac{d\tilde{v}}{dt}$ (i.e., a normalized droplet volume change per time unit) was rather well defined in a certain time period varying between t = 50 and > 1500 s depending on the relative humidity. In order to have a better comparison and to gain insight into the evaporation study of sessile droplets, the evaporation rate was always in this thesis measured between t = 50 and 100 s. This time period is marked in grey in Figure 2.2.

The inset in Figure 2.2 illustrates the variation of the evaporation rate $\frac{d\tilde{v}}{dt}$ as a function of the relative humidity. The evaporation rate is inversely proportional to the relative humidity of the sessile water droplet environment. The relative humidity had of course an impact on how long the evaporation process sustained, since RH stands for the ratio between the (imposed) vapour pressure above/at the droplet surface and the saturated vapour pressure of the liquid within the sessile droplet. More the water vapour pressure imposed in the ambient air increased towards the saturated vapour pressure of water (100% theoretically), which constituted the sessile droplet, less water molecules diffused from the droplet bulk to the ambient environment. Thus sessile water droplets should tend to an equilibrium condition with its environment when the ambient hygrometry augmented towards 100%. The equilibrium condition was observed when the relative humidity was 100%. As depicted in the inset of the Figure 2.2, the evaporation rate decreases with RH yields a zero value at RH = 100%. The relative humidity, where the sessile droplet neither evaporates nor condensates, is called the equilibrium relative humidity RH_{eq}. Our experimental RH_{eq} value determined for sessile droplets of pure water at T = 23°C agrees with the expected theoretical one [111].

2.3 EFFECT OF DROPLET CONTACT ANGLE AND SIZE ON EVAPORATION

Figure 2.3 shows the time evolution of the normalized droplet volume $\tilde{v}$ (Equation 2.1) during the evaporation of sessile water droplets with various contact angles θ ranging from 1 to 40° (Figure 2.3.A) and deposited with different initial droplet volumes V_0 from 1 to 10 μl (Figure 2.3.B) at a relative humidity RH of 0%.

As from 50 s after the droplets deposition, their volume was calculated from the measured $h(t)$ and $r(t)$ over the entire lifetime of the evaporating droplets. As shown in Figure 2.3.A, sessile droplets with higher contact angles adopt the typical evaporation profile that we observed at very low contact angle as depicted in Figure 2.1 (and also with a wide range of relative humidities, Figure 2.2). The droplet volume follows a temporal linear diminution and then, slowly decreases to reach a zero value. Similar behaviour is observed when the initially deposited droplet volume decreases from 10 to 1 μl (Figure 2.3.B). As a result the droplet contact angle and size has no influence on the evaporation profile of sessile droplets from pure water.

The detailed study of the temporal evolution of the droplet shape (from top and side aspects) at higher contact angles and at smaller droplet volumes revealed that the evaporation mode of sessile water droplets was retained. An example of this investigation at a higher contact angle and at a smaller droplet size is illustrated in detail in Appendix A.1. The footprint of the droplet contact area with the substrate receded over the lifetime of the evaporating droplet.

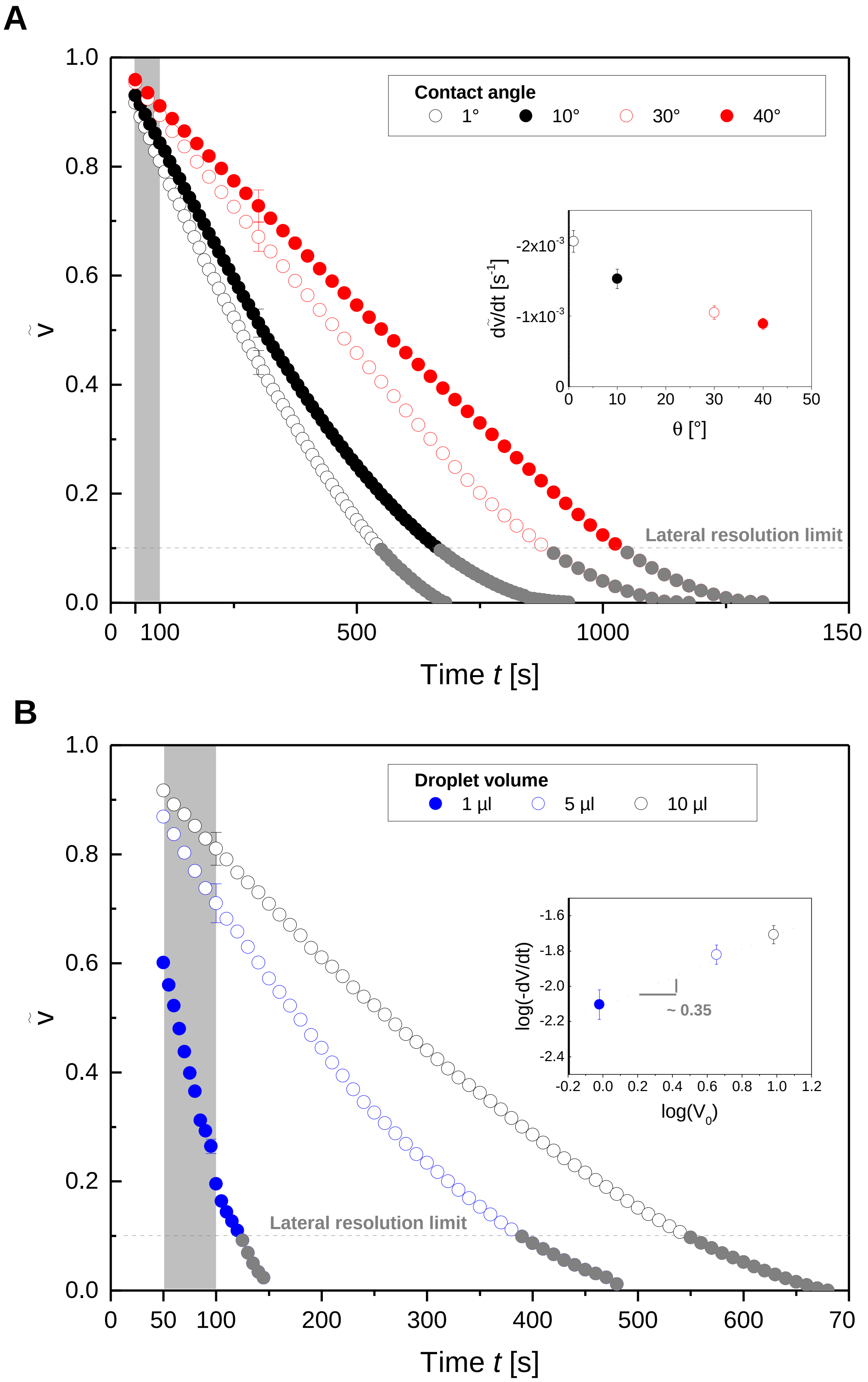

Figure 2.3 – *Evaporation of sessile droplets from pure water* ***A.*** *with various contact angles θ ranging from* 1 *to* 40° *(V_0* 10 *μl) and* ***B.*** *at different initial droplet volumes V_0:* 1, 5 *and* 10 *μl (θ ≈* 1°*) at RH* 0%*. The decrease of the normalized volume $\tilde{v}$ between t* = 50 *and* 100 *s after the sessile droplet deposition (marked in grey) was used to derive the evaporation rate $\frac{d\tilde{v}}{dt}$. The inset shows the variation of:* ***A.*** *the evaporation rate $\frac{d\tilde{v}}{dt}$ as a function of θ and* ***B.*** *the logarithm of the evaporation rate $\frac{dV}{dt}$ as a function of the logarithm of V_0.*

Meanwhile the contact angle of the droplet remained constant. Our evaporation experiments show that the contact angle of sessile water droplets on naturally oxidized silica wafers is independent of the droplet size. Irrespective of the geometrical parameters of sessile droplets (i.e., the size and contact angle), sessile droplets containing pure water evaporate in unpinned, constant contact angle mode.

The decrease of the normalized volume $\tilde{v}$ at the initial stage of the evaporation process (arbitrarily chosen between t = 50 and 100 s) was used to derive the evaporation rate $\frac{d\tilde{v}}{dt}$. The inset in Figure 2.3.A shows the variation of the evaporation rate as a function of the contact angle θ. It diminishes as the droplet contact angle increases. Thus increasing the contact angle of the sessile droplet led to an augmentation of its lifetime. The contact angle effect on the evaporation rate can be explained by the singularity of the vapour flux diffusing from the free surface of the droplet into the surrounding air at the droplet edge. At lower contact angles, the vapour flux diverged significantly in the droplet edge region. On contrary when the contact angle increased towards 90°, the non-uniformity of the vapour flux along the droplet free surface was reduced. Therefore increasing θ from 1 to 40° induced a more uniform vapour flux along the surface of sessile droplets from pure water and hence a temporal diminution of the evaporation process.

The opposite behaviour is observed when the initially deposited droplet volume is decreased from 10 to 1 μl as shown in Figure 2.3.B. A sessile droplet evaporates faster as its initial volume decreases. As a consequence the evaporation rate of sessile droplets $\frac{dV}{dt}$ (to simplify the argumentation) should depend on the droplet volume: $\frac{dV}{dt} \propto V_0^{\alpha}$, with α a constant. The inset in Figure 2.3.B shows the variation of the logarithm of the evaporation rate $\frac{dV}{dt}$ as a function of $log(V_0)$. We find that $\frac{dV}{dt}$ is proportional to approximately the third power of V_0 ($\alpha \approx 0.35 \pm 0.02$), as depicted in the inset of the Figure 2.3.B. Since the droplet volume is related to its radius[2] r, the evaporation rate was proportional to the droplet size. Our experimental results are consistent with the expected evaporation behaviour of sessile droplets from pure liquid [3]. The dependence of the evaporation rate on the geometrical droplet parameters will be explained in detail in the discussion section (see II.2.5).

2.4 THEORETICAL ANALYSIS OF EVAPORATION

According to Picknett and Bexon[3], the change of the normalized droplet volume $\tilde{v}$ with time t of a spherical cap shaped sessile droplet with a contact angle θ in the quasi steady-state with diffusion-driven evaporation is given by:

$$\frac{d\tilde{v}}{dt} = -4\,\pi\,\left(\frac{3}{\pi}\right)^{\frac{1}{3}}\,\frac{D\,M}{\rho\,R\,T}\,P_{sat}\,(1-RH)\,\frac{\tilde{v}^{\frac{1}{3}}}{V_0^{\frac{2}{3}}}\,\frac{f(\theta)}{\beta^{\frac{1}{3}}} \tag{2.2}$$

with D as diffusion coefficient of water in air, M as molecular weight of water, ρ as water density, R as gas constant, T as temperature, P_{sat} as saturated water vapour pressure at/above the droplet surface, RH as relative humidity in the background environment, β and $f(\theta)$ as functions of the contact angle θ, with:

$$\beta = (1 - cos(\theta))^2\,(2 + cos(\theta)) \tag{2.3}$$

---

[2] The volume of the sessile droplet V is proportional to the radius of the sphere forming the spherical cap R_S to the power of three which itself is related to the droplet radius r to the power of three: V $\sim R_S^3 \sim r^3$. The geometrical relationship between these three geometrical parameters was explained in the scientific background part (see I.1.2).

$$f(\theta) = \frac{1}{2} \cdot \begin{cases} 0.6366\ \theta + 0.09591\ \theta^2 - 0.06144\ \theta^3 & \text{for } \theta < 10^\circ \\ 0.00008957 + 0.6333\ \theta + 0.1160\ \theta^2 - 0.08878\ \theta^3 + 0.01033\ \theta^4 & \text{for } \theta \geq 10^\circ \end{cases} \tag{2.4}$$

The geometrical contributions can be combined as a function of the contact angle $\tilde{f}(\theta)$:

$$\tilde{f}(\theta) = \frac{f(\theta)}{\beta^{\frac{1}{3}}} \tag{2.5}$$

Note that $\tilde{f}(\theta)$ is as an exponentially decreasing function towards $\tilde{f}(\theta = 90^\circ)$ = 0.4 between θ = 0 and 90°.

Since the temperature and the contact angle θ remained constant over the whole evaporation experiments of sessile droplets from pure water, Equation 2.2 can be integrated as follows:

$$\tilde{v}^{\frac{2}{3}} = 1 - \frac{4}{3}\pi \left(\frac{3}{\pi}\right)^{\frac{1}{3}} \frac{V_0^{-\frac{2}{3}}\ M}{\rho\ R\ T}\ D\ P_{sat}\ (1 - RH)\ \tilde{f}(\theta)\ t \tag{2.6}$$

Equation 2.6 reveals that for sessile droplets evaporating in unpinned, constant contact angle mode, the (normalized) droplet volume to the power of two third $\tilde{v}^{\frac{2}{3}}$ decreases linearly with time. In addition the slope of $\tilde{v}^{\frac{2}{3}}$-versus-time is proportional to the relative humidity RH and also to a geometrical function of the contact angle $\tilde{f}(\theta)$ (Equation 2.5). Therefore a variation of the relative humidity or the contact angle will give us different slopes of the $\tilde{v}^{\frac{2}{3}}$-versus-time curves and hence an estimation of D, the diffusion coefficient of water in the surrounding environment [3].

Determination of the diffusion coefficient D

In order to facilitate the analysis of the evaporation results and to have a better comparison, the time t was scaled to the final time t_F, which was derived from the evaporation curve to V or $\tilde{v}$ = 0 μl:

$$\tilde{t}_F = \frac{t}{t_F} \tag{2.7}$$

Therefore with the rescaled time $\tilde{t}_F$, Equation 2.6 reads as:

$$\tilde{v}^{\frac{2}{3}} = 1 - \underbrace{\frac{4}{3}\pi \left(\frac{3}{\pi}\right)^{\frac{1}{3}} \frac{t_F\ V_0^{-\frac{2}{3}}\ M}{\rho\ R\ T}\ D\ P_{sat}\ (1 - RH)\ \tilde{f}(\theta)}_{S_i,\ i\ =\ \text{RH or } \theta}\ \tilde{t}_F \tag{2.8}$$

Figure 2.4 shows the evolution of the normalized droplet volume to the power of two third $\tilde{v}^{\frac{2}{3}}$ of evaporating sessile droplets from pure water as a function of the normalized time $\tilde{t}_F$ at different relative humidities from 0 to 80% (Figure 2.4.A) and at different contact angles ranging from 1 to 40° (Figure 2.4.B).

Irrespective of the relative humidity or the contact angle, the normalized droplet volume to the power of two third $\tilde{v}^{\frac{2}{3}}$ decreases linearly with the normalized time $\tilde{t}_F$. The linear decrease of

---

[3] A variation of the droplet size can also be used to estimate the diffusion coefficient of water in the background environment. For this purpose, the geometrical contributions in the evaporation rate equation (Equation 2.2) should be modified to highlight the droplet radius instead of the normalized droplet volume and the function β: $\left(\frac{3\tilde{v}}{\pi\beta}\right)^{\frac{1}{3}} = \frac{r}{V_0\ sin(\theta)}$. Furthermore the droplet radius should be approximated as a constant which is consistent, since the evaporation rate was determined as a constant in an initial short evaporation period. Nevertheless the evaporation of sessile droplets from pure water was only studied at three different volumes which may be insufficient to determine correctly D. This study supported the experimental value obtained for the diffusion coefficient of water in air.

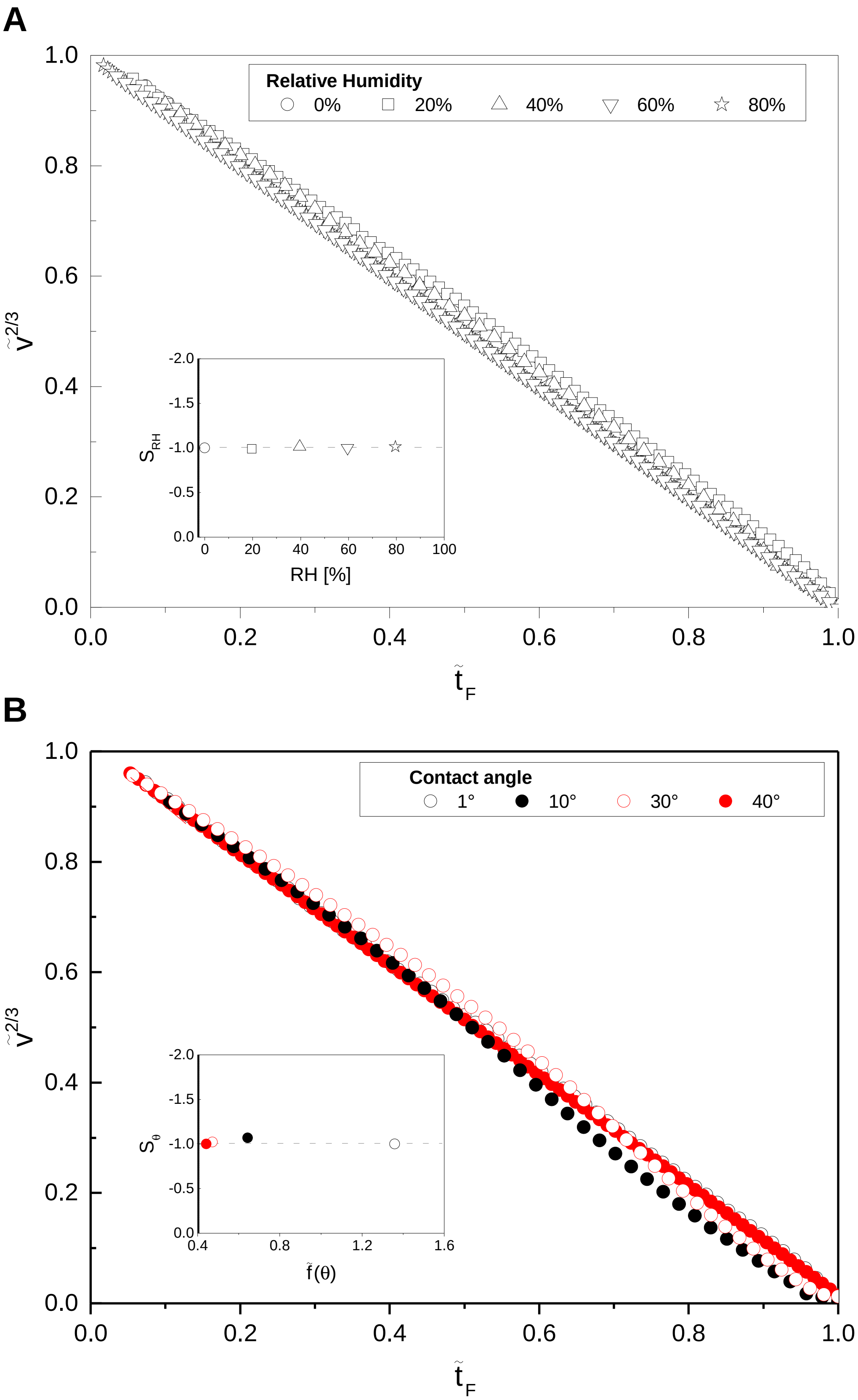

Figure 2.4 – *Evaporation of sessile droplets from pure water* **A.** *at different relative humidities RHs from* 0 *to* 80% *(V_0 10 μl, $\theta \approx 1^\circ$) and* **B.** *with various contact angles θ ranging from* 1 *to* 40° *(V_0 10 μ) at RH* 0%. *The linear decrease of the normalized volume to the power of two third $\tilde{v}^{\frac{2}{3}}$ with the normalized time $\tilde{t}_F$ was used to derive the slope S_i (i = RH or θ). The inset shows the variation of: the slope of the curve* **A.** *S_{RH} as a function of RH and* **B.** *S_θ as a function of $\tilde{f}(\theta)$.*

$\tilde{v}^{\frac{2}{3}}$ with time is a signature of evaporating sessile droplets with unpinned three-phase contact line [3]. Thus Figure 2.4 confirms the experimental observations of the top and side aspects of sessile water droplets evaporating with different RHs or with various θ, as described in the previous sections. Sessile droplets from pure water evaporated in unpinned, constant contact angle irrespective of the relative humidity and the droplet contact angle (and also the droplet size).

In all cases, $\tilde{v}^{\frac{2}{3}}$ decreased linearly with $\tilde{t}_F$. There were well-defined slopes S_i (i = RH or θ) for each studied relative humidity (0, 20, 40, 60 and 80%) or each contact angle adopted by sessile water droplets on the substrate (1, 10, 30 and 40°). The two insets depicted in Figure 2.4 show the linear variation of the slopes S_i ($i = RH$ or θ), derived from the linear decrease of $\tilde{v}^{\frac{2}{3}}$ with $\tilde{t}_F$ at different relative humidities or with different droplet contact angles, as a function of the relative humidity (Figure 2.4.A) or the function of the contact angle $\tilde{f}(\theta)$ (Figure 2.4.B). The slope values correlated to the experimental parameters and constants values allowed the determination of the diffusion coefficient of water in the surrounding air. At a temperature of 23°C, we found $D \approx 2.9 \text{ x } 10^{-5} \pm 0.2$ m^2.s^{-1}. This experimental value was comparable with the value of 2.5 x 10^{-5} m^2.s^{-1} from the literature [66, 112].

2.5 Discussion and outlook

Here we investigated the evaporation of sessile droplets from pure water on planar, horizontal and inert substrates. The study of the time evolution of the sessile droplet volume and shape (Figure 2.1) revealed the signature of evaporating sessile droplets in unpinned, constant contact angle mode. This evaporation mode was expected and experimentally observed for sessile droplets containing pure liquids [3, 64–66] since any particle or surface heterogeneities/roughness induce a pinning of the contact line.

The lifetime of an evaporating sessile droplet depends on the manner in which it evaporates. As explained in the scientific background part (I.2.3), sessile droplets can evaporate in unpinned, constant contact angle mode as sessile water droplets and/or in pinned, constant contact area mode (i.e., the diameter of the droplet footprint area remains constant while its contact angle decreases with time) [3, 113]. In particular the evaporation curves presented in Figures 2.1, 2.2 and 2.3 illustrate the sometimes overlooked result first qualitatively obtained by Picknett and Bexon[3] that a sessile droplet evaporating in constant contact angle mode has a longer lifetime than an initially identical droplet evaporating in pinned, constant contact area mode (i.e., any transition in the evaporation kinetics is observed for evaporating pinned sessile droplets). As Picknett and Bexon[3] described at the initial stage of the evaporation, the droplet volume decreased linearly with time in both evaporation modes. Nevertheless the evaporation curve for constant contact angle mode diverged significantly towards the end of the droplet lifetime. Any elusive reason of this behaviour was advanced by the Picknett and Bexon evaporation model [3].

Our experimental results confirmed the tendency of unpinned sessile droplets from water to evaporate slower at the end of the drying. This may arise from the formation of a thin water film at the very last stage of the droplet evaporation [114]. The disjoining pressure arising in the flattening drying droplet may favor the formation of a thin and stable water film. The evaporation rate of this thin water film should be markedly slower because of interfacial forces between the solid-liquid and the liquid-vapour interfaces. Therefore the formation of a thin water film close to the complete drying evaporation will retard the evaporation process. Our experimental results provided encouraging support for the theoretical predictions from the

Picknett and Bexon model [3].

Quantitative evaporation experiments on sessile droplets containing pure water were performed at different RHs from 0 to 80%, with various droplet contact angles ranging from 1 to 40° and initially deposited volumes from 1 to 10 μl. The evaporation characteristics of sessile droplets from pure water was retained with higher RH, at higher θ and at smaller V_0. The environmental condition and the geometrical contributions had no influence on the unpinning evaporation behaviour of sessile droplets from pure water.

Nevertheless the evaporation rate depended on these different parameters as illustrated in Figures 2.2 and 2.3. The temporal change of the normalized droplet volume $\frac{d\bar{v}}{dt}$ decreased as:

- RH decreased towards 100% as illustrated in Figure 2.2. When increasing the RH value, the environment of the sessile droplet from pure water became more saturated with vapour concentration. Since the evaporation process is diffusion-limited, the transfer of water molecules in air is lowered and thus the kinetics of evaporation slowed down.

- θ increased as shown in Figure 2.3.A. This relationship came from the presence of a wetted area limited by a contact line when the problem of an evaporating sessile droplet is considered. For a hemispherical droplet, the evaporative flux along the droplet surface is constant. A divergence of the vapour flux at the droplet edge occurred for contact angles smaller than 90°, i.e., for spherical-cap shaped (sessile) droplets [53]. Therefore as the contact angle decreased from 90 to 1°, the singularity of the evaporative flux near the droplet edge region was enhanced. Notwithstanding the relationship between the evaporation and the contact angle was simple and exact.

- The temporal change of the droplet volume $\frac{dV}{dt}$ decreased as $V_0^{\frac{1}{3}}$ decreased as depicted in Figure 2.3.B. The evaporation of a hemispherical or spherical-cap shaped droplet is proportional to the droplet radius ($R_S \sim r \sim V^{\frac{1}{3}}$). Thus the rate of droplet evaporation is proportional to the droplet radius and not to the surface area of the droplet [115]. Therefore large droplet evaporated faster than small droplet.

These experimental observations are in agreement with the Picknett and Bexon evaporation model [3] (Equation 2.2). As expressed in Equation 2.2, the evaporation rate depends on the vapour pressure difference $P_{sat}(1 - RH)$ (with P_{sat} the saturated water vapour pressure at/above the droplet surface), on the droplet size and on a function of the contact angle $\tilde{f}(\theta)$. Furthermore the normalized droplet volume to the power of two third derived from the evaporation rate equation decreased linearly with time. This linear decrease is a well-known property for sessile droplets evaporating in unpinned, constant contact angle mode. It was experimentally demonstrated in Figure 2.4 and theoretically useful to determine D, the diffusion coefficient of water in air.

To conclude we demonstrated in this chapter that the evaporation of sessile droplets from pure liquid was an unexpectedly complicated process. From an experimental viewpoint, the evaporation was controlled by the diffusion of the volatile compound in the atmosphere. The theoretical analysis of the evaporation process is acceptably understood and coherent with the experiments. Future project will include modelisation of the evaporation process of sessile droplet from pure liquid.

3

Evaporation of Sessile Droplets from Sodium Chloride Solutions*

In this chapter we investigated the evaporation of sessile droplets from sodium chloride solutions. The aim of this chapter was to understand how did an aqueous sessile droplet containing a non-volatile and soluble component evaporate?

The evaporation of this aqueous binary mixture was not as straightforward as simple and single liquid. The non-volatile component, in our case sodium chloride (NaCl), enriched as the volume of the evaporating droplet decreased. Thus, the following questions arose: where and when did the salt enrichment occurred inside the droplet? What was the impact of this enrichment on the evaporation behaviour and rate? Will it lead to a pinning of the three-phase contact line? Did the sessile salty droplet evaporate faster or slower than sessile water droplets? In the following, we addressed those questions.

For this purpose, as in the previous chapter, quantitative evaporation experiments were performed. We studied the impact of the relative humidity in the surrounding environment, the droplet size and contact angle as well as the initial sodium chloride concentration on the evaporation and particularly, on the evaporation rate. The main objective was to apprehend step-by-step the influence of each parameter on the evaporation of sessile salty droplet, based on the theoretical approach described in the previous chapter for the evaporation of sessile droplet from pure liquid.

The normalization step-by-step of the measured evaporation rate with the influential parameters (i.e., the environmental relative humidity and the geometrical contributions) had for objective to focus on the impact of salt concentration on evaporation and to ultimately achieve an universal, free-unit, evaporation rate equation. Particle tracking velocimetry experiments, correlated to a comparison of the theoretical/experimental value of the evaporation rate, allowed us to figure out the influence of the flow pattern, in particular the Marangoni effect along the evaporating droplet surface, and its feedback on the evaporation profile.

---

*Published as: Virginie Soulié, Stefan Karpitschka, Florence Lequien, Philippe Prené, Thomas Zemb, Helmuth Moehwald and Hans Riegler. The Evaporation Behavior of Sessile Droplets from Aqueous Saline Solutions. *Physical Chemistry Chemical Physics*, **17**, 22296-22303, 2015.

3.1 EVAPORATION BEHAVIOUR: PINNING OF THE CONTACT LINE

3.1.1 Evaporation Behaviour

Figure 3.1 shows the time evolution of the droplet volume calculated from the measured heights $h(t)$ and radii $r(t)$ during the evaporation of a sessile droplet containing 10^{-3}M NaCl (sodium chloride) at a relative humidity RH of 0%.

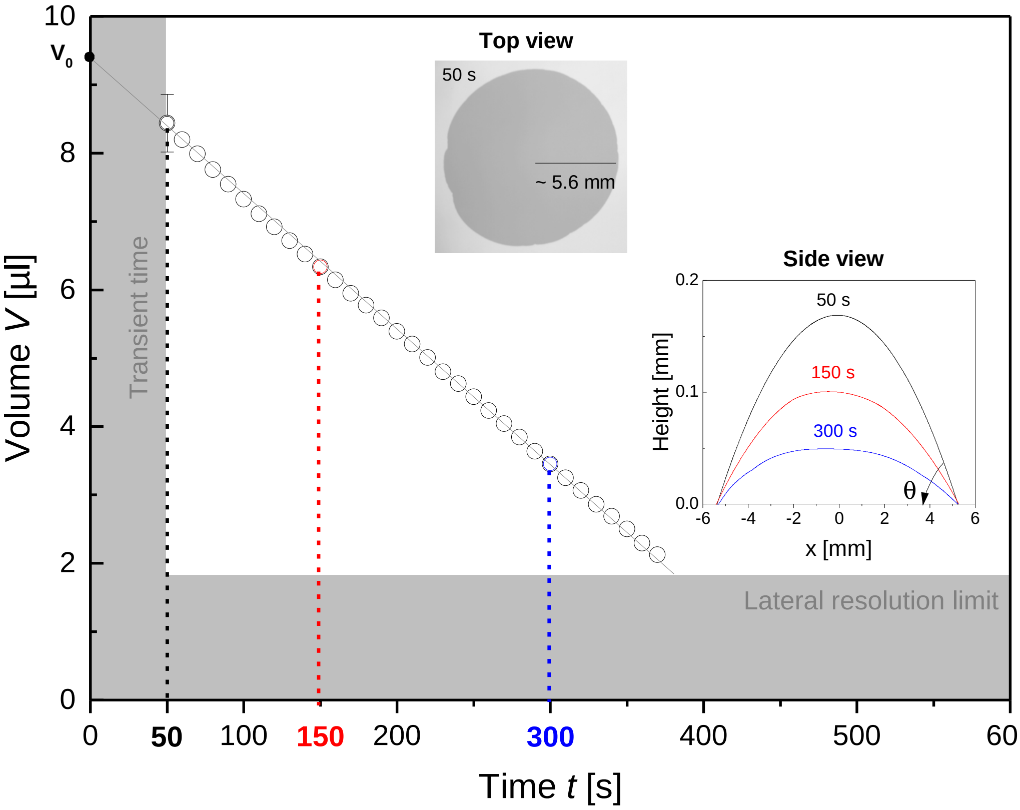

Figure 3.1 – *Evaporation of a sessile droplet from* 10^{-3}*M NaCl at a relative humidity RH of* 0%*. The inset plot shows the height profile at three different evaporation times:* 50, 150 *and* 300 *s. The other inset shows top view image* 50 *s after droplet deposition. The straight line depicts the linear decrease of the droplet volume with time experimentally observed. The extrapolation of this linear volume change yielded at* $t = 0$ *s the initially deposited volume* V_0.

At $t = 0$ s, the sessile droplet was deposited with a syringe on the substrate. Upon contact with the substrate the sessile droplet spread towards its equilibrium shape. Typically the spreading took few seconds, slowing down very quickly. Empirically we found that this transient (spreading) time last less than 50 s irrespective of the liquid (pure water or NaCl solutions) contained in the sessile droplet. After this transient time, the sessile droplet reached a quasi-steate condition from a macroscopic viewpoint. The sessile droplet from 10^{-3}M NaCl on the solid substrate adopted a (macroscopic) three-phase equilibrium contact angle θ_e of about $2 \pm 0.5°$. This value is relatively close to the equilibrium contact angle obtained with sessile water droplet in the same experimental conditions.

As explained in the previous chapter, the temporal change of the droplet shape was measured on a certain time window. Accurate height values were obtained from the transient time (i.e., 50 s after droplet deposition) until the lateral time whose its value depends on the salt concentration, the droplet size and contact angle and also on the relative humidity. Thus the evaporation behaviour of the sessile droplet (i.e., the time evolution of the droplet shape) was determined with confidence after the transient until the lateral times.

In particular the temporal change of the droplet volume was calculated in this time window. Figure 3.1 presents the measured droplet volume from the top and side aspects as a function of time. The volume of the sessile droplet containing 10^{-3}M NaCl decreases linearly with time over the whole studied evaporation range. As shown in Figure 3.1, the straight line depicts the linear temporal decrease of the sessile droplet volume. In comparison with sessile water droplets, there was no deviation of the droplet volume at further times. This indicates that the evaporation behaviour of sessile droplets from aqueous sodium chloride solutions may behave differently as pure water. The linear extrapolation of the sessile droplet volume decrease to t = 0 s revealed typically a variation of the initially deposited volume V_0 by about 5%.

The side view inset in Figure 3.1 shows the droplet height profiles at three different evaporation times (i.e., t = 50, 150 and 300 s) as determined from the side view imaging. The other inset shows the top view image of the sessile droplet at t = 50 s. These two insets in Figure 3.1 illustrate that the sessile droplet keeps its spherical-cap shape over the evaporation process[1]. Thus as for sessile water droplets the volume of salty droplets can be calculated accurately (Equation 1.1) assuming a spherical cap shape during the whole evaporation experiment (observed in the time window).

Additionally the height profiles show that the contact angle θ decreases between t = 50 and 300 s. Meanwhile the sessile droplet radius remains constant ($r \sim 5.6$ mm), as depicted in the side aspect profiles. After deposition and spreading the three-phase contact line of a sessile droplet from 10^{-3}M NaCl pinned. As a result the footprint area of the sessile droplet from 10^{-3}M NaCl remained constant while its contact angle decreased during its evaporation. Sessile droplets from 10^{-3}M NaCl evaporated in the pinned, constant contact area mode.

The evaporation experiments of sessile droplets from aqueous NaCl solutions were performed with seven decades of initial sodium chloride concentrations from 10^{-8} to 6.1M (i.e., to the saturation limit). Above a concentration of 10^{-6}M NaCl, the sodium chloride concentration had no influence on the evaporation curve (i.e., on the droplet volume-versus-time curve). The droplet volume-versus-time curve depicted in Figure 3.1 was representative of the typical evaporation curve obtained with NaCl concentrations ranging from 10^{-6} to 6.1M. In fact the entire evaporation behaviour presented in Figure 3.1 was unchanged when the salt concentration varied between 10^{-6}M to to the saturation limit. The characteristic temporal patterns of pinned evaporating sessile droplets were observed: the contact angle decreased with time while the footprint of the droplet contact area with the substrate remained constant over the lifetime of the evaporating droplet. Examples of the time evolution of the sessile droplet volume and shape (from top and side views) at different representatives sodium chloride concentrations are shown in detail in Appendix A.2.1. Sessile droplets from aqueous sodium chloride solutions evaporated in pinned, constant contact area mode for NaCl concentrations higher than 10^{-6}M.

In contrast for sodium chloride concentrations smaller than 10^{-7}M we found that the sessile droplets evaporated in unpinned, constant contact angle mode as sessile water droplets. After deposition and initial spreading the sessile droplets containing very low NaCl concentrations did not pinned and retained a constant shape (constant contact angle) with a decreasing footprint area during evaporation. Thus our evaporation experiments performed in a wide range of NaCl concentrations revealed that a very small amount of sodium chloride in sessile water

---

[1] Since the three different droplet height profiles were presented in the same plot the side aspect of the sessile droplet appeared as geometrically distorted for $t \geq 150$ s. Different scaling for each droplet height profile confirms the spherical caps during the whole evaporation process.

droplets changed drastically the evaporation behaviour. The transition between pinning and no-pinning evaporation occurred at a quite very low NaCl concentrations.

3.1.2 Pattern Formation

Figure 3.2 shows top views of the deposition pattern obtained after complete evaporation of sessile droplets from aqueous sodium chloride solutions at different concentrations of NaCl ranging from 10^{-6} to 6.1M at a relative humidity of 0%.

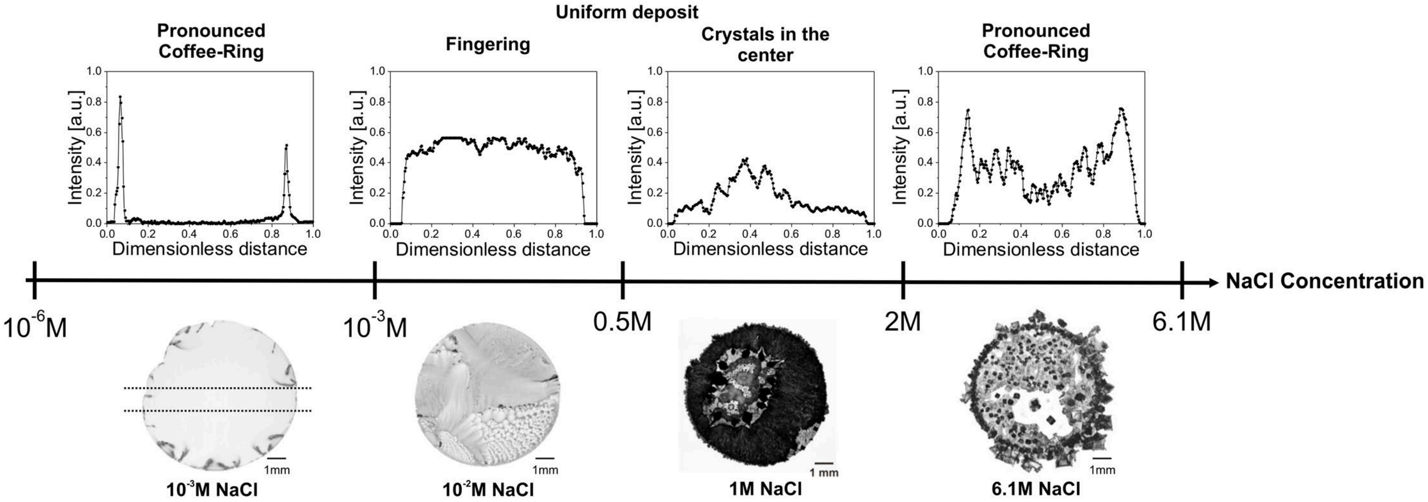

Figure 3.2 – *Morphologies of the final deposit obtained after complete drying of sessile droplets containing aqueous NaCl solutions at different initial salt concentrations from* 10^{-6} *to* 6.1*M NaCl. The evaporation experiments were performed at a relative humidity RH of* 0% *with* 10 *µl-sessile droplets. At the top of each final deposition pattern is shown the corresponding intensity profile illustrating the deposition distribution over the droplet footprint diameter. Note that the profile shows the inverted grey scale of the corresponding top view image of the sessile droplet, measured with an image analysis software.*

Figure 3.2 reveals that the morphologies of the final dried deposit change with increasing sodium chloride concentration. The corresponding plot of each dried sessile picture shows its reflected light intensity profile as a function of the radial position along the droplet diameter (i.e., the radial position scaled with the droplet diameter). The intensity profile was derived from the middle of the droplet footprint area along its diameter and averaged over 10% of the deposition diameter (i.e., within the dotted lines depicted on 10^{-3}M NaCl deposit picture). The intensity is proportional to the inverse of the grey scale in the final deposit picture, which in turn may correspond to the concentration of the precipitated salt. The intensity was determined from the grey scale of the top view image of the sessile droplet, measured with an image analysis software (Image J). To better reveal the pattern deposit, the image contrast was enhanced so that the background substrate appears white and the sessile droplet in grey scale. As a first approximation, we assumed a linear relationship between the grey scale and salt area enrichment. Notwithstanding the intensity profile plot was relatively useful to illustrate the deposition distribution of each final deposit picture but was not at all an absolute measure of the salt density.

From 10^{-6} to 10^{-3}M NaCl, the final deposit obtained after complete evaporation exhibits the classical "coffee-ring" deposition (see I.3.1). Most of the precipitation of sodium chloride is concentrated at the droplet edge. A closer examination with optical microscopy confirmed the outer deposition ring of salt in this NaCl concentration range[2]. Very few NaCl precipitates occupied the droplet center. Similar deposition patterns are observed at very high sodium chloride concentrations. Above a NaCl concentration of 2M nearly all the precipitated sodium chloride are deposited at the initial pinned contact line. A very pronounced salt-ring at the droplet edge is observed as shown in the fourth picture in Figure 3.2. In comparison to very low NaCl concentrations (below 10^{-3}M NaCl), some sodium chloride crystals surrounding by dendrites are deposited in the droplet center.

For intermediate NaCl concentrations (i.e., between 10^{-2} to 1M NaCl), the deposition patterns change dramatically as depicted by the second and third pictures in Figure 3.2. A more uniform salt deposition is observed as illustrated in the corresponding intensity profiles. The complete footprint area is covered with micro-crystallites of different morphologies including fingers, fractal aggregates, fractal branches and even crystals which appeared in the droplet center.

Our observations suggest that the different morphologies of the final pattern obtained after complete drying of sessile droplets containing sodium chloride solutions at different initial NaCl concentrations originated from a complex interplay of flows dynamics including capillary flow [1] and other instabilities such as solutal Marangoni effect [76]. The visualization of the flow pattern will be shown in the section 3.5. Furthermore the flow dependence on the final deposit will be explained in detail in the discussion section 3.7.

3.2 INFLUENCE OF RELATIVE HUMIDITY ON EVAPORATION

3.2.1 Evaporation Behaviour

Figure 3.3 shows the time evolution of the normalized droplet volume $\tilde{v}$ (Equation 2.1) during the evaporation of sessile droplets containing 10^{-3}M NaCl at different relative humidities RHs of 0, 20, 40 and 60% [3].

After droplets deposition at $t = 0$ s, their (normalized) volume decreased linearly with time. Therefore even at higher relative humidities the typical evaporation curve of sessile salty droplets (i.e., a linear temporal change of the droplet volume during its whole evaporation) was retained. As for sessile water droplets, we found that the evaporation behaviour of sessile salty droplets was preserved over the studied range of RHs. The characteristic temporal patterns of pinned evaporating sessile droplets were observed: the droplet contact angle decreased with time while its footprint area remained constant during the whole evaporation process. An example of the time evolution of the sessile droplet volume and shape (from top and side imagings) at higher relative humidity is presented in detail in Appendix A.2.2.1. As observed for sessile droplets from pure water, the equilibrium contact angle adopted by the sessile droplet from 10^{-3}M NaCl just 50 s after deposition onto the silicon wafer kept the same value for all evaporation experiments at different RHs, i.e., $\theta_e \approx 2^\circ$. Sessile droplets from 10^{-3}M NaCl evaporated in pinned, constant contact area mode irrespective of the relative humidity.

However, the relative humidity had an (expected) influence on the evaporation kinetics of sessile salty droplet. Within the initial evaporation time period (i.e., between $t = 50$ and 100 s) and also later, the droplet (normalized) volume decreased linearly with time. This decrease marked in grey in Figure 3.3 was used to derive the evaporation rate $\frac{d\tilde{v}}{dt}$, i.e., the normal-

---

[2] For sessile droplets containing initially sodium chloride concentration smaller than 10^{-4}M the top view image did not show to the naked eye the salt ring at the droplet edge. Optical microscopy was used to confirm the presence of precipitated salt at the initial pinned contact line.

[3] Since a saturated NaCl solution condensed for RH higher than 75%, the relative humidity impact on the evaporation of sessile droplets from NaCl solutions was only presented in this thesis between 0 and 60%.

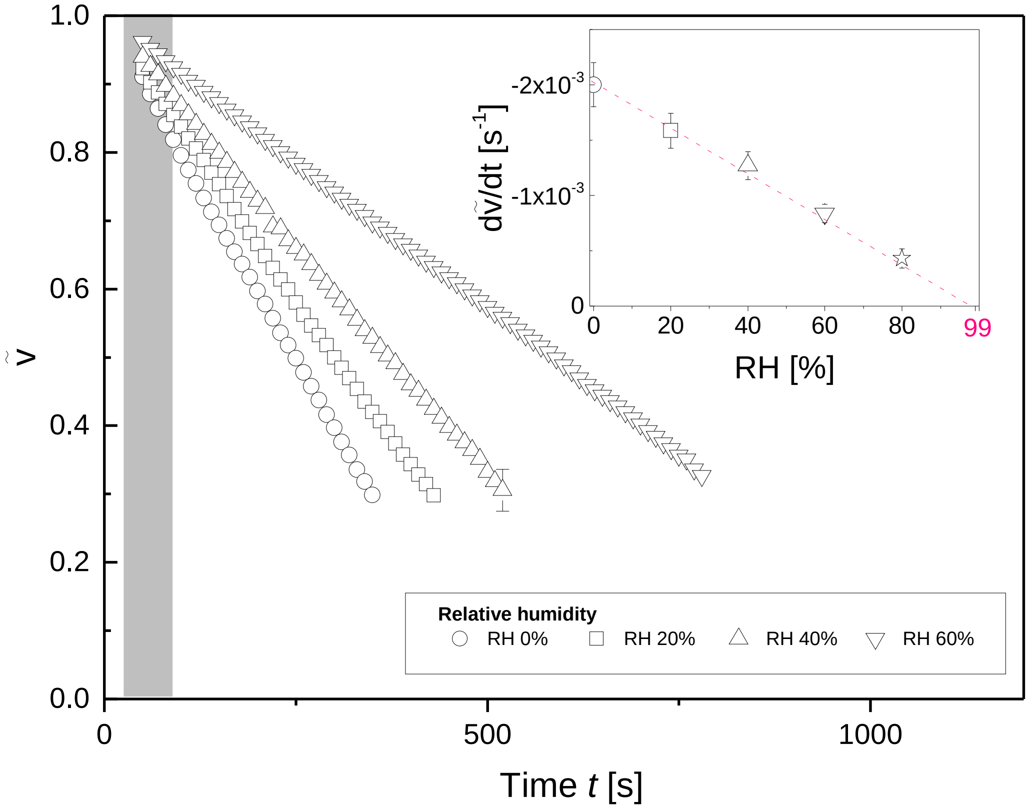

Figure 3.3 – *Evaporation of sessile droplets from* 10^{-3}*M NaCl at different relative humidities RHs of* 0, 20, 40 *and* 60% *(*V_0 = 10 μl*,* $\theta \approx 2°$*). The decrease of the normalized volume* $\tilde{v}$ *between* t = 50 *and* 100 *s after the sessile droplet deposition (marked in grey) was used to derive the evaporation rate* $\frac{d\tilde{v}}{dt}$*. The inset shows the variation of the evaporation rate* $\frac{d\tilde{v}}{dt}$ *as a function of the relative humidity RH.*

ized droplet volume change per time unit. The inset in Figure 3.3 shows the variation of the evaporation rate $\frac{d\tilde{v}}{dt}$ as a function of the relative humidity. The evaporation rate is inversely proportional to the relative humidity. This effect was experimentally demonstrated with sessile droplets from pure water in the previous chapter and theoretically expressed in Equation 2.2 according to the Picknett and Bexon evaporation model [3]. A linear extrapolation of the evaporation rate decrease with RH yielded at $\frac{d\tilde{v}}{dt} = 0$ s^{-1} to the equilibrium relative humidity RH_{eq} for 10^{-3}M NaCl solution. We found an experimental value for RH_{eq} of about 99%. This value agreed quite well with the expected value of 99.8% at T = 23°C [116].

For sessile droplets from aqueous solutions with/without salt the evaporation rate depends on the vapour pressure difference ($P_{sat}^{H_2O} - P$) with $P_{sat}^{H_2O}$ the saturated water vapour pressure at/above the droplet surface (due to the local equilibrium at the droplet-air interface) and P the water vapour pressure at infinite distance from the droplet, i.e., the water vapour pressure of the ambient environment. Since the resulting influence of the relative humidity on the evaporation rate is known and experimentally identified, the time t was scaled with the vapour pressure difference normalized to the saturation vapour pressure of pure water:

$$\tilde{t}_{RH} = t\,\frac{P_{sat}^{H_2O} - P}{P_{sat}^{H_2O}} = t\,(1 - RH) \tag{3.1}$$

As a reminder the relative humidity RH stands for the ratio between the water vapour pressure of the surrounding air with the saturation vapour pressure of water. With the time scaling based on the normalization with the relative vapour pressure (Equation 3.1) all the evaporation curves experimentally measured at different *RHs* should result in a single $\tilde{v}$-versus-$\tilde{t}_{RH}$, since the geometrical contributions (droplet volume and contact angle) were approximately constant over the studied range of *RHs*.

Figure 3.4 shows the measured normalized droplet volume $\tilde{v}$ (Equation 2.1) as a function of the rescaled time $\tilde{t}_{RH}$ (Equation 3.1) for evaporating sessile droplets of 10^{-3}M NaCl at different relative humidities from 0 to 60%. All the evaporation curves measured at different RH level collapse nicely into a single curve corresponding to the evaporation curve at RH = 0%. Figure 3.4 demonstrates that the evaporation of sessile droplets does not depend on the environmental relative humidity if the droplet volume and the time are appropriately normalized according to Equations 2.1 and 3.1, respectively. Therefore the evaporation rate $\frac{d\tilde{v}}{d\tilde{t}_{RH}}$ in the initial evaporation period (i.e., the slope of the obtained single evaporation curve between t = 50 and 100 s, marked in grey in Figure 3.4) has from now one and only one value irrespective of the relative humidity.

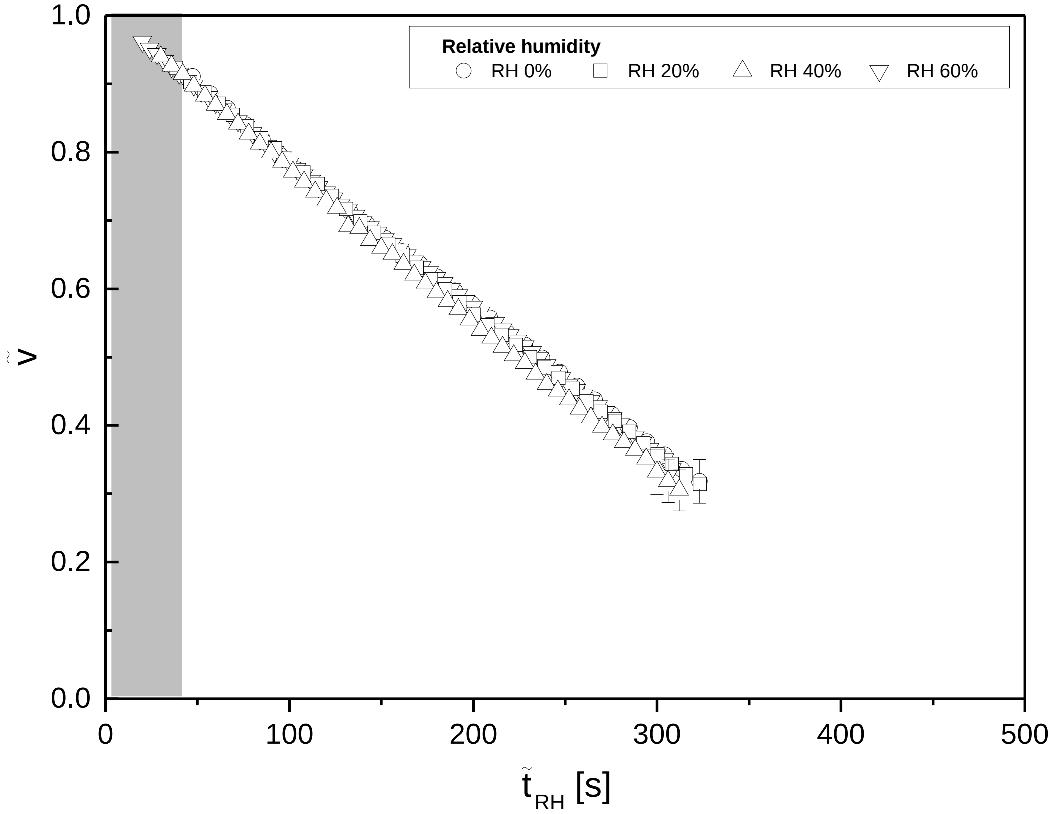

Figure 3.4 – *Normalized droplet volume $\tilde{v}$ (Equation 2.1) as a function of the scaled time with the normalized relative vapour pressure $\tilde{t}_{RH}$ (Equation 3.1). The experiments were performed with sessile droplets containing an initial NaCl concentration of* 10^{-3}*M (V_0 = 10 μl, $\theta \approx 2°$) at different relative humidities RHs of* 0, 20, 40 *and* 60%.

3.2.2 Salt-concentration dependence

The influence of the relative humidity on the evaporation of sessile droplets containing different initial NaCl concentrations from 10^{-6} to 6.1M was investigated. For higher initial NaCl concentrations, an increase of the relative humidity from 0 to 60% had no impact on the evaporation behaviour of the sessile droplets. The typical evaporation curve of pinned drying sessile droplets from salty solution as depicted in Figure 3.3 was retained at higher relative humidity over the wide studied range of initial NaCl concentrations. Examples of the temporal change of the sessile droplet volume measured from top and side views at different relative humidities (from 0 to 60%) for sessile droplets containing higher initial salt concentrations are presented in Appendix A.2.2.2. Irrespective of the relative humidity sessile droplets from aqueous sodium chloride solutions evaporated in pinned, constant contact angle mode for NaCl concentrations higher than 10^{-6}M.

The evolution of the evaporation rate as a function of the relative humidity was also studied for concentrated NaCl solutions. The detailed investigation is illustrated in Appendix A.2.2.2. Our results reveal that the evaporation rate $\frac{d\tilde{v}}{dt}$ is inversely proportional to the relative humidity as observed for lower NaCl concentrations. The absolute values of the evaporation rate depend on NaCl concentration. Concentrated sessile salty droplets evaporated slower: they had a longer lifetime than lower NaCl concentrated droplets. According to Raoult's law the addition of a non volatile solute such as sodium chloride to an aqueous solution provokes a diminution of the vapour pressure of the salty solution [116]. Therefore, since the evaporation rate depends on the vapour pressure difference $P_{sat}(1 - RH)$, increasing c_o and equivalently decreasing P_{sat} induces a diminution of the evaporation rate. The decrease in P_{sat}, and by extrapolation the equilibrium relative humidity RH_{eq}, with the initial salt concentration was experimentally demonstrated. Indeed, the measured RH_{eq} derived from the extrapolation of the evaporation decrease with RH at $\frac{d\tilde{v}}{dt}$ = 0 s^{-1} decreased from 99 to 75.4% if the NaCl concentration in the sessile droplet increased from 10^{-3} to 6.1M. Our experimental values are consistent with the expected values obtained from Raoult's law and also in the literature at T = 23°C [116].

For evaporating sessile droplets from higher initial NaCl concentrations the rescaled evaporation curves (i.e., the normalized droplet volume $\tilde{v}$-versus-$\tilde{t}_{RH}$) measured at different RHs coincided as well into a single evaporation curve. The corresponding figures are shown in Appendix A.2.2.2. Thus for sessile droplets from aqueous saline solutions the environmental relative humidity has no influence on the evaporation process if the droplet volume and the time are appropriately normalized according to Equations 2.1 and 3.1, respectively.

3.2.3 Pattern formation

The influence of relative humidity on the pattern at the end of the evaporation of sessile droplets from aqueous NaCl solutions was investigated by considering same initial volume of sessile droplet evaporating at four different representative NaCl concentrations in different RH levels. Final sessile droplet pictures are presented in Figure 3.5. This figure shows morphological and structural evolutions of drying droplets of NaCl solutions at two extreme different values of RH: 0 and 60%.

In both relative humidity cases, the shape of the final structures after complete evaporation of sessile droplets from aqueous NaCl solutions changes as NaCl concentration increases from 10^{-6} to 6.1M. However, the three different characteristics patterns identified at low humidity are preserved in high-humidity environment. At low NaCl concentrations (from 10^{-6} to 10^{-3}M) the final dried structure exhibits the classical "coffee-ring" but in a wider circular shape (i.e., the salt ring is less focused at the droplet periphery) in higher relative humidity environment. Above a concentration of 2M NaCl the peripheral salt deposition is retained. At a relative humidity of 60% in the surrounding air of the sessile droplets, the observed crystals at the end of the evaporation appear bigger and devoid of dendrites structures around them. For intermediate NaCl concentrations (i.e., between 10^{-2} and 1M NaCl) the uniform deposition over the entire footprint area of the dried sessile droplet is preserved at higher relative humidity.

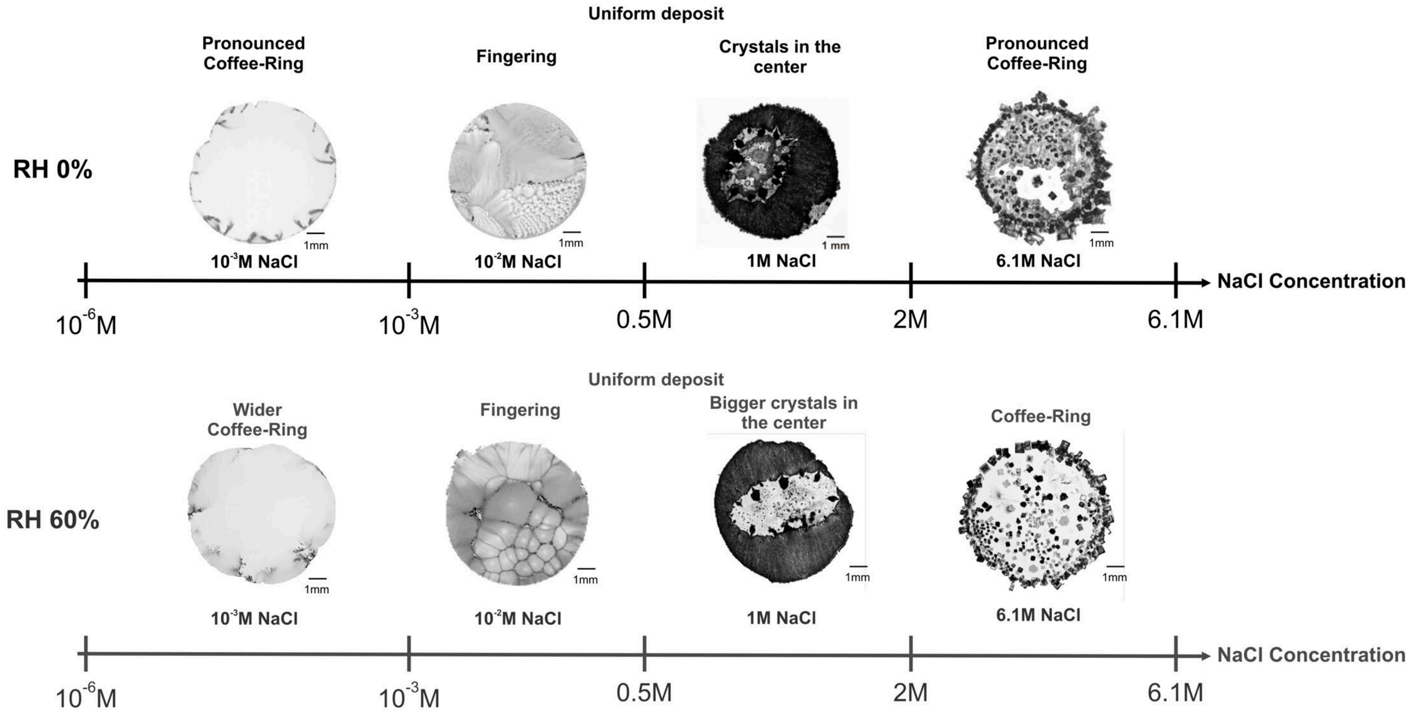

Figure 3.5 – *Morphologies of the final deposit obtained after complete drying of sessile droplets containing aqueous NaCl solutions at different initial salt concentrations from* 10^{-6} *to* 6.1*M NaCl. The evaporation experiments were performed at two different relative humidities RHs of* 0% *and* 60% *with* 10 *μl-sessile droplets.*

Our observations suggest that relative humidity has a non-negligible impact on the final structures obtained at the very last stage of evaporation. Increasing the relative humidity from 0 to 60% led to double/triple the drying time. Therefore a high-humidity environment imposed a slower evaporation rate which in turn, produced a slower capillary drift towards the droplet edge (i.e., the vapour flux at the droplet edge was reduced) [71]. As the evaporation rate was slow the salt ions had more time to diffuse towards the formed crystal nuclei. As a result smoother and bigger crystals emerged when the relative humidity of the ambient air of the sessile droplet from aqueous NaCl solutions increased.

3.3 Influence of Droplet Contact Angle and Size on Evaporation

Figure 3.6 shows the temporal change of the normalized droplet volume $\tilde{v}$ (Equation 2.1) during the evaporation of sessile droplets containing initially a NaCl concentration of 10^{-3}M (A) with various contact angles θ from 2 to 40° and (B) at different initial droplet volumes V_0 from 1 to 10 μl at a relative humidity RH of 0%.

As from 50 s after the droplets deposition, the volume calculated from the measured $h(t)$ and $r(t)$ decreases quite linearly with time within the studied time period (i.e., from the transient to the lateral times) in all cases (Figure 3.6). As shown in Figure 3.6.A, sessile droplets with higher contact angles adopt the typical evaporation profile that we observed at very low contact angles (Figure 3.1). Similar behaviour is preserved when the initially deposited droplet volume is increased from 1 to 10 μl as depicted in Figure 3.6.B. Therefore the evaporation profile of sessile droplets from 10^{-3}M NaCl is unchanged with varying the droplet contact angle ($\theta < 90°$) and size.

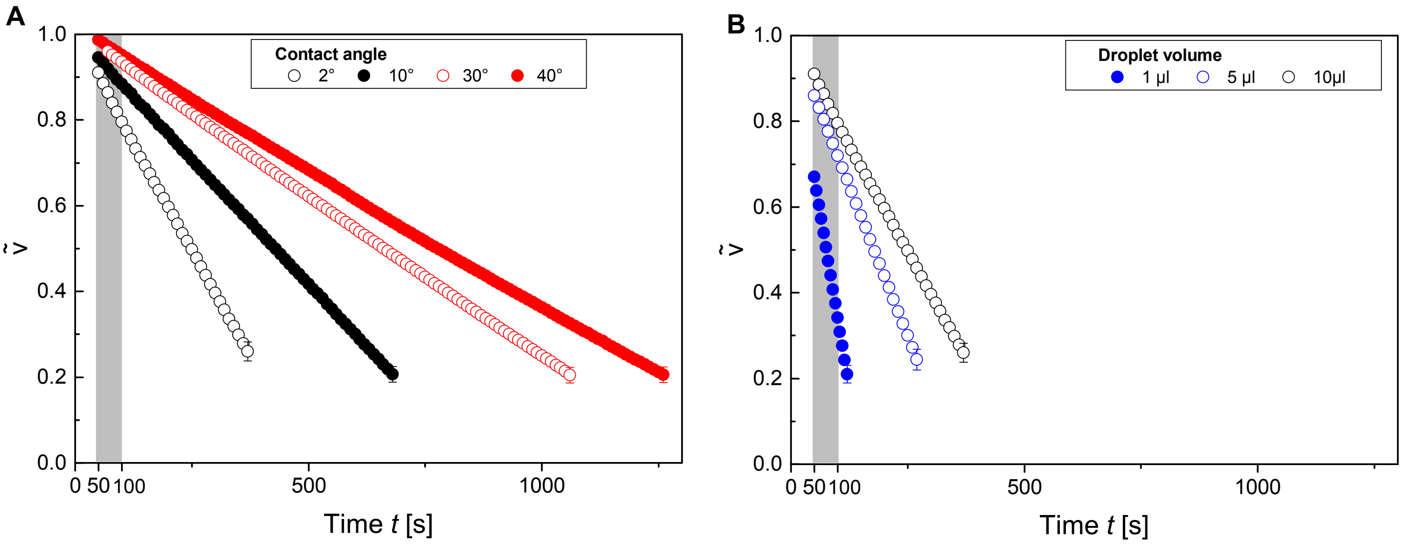

Figure 3.6 – *Evaporation of sessile droplets from* 10^{-3}*M NaCl* ***A.*** *with various contact angles:* 2, 10, 30 *and* 40° *(*V_0 10 *µl) and initially deposited* ***B.*** *with different volumes:* 1, 5 *and* 10 *µl (*$\theta \approx 2°$*) at a relative humidity RH of* 0%. *The decrease of the normalized volume* $\tilde{v}$ *between* t = 50 *and* 100 *s after the sessile droplet deposition (marked in grey) was used to derive the evaporation rate* $\frac{d\tilde{v}}{dt}$.

The detailed investigation of the temporal change of the droplet shape (from top and side aspects) at higher contact angles and at smaller initial droplet volumes confirmed that the evaporation mode of sessile droplets containing 10^{-3}M NaCl was retained. An example of this study at a higher contact angle and at a smaller droplet size is shown in detail in Appendix A.2.3.1. The footprint of the droplet diameter remained constant over the studied lifetime of the evaporating droplet. Meanwhile the contact angle of the droplet decreased. Our experimental evaporation results revealed that the contact angle of sessile droplets from 10^{-3}M NaCl deposited onto naturally oxidized silicon wafers was independent of the droplet size. Irrespective of the geometrical parameters of sessile droplets (i.e., r and θ), sessile droplets from 10^{-3}M NaCl evaporated in pinned, constant contact area mode.

Within the initial evaporation range (i.e., between t = 50 and 100 s) and later, the droplet (normalized) volume decreases linearly with time. For this initial temporal decrease marked in grey in Figure 3.6, we determined the evaporation rate $\frac{d\tilde{v}}{dt}$. The evaporation rate decreases with increasing the contact angle θ (Figure 3.6.A). θ is calculated from the droplet shape at t = 50 s. Similar results were obtained with sessile droplets from pure water. As the contact angle increases towards 90°, the singularity of the vapour flux (diffusing from the free surface of the droplet into the surrounding air) at the droplet edge is reduced, resulting in a global diminution of the evaporation rate. Furthermore, as the droplet size decreases, $\frac{d\tilde{v}}{dt}$ increases (Figure 3.6 .B). As illustrated with sessile water droplets, larger droplets evaporated slower than smaller ones.

Our experimental evaporation results showed that the evaporation rate of sessile droplets from 10^{-3}M NaCl solution was dependent on the droplet size and contact angle. According to the Picknett and Bexon model [3], the change of the normalized droplet volume $\tilde{v}$ with time t of a spherical-cap shaped sessile droplet with a contact angle θ in the quasi-steady state with diffusion-driven evaporation is given by:

$$\frac{d\tilde{v}}{dt} = -4\,\pi \frac{1}{V_0}\,\frac{D\,M}{\rho\,R\,T}\,(P_{sat}-P)\,f(\theta)\,\frac{r}{sin(\theta)} \tag{3.2}$$

with D as diffusion coefficient of water in air, M as molecular weight of water, ρ as water density, R as gas constant, T as temperature, P_{sat} as saturated vapour pressure at/above the droplet surface, P as water vapour pressure in the background environment and $f(\theta)$ as function of the contact angle θ (Equation 2.4).

Equation 3.2 is equivalent of the evaporation rate equation presented in the previous chapter for sessile water droplets (Equation 2.2), since the Picknett and Bexon evaporation model [3] is valid for pinned and unpinned sessile droplets. The geometrical contributions in Equation 2.2 (i.e., the normalized droplet volume $\tilde{v}$ and the functions of the contact angle β and $f(\theta)$) were expressed as function of the droplet radius r and contact angle θ ($r \approx$ constant since sessile droplets from 10^{-3}M NaCl evaporated in pinned, constant contact area mode) and combined as an equivalent droplet size factor $\tilde{r}$:

$$V_0^{\frac{1}{3}}\ f(\theta)\ \left(\frac{3\ \tilde{v}}{\pi\ \beta}\right)^{\frac{1}{3}} = f(\theta)\ \frac{r}{sin(\theta)} = \tilde{r} \tag{3.3}$$

We focused in this thesis on the evaporation behaviour at times between 50 and 100 s after droplet deposition, i.e., typically only about 10% of the time for the complete evaporation of the droplets. During the initial evaporation period, we found that the evaporation rate was constant, irrespective of the evaporation mode (i.e., either constant contact angle mode or constant contact area mode) [3]. Therefore the droplet size factor $\tilde{r}$ can be assumed as constant with excellent approximation during the initial evaporation times range according to Equation 3.2. For the data analysis $\tilde{r}$ (particularly θ since r remained constant for sessile droplets from 10^{-3}M NaCl over their evaporating lifetime) was calculated from the droplet shape at $t = 50$ s.

Since the resulting effect of the geometrical parameters (i.e., r and θ) on the evaporation rate was experimentally identified, the time $\tilde{t}_{RH}$ (i.e., the time t scaled to the relative vapour pressure difference, Equation 3.1) was scaled with the droplet size factor $\tilde{r}$:

$$\tilde{t} = \tilde{t}_{RH}\ \tilde{r} = t\ \frac{P_{sat}^{H_2O} - P}{P_{sat}^{H_2O}}\ \tilde{r} \tag{3.4}$$

Figure 3.7 shows the normalized droplet volume $\tilde{v}$ (Equation 2.1) as function of the scaled time $\tilde{t}$ (Equation 3.4) for sessile droplets containing initially a concentration of 10^{-3}M NaCl. The experiments were performed at different RHs, with various θ and at different V_0. The evaporation curves measured at different relative humidities and droplet contact angles collapse nicely into a single curve if the droplet volume and time are scaled appropriately according to Equations 2.1 and 3.4, respectively. Therefore the evaporation rate $\frac{d\tilde{v}}{d\tilde{t}}$ calculated in the initial evaporation period (marked in grey in Figure 3.7) has from now one and only one value irrespective of RH and θ. Figure 3.7 demonstrates that the evaporation behaviour of sessile droplets from 10^{-3}M NaCl may be described by an universal equation. This will be explained and demonstrated in detail in the next section. The scaled evaporation curves measured at different V_0 do not coincide with others evaporation curves, since the normalized evaporation rate $\frac{d\tilde{v}}{d\tilde{t}}$ is still inversely dependent on the initial droplet volume V_0 (Equation 3.2).

The impact of the droplet size and contact angle on the evaporation of sessile droplets from different initial NaCl concentrations (i.e., between 10^{-6} to 6.1M) was studied. The evaporation curves presented in Figure 3.6 are representative for all the experimental evaporation experiments obtained over the wide studied range of NaCl concentrations with different θ and V_0. Examples of the time evolution of the sessile droplet volume measured from top and side aspects at different droplet sizes and contact angles for sessile droplets containing NaCl concentrations $\geq 10^{-6}$M are illustrated in Appendix A.2.3.2. Irrespective of the droplet contact angle and size, sessile droplets from aqueous sodium chloride solutions evaporated in pinned,

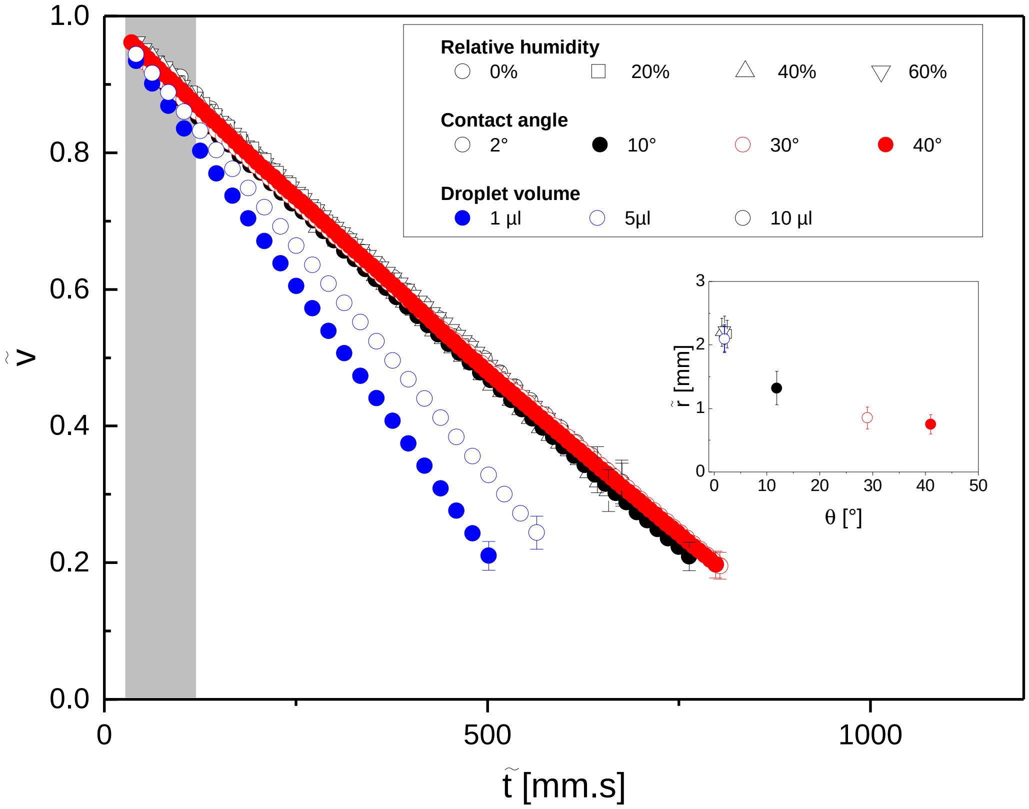

Figure 3.7 – *Normalized droplet volume* $\tilde{v}$ *(Equation 2.1) as a function of the scaled time* $\tilde{t}$ *(Equation 3.4). The experiments were performed with sessile droplets containing an initial NaCl concentration of* 10^{-3}*M at different relative humidities RHs of* 0, 20, 40 *and* 60% *(*$V_0 = 10\ \mu l$*,* $\theta \approx 2°$*), with various contact angles* θ*:* 2, 10, 30 *and* 40° *(*V_0 10 μl*) and at different droplet volumes* V_0*:* 1, 5 *and* 10 μl *(*$\theta \approx 2°$*). The inset shows the droplet size factor* $\tilde{r}$ *(Equation 3.3) as a function of the initial contact angle* θ_0*.*

constant contact angle mode for NaCl concentrations higher than 10^{-6}M.

Similar trend for the evaporation rate evolution with the droplet contact angle and size was observed at higher NaCl concentrations. Sessile droplets with a higher contact angle or with a higher initial deposited droplet volume evaporated more slowly. The absolute values of the evaporation rate $\frac{d\tilde{v}}{dt}$ depended on NaCl concentration. $\frac{d\tilde{v}}{dt}$ decreased as NaCl concentration within the aqueous sessile droplet increased. Since $\frac{d\tilde{v}}{dt}$ depends on the saturated vapour pressure P_{sat} (Equation 3.2) and P_{sat} is dependent on the salt concentration (as demonstrated in the previous section, RH_{eq}, by extension, P_{sat} decreased with increasing NaCl concentration), concentrated NaCl induced a diminution of the evaporation rate $\frac{d\tilde{v}}{dt}$.

Nevertheless, for evaporating sessile droplets from higher NaCl concentrations ($\geq$ 1M NaCl), the rescaled evaporation curves (i.e., the normalized droplet volume $\tilde{v}$-versus-$\tilde{t}$, the scaled time with the relative vapour pressure difference and the droplet size factor) observed at different θ and V_0 do not coincide into a single curve as partially obtained at lower NaCl concentrations (Figure 3.7). The corresponding figures are presented in Appendix A.2.3.2. As a result the evaporation behaviour of sessile NaCl droplets seems to be strongly affected by initial salt concentration.

3.4 UNIVERSAL EVAPORATION BEHAVIOUR

In this chapter we presented the different experimental influences of the environmental relative humidity and the geometrical droplets parameters (i.e., r and θ) on the evaporation rate

$\frac{dV}{dt}$ of sessile droplets from NaCl solutions. Step by step we introduced a normalization of the droplet volume and the time as function of the experimental observations made at different relative humidities, with various droplet contact angles and sizes. The droplet volume V was normalized to the initial volume V_0, which was derived from the linear extrapolation of the evaporation curve V-versus-t to t = 0 s (Equation 2.1). The time t was scaled with the normalization of the relative vapour pressure and with the droplet size factor $\tilde{r}$ (Equation 3.4). RH is the environmental relative humidity as adjusted by the flow of moist nitrogen and also measured in the sample chamber. $\tilde{r}$ was determined from the droplet shape and size at t = 50 s (Equation 3.3).

Equation 3.2 strictly describes the evaporation rate of sessile droplets from pure liquids such as pure water since the saturated vapour pressure P_{sat} is assumed constant along the droplet surface [3]. In a complex fluid such as a binary aqueous mixture of a non-volatile and soluble solute, the evaporation of the solvent (water) will change the local composition of the mixture solution and thus the vapour pressure will depend on the the radial position and also on the solute concentration. As demonstrated with the determination of RH_{eq} (see II.3.2), the saturation vapour pressure P_{sat} depends on the salt concentration c in the droplet. Thus the time scaling based on the saturation vapour pressure for pure water $P_{sat}^{H_2O}$ allowed us to focus our study on the impact of the salt on the evaporation rate, since neither the precise spatial composition nor the resulting influence on the evaporation rate was known. We only experimentally determined a global effect of the initial NaCl concentration on the evaporation rate.

As a consequence with the scaled time, $\tilde{t}$ (Equation 3.4), Equation 3.2 reads as:

$$\frac{d\tilde{v}}{d\tilde{t}} = -4\,\pi \frac{D\ M\ P_{sat}^{H_2O}}{\rho\ R\ T\ V_0}\ g(c) \tag{3.5}$$

$g(c)$ describes the deviation of the evaporation rate for an aqueous salt solution with salt concentration c in comparison to the case of pure water. Thus $g(c)$ is a spatio-temporal function of the salt concentration within (at the surface) of the sessile droplet.

All the parameters involved in Equation 3.5 can be assumed as constant. As saturation water vapour pressure and diffusion coefficient we assumed the literature constant value of $P_{sat}^{H_2O}$ = 3175 Pa[116] and D = 2.5 x 10^{-5} $\mathrm{m}^2.\mathrm{s}^{-1}$ [66, 112] at $T \approx 23$°C. V_0 can be assumed approximately constant from the experimental determination/measurement even if we observed a typical variation of the deposited volume by about 5%. Since the evaporation experiment is principally limited to a short initial time period (between 50 and 100 s after droplet deposition), we can consider that the function $g(c)$ was constant. Assuming that the salt concentration within the sessile droplet barely changed during the initial evaporation period, we can consider that $g(c) \simeq g(c_0)$ = *constant*, with c_0 as initial (inweight) salt concentration. As a result, during the initial short evaporation period,

$$\frac{d\tilde{v}_i}{d\tilde{t}}(c_0) = constant \tag{3.6}$$

Furthermore, we assumed that the salt was distributed homogeneously inside the droplet and in particular at the droplet surface. In Equation 3.2 we consider the saturated vapour pressure P_{sat} as the water vapour pressure in the aqueous NaCl solution (with a NaCl concentration c) above/at the droplet surface, $P_{sat} = P_{sat}(c) \simeq P_{sat}(c_0)$. Therefore $g(c)$ had a simple form:

$$g(c) = \frac{P_{sat}(c) - P}{P_{sat}^{H_2O} - P} = \frac{(P_{sat}(c)/P_{sat}^{H_2O} - RH)}{(1 - RH)} \tag{3.7}$$

Thus with relative humidity, RH, the initial evaporation rate of sessile droplets containing an initial salt concentration c_0 can be described by the following equation:

$$\frac{d\tilde{v}_i}{d\tilde{t}}(c_0) = -4\,\pi \frac{D\,M\,P_{sat}^{H_2O}}{\rho\,R\,T\,V_0}\,\frac{(P_{sat}(c)/P_{sat}^{H_2O} - RH)}{(1-RH)} = constant \tag{3.8}$$

With Equation 3.8, the evaporation rate was still inversely proportional to the droplet size. Therefore Equation 3.8 can be transformed into a unit-free, normalized evaporation rate $\tilde{Q}_i$, with $\tilde{Q}_i$ = 1:

$$\tilde{Q}_i = -\frac{d\tilde{v}_i}{d\tilde{t}}(c_0)\,\frac{1}{4\,\pi}\,\frac{\rho\,R\,T\,V_0}{D\,M\,P_{sat}^{H_2O}}\,\frac{(1-RH)}{(P_{sat}(c)/P_{sat}^{H_2O} - RH)} = 1 \tag{3.9}$$

Thus Equation 3.9 describes an universal normalized evaporation rate equation: all the initial evaporation rates $\frac{dV}{dt}$ measured experimentally for different relative humidities RHs, droplet contact angles θ, initial droplet volumes V_0 and initial NaCl concentrations c_0, should result in a value of 1 if:

- the droplet volume V and the time t are scaled according to Equations 2.1 and 3.4;
- c_0 was translated into the corresponding saturated water vapour pressure in NaCl solutions, $P_{sat}(c)$ (approximated as $P_{sat}(c_0)$) at $T \approx 23°C$ [116];
- the evaporation of sessile droplets from pure water was correctly described by Equation 3.2 [3];
- the initial scaled evaporation rate $\frac{d\tilde{v}}{d\tilde{t}}(c_0)$ was approximately as a constant (Equation 3.6); and,
- the distribution of salt within the droplet (in particular, at the droplet surface) was homogenous, i.e., the assumption described in Equation 3.7 was valid.

Equation 3.9 was determined as function of each experimental parameter (i.e., RH, θ, V_0 and c_0). If $\tilde{Q}_i$ = 1, the different conditions cited above were valid: the evaporation behaviour can be described by the universal Equation 3.8. If not, $\tilde{Q}_i \neq 1$, the conditions were not valid, in particular the last one assuming an homogeneous distribution of the salt within the droplet. Therefore Equation 3.9 provides a convenient approach to test the validity of the different assumptions.

Figure 3.8 presents the experimentally observed normalized evaporation rates $\tilde{Q}_i$ as function of the initial NaCl concentration c_0 from 0 to 6.1M for various contact angles varying from 1 to 50°, various initial droplet volumes from 1 to 10 μl and at different relative humidities from 0 to 60%. The dashed line depicts the theoretically expected normalized evaporation rate, scaled to a value of 1 according to Equation 3.9. The main assumption of the theoretical predictions was an uniform distribution of the (inweight) salt concentration inside the droplet.

Up to a NaCl concentration of 0.5M, the measured normalized evaporation rates $\tilde{Q}_i$ agree quite well with the theoretical predictions irrespective of the relative humidity, the contact angle and the droplet size. This holds for the evaporation with unpinned, constant contact angle mode (i.e., $c_0 > 10^{-7}$M NaCl) as well as with pinned, constant contact area mode for $10^{-6} \geq c_0 \geq 0.5$M NaCl. As an example, Figure 3.7 confirms that the evaporation behaviour of sessile droplets from 10^{-3}M NaCl at different RHs and θ for an initial volume of 10 μl is described by an universal evaporation equation depicted in Equation 3.8. Several control experiments with

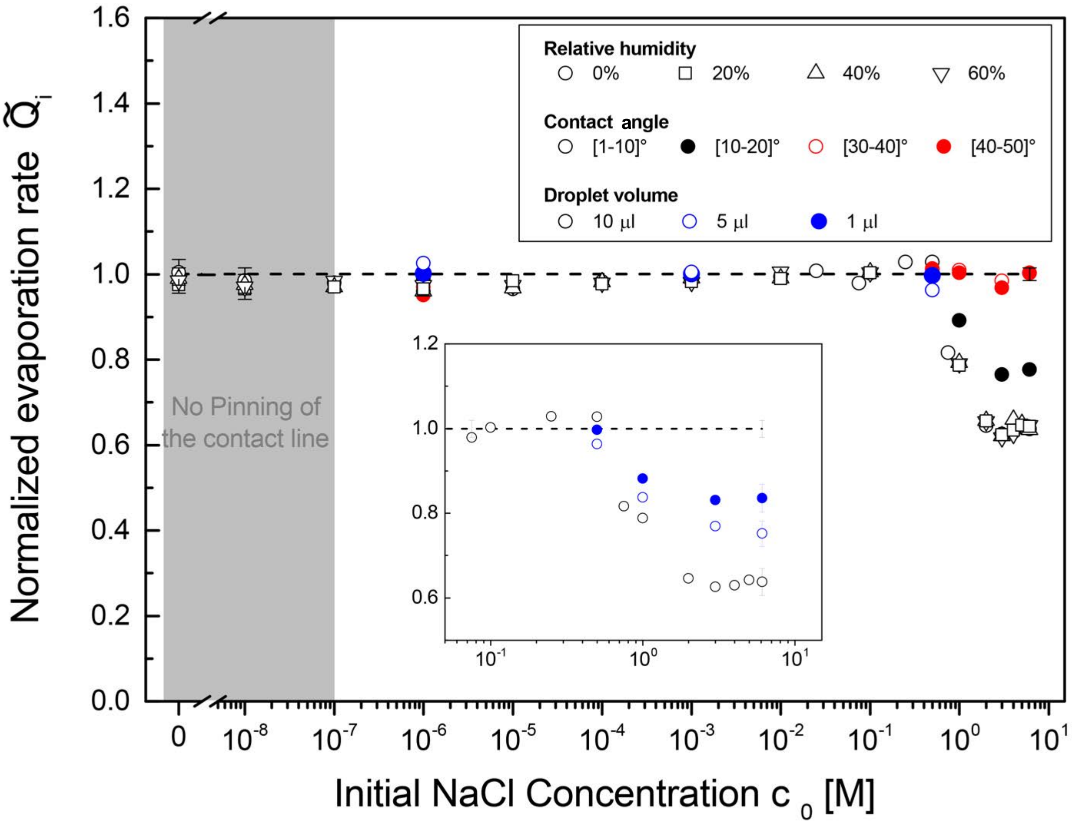

Figure 3.8 – *Experimentally observed normalized evaporation rates $\tilde{Q}_i$ as function of the initial NaCl concentration c_0 from 0 to 6.1M for various contact angles varying from 1 to 50°, various initial droplet volumes from 1 to 10 µl and at different relative humidities from 0 to 60%. The dashed line depicts the theoretically expected normalized evaporation rate according to Equation 3.9 with the assumption of the (inweight) salt concentration distributed uniformly inside the droplet. The droplets evaporated in pinned, constant contact area mode except for NaCl concentrations $\leq 10^{-7}$M. The inset plot shows more precisely the evolution of $\tilde{Q}_i$ as function of c_0 with different V_0 at NaCl concentrations $\geq 10^{-1}$M.*

salt concentrations $c_0 < 10^{-8}$M NaCl (data not presented in Figure 3.8) match quantitatively as well as qualitatively the evaporation and the non-pinning behaviour as depicted in Figure 3.8.

Above a NaCl concentration of 0.5M, the measured normalized evaporation rates $\tilde{Q}_i$ agree with the theory only for a droplet contact angle higher than 30° with an initial droplet volume of 10 μl. For $\theta \leq 20°$ at $V_0 = 10$ μl, the measured normalized evaporation rates $\tilde{Q}_i$ are significantly smaller than expected. The deviation is most pronounced for the small contact angles. Similar trend is observed for $V_0 \leq 10$ μl with $\theta \leq 10°$. On contrary the deviation is less pronounced at smaller droplet size. Thus the deviation of the experimental measurements from the theory depends either on the contact angle at fixed droplet volume or on the droplet volume at fixed small contact angles. However, with the scaling described in Equation 3.9 the deviation from the theoretical predictions is independent from the relative humidity. This behaviour was identified in the previous section I.3.2. Figure 3.4 (and also Figures A. 6 and A. 7 in Appendix A.2.2.2 for higher NaCl concentrations) confirm that the rescaled evaporation rate does not depend on the relative humidity.

Within the time period under consideration in this thesis, i.e., from the deposition of the droplet to the end of the initial evaporation period (100 s after the droplet deposition), at most up to about 20% of the initial liquid droplet volume may evaporate. This initial evaporation times range was marked in grey in each presented figure of this thesis part. A decrease of the droplet volume due to its evaporation will lead to a corresponding increase of the salt concentration since only water evaporated in the binary system. Therefore an enrichment in salt within the droplet will induce a decrease in $P_{sat}(c)$ and hence a diminution of the evaporation rate according to Equation 3.2. If this salt concentration increase was $uniform$ within the entire droplet volume and provoked a measurable change in the evaporation rate value (by decreasing $P_{sat}(c)$ as described in Equation 3.2), then the observed rescaled evaporation rates $\frac{d\tilde{v}}{d\tilde{t}}$ as presented in Figure 3.7 (for instance for 10^{-3}M NaCl) should *not* be constant with the scaled time $\tilde{t}$ and by extention, with the time t. Instead the evaporation rate should decrease as the droplet volume decreases, particularly at rather late stages, when the sessile droplet volume has been reduced considerably. This was not the experimental observed case. Therefore an $uniform$ increase of NaCl concentration as cause for the difference between experimental results and theory of the evaporation rates as obtained for high initial salt concentrations (Figure 3.8) must be discarded.

An analysis of the different assumptions as described above suggests that the main reason for the deviation between the theoretical predictions and the experimental findings was an *inhomogeneous* salt distribution within the droplet. A non-uniform salt distribution within the evaporating sessile droplet altered the evaporation profile and thus $g(c)$ can not be approximated as we assumed in Equation 3.7.

3.5 Flow Patterns within Evaporating Sessile Salty Droplets

A detailed study of the evaporation rate as function of the initial NaCl concentration showed us that a heterogeneous salt distribution within the evaporating sessile droplet caused a deviation of the experimental evaporation results with the theoretically predicted values for high initial NaCl concentrations. The origin of the inhomogeneous salt distribution within the droplet was investigated by particle tracking velocimetry (PTV) experiments. PTV experiments consisted of adding fluorescent particles within the sessile salty droplet. The observation of the particles movement inside the evaporating droplet will reveal the direction of the flow field within the droplet as well as the resulting particle area enrichment.

Figure 3.9 and 3.10 show the particle tracking velocimetry experiments performed with evaporating sessile droplets from 10^{-3}M NaCl (Figure 3.9) and 1M NaCl (Figure 3.10) at a relative humidity RH of 0% with an initial droplet volume of 10 μl. To improve the contrast and to better reveal the particle movement, the image contrast as measured originally by the camera was inverted. Originally bright, the fluorescing particles appear from now dark.

A sequence of four frames are presented in each figure. Figure 3.9 shows a time span of 300 s. It was recorded about 50 s after the droplet deposition, i.e., long after the droplet had initially spread to its final perimeter and the three-phase contact line was pinned in this position. On contrary Figure 3.9 shows a time span of slighly less than 1 s. At the top of each image of Figures 3.9 and 3.10 is depicted the side aspect of the sessile droplet as it was recorded from the side view camera (and also used for the determination of the droplet shape for the droplet volume measurement). The dashed line indicates the position of the substrate surface. The depth of focus of the imaging exceeded the droplet height. Therefore the imaging was not able to reveal the vertical position of the fluorescent particles within the sessile droplet. The main part of each image shows the top aspect of the sessile droplet. The fluorescent particles appear as dark dots or streaks. The length and direction of the streak reflect the speed and direction of the particle movement during the exposure (oversampling) time.

As indicated, the inset in each of the four frames magnifies the same area at the droplet edge region. In each inset of Figure 3.10 the location/path of a selected, individual particle is marked with red circles. The selected and individual particle is identified in the first frame in Figure 3.10 with a red dashed arrow. In Figure 3.10 the black arrows indicate the observed direction of the movement of this individual particle and thus the direction of the flow of the solution environment in which the particle is embedded. On contrary in Figure 3.9 any particle was needed to be selected and identified to show up the flow direction.

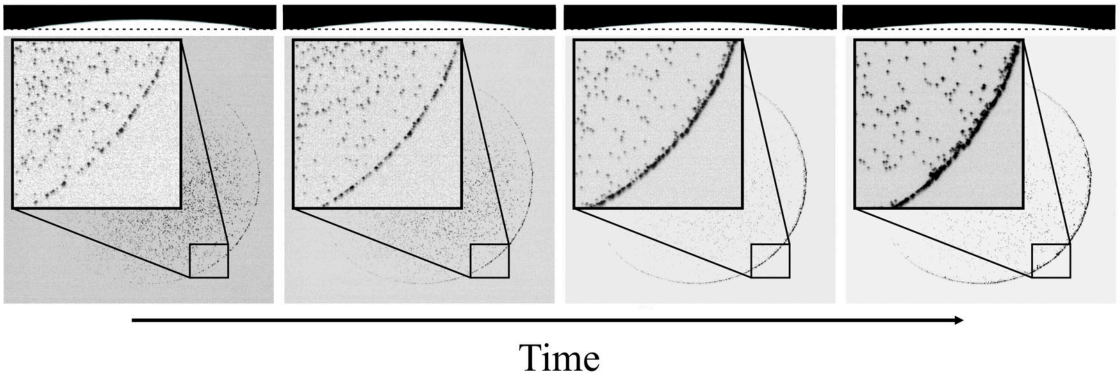

Figure 3.9 – *PTV experiments in a sessile evaporating droplet from* 10^{-3}*M NaCl at a relative humidity of* 0% *and with an initial deposited volume of* 10 *µl. For better contrast the image is inverted with the fluorescing particles appearing in dark. The sequence of frames shows a time span of* 300 *s recorded about* 50 *s after the droplet deposition. At the top of each image is illustrated the side view of the droplet with the dashed line indicating the position of the substrate surface. The main part of the images depicts a top view of the droplet with the fluorescing particles showing up as dots or streaks the amount of particle movement during the camera exposure time. The inset magnifies in all four frames the same area at the droplet edge region.*

Figure 3.9 reveals an unique liquid flow only directed *towards* the droplet edge region. The observed liquid flow towards the three-phase contact line induces a peripheral deposition of fluorescing particles. Over the evaporation process the peripheral deposit of fluorescent particles is enhanced. Few fluorescing particles are visible at the end of the evaporation in the droplet center region. At low initial NaCl concentrations we observed the typical volume liquid flow directed towards the droplet periphery in evaporating sessile droplets. It is caused by the excess of liquid loss in the peripheral area due to the spatially non-uniform evaporative flux along the droplet surface. This capillary flow results classically in the peripheral deposition of coffee powder particles, the "coffee-stain effect"' [1].

Figure 3.10 shows a different flow field within the evaporating sessile droplet containing an higher initial NaCl concentration. In the first two images the selected and individual particle depicted in the inset figure moves towards the droplet periphery. In the last two images it moves away from it. The salt concentration has an impact on the observed flow pattern. At higher NaCl concentration, it changes dramatically. The observed liquid flow *away* from the three-phase contact line reveals an additional flow mechanism: a Marangoni flow component [76]. This will be explained in detail in the discussion section.

3.6 Discussion and outlook

Here we investigated the evaporation of sessile droplets from sodium chloride solutions on planar, horizontal and inert substrates. The evaporation experiments were performed over height decades of initial NaCl concentrations, with various droplet contact angles from 2 to 50°, with various initially deposited volumes ranging from 1 to 10 μl and at different relative humidities varying from 0 to 60%. The study of the temporal change of the sessile droplet volume and shape (Figure 3.1) revealed the signature of sessile droplets evaporating in pinned, constant

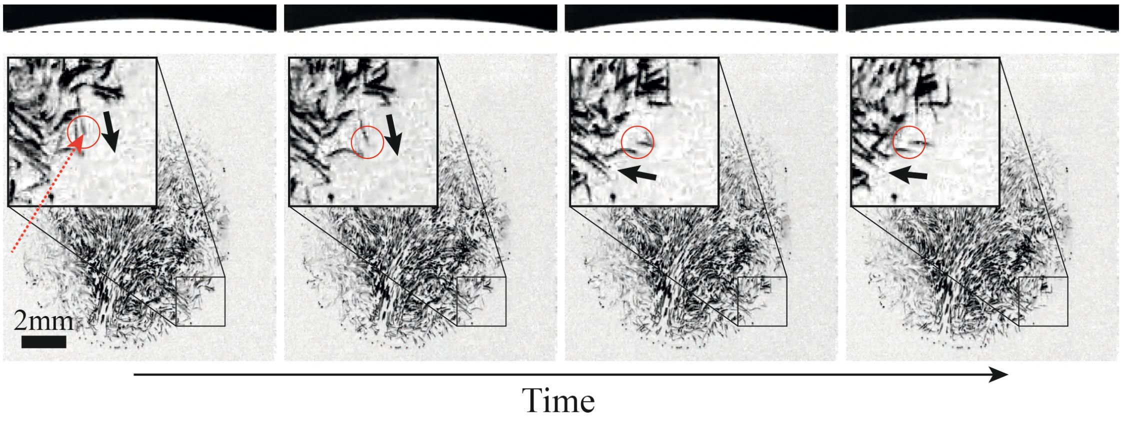

Figure 3.10 – *Tracing of fluorescing particles (appearing in dark) in a sessile evaporating droplet from* 1M *NaCl at a relative humidity of* 0% *and with an initial deposited volume of* 10 *µl. The sequence of frames shows a time span of less than* 1 *s recorded about* 80 *s after the droplet deposition. At the top of each image is illustrated the side view of the droplet with the dashed line indicating the position of the substrate surface. The main part of the images depicts a top view of the droplet with the fluorescing particles showing up as dots or streaks the amount of particle movement during the camera exposure time. The inset magnifies in all four frames the same area at the droplet edge region. The circles identify the location/path of an individual particle, the black arrows the direction of the movement.*

contact area mode for NaCl concentrations higher than 10^{-6}M. This evaporation mode was expected [1] for aqueous sessile droplets containing non-volatile component and also experimentally observed before for salty droplets [71, 83, 117, 118]. The environmental condition and the geometrical contributions (i.e., the droplet radius and contact angle) did not alter the pinning evaporation behaviour observed for sessile droplets from NaCl solutions as depicted in Figures 3.3 and 3.6.

However, the observed pinning evaporation behaviour was not retained over the wide studied range of NaCl concentrations. For initial NaCl concentration $c_0 \leq 10^{-7}$M, the sessile droplets evaporated in unpinned, constant contact angle mode. This was remarkable that the transition between pinning and non-pinning of the three-phase contact line occurred at relatively quite low salt concentrations. The origin of the threshold between pinning and non-pinning at $c_0 \approx 10^{-6}$M NaCl was not obvious. That may arise from the too low initial salt concentration to induce quickly (after the droplet deposition and a short initial spreading) a pinning of the contact line or from the too fast evaporation process occurring at RH 0% to promote a sufficient transient excess salt concentration at the droplet edge to provoke its self-pinning. Future work will include a more detailed investigation on the pinning/non-pinning transition in the evaporation behaviour of NaCl solutions. In particular the influence of a high-humidity environment or droplet size on its threshold value will be interesting.

As for sessile water droplets (studied in the previous chapter), the evaporation rate of evaporating sessile droplets from NaCl solutions was dependent on the relative humidity of the surrounding environment (Figure 3.3) and on the droplet shape (contact angle) and size (Figure 3.6). Therefore we analyzed step-by-step the experimental evaporation experiments measured for saline solutions by following the theoretical description of the evaporation of sessile droplets from single volatile pure liquid [3, 53]. To this end the droplet volume was scaled by the initially deposited volume V_0 (Equation 2.1) and the evaporation time was scaled with the relative vapour pressure difference (we used the saturation vapour pressure of pure water, Equation 3.1) and with the geometrical contributions of the droplet (radius and contact angle, Equation 3.3). The evaporation behaviour of sessile droplets from NaCl solutions as depicted in Figure 3.7 cannot be rescaled as straightforward as in the case of pure water. In order to investigate the influence of salt concentration on the evaporation rate, the evaporation rate was approximated as a constant during the initial short studied evaporation period between t = 50 and 100 s (Equation 3.6) and an uniform salt distribution within the droplet (at the droplet surface) was assumed (Equation 3.7). With the step-by-step normalization of the evaporation rate, we achieved a single, universal, unit-free initial volume evaporation rate $\tilde{Q}_i$ described by Equation 3.9.

For initial salt concentrations $c_0 \leq 0.5$M NaCl, the experimentally measured normalized evaporation rate $\tilde{Q}_i$ agreed with the theoretical predictions as shown in Figure 3.8. On contrary, above an initial NaCl concentration of 0.5M, the measured $\tilde{Q}_i$ were smaller than the theoretically predicted values (Figure 3.8). The origin of the deviation between the predicted and the measured evaporation behaviour at hight salt concentrations was an inhomogeneous salt distribution inside the droplet. This was revealed by particle tracking velocimetry (PTV) experiments presented in Figure 3.10.

The evaporative flux diffusing from the free surface of the droplet into the surrounding air is non-uniform along the droplet surface. The vapour flux is enhanced at the edge of the evaporating sessile droplet as shown in Figure 3.11.a. The singularity of the evaporative flux induces a capillary flow towards the peripheral region of the droplet [1]. In the case of sessile droplets containing volatile and non-volatile components, the capillary flow, in combination with the pinning of the contact line, leads to an enrichment of the non-volatile component in the droplet edge region. In our case, a local enrichment of sodium chloride is induced in the droplet peripheral region as illustrated in Figure 3.11.a. This will lead to a surface tension gradient within the evaporating sessile droplet. With sodium chloride the surface variations can become quite substantial since the surface tension γ increases with increasing the salt concentration. The surface tension of a saturated sodium chloride solution is about 84 mN.m^{-1} [44]. In comparison, pure water and low NaCl concentrations solutions (i.e, $c_0 \leq 10^{-1}$M) have a surface tension of about 73 mN.m^{-1}. Therefore, as NaCl concentration increases, a surface tension gradient may evolve in evaporating sessile droplets from NaCl solutions. It can be sufficiently high to induce a Marangoni flow [104, 105]. Since a local and transient excess of sodium chloride is produced in the droplet peripheral region, the surface tension is higher at the droplet edge than at its center. Thus the Marangoni flow is directed towards the droplet edge, i.e., *in the same direction* as the usual replenishment flow for evaporating sessile droplets without surface tension gradient as presented in Figure 3.11.b.

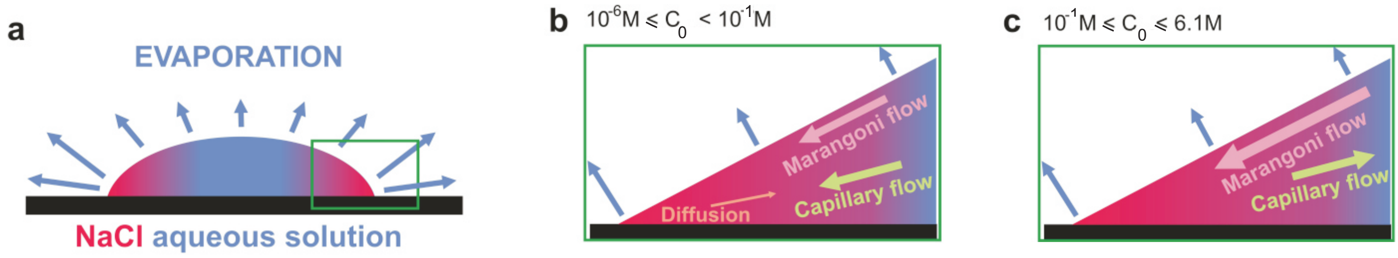

Figure 3.11 – ***a.*** *Evaporation behaviour of a sessile droplet from aqueous sodium chloride solutions. Locally varying evaporation rate and resulting concentration gradient. :* ***b.*** *below and* ***c.*** *above* 10^{-1}*M NaCl.*

Figure 3.11.b illustrates the flow pattern that PTV experiments revealed for evaporating sessile droplets containing an initial NaCl concentration lower than 10^{-1}M (Figure 3.9). Figure 3.9 shows an unique particle movement towards the three-phase contact line. This may arise from the capillary flow compensating for the local evaporative losses at the droplet edge region, possibly increased by a Marangoni flow component. Theoretically diffusive dilution resulting from the salt concentration gradient should reduce the evaporation-induced gradient.

The diffusive dilution effect is not negligible, but the capillary flow (as well as the Marangoni flow) are preponderant. This only flow towards the droplet edge may favor the formation of a salt-ring deposition. This pattern formation was observed for low initial NaCl concentrations as depicted in Figure 3.5.

For higher initial NaCl concentrations, the surface tension gradient will lead to a stronger Marangoni flow towards the droplet edge. However, in the end, the system stabilizes in a quasi-stationary state with minimum interfacial and hydrodynamic energy (viscous dissipation). Thus, as illustrated in Figure 3.11.b, the replenishment flow component will still exactly compensate for the evaporative losses at the droplet periphery. In contrast, the Marangoni flow will transport towards the peripheral droplet region extra liquid, which will be in excess of the evaporative losses. As a result, the capillary pressure will increase near the droplet edge and will decrease in its center. Therefore, because of the liquid/mass conservation, a compensating capillary (volume) flow *away* from the three-phase contact line will be driven to transport the excess amount of liquid towards the droplet center. The flow back will occur preferentially within the droplet volume, near the liquid-substrate interface to minimize frictional losses with the opposite Marangoni flow component at/near the air-water interface. The result will be a convective flow pattern within the evaporating sessile droplet as presented in Figure 3.11.c.

For high initial NaCl concentrations (i.e., $c_0 \geq 10^{-1}$M), PTV experiments revealed a liquid flow towards and *away* from the droplet periphery as depicted in Figure 3.10. The top view imaging of Figure 3.10 did not show the vertical location of the flow directions because the entire vertical droplet was in focus. Nevertheless we observed a convection flow near the droplet periphery. Aside from a volume flow component away from the droplet edge region, the observation of convection rolls confirmed the Marangoni flow scenario illustrated in Figure 3.11.c. The circulating flows within the evaporating sessile droplet may favor the formation of a more uniform salt deposit or a wider salt-ring at the droplet periphery. This pattern formation was observed at higher NaCl concentration (i.e. $c_0 > 10^{-3}$M) as presented in Figure 3.5

PTV experiments presented in Figures 3.9 and 3.10 revealed significant local variations in the liquid composition within the sessile droplet (and at the air/water interface) over the studied range of NaCl concentrations. Therefore the assumption of an homogeneous salt distribution within the droplet (Equation 3.7) was not strictly valid. The singularity of the evaporative flux at the droplet edge induces an enrichment of NaCl in this peripheral region. The local enrichment of sodium chloride in the vicinity of the droplet periphery will induce a decrease in $P_{sat}(c)$ (i.e., the water vapour pressure in the aqueous solution containing a NaCl concentration, c, above/at the droplet surface) and hence a diminution of the evaporation in the droplet edge region (Equation 3.2). Since the evaporative losses from the peripheral droplet region contribute significantly to the entire droplet ones, a change of the evaporation at the droplet edge can substantially alter the overall droplet evaporation behaviour. Figure 3.8 shows that this is the case for initial NaCl concentrations c_0 higher than 0.5M. Thus the Marangoni effect induced in evaporating sessile salty droplet at high NaCl concentrations had a feedback on the evaporation behaviour.

Quantitative evaporation experiments on sessile droplets containing aqueous sodium chloride solutions were performed at different RHs, with various θ and V_0 in order to analyze the influence of these different parameters on the evaporation behaviour. As shown in Figure 3.8, above a NaCl concentration of 0.5M, the experimentally measured normalized evaporation rate $\tilde{Q}_i$ at smaller contact angles (i.e., $\theta \leq 20°$ for a fixed initial droplet volume V_0 of 10 μl) and at smaller droplet sizes (for a fixed range of contact angles) were significantly smaller than the theoretically predicted values (Equation 3.9). The sensitivity of the discrepancy between theory and experiment with the contact angles confirmed the proposed scenario, depicting the impact of Marangoni flow and its feedback on the evaporation behaviour. When the droplet contact angle increases towards 90° the singularity of the evaporative flux near the droplet edge region was reduced. Increasing the droplet contact angle from 2 to 50° leads to decrease the inhomogeneity of the evaporation rate between the droplet edge and its center. Therefore the relative contribution of the evaporative losses from the droplet periphery compared to the overall evaporation decreased as the contact angle increased. In addition, the more homogeneous evaporation rate along the droplet surface leads to less pronounced Marangoni flows.

Furthermore, the deviation between theory and experiment was less pronounced for smaller droplet sizes with a fixed range of low contact angles as shown in Figure 3.8. The divergence of the evaporative flux at the droplet edge region induced a peripheral enrichment of sodium chloride within the evaporating sessile droplet, leading to pronounced Marangoni flow at high salt concentrations. Nevertheless the Marangoni effect may be affected by the droplet dimensions. In smaller droplet size the diffusive dilution effect may reduce the concentration (surface tension) gradient and subsequently annihilate the own origin of the Marangoni effect. Thus the relative contribution of Marangoni effect in the evaporation behaviour was reduced as the droplet size decreased.

To conclude we demonstrated in this chapter that the evaporation of sessile droplets from NaCl solutions was quite complex process. The flow behaviour was strongly affected by the initial NaCl concentration. The flow behaviour within an evaporating droplet of saline solution was dominated by a solely outward flow (combination of Marangoni and capillary forces) at low initial salt concentrations. At high salt concentrations, the flow behaviour changed drastically and was governed by the compensating Marangoni and capillary flows that lead to convection rolls. Thus the evaporation induced constitutional gradients and the resulting surface tension gradients lead to Marangoni effect. In return, this changed the evaporation behaviour, particularly the evaporative losses from the droplet edge region. These processes are dependent on the droplet shape and size.

For a better understanding of the evaporation of the sessile droplets from aqueous saline solutions, future project should include the investigation with different salts having positive and negative surface tension increments σ (Equation 2). It will be interesting to study a wide range of salts exhibiting positive σ such as NaCl in order to gain insight in the impact of Marangoni flow on the evaporation behaviour. On the other hand, salts with a negative σ will induce a Marangoni flow directed away from the three-phase contact line and may lead to different evaporation behaviours and salt distributions within the evaporating sessile droplet.

3.7 Towards a General Evaporation Behaviour of Sessile Droplets of Aqueous Saline Solutions

In order to have a better understanding of the influence of the Marangoni flow on the evaporation behaviour of sessile droplets from aqueous saline solutions, we studied the evaporation of sessile droplets containing another salt solution having a positive surface tension increment σ. Magnesium chloride solutions ($MgCl_2$) were selected since the surface tension increment of $MgCl_2$ solutions is two times bigger than the one of NaCl solutions for a similar salt concentration range (i.e., from pure water to saturated salt solution of about 6M) at (20-25)°C [44] (see I.1.1).

The evaporation experiments were performed for different $MgCl_2$ concentrations from 10^{-3} to 5.7M at a relative humidity of 0% with an initial droplet volume of 10 μl. Within the studied range of $MgCl_2$ concentrations, the evaporation of sessile droplets from aqueous magnesium chloride solutions complied for all significant aspects with the ones experimentally identified in the case of NaCl:

- the contact angle values: θ was about [2-10]°;
- the pinning regime: these salty sessile droplets evaporated in constant contact area mode;
- the subsequent evaporation behaviour: the droplet volume decreased linearly with time, particularly during the initial evaporation period (i.e., between t = 50 and 100 s); and,
- the deposit morphology as result of the evaporation process: as the initial $MgCl_2$ concentration increased, it evolved from a salt-ring structure to an uniform pattern.

The final deposits of drying sessile droplets from aqueous magnesium chloride solutions are presented in Figure 3.12. In comparison to Figure 3.2 illustrating the three different morphological regimes of NaCl deposits, the main difference between these two salts resides in the compositional structure of the dried salt pattern at (very) high salt concentration. As depicted in Figure 3.12, the evaporation of concentrated $MgCl_2$ solutions does not induce a pronounced salt-ring at the droplet edge with some crystals in the droplet center as observed for saturated NaCl solution (Figure 3.2) but causes a dense and uniform salt deposit over the complete footprint droplet area. One of the first reasons that we can mention is the viscosity effect on flow during the evaporation process. The dynamic viscosity η_0 increases with increasing salt concentration [119, 120]. At 20°C, the dynamic viscosity of pure water is about 1.0 mPa.s [120]. With saturated $MgCl_2$ solution η_0 increases by a factor of 7 [120] whereas with for NaCl saturation limit, only by a factor of less than 2 [119]. Therefore, the viscosity effect inside the evaporating sessile droplet becomes non negligible for aqueous magnesium chloride solutions. However, the observation of uniform patterns at higher c_0 promotes qualitatively the occurrence/influence of Marangoni flow within evaporating sessile droplets from aqueous saline solutions.

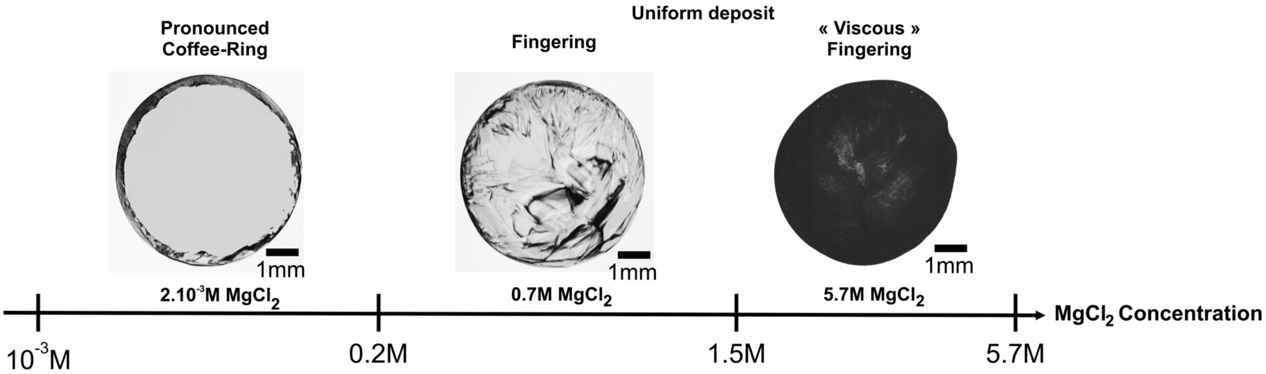

Figure 3.12 – *Morphologies of the final deposit obtained after complete drying of sessile droplets containing aqueous* $MgCl_2$ *solutions at different initial salt concentrations from* 10^{-3} *to* 5.7*M. The evaporation experiments were performed at a relative humidity RH of* 0% *with* 10 *µl-sessile droplets.*

We focused our experimental analysis on the evaporation rate of sessile droplets from magnesium chloride solutions. The normalized initial evaporation rate $\tilde{Q}_i$ (Equation 3.9) was experimentally determined for each initial $MgCl_2$ concentration. We still assumed for the determination of $\tilde{Q}_i$ that the distribution of salt within the sessile droplet was homogeneous (Equation 3.7). The droplet volume and the evaporation time was scaled according to Equations 2.1, 3.3 and 3.4. For Equation 2.1, the scaling of the volume was based on the measurement/determination of the initial droplet volume V_0. The time scaling according to Equation

3.4 was based on the normalization of the relative vapour pressure and the droplet size factor $\tilde{r}$ (Equation 3.3). The relative humidity RH of the surrounding environment was adjusted by the flow of moist nitrogen and also measured in the sample chamber as the temperature T. The droplet size factor $\tilde{r}$ was determined from the measured droplet size and shape at $t = 50$ s. The saturated water vapour pressure in $MgCl_2$ solutions was the literature value corresponding to the initial $MgCl_2$ concentration, c_0 at $T \approx 23°C$ [109].

Figure 3.13 presents the experimentally observed normalized evaporation rates $\tilde{Q}_i$ as function of the initial salt concentration for two different salts having positive σ: NaCl and $MgCl_2$. The dashed line depicts the theoretically expected normalized evaporation rate, scaled to a value of 1 according to Equation 3.9.

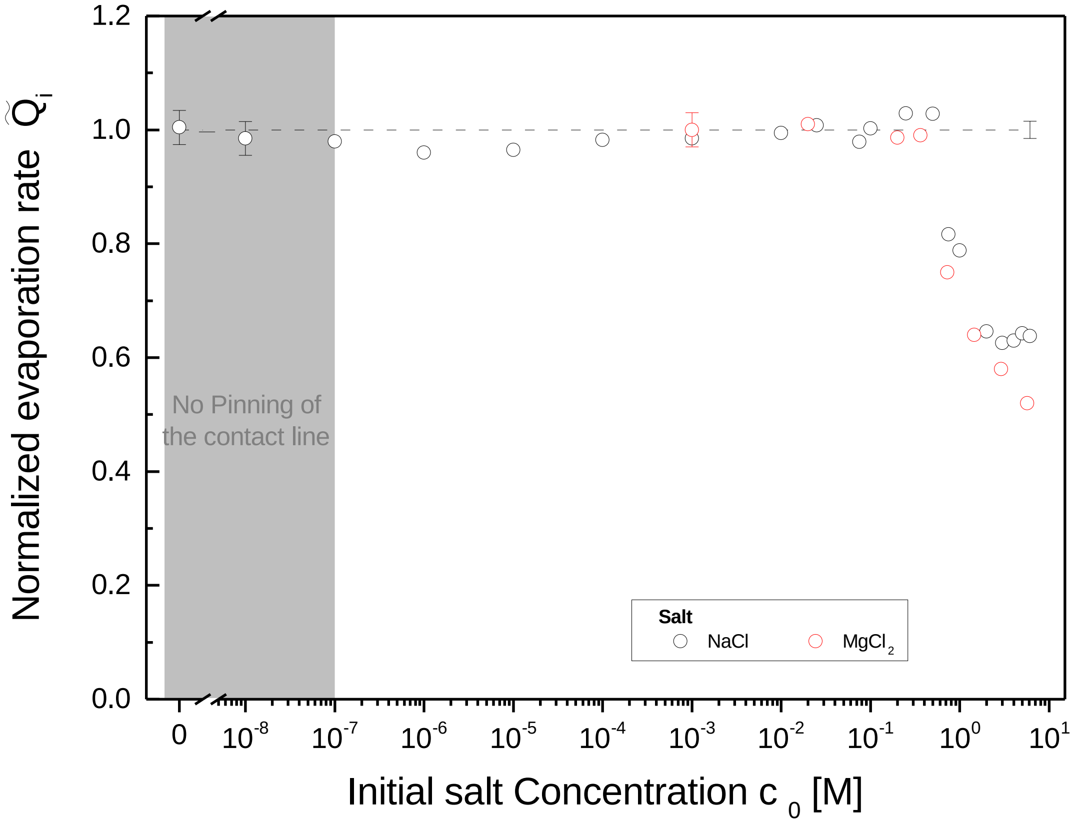

Figure 3.13 – *Experimentally observed normalized evaporation rates* $\tilde{Q}_i$ *as function of the initial salt concentration* c_0 *from* 0 *to* 6.1*M NaCl or from* 10^{-3} *to* 5.7*M* $MgCl_2$ *at a relative humidity of* 0%. *The dashed line depicts the theoretically expected normalized evaporation rate according to Equation 3.9 with the assumption of the (inweight) salt concentration distributed uniformly inside the droplet. The droplets evaporated in pinned, constant contact area mode except for NaCl concentrations* $\leq 10^{-7}$*M.*

Up to a $MgCl_2$ concentration of 0.7M, the measured normalized evaporation rates $\tilde{Q}_i$ agreed quite well with the theoretical predictions. Above this critical $MgCl_2$ concentration, the measured normalized evaporation rates $\tilde{Q}_i$ were smaller than expected. As for NaCl solutions, we observed a deviation between the theoretical predictions and the experimental results for high initial salt concentrations.

The origin of the discrepancy between theory and experiment is the non-uniform salt distribution within the evaporating sessile droplet. Capillary flow originating from a non-uniform evaporative flux along the droplet surface induces a peripheral salt enrichment. This inhomogeneous salt concentration inside the droplet results in surface tension gradients, leading to

Marangoni flows. Since the two studied salts have positive σ, the Marangoni flow is also directed in the same direction as the usual capillary (volume) flow, i.e., towards the three-phase contact line. The resulting local enrichment of salt in the vicinity of the droplet periphery provokes a decrease in $P_{sat}(c)$ and hence a diminution of the evaporation in the droplet edge region. Since the evaporative losses contribute significantly to the entire droplet evaporative losses (in particular, at very small contact angles < 10°), a change of the evaporation at the droplet periphery alters the overall droplet evaporation behaviour.

Another remarkable result revealed in Figure 3.13 is the critical initial salt concentration, c_0^* at which the experimental results start to deviate from the theoretical predictions. For sessile droplets from NaCl solutions, c_0^* was about 0.5M whereas for $MgCl_2$ solutions, it was about 0.3M. This critical initial salt concentration corresponds to a surface tension difference between the salt solution containing c_0^*M, γ^*, and pure water, γ°, $\Delta\gamma = \gamma^* - \gamma^\circ$, of about 0.8 mN.m^{-1} at $T \approx 23$°C [44]. The surface tension difference $\Delta\gamma$ characterizes the Marangoni force. If $\Delta\gamma \geq 0.8$ mN.m^{-1}, it induces a sufficiently strong Marangoni flow to influence the evaporation behaviour of sessile droplets from aqueous saline solutions.

Furthermore the deviation between theory and experiment did not depend on the salt involved in the evaporating droplet except for the saturation limit. The discrepancy between the experimental $\tilde{Q}_i$ and its excepted value was most pronounced for saturated $MgCl_2$ solution than NaCl solution. This difference may come from the surface tension difference between the saturated salt solution and pure water: $\Delta\gamma$ (5.7M $MgCl_2$) $\approx 2\ x\ \Delta\gamma$ (6.1M NaCl) (Figure 1.2).

To conclude, this on-going investigation suggests a potential general evaporation behaviour for sessile droplets from aqueous saline solutions. The evaporation experiments performed with another salt exhibiting a higher surface tension increment aimed in particular at the influence of induced-surface tension forces on the evaporation behaviour. The observations revealed a critical surface tension difference, at which the evaporation behaviour is modified by Marangoni flow, which is induced by surface tension gradients originating from the local evaporative peripheral salt enrichment.

III

Corrosion of Iron under Sessile Droplets from Chloride Solutions[*]

---

[*] Oral contribution containing main results of this PhD part has been presented as: Virginie Soulié, Stefan Karpitschka, Florence Lequien, Philippe Prené, Damien Féron, Thomas Zemb, Helmuth Moehwald and Hans Riegler. *Atmospheric Corrosion of Iron Induced by Sessile Droplets from Aqueous Saline Solutions*. **European Corrosion Congress EUROCORR**, Graz, Austria, September 2015.

1

EXPERIMENTAL METHODS AND EQUIPMENT

1.1 EXPERIMENTAL METHODS

General principle

In this thesis part the experimental purpose was the observation and investigation of the corrosion phenomenon induced by a sessile droplet from chloride solutions deposited onto a planar metal substrate. The main requirement on the corrosion experiment was to avoid significant evaporation/condensation of the droplet in the timescale of the set of experiments (typically less than few months) in order to barely change the bulk droplet composition. The latter was achieved by fixing the environmental conditions of the gas surrounding the droplet (air). At fixed temperature and for a given (fixed) relative humidity, called the equilibrium relative humidity RH_{eq}, the droplet containing the aqueous saline solution was in dynamic equilibrium with its vapour phase environment. There was a constant exchange of water (i.e., evaporation or condensation) between the solution droplet and the vapour phase.

Figure 1.1 shows a schematic illustration of the experimental principle for investigating the corrosion phenomenon occurring under sessile droplets. The corrosion experiments were performed in a closed and airtight container (ThermoScientific^{TM} Nalgene^{TM} Acrylic Desiccator Cabinets) under controlled temperature T and relative humidity RH. The relative humidity was adjusted with a reservoir of saturated salt solutions [111]. The nature and composition of the reservoir solution was dependent on the aqueous saline solution in the sessile droplet (see next section for more detailed information). The reservoir was positioned in the upper place of the container (i.e., above the samples) in order to avoid convective flow effects on the equilibrium behaviour of sessile droplets. The temperature was controlled using the environmental conditions fixed in the air-conditioned room where the container was placed. Additionally the temperature and the relative humidity were also directly monitored with a temperature and humidity sensor (Rotronic Hygrolog, Switzerland) in the controlled environmental container. All the corrosion experiments were carried out at $T = (20 \pm 2)°\mathrm{C}$.

The sessile droplet with an initial volume V_0 of 10 μl was deposited onto the substrate with a syringe, and then the sample was transferred quickly and carefully into the environmental chamber. The transfer had to be rapid in order to avoid evaporative losses from the deposited sessile droplet and also to minimize destabilization of the relative humidity inside the environmental chamber, particularly for high-humidity environment.

Although visible to the naked eye, the physical development of the initiation of the corrosion process was best observed with the experimental setup used for evaporation experiments and presented in the previous part (see II.1.1). The latter allowed a real-time observation of

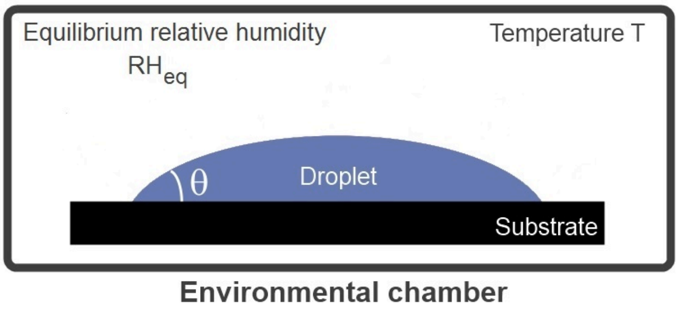

Figure 1.1 – *Schematic illustration of the experimental method for investigating the corrosion phenomenon under sessile droplets. The corrosion experiments were performed in an environmental chamber under controlled temperature T and relative humidity RH.*

sessile droplets from the top and the side simultaneously. Time-lapse recording of the imaging allowed the entire process to be viewed in a shortened time period. Any gas flux was used to adjust the relative humidity and the temperature in the environmental chamber. RH was also controlled with a reservoir of saturated salt solutions, placed in a beaker around the sample. T was the ambient temperature: $T = (20 \pm 2)°\mathrm{C}$. The experimental method conducted either in the environmental container or in the experimental evaporation setup showed both the same consistent and reproducible corrosion results.

Scanning electron microscopy with energy dispersive X-ray spectroscopy

Samples were analyzed ex-situ using a Leica Stereoscan 440 SEM (Scanning Electron Microscope) equipped with an EDS (Energy Dispersive X-ray Spectroscopy) analysis system. Secondary electron images and X-ray analysis were obtained using a working distance of 6.5 mm and an accelerating voltage of 15 kV.

1.2 MATERIAL AND SAMPLE PREPARATION

Saline solutions and substrates

Four different chloride solutions have been chosen for the corrosion experiments: sodium chloride NaCl (Sigma Aldrich), potassium chloride KCl (Sigma Aldrich), lithium chloride LiCl (VWR Chemicals) and magnesium chloride $MgCl_2$ (magnesium chloride hexahydrate, VWR Chemicals) solutions. Most experiments were performed with saturated salt solutions [108, 109, 121]. Additionally concentrated aqueous solutions of sodium chloride and magnesium chloride were also used. The aqueous saline solutions were prepared with Millipore^{TM} water (resistivity 18 $\mathrm{M\Omega.cm^{-1}}$). The different chloride solutions were selected to cover a wide range of relative humidities, i.e., from 10.5 to 99% at $T = 20°\mathrm{C}$ [109, 111, 116]. Furthermore the surface tension of the different studied chloride solutions varied between 73.8 and 92.8 $\mathrm{mN.m^{-1}}$ at $T = 20°\mathrm{C}$ (Table 1.1) [44]. The nature and composition of the reservoir solution used to control the relative humidity in the environmental chamber was either the same as in the bulk droplet or binary saturated aqueous solutions whose RH value was equivalent to the RH_{eq} value of the bulk solution droplet [111]. The different corresponding bulk droplet/reservoir solutions used in this study are listed in Table 1.1.

The main uncertainty for the equilibrium relative humidity RH_{eq} value came from fluctuations of temperature. Typical variations in temperature were 2°C, resulting in fluctuations of the measured relative humidities value: $RH_{eq} \pm 0.5\%$.

Table 1.1 – *Surface tension γ and equilibrium relative humidity RH_{eq} at T = 20°C with the corresponding reservoir solution for each studied droplet bulk solution.*

Bulk droplet solution	**γ [mN.m^{-1}] [44]**	**RH$_{eq}$ at 20°C**	**Reservoir saturated solution**
10.5M LiCl	90.7	10.5%	Lithium chloride LiCl
5.7M $MgCl_2$	92.8	33%	Magnesium chloride $MgCl_2$
3M $MgCl_2$	86.1	64%	3M $MgCl_2$
6.1M NaCl	84.5	75.4%	Sodium chloride NaCl
4.6M KCl	81.3	85.1%	Potassium chloride KCl
3M NaCl	79.0	89.2%	Potassium nitrate KNO_3
1M NaCl	74.9	96.5%	Potassium sulfate K_2SO_4
0.5M NaCl	73.8	99%	Water H_2O

As substrates served pieces of pure iron ARMCO Telar 57 (Fe = 99.85%). Pure iron stood for the ideal case of a metal substrate. All the samples were supplied from the same sheet of iron by WEBER, France. They were cut into pieces of approximately 2 cm x 2 cm x 0.5 cm. Each iron sample was mechanically polished with a Stuers Abramin polishing machine with an applied force of 10 kN. The iron surfaces were abraded successively with 500 and 800 grid SiC paper, each for one minute, and then polished with 1200 and 2400 grid SiC paper, each for two minutes. Then, they were diamond polished down sequentially to 3 and 1 μm, each for two minutes, and finally 0.25 μm for four minutes. Prior to each polishing, the samples were cleaned with distilled water, and dried by blowing with compressed air in order to remove polishing impurities. The polishing of the iron surfaces was concluded by an ethanol rinse and sonication for 15 minutes. After polishing treatment, the iron substrates were dried by blowing with nitrogen (purity 5.0) and stored in a vacuum desiccator with silica gel at room temperature. The surface roughness was measured about less than 2 nm as determined by non-contact atomic force microscopy (experimental analysis done by Rodrigo Pérez-García, Max Planck Institute of Colloids and Interfaces, Potsdam).

Corrosion experiments were also conducted with pieces of single-sided polished silicon wafers with naturally oxidized surfaces. They were presented in the previous part (see II.1.2). In the present study silicon wafers were selected as substrate references because of their corrosion resistance.

Cleaning procedure

To avoid/minimize contamination by dust or any remaining chemical product, a precise and conscientious cleaning was done for the substrates, the syringe/needle and also the vessel. The cleaning procedure for the silicon wafers, the syringe and the glassware were presented in detail in the previous part (see II.1.2).

All corrosion experiments were performed with freshly polished iron surfaces, i.e., stored no more than 48 hours in the vacuum desiccator after polishing. Before further usage, the iron substrates were ultrasonically cleaned with a mixed solution of ethanol (purity > 99.8%, Sigma Aldrich) and acetone (purity > 99.5%, Baker Analyzed) at a volume fraction of 1:1, for 15 minutes. Then, they were dried in a flow of pure nitrogen and immediately used [26].

After exposure under sessile droplets from aqueous saline solutions, the iron surfaces were covered with corrosion products and also unreacted and soluble salt. They were first removed by sonicating the iron samples in milli-q water for 1-3 minutes and then in ethanol for 15 minutes [122, 123]. Sometimes few deposits remained on the iron surfaces. They were removed by cleaning the iron surfaces with a nylon brush and then the cleaning procedure was repeated.

The iron samples were dried by blowing with pure nitrogen and then, stored in a vacuum desiccator.

1.3 DATA ANALYSIS OF CORROSION EXPERIMENTS

In a typical corrosion experiment, the exposure effect of sessile droplets from aqueous saline solutions on iron samples was quantitatively measured. Most relevant was the time evolution of the weight loss of the iron substrates. The weight loss of the iron samples was derived from the weigh difference before and after exposure measured using an analytical microbalance with a precision of 12.5 μg (Mettler Toledo), in an air-conditioned room ($T = 20 \pm 2°$C). Prior to weighing, the samples were stored in an air-conditioned balance room for two hours in order to achieve a thermal equilibrium of the iron substrates.

The iron samples were weighed after polishing treatment and before cleaning with an ethanol/acetone mixture. Their initial weight m_0 was about 4.55 ± 0.10 g. Selected samples were weighted again immediately after polishing or after 48 hours-exposure in a vacuum desiccator to assure that the contribution from reversible adsorbed water was insignificant. The difference in mass gain was less than 1% before and after exposure in the desiccator. Similar fluctuations were determined before and after cleaning of the iron substrates.

At the end of the corrosion experiment, after a time exposure t, the remaining liquid within the sessile droplet was sucked up into the syringe. Immediately after that the samples were stored in a desiccator for 24 hours, and then weighted and imaged with a camera. After completion of the corrosion experiment, selected samples were dried in a flow of pure nitrogen in one direction only in order to verify that the presence of the observed structures was not influenced by the drying phase. Remaining liquid did not spread over the iron sample during the drying phase. Thereafter, the iron samples were cleaned to remove the "corrosion" products and then further imaged and weighed to determine their final weight m_F.

After a time exposure t to sessile salty droplets, the weight loss of the iron sample Δm was calculated from the measured weights m_0 and m_F:

$$\Delta m(t) = m_0 - m_F(t) \tag{1.1}$$

All iron samples were exposed to sessile droplets of saline solutions for different time periods t: from 1 day to 1 month. The uncertainties of the weight loss of iron samples were determined by the repeatability of the corrosion experiment for each exposure time period. For all aqueous saline solutions and for each exposure time period, the corrosion experiments were repeated about three times, with consistent and reproducible results. Typical variations of the weight loss were smaller than 5%.

2

CORROSION OF IRON UNDER SODIUM CHLORIDE SESSILE DROPLET

In marine environment, chloride is the main stimulator of corrosion, since oceans provide a source of chlorine, mainly NaCl. A substantial amount of research on NaCl-induced corrosion has been done by increasing the environmental relative humidity in order to "wet" the metal surface [123–127]. The bulk phase transformation whereby a solid salt (particle) absorbs water to form an aqueous electrolyte, a process well-known as deliquescence, occurs when the relative humidity of the vapour gas phase of the environment is higher than the equilibrium (deliquescence) point of a salt. In atmospheric conditions, this critical humidity threshold delineates a surface sufficiently wet for considerable corrosion to take place from a relatively dry surface, for which corrosion is insignificant [128, 129].

However, regarding atmospheric corrosion, sessile droplets from sea salt (i.e., containing a typical realistic chloride level of about 0.5M) may be formed on metal surfaces. In the literature, under-droplet corrosion experiments are always performed in constant low or high relative humidity environment [20–25], but to the best of our knowledge, not at the equilibrium (deliquescence) relative humidity, where literally, the sessile droplet is in dynamic equilibrium with its surrounding environment. This macroscopic equilibrium condition assumes the steady state system encountered in the Evans droplet model [18] (see I.4.2).

In this chapter we investigated the corrosion phenomenon of a model metal substrate, i.e., iron surface with a sea salt sessile droplet deposited and containing 0.5M NaCl. In the present study, metal samples were subjected to isohumidity exposure, at the equilibrium relative humidity. The aim of this chapter was to apprehend the classical under-droplet corrosion model, well-known as Evans drop experiment [18]. Our experimental study revealed that refinement of the traditional understanding of the corrosion processes were necessary. In particular, a scenario was developed to interpret the localisation of the anodic and cathodic activities.

2.1 OBSERVATION OF DEPOSITS OUTSIDE OF THE SESSILE DROPLET

Iron samples, onto which aqueous sessile droplets from 0.5M NaCl solutions were deposited, were exposed to air with a relative humidity RH of 98% at $T = 20°\mathrm{C}$. Figure 2.1 shows a microscopy image of a dried iron surface, on which a 0.5M NaCl sessile droplet was deposited, after 1 day of exposure to humid air with 98% RH. Immediately after the experiment, remaining liquid was removed from the iron sample, which was then dried in a vacuum desiccator in order to stop the on-going corrosion process.

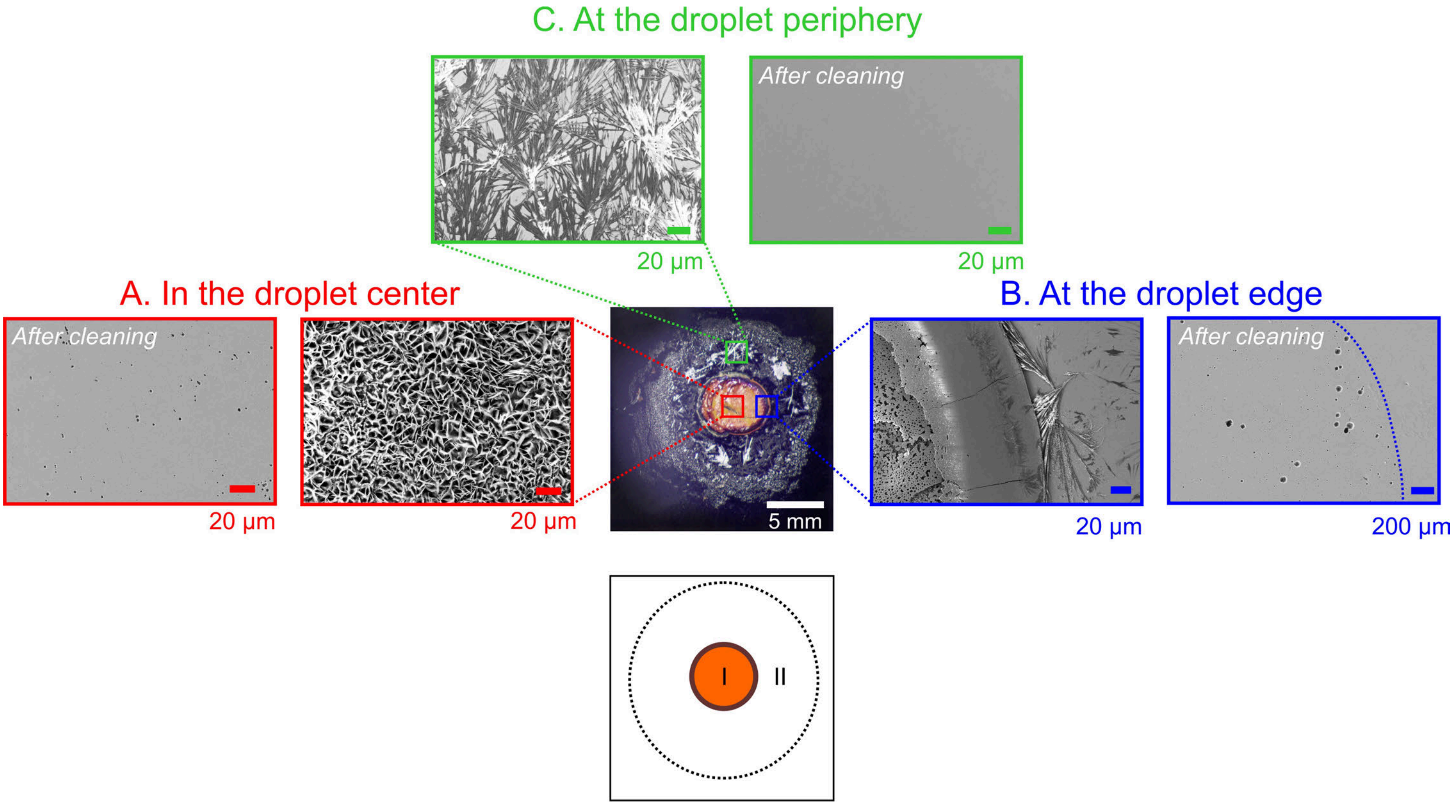

Figure 2.1 – *Microscopy image of a dried iron surface, onto which an aqueous sessile droplet from* 0.5M NaCl *was deposited, after* 1 *day of exposure to air with a relative humidity RH of* 98% *at* $T = 20°\mathrm{C}$. *Two distinct regions on the iron substrate were identified: the footprint region of the initially deposited droplet (labelled area I) and the circular peripheral region around the main droplet (labelled area II) as schematically illustrated at the bottom of the microscopy image. The three insets show SEM micrographs of three different locations on iron corroded under* 0.5M NaCl *sessile droplets:* ***A.*** *in the main droplet center,* ***B.*** *at the main droplet edge, and* ***C.*** *at the main droplet periphery. SEM analysis was carried out on dried iron surfaces after experiment and after removing of the products formed.*

Figure 2.1 shows two distinct regions on a typical iron surface corroded under aqueous sessile droplets from 0.5M NaCl: the droplet footprint region and a peripheral region around the main droplet. The morphological spatial distribution over the iron surface is schematically illustrated in Figure 2.1. Area I almost depicts the footprint region of the main droplet initially deposited onto the iron substrate. Its diameter is about 6 mm. The primary droplet area appears yellowish/dark brown after 1 day of exposure to humid air with 98% RH, indicating the formation of rust phases through the corrosion process [18, 102, 127]. Area II is the peripheral region around the initially deposited main droplet. The formation of this area outside of the main droplet is closely related to the occurrence of corrosion induced by sessile salty droplets. The peripheral region formed around the primary droplet appears as a circular ring of white precipitates, over a distance of about 5.4 ± 0.8 mm from the edge of the main droplet. The drying phase of the iron substrate after the corrosion experiment, either occurring in a vacuum desiccator or in a flow of pure nitrogen, caused the peripheral region to precipitate into islands. Within one day, the width of the peripheral region (i.e., the distance from the droplet edge region to the perimeter of the peripheral region) achieved a value of 2 times that of the radius of the original droplet.

Morphological analysis of the products formed on iron under aqueous sessile droplets from 0.5M NaCl was carried out through SEM for the different observed areas. The three insets in Figure 2.1 show the resultant morphologies, after 1 day of exposure, before and after cleaning of the different products formed, at three different locations on the iron surface: in the main droplet center (Figure 2.1. A), at the main droplet edge (Figure 2.1. B) and at the main droplet periphery (Figure 2.1. C). In the central area of the main droplet, we observe a prolific flowery-like structure as presented in Figure 2.1. A. This is the characteristic pattern of lepidocrocite [130, 131], an iron hydroxide originating from the reaction between the ferrous ions and the dissolved oxygen [127, 132, 133]. After cleaning of the corrosion products, SEM analysis shows numerous pits (i.e., small holes in the iron surface) with a diameter of few microns over the droplet center region (Figure 2.1. A). At the inner edge of the main droplet, similar morphologies on a dried iron surface after the experiment and cleaning are observed as depicted in Figure 2.1. B. A ring of ferrous hydroxide, most likely lepidocrocite, was formed at the droplet edge. The cleaning of this corrosion ring revealed also the presence of few pits in the iron surface, but only under the initially deposited sessile droplet. The edge of the footprint droplet area on the cleaned iron surface is depicted in Figure 2.1. B with a dotted line. At the vicinity of the droplet outer edge, the observed morphology is different. SEM analysis shows needle-like species over the entire peripheral droplet region as illustrated in Figure 2.1. C. After cleaning, any pits were observed in this iron surface region.

Sessile droplets from 0.5M NaCl solutions deposited onto iron surfaces induced pitting corrosion of the metal over the entire footprint of the initially deposited droplet. Two different corrosion products have been identified on the iron surface corroded under aqueous sessile droplets from 0.5M NaCl. The main product identified in the droplet region was iron hydroxide, most likely lepidocrocite. In the peripheral region of the primary droplet, the major identified compound presented a different structure. This observation may indicate some compositional differences between the droplet area and the peripheral region.

2.2 Composition of the Peripheral Part of the Sessile Droplet

The compositional spatial distribution over the dried iron surface corroded under aqueous sessile droplets from 0.5M NaCl, after 1 day of exposure to humid air with 98% RH at $T = 20°\mathrm{C}$ was investigated using SEM/EDS. Figure 2.2 illustrates the distribution of four different elements: iron, oxygen, chloride and sodium on a selective surface area showing the droplet edge region (on the left) and some peripheral deposits around the main droplet (on the right). The backscatter secondary electron image was included to allow direct comparison and to associate element distribution with the different compounds identified in the pattern as explained in the previous section.

The elemental map of iron shown in Figure 2.2.a indicates that this element extends over the entire selective surface area: in the droplet area, in the peripheral deposits and of course, on the unaffected and "naked" iron surface. As presented in Figure 2.2.b, the regions where oxygen element is concentrated are preferentially the main droplet but also in the peripheral species. The spatial distribution of chloride and sodium elements, respectively depicted in 2.2.c

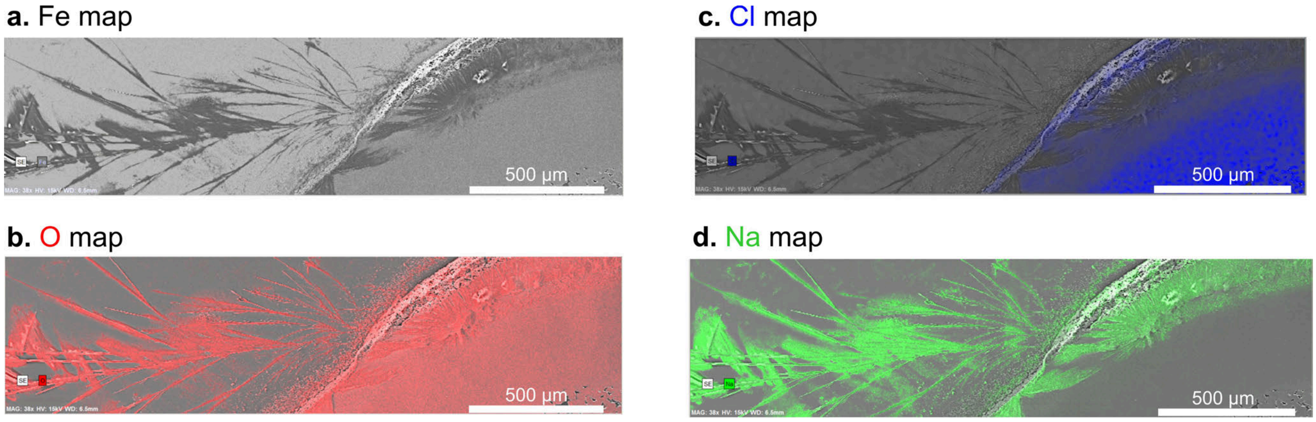

Figure 2.2 – *Identification of chemical composition over a dried iron surface obtained after* 1 *day of exposure to aqueous sessile droplets from* 0.5M NaCl, *in humidified air with* 98% *RH at* $T = 20°C$. *Elemental mapping results using SEM/EDS on a selective surface area showing the droplet edge region (on the left) and some peripheral deposits around the main droplet (on the right) corresponding to the distribution of:* ***a.*** *iron (in grey),* ***b.*** *oxygen (in red),* ***c.*** *chloride (in blue) and* ***d.*** *sodium (in green), associated with the different compounds in the pattern, with the backscatter secondary electron image included.*

and 2.2.d, is the most obvious and interesting features of the corrosion phenomenon induced by sessile droplets from 0.5M NaCl. The chloride element is only concentrated in the initially deposited droplet. On contrary the sodium element is detected not only at the droplet edge region but also in the peripheral deposits. Therefore oxygen element is predominantly combined with sodium in the peripheral deposits whereas with chloride in the main droplet area, while iron, which is the chemical element of the substrate, may be combined with these elements. Thus SEM/EDS analysis is in accordance with the main droplet area mainly composed of ferrous hydroxide resulting from the reaction of ferrous ions with dissolved oxygen. It also reveals that chloride element is mainly distributed in the primary droplet area, which is immediately surrounding by concentrated sodium element regions. As a result sodium element which was initially only concentrated in the main deposited droplet, migrated from its edge region.

Based on the morphological and compositional spatial distribution of the different identified compounds on the corroded iron surface, it was reasonable to assume the occurrence of a film, with a considerable thickness to support the cation migration, emanating from the three-phase contact line of the main droplet. After one day of exposure, the peripheral region surrounding the initially deposited droplet had covered a large area (estimated to about two times the droplet radius from Figure 2.1). Slivers of pH indicator paper were used to estimate pH value of the solution within this peripheral droplet region and also in the main droplet. In the peripheral droplet area, they changed in color to blue (i.e., pH of about 10), indicating an alkaline environment whereas for the primary droplet solution, they turned into red (i.e., pH of about 3-4), revealing an acidified solution. Initially the aqueous saline solution containing in the sessile droplet had a pH of about 6.

2.3 TEMPORAL EVOLUTION OF THE PERIPHERAL DROPLET REGION

The initial development of the peripheral droplet region was investigated by observing the temporal evolution of the top aspect of the iron surface onto which a sessile droplet from aqueous saline solution was deposited. The detailed experimental procedure was described in the previous chapter (see III.4.1). Figure 2.3 shows the initiation of the corrosion process induced with a sessile droplet from 0.5M NaCl, in humid air with 98% RH at $T = 20°C$. To better reveal the formation and growth of the peripheral droplet region, the iron substrate background image (obtained before starting the corrosion experiment) was subtracted from the observed top aspect imaging. In addition the image contrast was specifically focused on this peripheral area. Originally bright, the main droplet appears from now dark. The corrosion product formation, which appeared within the sessile droplet as dark dots or areas, was deliberately not shown in Figure 2.3.

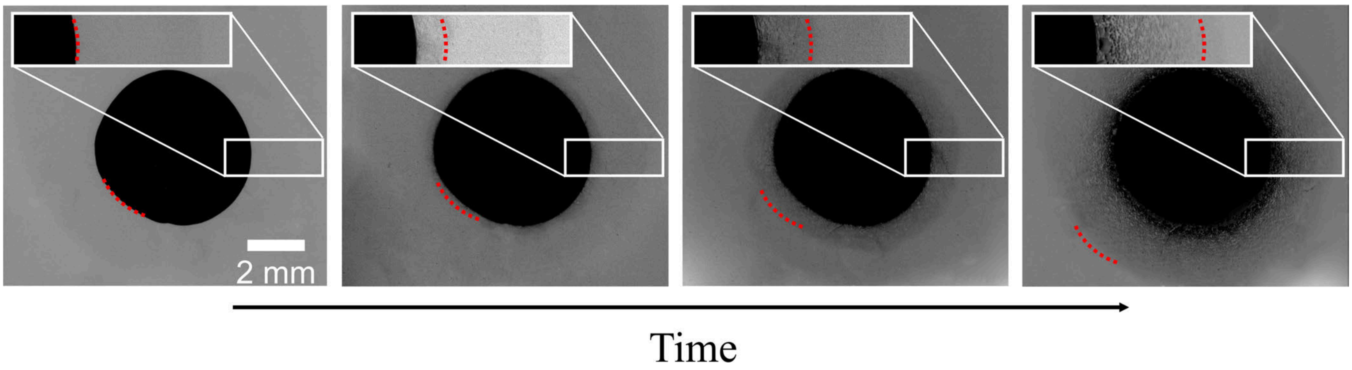

Figure 2.3 – *Initiation of the corrosion process induced with a sessile droplet from* 0.5*M NaCl (with an initial volume of* 10 *μl and contact angle of* 17°*), in humidified air with* 98% *RH at* $T = 20°C$*. For better contrast the iron substrate background image was subtracted and the focus was done on the peripheral region with the main droplet appearing in dark. The sequence of frames shows a time span of* 3 *hours starting* 1 *minute after the droplet deposition. The main part of the images depicts a top view of the iron surface onto which the sessile droplet was deposited. The inset magnifies the same area at the droplet edge/periphery region.*

Figure 2.3 presents a sequence of four frames showing a time span of 3 hours. It was recorded 1 minute after droplet deposition, i.e., long after the droplet had initially spread to its final perimeter and the three-contact line was pinned in this position. The main part of each image displays the top aspect of the iron surface onto which the sessile droplet with an initial volume of 10 μl and contact angle of 17° was deposited. The dashed line indicates the position of the perimeter of the observed peripheral droplet region. As indicated, the inset in each of the four frames magnifies the same area at the droplet edge/periphery region.

Figure 2.3 reveals the formation and growth of a film radiating outwards from the edge of the initially deposited droplet. The position of the main droplet does not change over the corrosion process, i.e., there is no macroscopic contact line motion of the initially pinned sessile droplet on the iron substrate. Few minutes after the sessile droplet was deposited, we observe the formation of a halo in the vicinity of the main droplet edge. The aspect of the film becomes more precise in the course of the corrosion experiment. Micro-pools with an approximately hemispherical shape appear initially nearby the edge of the primary droplet and then over the entire peripheral film. They seem to grow up with time. Additionally the covered area of the peripheral film emanating from the main droplet edge region increases with time. The top view images depicted in Figure 2.3 (and also the optical image presented in Figure 2.1) reveal that the peripheral droplet region is reasonably circular in shape. The symmetry of the peripheral area on both sides of the main droplet is not always achieved, resulting in fluctuations of its measured front position smaller than 15%. Thus an averaged peripheral film width (i.e., the distance from the droplet edge region to the perimeter of the peripheral region) is measured. After three hours of exposure, the width of the peripheral film is about 2 ± 0.3 mm.

Figure 2.4 shows the evolution of the width of the peripheral film as a function of the square root of the experimental time. The expanding perimeter of the film was determined for all corrosion experiments conducted either in the environmental container (Figure 2.1) or in the experimental evaporation setup (Figure 2.3). This allowed to acquire data on the radial displacement of the peripheral droplet region on short- and long-time period. For the corrosion experiments conducted in the experimental setup, the film width was determined from the top view imaging of the iron surface each hour over a time period of 12 hours. On contrary for the corrosion experiments conducted in the environmental container, the film width was deduced from the front position of the peripheral deposits area, observed after drying of the iron sample. The perimeter of the peripheral droplet region was measured using a microscopy image of the dried iron sample, obtained with a camera and SEM micrographs. The width of the peripheral film was measured over a time period of 2 days.

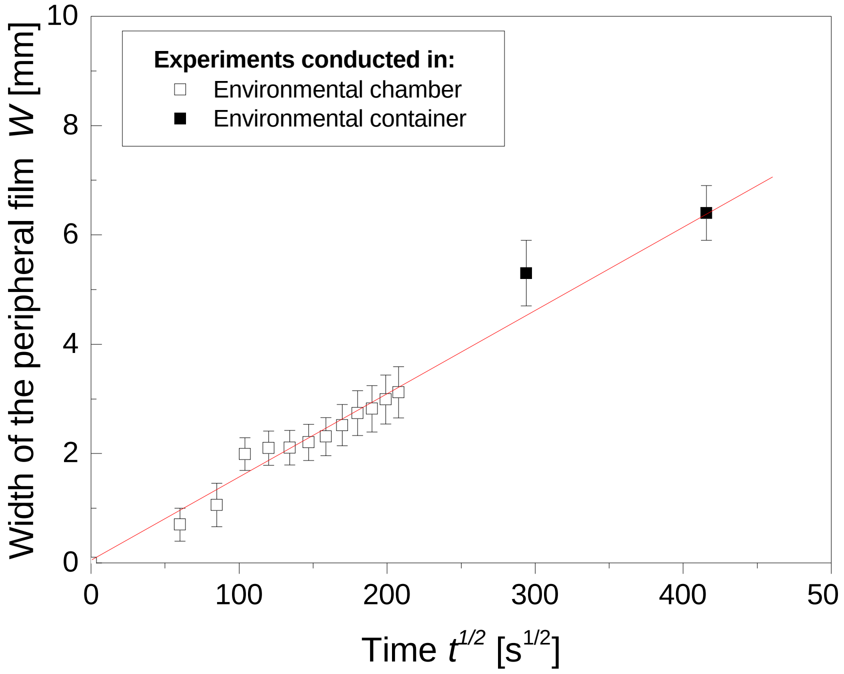

Figure 2.4 – *Evolution of the peripheral film width W (i.e., the distance from the droplet edge to the perimeter of the peripheral region) as function of the square root of the experimental time t. The corrosion experiments were performed with a sessile droplet from* 0.5M NaCl *deposited onto an iron substrate, in humidified air with* 98% *RH at* $T = 20°C$*. The radial displacement of the peripheral droplet region was measured for all corrosion experiments either conducted in an environmental container or a chamber in the experimental evaporation setup. The linear increase of the film width with the square root of time reveals a "diffusive" phenomenon.*

As shown in Figure 2.4, the averaged peripheral film width measured from both corrosion experiments increases in proportion to the square root of time. Thus, the width of the peripheral region increased "diffusively". We can introduce a simple equation describing the characteristic diffusion length scale[1] of the peripheral film width W as function of time t:

$$W(t) = \sqrt{D_p\ t} \tag{2.1}$$

with $\sqrt{D_p}$ as the slope of the curve W-versus-$t^{1/2}$. D_p has the physical dimension of a diffusion coefficient and will be defined as a growth diffusion coefficient. For an iron surface corroded under an aqueous sessile droplet containing 0.5M NaCl in humid air with 98% RH at $T = 20°C$, the growth diffusion coefficient D_p of the solution within the peripheral film in air was about $2.3 \pm 0.2\ x\ 10^{-10}$ $m^2.s^{-1}$.

---

[1] The dimensionality d of the characteristic length scale for diffusion is sometimes included where a coefficient of $\sqrt{d}$ is added. In the present case, Equation 2.1 is reduced to one direction.

Since the cations are considered to migrate through the peripheral film from the droplet edge region, the thickness of the film can be estimated to be in order of the micron scale. If such a thick film is illuminated with monochromatic light falling on it normally, concentric bright and dark circular fringes are formed due to the constructive and destructive interferences of light reflected from the upper and lower surfaces of the film [134–136]. Newton's rings experiments can be performed with the experimental evaporation setup by focusing the observation on a selective area covering the droplet edge and its close vicinity. The experimental evaporation setup illuminates this selective area with a monochromatic and parallel light source (with a wavelength λ of about 550 nm) as described in the previous part (see II.1 for more detailed information). Figure 2.5 shows a Newton interference pattern observed on a micro-pool located nearby the edge of a sessile droplet from 0.5M NaCl deposited onto an iron substrate, after 3 hours in humid air with 98% *RH*.

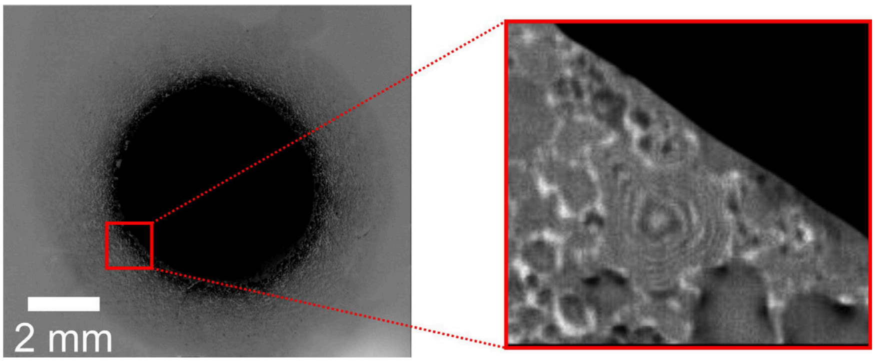

Figure 2.5 – *Newton interference pattern observed on a micro-pool located nearby the edge of a sessile droplet from 0.5M NaCl deposited onto an iron substrate, after 3 hours in humid air with 98% RH at $T = 20°C$. The inset magnifies the selective area covering the droplet edge and its vicinity, on which Newton's rings experiments were performed with the experimental evaporation setup.*

Knowing the exact number n of destructive interferences (i.e., the number of dark fringes), the thickness of the film t, illuminates with a parallel beam of light with a wavelength λ, is given by [136]:

$$2\,t + \frac{\lambda}{2} = (2\,n + 1)\,\frac{\lambda}{2} \tag{2.2}$$

The number of dark fringes n observed in Figure 2.5 is estimated at 6-7. Using Equation 2.2 we found a thickness value for the micro-pool region of about 1.5-2 μm. Most likely, the thickness of the peripheral film may be estimated to be less than 2 microns, with the exception of regions which have formed micro-pools.

In order to have a better understanding on the main ingredients causing the observation of the peripheral droplet region, the influence of two main physico-chemical factors was studied: the nature of the ambient environment surrounding the sessile droplet and the nature of the substrate. In humidified high-purity nitrogen environment with 98% *RH* at $T = 20°C$, the observation of a peripheral droplet region did not occur, if an aqueous sessile droplet containing 0.5M NaCl was deposited onto an iron substrate. Otherwise, any corrosion was observed in these experimental conditions. Similar results were obtained, if the sessile droplet was deposited onto a silicon wafer in humidified air. It is also interesting to notice that the sessile droplet deposited either onto silicon wafers or iron substrates was kept for months without evaporating or condensing in this high-humidity environment. As a result, the occurrence of the peripheral droplet region was sensitive to the air environment surrounding the sessile droplet and also to the corrosion resistivity of the substrate.

2.4 DISCUSSION

Here we investigated the corrosion phenomenon of planar iron under aqueous sessile droplets containing 0.5M NaCl. The sessile droplets were in dynamic equilibrium with their surrounding air environment. The contact of a macroscopic and stationary aqueous electrolyte droplet with a metal surface creates a localized electrochemical cell known as "Evans droplet"[2] [18]. In the classical Evans droplet model, the oxygen O_2 reduction, which results in the production of hydroxyl ions OH^-, occurs mainly at the droplet edge at the substrate-solution interface, because the diffusion path of oxygen from the environmental vapour phase to the substrate-solution is shortest at the contact line region. Thus a cathode is formed at the perimeter of the droplet as depicted in Figure 2.6.a.

$$O_{2(dis)} + 4\ e^- + 2\ H_2O \rightarrow 4\ OH^-_{(aq)} \tag{2.3}$$

The corresponding anode is established at the substrate-solution interface where oxygen is deficient (i.e., away from the contact line). There ferrous ions Fe^{2+} generated from the metal are released into the droplet solution. This reaction forms pits in the iron surface somewhere close(r) to the droplet center as illustrated in Figure 2.6.a. via:

$$Fe_{(s)} \rightarrow Fe^{2+}_{(aq)} + 2\ e^- \tag{2.4}$$

Classically, the anodic and cathodic products will interact with the electrolyte solution to give for instance, ferrous chloride, $FeCl_2$, which will generally precipitate into the pit solution [102, 127] and also together to form a ring of rust in an intermediate zone located between the perimeter and the center of the sessile droplet [18, 19]. The ring rust comes from the oxidation of the initially formed ferrous hydroxide[3] $Fe(OH)_2$ [102, 103] or arises from the reaction between the dissolved oxygen and the ferrous ions, leading to the formation of lepidocrocite γ-$FeOOH$:

$$2\ Fe^{2+}_{(aq)} + \frac{1}{2}\ O_{2(dis)} + 3\ H_2O \rightarrow 2\ \gamma\text{-}FeOOH_{(s)} + 4\ H^+_{(aq)} \tag{2.5}$$

In both cases, the rust formation induces an acidification of the surrounding solution, i.e., in the droplet center. On contrary the oxygen reduction causes high pH values at the droplet perimeter.

Figure 2.1 supports the general mechanism involved in the Evans droplet model, since formation of rust, preferably lepidocrocite, at the substrate-solution interface and pits in the iron surface occurs in the droplet center, but not exclusively. They are widespread across the entire surface covered by the main droplet as depicted in Figure 2.1. Besides an unexpected peripheral film radiating outwards the initially deposited droplet is observed as illustrated in Figures 2.1 and 2.3. These different observations foreshadow that the Evans droplet model does not describe entirely/exactly the observed corrosion phenomenon induced under an aqueous ses-

---

[2] The Evans droplet model describes an iron surface corroded under a sessile droplet containing a jelly electrolyte solution, a mixture of agar-agar and sodium chloride solution in order to demonstrate the electro-chemical mechanism of aqueous corrosion and particularly the natural distribution of anodic and cathodic reactions within the sessile droplet [18, 103] (see I.4.2).

[3] Nonstable in oxygenated aqueous media, the ferrous hydroxide $Fe(OH)_2$, originating from the reaction between the ferrous ions Fe^{2+} and the hydroxyl ions OH^-, further reacted to form other iron oxides or oxy-hydroxides such as lepidocrocite.

sile droplet from 0.5M NaCl, deposited onto an iron surface. Our experimental observations aroused considerable interest on the main reasons for why the peripheral film was formed and by what mechanisms it evolved.

The microscopically film ahead of the macroscopic contact line as schematically shown in the inset of Figure 2.6.a appeared to be initiated by the corrosion phenomenon itself and more precisely by the localised cathodic reaction occurring at the droplet perimeter. A corrosion-resistant substrate (silicon wafer) or a free oxygen (high-purity nitrogen) environment surrounding the deposited droplet on the iron surface prevented the observation of a peripheral film nearby the droplet edge. Most likely the peripheral film was emanating from the three-phase contact line region of the main droplet. But its thickness, estimated to less than 2 microns (Figure 2.5), was rather thick to explain its origin from a "classical" molecularly (nanometer) thin precursor film [36] (see I.1.1) or from adsorbed water layers on the iron surface (for a relative humidity of 98%, the water layer thickness is about 1.7 nm) [94, 95] (see I.4.1).

The origin of the peripheral film was the three-phase contact line. At the droplet edge, hydroxide ions were generated by oxygen reduction. This created a highly localised alkaline environment in this droplet perimeter region. As a consequence, cations migrated towards the droplet edge to maintain electroneutrality. This cation displacement towards the droplet contact line provoked changes in the ionic composition of the liquid in this region. Thus in the three-phase contact line region, there were surface tension changes along the peripheral droplet surface, which led to a Marangoni flow [76]. The three-phase contact line was destabilized by surface tension gradients, induced by ionic composition changes during the course of the cathodic reaction and migration of cations towards the droplet perimeter. Most unlikely, the surface tension gradients may arise from a pH gradient within the entire droplet. Some authors [137] considered that the surface tension of water is independent of the pH of the solution. Thus, we can consider that for water-based solution such as aqueous saline solution, the pH of the solution does not impact the surface tension of the salt solution.

Figure 2.3 and Figure 2.4 demonstrate that once the peripheral film was formed (i.e., it was observed few seconds after the sessile droplet was deposited onto iron substrate), its width was expanding "diffusively" with time. At the peripheral part of the sessile droplet (either the droplet edge or the resulting peripheral film), extensive oxygen reduction occurred since the diffusion path length of oxygen from the environmental vapour phase to the substrate/solution was more and more shortest along this peripheral region. This led to a highly localised alkaline peripheral film, mainly composed of hydroxyl ions resulting from the preferential oxygen reduction in this droplet area. As a consequence, the cathodic activity of the electrochemical cell was developed along this peripheral film emanating from the three-phase contact line of the main droplet (Figure 2.6.b). On contrary, the corresponding anode was established and limited at the interface of the initially deposited sessile droplet with the iron substrate. It could be added that the rust formation led to the generation of protons (Equation 2.5) and as a consequence, anions like chlorides migrated towards the anodic area. The localization of the anodic and cathodic activities across the substrate-solution interface was confirmed by pH value changes of the initially deposited solution. The observed corrosion products and pits under the main droplet as shown in Figure 2.1 were consistent with the anode/cathode separation at the droplet edge, with anodic attack of the iron surface at the primary droplet supported by cathodic regions at the peripheral part of the droplet.

In order to balance the negative electrical charges concentrated in the cathodic peripheral film, the cations mainly the sodium ions[4] originating from the sessile droplet solution, mi-

---

[4] In highly alkaline environment, the solubility of ferrous Fe^{2+} or ferric ions Fe^{3+} is too low (smaller than 10^{-6}M) [138] to allow the migration of these ions towards the highly alkaline peripheral film.

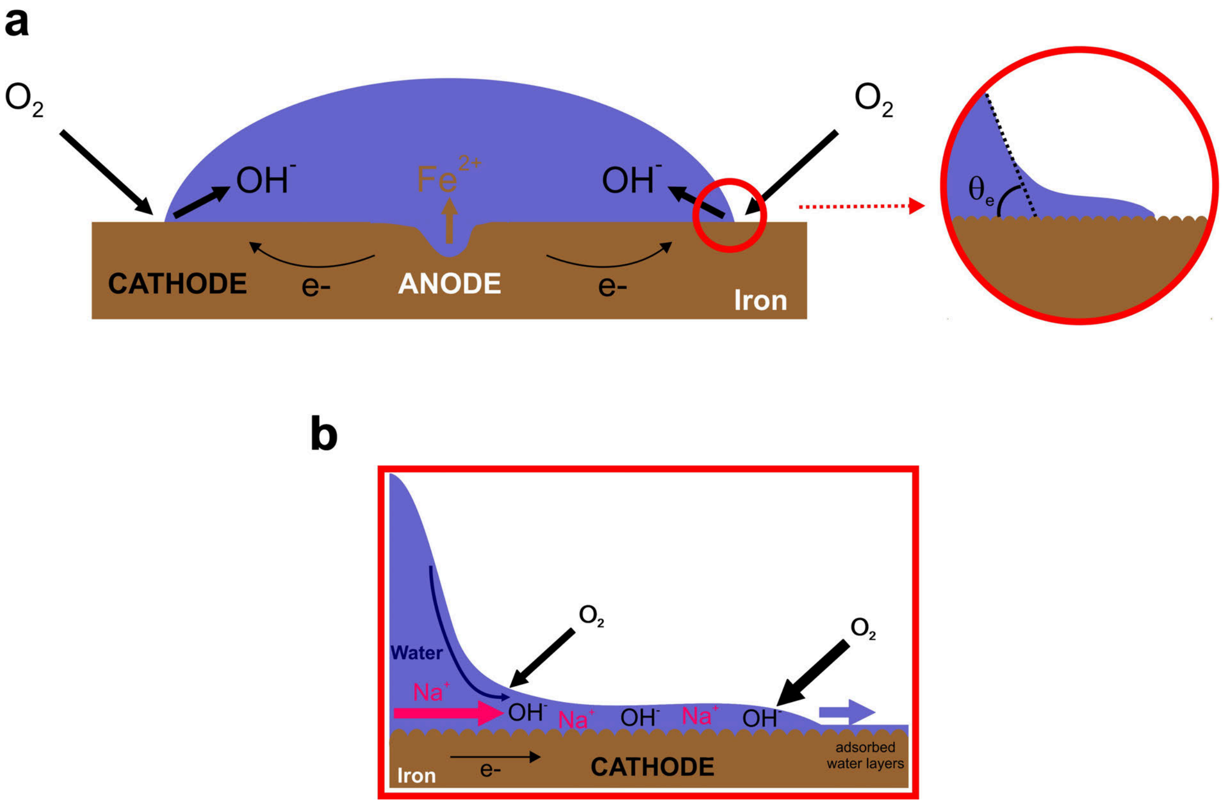

Figure 2.6 – ***a.*** *The classic Evans droplet model under an electrolyte droplet: the oxygen is reduced at the droplet edge, acting as the cathode whereas the iron dissolution occurs in the droplet center acting as the corresponding anode. The inset shows the occurrence of a microscopically film ahead of the macroscopic contact line.* ***b.*** *Expansion of the alkaline thick film by sodium ion displacement compensating the electroneutrality within the droplet and water movement induced by a concentration gradient for a sessile droplet of aqueous NaCl solution deposited onto an iron surface.*

grated towards the peripheral film (Figure2.6.b). This selective ion distribution resulting from the large-scale anode/cathode separation was confirmed by SEM/EDS analysis performed on a dried iron sample as depicted in Figure 2.2. Most chlorides are found in the footprint area of the main droplet, which contained the iron corrosion products. The cations, on the other hand, are concentrated around the droplet, at the peripheral film (cathode) area.

As a result, a concentrated cation-hydroxyl solution was formed in the peripheral film (cathode) region. Therefore there was a concentration gradient between the peripheral film and the droplet bulk. This caused a water movement from the droplet bulk towards its edge (Figure 2.6.b). This water displacement originating from a concentration gradient may arise from a solutal Marangoni effect along the droplet surface [76]. Finally, since oxygen reduction preferentially occurred at the peripheral part of the droplet, the expansion of the peripheral film was controlled by the cation displacement and water movement through it as illustrated in Figure 2.6.b.

During the development of the peripheral film localised micro-pools, or regions of the film, which were slightly thicker than other ones (Figures 2.3 and 2.5), were observed. The observation of these micro-pools on a metal substrate was not unexpected and has been observed before. Numerous studies [22, 28, 124–126, 135, 139, 140] report the formation of "micro-droplets" around the edge of the main droplet formed by deliquescence of salt particles deposited onto metals in humid atmosphere, i.e., above a relative humidity of 80%. This additional wetting of the metal surface around the edge of the electrolyte droplet, called "secondary spreading" was firstly reported by Neufeld *et al*.[124] who studied the deliquescence of NaCl particles on zinc. However, why these micro-droplets are formed and grow with time is not obvious. One group of researchers suggest that the formation of the secondary spreading [124–126, 135, 139, 140] is the result of moisture absorption from the surrounding environment, while other groups associate this phenomenon with formation of particulate gel formed at the edge of the main droplet, which may lead to the formation of a membrane-like barrier that allowed pH gradients to be established between the central droplet and the secondary spread area [22, 28]. Thus the occurrence of localised thicker micro-pools along the peripheral film remains an open issue. We propose the following scenario controlling the micro-droplets process: in the course of the peripheral film formation, reservoirs of cations are formed locally. Due to the high-humidity environment surrounding the droplet, the latter adsorb water and form water clusters. The observed peripheral deposits in the shape of "islands" may arise from these micro-pools after drying of the exposed iron sample (Figures 2.1 and 2.2). To better elucidate the role of the environmental relative humidity, the formation of these water clusters during the peripheral film development deserves more detailed investigation. It will be interesting to measure the width of the peripheral film, or more precisely the thickness of a water cluster over the experimental time. To gain insight into the environmental effect, this study should be widened at different relative humidities (by changing the salt solution inside the droplet bulk to consider the macroscopic equilibrium system) to include information on the impact of RH on the peripheral film formation and particularly on its thickness.

To conclude we demonstrated in this chapter an extension of the classical Evans droplet scenario describing the contact of a macroscopic and stationary aqueous electrolyte droplet (i.e., the droplet was in equilibrium with its environment) with a metal surface. We found that the cathodic site was established along a peripheral film emanating from the three-phase contact line of the initially deposited sessile droplet. Its expansion was related to the cathodic reaction and the cation displacement from the droplet bulk through it.

3

INFLUENCE OF CHLORIDE CONCENTRATION AND DROPLET SIZE EFFECT ON CORROSION OF IRON UNDER SESSILE DROPLETS FROM AQUEOUS SALINE SOLUTIONS

In the previous chapter considerable attention has been paid to the corrosion process which took place, when sea salt sessile droplets (i.e., containing 0.5M NaCl) were deposited onto iron surfaces.

In this chapter we expanded the study of the under-droplet corrosion experiments on iron surfaces to different aqueous saline solutions. The bulk solution within the initially deposited sessile droplet consisted of various aqueous chloride electrolytes of different counter-cations (sodium NaCl, potassium KCl, lithium LiCl and magnesium $MgCl_2$) with an initial chloride concentration c_0 ranging from 0.5 to 11.4M and equilibrium relative humidities RH_{eq} between 10.5 and 99% (Table 1.1). The aim of this chapter was to analyze quantitatively the under-droplet corrosion process and in particular, the peripheral film phenomenon. Our experimental study revealed the main influence of certain parameters on the peripheral film formation.

3.1 TOWARDS A GENERAL PERIPHERAL FILM PHENOMENON

Iron samples, onto which sessile droplets from aqueous saline solutions were deposited, were exposed to isohumid air environment at $T = 20 \pm 2°C$. Experiments were performed with different chloride-based salts (NaCl, KCl, LiCl and $MgCl_2$) and for a wide range of initial chloride concentration c_0, i.e., from 0.5 to 11.7M. As explained in the experimental procedure (see II.4.2), the imposed relative humidity in the surrounding air environment, in which under-droplet corrosion experiments were conducted, was dependent on the bulk solution droplet in order to achieve a dynamic equilibrium of the sessile droplet with its atmosphere and therefore avoid significant evaporation/condensation. As a consequence, the iron samples were exposed to air with different relative humidities *RHs* ranging from 10.5 to 99% as function of the nature and composition of the sessile droplet solution. Figure 3.1 shows microscopy images of dried iron surfaces, on which sessile droplets from 4.6M KCl, 6.1M NaCl, 10.5M LiCl and 5.7M $MgCl_2$ were deposited, after 1 day of exposure to humid air with 85.1%, 75.4%, 33% and 10.5%, respectively.

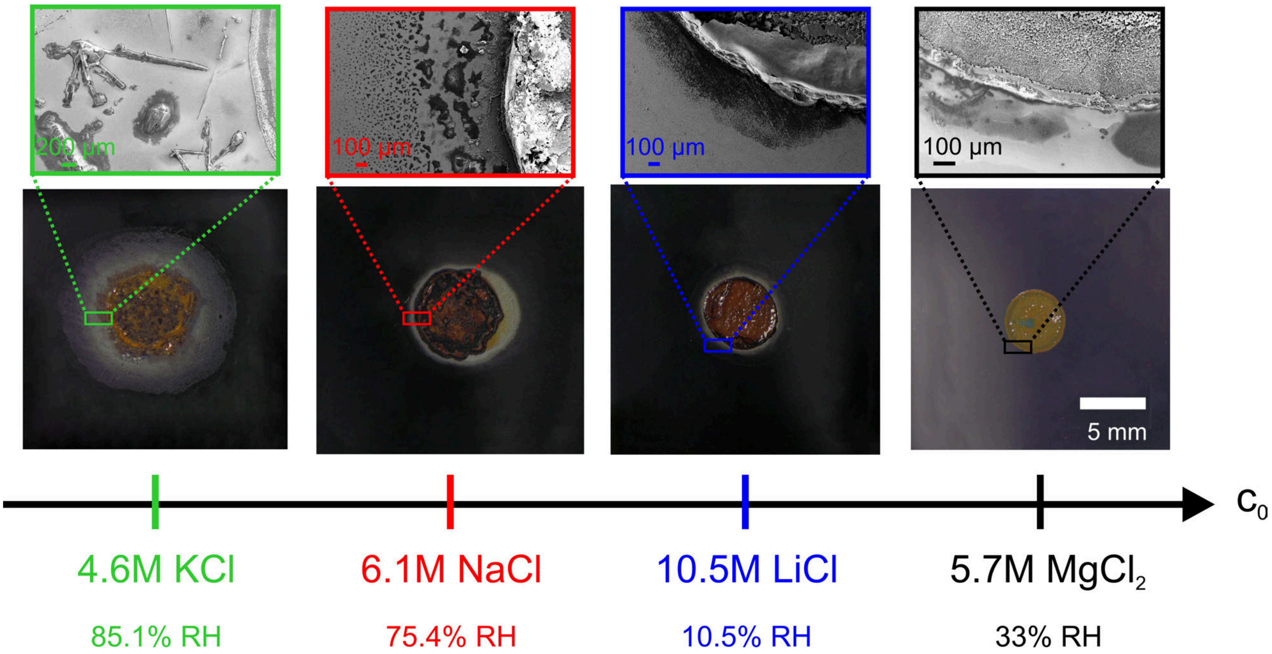

Figure 3.1 – *Microscopy images of a dried iron surface, onto which an aqueous sessile droplet, initially containing a chloride concentration* c_0, *from* 4.6*M KCl,* 6.1*M NaCl,* 10.5*M LiCl and* 5.7*M* $MgCl_2$ *(from the left to the right) was deposited with an initial volume of* 10μl, *after* 1 *day of exposure to air with a relative humidity RH of* 85.1%, 75.4%, 33% *and* 10.5%, *respectively at* $T = 20°C$. *The insets in all four images show SEM micrographs of the droplet edge/peripheral region.*

Figure 3.1 shows two distinct regions on an iron surface corroded under sessile droplets from chloride solutions: the droplet footprint area and its peripheral region. These two characteristic areas were typically observed on an iron surface corroded under sea salt sessile droplets as depicted in Figure 2.1. The initially deposited droplet area appears yellowish/dark brown, indicating the formation of rust phases through the corrosion process. In the main microscopy images shown in Figure 3.1, the peripheral droplet region appears as a circular white ring around the reddish primary droplet [1]. Figure 3.1 reveals that after 1 day of exposure, the width of the peripheral region (i.e., the distance from the droplet edge region to the perimeter of the

---

[1] Since the iron samples were imaged with the same magnification on the camera the peripheral region formed on an iron surface under a 5.7M $MgCl_2$ sessile droplet did not appear clearly on the microscopy image.

peripheral region) decreases as the initial chloride concentration c_0 within the sessile droplet increases.

A morphological SEM analysis was carried out on the different iron samples presented in Figure 3.1. It revealed the formation of lepidocrocite across the entire droplet area and a corroded (pitted) iron surface under the main droplet, as observed and described in the previous chapter. The acidic environment induced by the ferrous hydroxide formation (originating from the reaction between the ferrous and hydroxyl ions) promoted pit initiation and growth in the droplet region, resulting in the large (droplet) surface area of the anodic attack. The inset of each dried iron image in Figure 3.1 shows the resulting morphologies of the peripheral deposits formed in the vicinity of the droplet edge region, after 1 day of exposure and drying of the iron surface. Depending on the chloride cation type, the peripheral deposits present different structures. This structural diversity arose from the characteristic composition of the peripheral region, mainly composed of iron, oxygen and cation (either potassium or sodium or lithium or magnesium) as illustrated in Figure 2.2.

As a result, irrespective of the type and composition of the chloride solution within the sessile droplet, the corrosion process which took place when a sessile droplet was deposited onto an iron surface, provoked the formation of a peripheral film. For each studied chloride solution, the temporal evolution of the peripheral film was also investigated with confidence over a maximum exposure time period of eight days [2]. Figure 3.2.a shows the evolution of the averaged peripheral film width W as a function of the square root of the experimental time t. As explained in the previous chapter (see III.5.3), the radial displacement of the peripheral droplet region on long-time (day) period was deduced from the circular front position of the peripheral deposits area, observed after drying of the iron sample (Figure 3.1). For shortest time period, i.e., $t < 12$ hours, the peripheral film width was determined from the top view imaging, observed, when the corrosion experiment was performed in the environmental chamber in the experimental evaporation setup. The determination of W from both corrosion experiments (either conducted in the environmental chamber or container) showed consistent results between the two experimental methods.

Over the corrosion process, the peripheral film width W increases linearly with the square root of the experimental time t, as depicted by the dotted lines in Figure 3.2.a. This linear increase is observed for each formed peripheral film, immediately obtained after deposition of the sessile droplet from different aqueous chloride solutions onto iron substrates. Figure 3.2.a reveals a "diffusive" increase of the peripheral film width, irrespective of the type and composition of the chloride solution within the deposited sessile droplet. It also confirms, that at a given time, the peripheral film perimeter increases, as c_0 within the main droplet decreases. Using Equation 2.1 a growth diffusion coefficient D_p of the solution within the peripheral film (i.e., the square of the slope of the W-versus-$t^{1/2}$ curve, presented in Figure 3.2.a) was determined for each initial concentration of cation of the chloride solution droplet as illustrated in Figure 3.2.b. Since we demonstrate in the previous chapter that cations migrate towards the droplet periphery, D_p stands for the diffusion coefficient of cation in the peripheral film. Figure 3.2.b shows that D_p decreases with increasing the salt concentration (e.g., NaCl) but also decreases, if the valence of the cation increases for a given cation concentration (e.g., at 3M). These observed trends for the diffusion coefficient are in accordance with the literature [141, 142]. In a general way the diffusion coefficient is slightly affected by the nature (i.e, the size, the charge) of the ion and also by the nature and composition of the electrolyte solution [142]. The relative sensitivity of the diffusion coefficient with the cation suggest that there is no major influence

---

[2] Since the iron sample was 2 cm and the droplet diameter was about less than 6 mm, the droplet peripheral region was determined with accuracy when the latter did not exceed 7 mm.

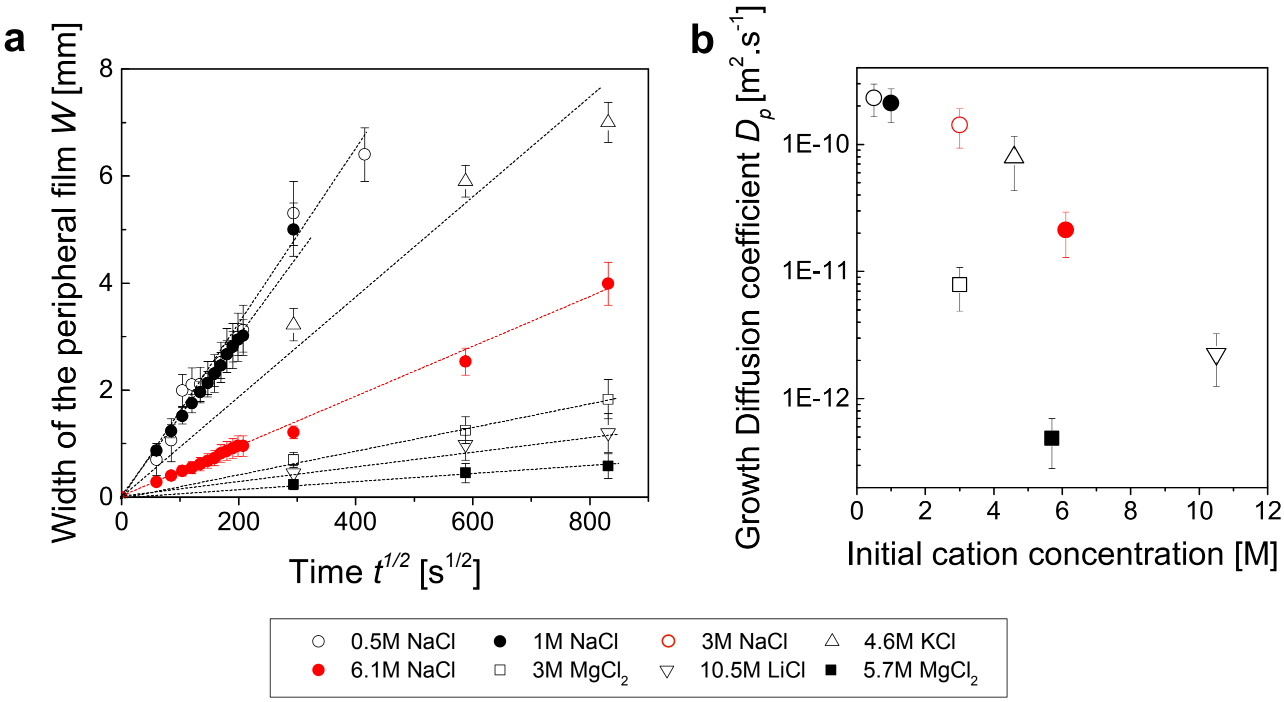

Figure 3.2 – *a. Evolution of the peripheral film width W (i.e., the distance from the droplet edge to the perimeter of the peripheral region) as function of the square root of the experimental time t. The corrosion experiments were performed with a sessile droplet from chloride solution deposited onto an iron surface, in humidified air with RH_{eq} at $T = 20°C$. The radial displacement of the peripheral droplet region was measured for a short-time period ($t < 12$ hours) and long-time period ($t > 1$ day) from corrosion experiments, respectively, conducted in the environmental chamber or container. The linear increase of the film width with the square root of time depicted with a dotted line reveals a "diffusive" phenomenon. b. The growth diffusion coefficient D_p of the (cation) solution within the peripheral film, corresponding to the square of the W-versus-$t^{1/2}$ slope curve (Equation 2.1) as function of the initial cation concentration within the initially deposited sessile droplet onto iron surface.*

of the cation itself. However, the measured values for D_p are much (about 10-100 times) lower than the diffusion coefficient of the cation in water or in salt solution. Just to give an order of magnitude, in comparison, for 0.5M NaCl solutions, the self-diffusion coefficient of sodium ion D in the same concentrated sodium chloride solution at $T = 20°C$ is about $1.4\ x\ 10^{-9}$ m^2.s^{-1}) [141].

Our experimental results shows that, when a sessile droplet from aqueous chloride solution was deposited onto an iron surface, a "diffusive" peripheral film emanated from the droplet edge region, at the three-phase contact line. The most obvious and interesting feature of this general peripheral film phenomenon was the change of its width, at a given time, depending on the nature and composition of the chloride solution within the initially deposited sessile droplet. Different parameters may explain the origin of this observed discrepancy:

- the relative humidity RH in the surrounding air environment in which the under-droplet corrosion experiment was performed. Its value varied from 10.5 to 99%;
- the salt solution itself: e.g., its initial concentration ranging from 0.5 to 5.7M and its viscosity η_0; and,
- the droplet parameters such as its size, and more particularly, the three-phase contact line topology characterized by the surface tension of the liquid-vapour interface.

The influence of these parameters on the corrosion process have been assessed by determining the rate of iron corrosion under sessile droplets from aqueous chloride solutions.

3.1.1 Corrosion Rate Determination

The corrosive effects of chloride under-droplet deposition on iron have been quantified by performing weight loss measurements at different exposure times t. At a given exposure time t, the weight loss of iron samples $\Delta m(t)$ was calculated from the measured weights m_0, the initial (before experiment) weight and, $m_F(t)$, the final (after experiment and cleaning of the "corrosion" products) weight using Equation 1.1 (see III.4.3 for more detailed information). Figure 3.3 presents the measured weight loss of iron substrates, onto which sessile droplets from aqueous chloride solutions were deposited, over the corrosion process, at several exposure times ranging from 1 day to 1 month.

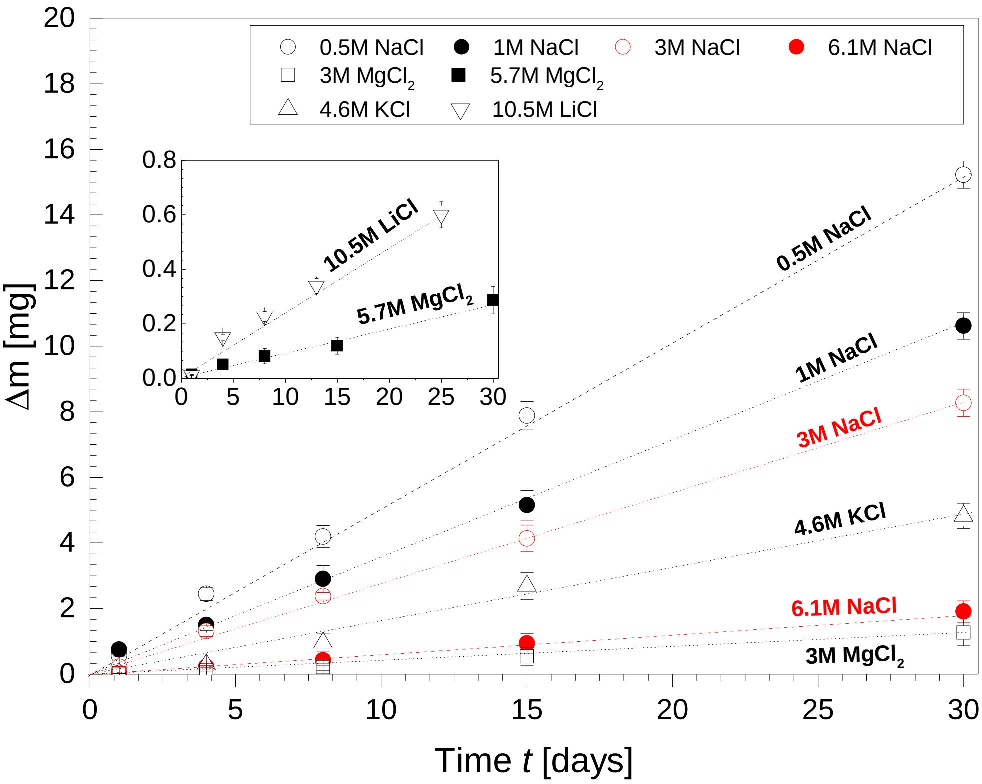

Figure 3.3 – *Weight loss of the iron substrate* Δm, *onto which sessile droplets containing different aqueous chloride solutions were deposited, as function of the exposure time* t. *Over the corrosion process,* $\Delta m(t)$ *was calculated from the measured initial weight* m_0 *and the final weight* m_F *using Equation 1.1. The linear increase of* Δm *between* $t = 1$ *day and* 1 *month was used to determine the corrosion rate* V_{corr}.

Figure 3.3 shows that the weight loss of iron samples increases over the whole corrosion process. A temporal increase of Δm is observed for the different studied chloride solutions within the initially sessile droplets deposited onto iron substrates. Between $t = 1$ and 30 days, the weight loss increase is linear with time as depicted by the dotted lines in Figure 3.3. Thus a weight loss rate (i.e., a change of the weight loss of the iron sample per time unit: $\frac{\Delta m}{t}$) is rather well defined and can be measured in this exposure time interval.

The rate of the corrosion process, which took place when sessile droplets from aqueous chloride solutions were deposited onto iron, was evaluated as the weight loss rate per area unit. The surface covered by the initially deposited sessile droplet on the iron substrate S_{drop} was considered as exposed area for the corrosion rate determination since the corrosive effects on iron (i.e., in the present case, the pitting corrosion in the metal) was solely observed under the main droplet area as illustrated in Figure 2.1. Thus the corrosion rate V_{corr}, the change of the weight loss of the iron sample Δm per time unit t and per area unit S_{drop}, corresponding to the contact area of the initially deposited sessile droplet from aqueous chloride solution with the iron substrate, was given by:

$$V_{corr} = \frac{\Delta m}{t} \frac{1}{S_{drop}} \approx constant \tag{3.1}$$

All the parameters involved in Equation 3.1 can be assumed as constant. The weight loss per time unit $\frac{\Delta m}{t}$ can be considered as constant from the experimental determination/measurement (Figure 3.3). Over the corrosion process we observed that the initial contact area of the deposited sessile droplet with the substrate remained approximately constant as depicted in Figure 2.3. The formation of the peripheral film from the droplet edge region did not alter the footprint diameter of the initially deposited sessile droplet. As a consequence, we can assume that the corrosion rate V_{corr} was constant for a given salt solution. Thus we found an unique value of V_{corr} for each of the eight studied under-droplet corrosion experiments. V_{corr} is on the order of hundreds of mg.cm^{-2}.an^{-1}, i.e., about 1-6 μm.an^{-1}. Comparing to corrosion rates of iron in marine atmospheric environments, which are about 10-100 μm.an^{-1} [143], exposures to sessile droplets from saline solutions exhibit lower corrosion rates.

3.1.2 Peripheral Film Growth

In aqueous chloride systems, corrosion is the result of the coupling of at least one anodic (dissolution) reaction (Equation 2.4) with at least one cathodic (reduction) process (Equation 2.3). Anodic and cathodic reactions proceed in step with each other, but the overall rate of the electrochemical corrosion is governed by either the anodic or the cathodic reaction. Corrosion of iron under sessile droplets from aqueous chloride solutions induces the spatial separation of the anodic and cathodic processes, leading to localized corrosion under the initially deposited main droplet. The main droplet acts as an anode supporting by cathodic reaction along the peripheral film emanating from the droplet edge region. As a consequence, the governing reaction of the overall corrosion process may be determined by considering the impact of its surface area on the corrosion rate. The droplet surface (anodic) area barely changed independent of the nature and composition of the chloride solution inside the sessile droplet: $S_{drop} \approx 0.24 \pm 0.06$ cm^2. Otherwise, the initial footprint area of the deposited sessile droplet was not altered over the corrosion process. On contrary, the surface area of the cathodic process S_C, which is proportional to the peripheral film width W [3], increased over time as depicted in Figure 3.2, and also differently depending on the type of chloride solution. Therefore, if the cathode surface area is the peripheral part of the droplet (i.e., the droplet edge and the resulting peripheral film), S_C will *not* be constant over the corrosion process and by extension, the rate of the overall corrosion process V_{corr} will increase with time. This was not the experimentally observed case: V_{corr} was determined as *constant* for a given salt solution (Equation 3.1). Thus, we can assume that the effective cathodic surface area, which contributes significantly to the overall kinetics, is essentially limited to the three-phase contact line region.

However, the V_{corr} value varied from one system to the next by changing the type and composition of the chloride solution within the sessile droplet. Figure 3.4 shows the rate of the overall corrosion process V_{corr} as function of the square root of the growth diffusion coefficient D_p (Equation 2.1). D_p was experimentally determined for each salt solution from the measurement of the peripheral film width with time (Figure 3.2).

---

[3] $S_C = (r+W)^2\,\pi - S_{drop} = 2\,r\,W + W^2$ with r as the radius of the initially deposited sessile droplet and S_{drop} as the droplet surface area. Since W^2 is negligible compared to the first term, the surface area of the cathodic process S_C can be approximated by $2\,r\,W$.

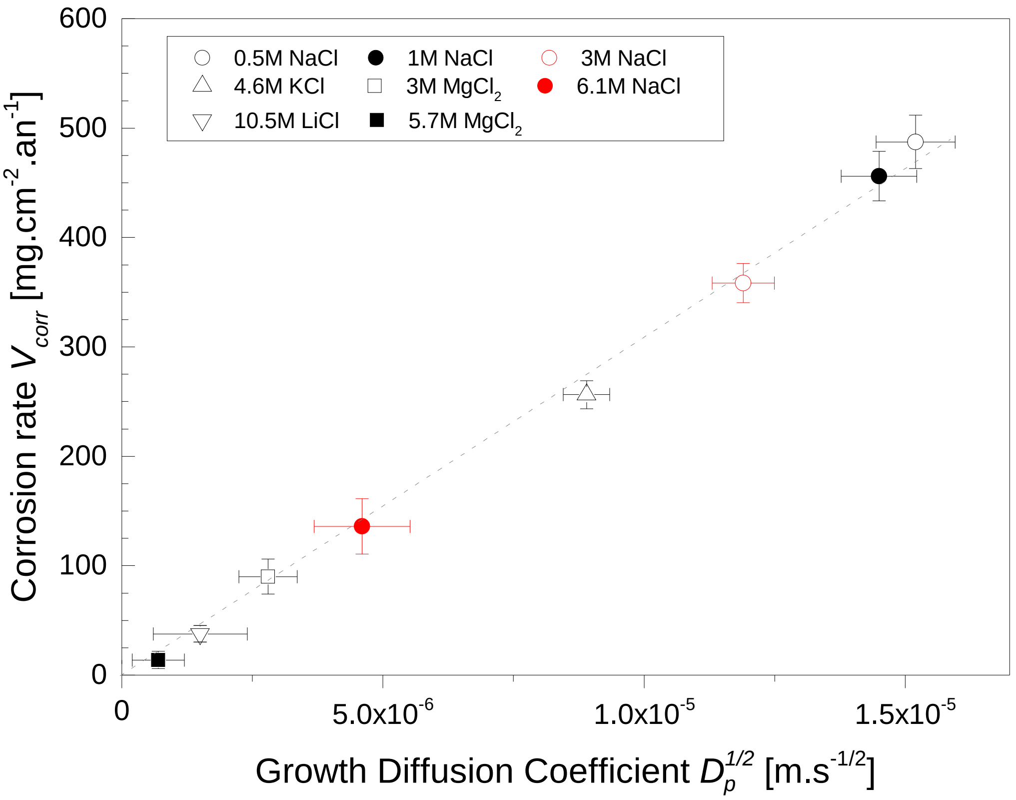

Figure 3.4 – *The rate of the corrosion process induced when a sessile droplet from aqueous chloride solution was deposited onto an iron substrate* V_{corr} *(Equation 3.1) as a function of the square root of the growth diffusion coefficient* D_p *(Equation 2.1). The corrosion experiments were performed in humidified air with* RH_{eq} *at* $T = 20°C$.

The rate of the overall corrosion process V_{corr} increases as the square root of the growth diffusion coefficient D_p increases. More precisely, we observed a linear increase of V_{corr} with $\sqrt{D_p}$ as depicted by a dotted line in Figure 3.4. Figure 3.4 reveals that the rate of iron corrosion under sessile droplets from aqueous chloride solutions, and by extension the overall droplet induced-corrosion process, is governed by the ion (cation) transport from the droplet bulk through the peripheral film, which emanates from the (cathodic) three-phase contact line. As the displacement of cations towards the droplet edge is enhanced or facilitated, the corrosion process is accelerated considerably.

In the following sections, the corrosion rate V_{corr} (Equation 3.1) will be determined as function of each experimental parameter: the relative humidity RH, the initial chloride concentration c_0 and the initial droplet volume V_0.

3.2 RELATIVE HUMIDITY DEPENDENCE

The relative humidity RH in the surrounding air environment, in which corrosion experiments under sessile droplets from aqueous chloride solutions were performed, was adjusted varying the equilibrium relative humidityRH_{eq} from 10.5 to 99% as function of the bulk solution droplet. Figure 3.5 presents the evolution of the rate of the corrosion process induced when a sessile droplet from aqueous chloride solution was deposited onto an iron substrate as a function of the imposed equilibrium relative humidity in the surrounding air droplet environment at $T = 20°C$.

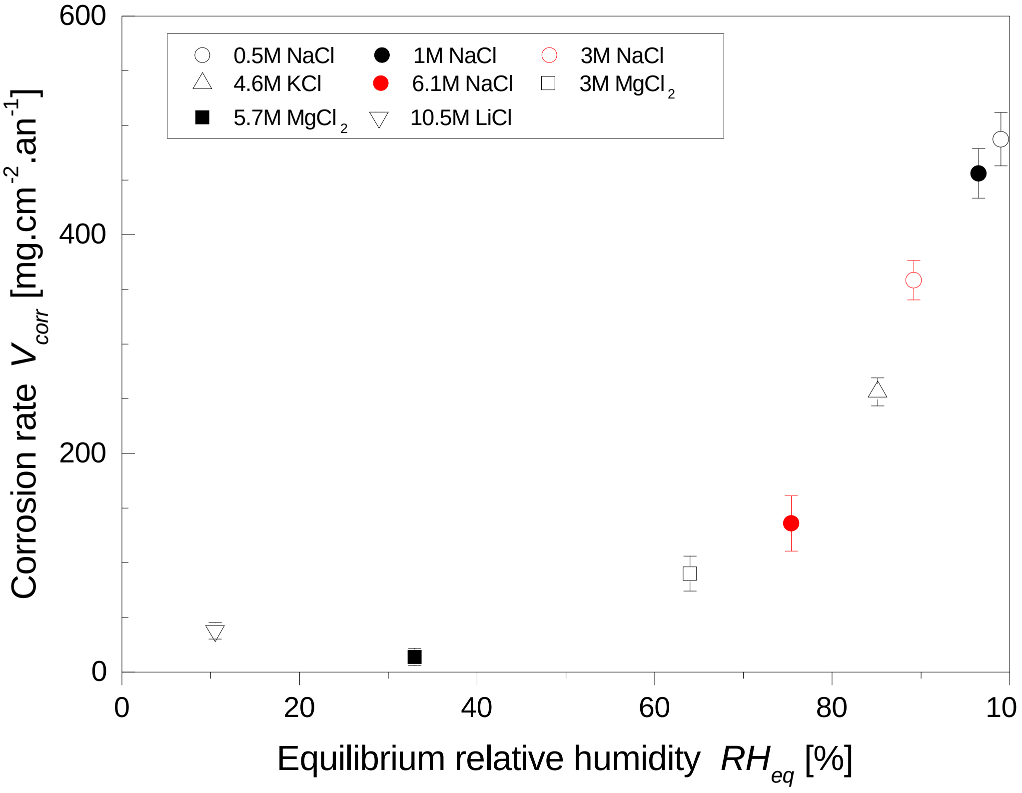

Figure 3.5 – *The rate of the corrosion process induced when a sessile droplet from aqueous chloride solution was deposited onto an iron substrate* V_{corr} *(Equation 3.1) as a function of the equilibrium relative humidity* RH_{eq} *imposed in the surrounding air environment at* $T = 20°C$.

Figure 3.5 shows that the curve V_{corr}-versus-RH has a sigmoidal shape response. Below a relative humidity of 70%, the corrosion rate is less than 100 mg.cm^{-2}.an^{-1}. Between RH = 70 and 99%, V_{corr} significantly increases: its value augments from 130 to 490 mg.cm^{-2}.an^{-1}. Figure 3.5 illustrates that the moisture content in the atmosphere influences the corrosion rate.

The first evidence of ambient relative humidity-dependent atmospheric corrosion was demonstrated by Vernon [96, 97]. He showed a dramatic increase in weight gain in iron samples when the relative humidity exceeded a certain value, called ”critical relative humidity”, in the presence of SO_2, a well-known oxidizing gas contaminant in industrial atmosphere [97]. Water layers may be adsorbed from the vapour phase environment. The thickness of the water layer ranges from less than one to tens of monolayers and depends primarily on the relative humidity [89, 144] and the surface of the substrate material such as its roughness or its wetting properties [95]. At 20% RH, approximately one monolayer exists on average, whereas at 75% RH, the thickness increases to about five monolayers [89, 144]. The corrosion rate is a function of the thickness of the adsorbed water layer and therefore the relative humidity (see I.4.1). Figure 3.5 is representative of the V_{corr}-versus-RH curve usually observed for most metals. Typically the critical humidity level above which the corrosion rate drastically increases is more than 50% and is thought to be the relative humidity at which at least three monolayers of water exist. In general if the RH is lower than the critical level, the corrosion rate is minimal and the reaction process is essentially dry (requiring a direct gas-metal ambient-temperature interaction) [144]. Above this critical relative humidity, the adsorbed water phase becomes ”quasi-aqueous” and can support faster electrochemical charge transfer reactions [89]. The final important water-adsorption aspect is associated with the chemical and physical properties of the products, deposited or formed by corrosion, on the metal surface. These surface (hygroscopic) contaminants may absorb water from the vapour phase of the atmosphere and can give rise to a drastic increase of the corrosion rate [89, 145]. As a consequence the corrosion rate is directly related to the amount of water present on the corroding surface.

The rate of iron corrosion under sessile droplets from aqueous chloride solutions was affected by the surrounding environment humidity. However, the peripheral film formation from the droplet edge was observed even in low-humidity environment. The relative humidity have an impact on the corrosion process once the peripheral film is obtained. This will be discussed in detail in the discussion section. Moreover, it is interesting to notice that in low-humidity environment ($RH < 40\%$), the corrosion rate was not negligible and in particular, was higher at 10.5% (10.5M LiCl) than 33% (5.7M $MgCl_2$). This suggests that the electrolyte solution within the sessile droplet may have an influence on the corrosion process.

3.3 INFLUENCE OF CHLORIDE CONCENTRATION

Different nature and composition of electrolyte solutions within the initially deposited sessile droplet onto iron samples were investigated. In particular, the influence of the initial chloride concentration c_0 on the corrosion rate V_{corr} (Equation 3.1) was studied as depicted in Figure 3.6.a.

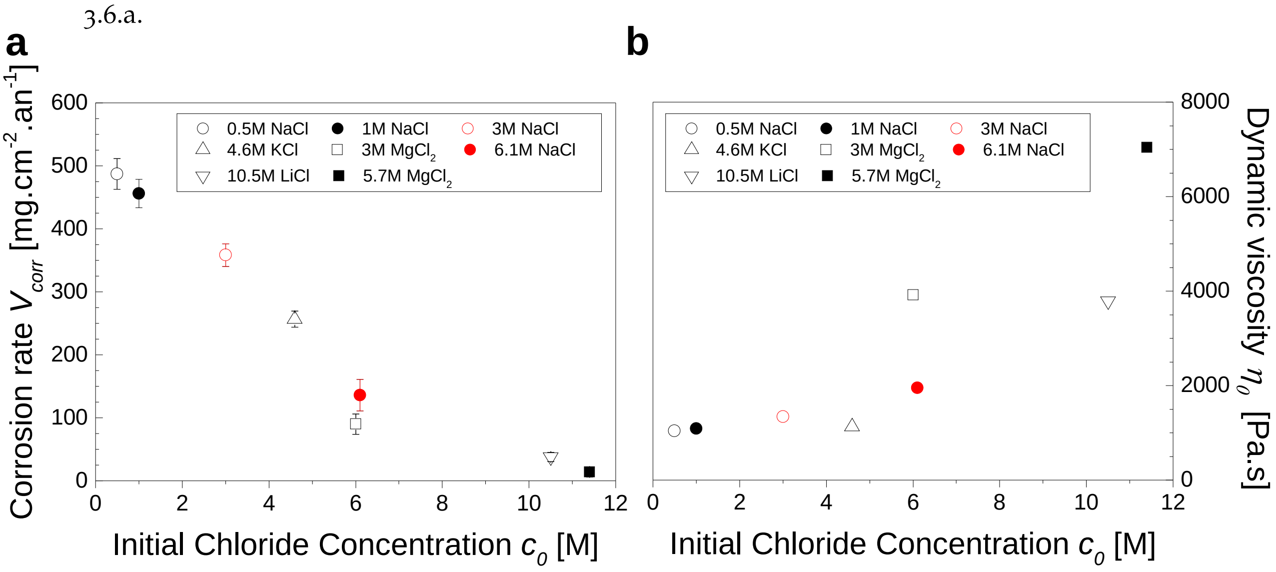

Figure 3.6 – ***a.*** *Corrosion rate* V_{corr} *(Equation 3.1) as function of the initial chloride concentration* c_0 *of the aqueous electrolyte solution in the sessile droplet deposited onto iron surfaces. The corrosion experiments were performed in air environment with* RH_{eq} *at* $T = 20°C$. ***b.*** *The influence of* c_0 *on the dynamic viscosity* η_0 *of the droplet bulk salty solution. As dynamic viscosity* η_0 *we assumed the literature values corresponding to initial inweight chloride concentration* c_0 *within the initially sessile droplet deposited onto iron samples, at* $T = 20°C$ *[119, 120, 146, 147].*

Figure 3.6.a reveals that V_{corr} decreases as c_0 increases from 0.5 to 11.4M. This experimental result is really surprising and counter-intuitive, since it is not consistent with the current understanding, that the corrosion behaviour of metal in aqueous chloride solutions and under sessile chloride droplets increases with higher chloride ion concentrations [20, 25]. The general thinking is that chloride ions influence the corrosion rate by virtue of the type of metal-chloride ion complex (compound) that is formed. Thus solutions of chloride ions would form a $FeCl_x$ (x = 2, 3) complex which would readily dissociate and have the net effect of carrying Fe^{2+} away from the surface, within the droplet solution [148]. This would imply that chloride ions are involved in the anodic process. Increasing the chloride concentration within the sessile droplet will increase the anodic kinetics. Therefore an augmentation in chloride

ion concentration should accelerate considerably the corrosion process if the anodic reaction contributed significantly to the overall kinetics [148]. This is completely the opposite of what is observed in Figure 3.6.a. As a result, Figure 3.6.a supports that the corrosion process is not controlled by the anodic reaction but rather influenced by the cathodic reaction occurring at the droplet perimeter, and more particularly by the oxygen uptake at the droplet edge region. Since an increase in salt concentration in the droplet bulk reduces the solubility of oxygen at the electrolyte-metal interface near the contact line region [149, 150], the corrosion rate V_{corr} shifts to less positive values, as the droplet aqueous solution is more concentrated in salt (chloride).

Otherwise the nature and composition of the electrolyte may also influence the intrinsic parameters of the solution inside the initially sessile droplet deposited onto iron surfaces. Since we demonstrated that the diffusive ion transport towards the droplet edge influences the under-droplet corrosion process (Figure 3.4) and we also showed that the growth diffusion coefficient D_p changes by two orders of magnitude (Figure 3.2.b), viscous stresses at the electrolyte-air interface may slow down the corrosion process. Figure 3.6.b presents the initial dynamic viscosity η_0 of the salt solution within the sessile droplet as function of the initial chloride concentration c_0. As dynamic viscosity η_0 we assumed the literature values corresponding to initial inweight chloride concentration c_0 within the initially sessile droplet deposited onto iron samples, at T = 20°C [119, 120, 146, 147]. Figure 3.6.b shows that η_0 increases with increasing c_0 for a given salt (e.g., NaCl), but also in a general way for all the studied range of aqueous chloride solutions. For an approximately constant c_0 (e.g., at 3M), the initial viscosity properties of the magnesium and sodium chloride solutions differ obviously: η_0 (3M $MgCl_2$) $\approx 2 \cdot \eta_0$ (6.1M NaCl) [119, 120]. However, Figure 3.6.a depicts that the corrosion rate of these two different systems is only slightly different. This slight variation in V_{corr} at constant c_0 suggests that the effect of viscous forces on the corrosion process, and particularly on the diffusion limiting transport of cations in the peripheral film, is relatively unimportant.

In the previous chapter, our scenario of the extended Evans droplet model included the occurrence of interfacial forces in the three-phase contact line region, induced by ionic composition changes during the course of the cathodic reaction and migration of cations towards the droplet perimeter. Depending on the nature and composition of initial chloride solutions inside the sessile droplet, the surface tension γ varied between 73.8 and 92.8 mN.m^{-1} at $T = 20$°C [44] (Table 1.1). Figure 3.7 shows the effect of the surface tension (at the interface air-liquid) γ of the aqueous chloride solution on the corrosion rate V_{corr} (Equation 3.1) placed under sessile droplets in air with RH_{eq} at $T = 20°C$.

Figure 3.7 reveals that V_{corr} decreases as γ increases. Between γ = 73.8 and 92.8 mN.m^{-1}, the corrosion rate is linear with the surface tension of the aqueous electrolyte solution as depicted by the dotted line in Figure 3.7, in the course of the formation of the peripheral film. The latter confirms some peripheral/radial flow/transport which is influenced by (peripheral) surface tension gradients. This will be discussed in greater detail in Discussion.

3.4 Droplet size effect

The droplet size effect on the corrosion process induced when a sessile droplet from chloride solution was deposited onto iron samples was investigated. For this purpose, we focused our study only on sessile droplets from aqueous 6.1M NaCl solution exposed to air environment

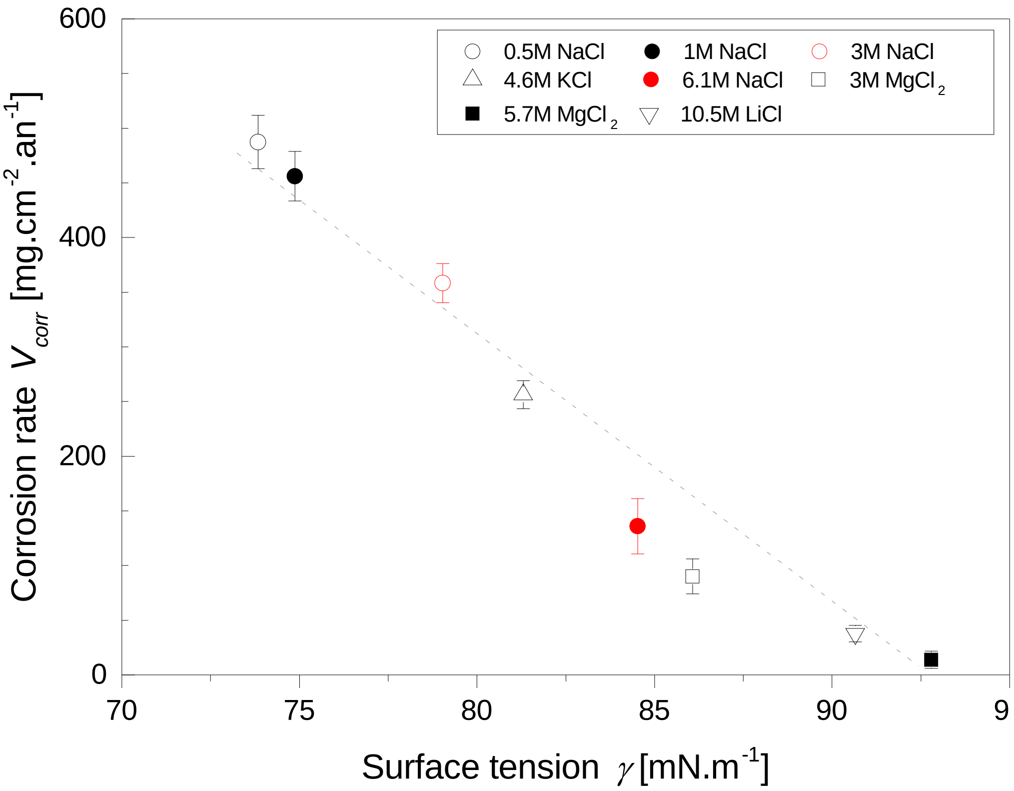

Figure 3.7 – *Corrosion rate V_{corr} (Equation 3.1) as function of the surface tension γ of the aqueous electrolyte solution in the sessile droplet initially deposited onto iron surfaces. The corrosion experiments were performed in air environment with RH_{eq} at $T = 20°C$*

with RH_{eq} 75.4% at $T = 20°C$. The initial droplet volume V_0 varied between 5 and 60 μl, inducing a change of the sessile droplet radius r from 0.22 to 0.60 ± 0.02 cm.

Irrespective of the size of the initially deposited sessile droplet, a peripheral film was observed ahead of its macroscopic contact line. The peripheral film development depicted in the first section of this chapter (Figure 3.1) and its consequences on the morphological and compositional spatial distribution of the "corrosion" products over the dried iron surface (Figures 2.1 and 2.2) are representative for all corrosion experiments obtained with sessile droplets from 6.1M NaCl with various sizes (initial volumes). An example of the microscopy images of dried iron surfaces, onto which an aqueous sessile droplet from 6.1M NaCl with different sizes was deposited, is illustrated in Appendix B.

Figure 3.8.a. presents the temporal evolution of the width of the peripheral film W for different sizes of the initially deposited sessile droplet from 6.1M NaCl over an exposure time period of eight days. As usually observed for all under-droplet corrosion experiments presented in this chapter (Figure 3.2.a), the peripheral film width W increases linearly with the square root of the experimental time t as depicted by the dotted line in Figure 3.8.a. The size-independent temporal increase of the peripheral film width was the most interesting feature of the corrosion phenomenon induced by sessile droplets from 6.1M NaCl with different V_0. The peripheral film expansion over the corrosion process did not depend on the droplet radius r of the initially deposited sessile droplet.

However, the temporal weight loss of the iron substrate Δm increases, if the initial size of the sessile droplet in contact with the iron substrate increases. The measured Δm of iron samples, onto which sessile droplets from 6.1M NaCl with different V_0 were deposited, over the

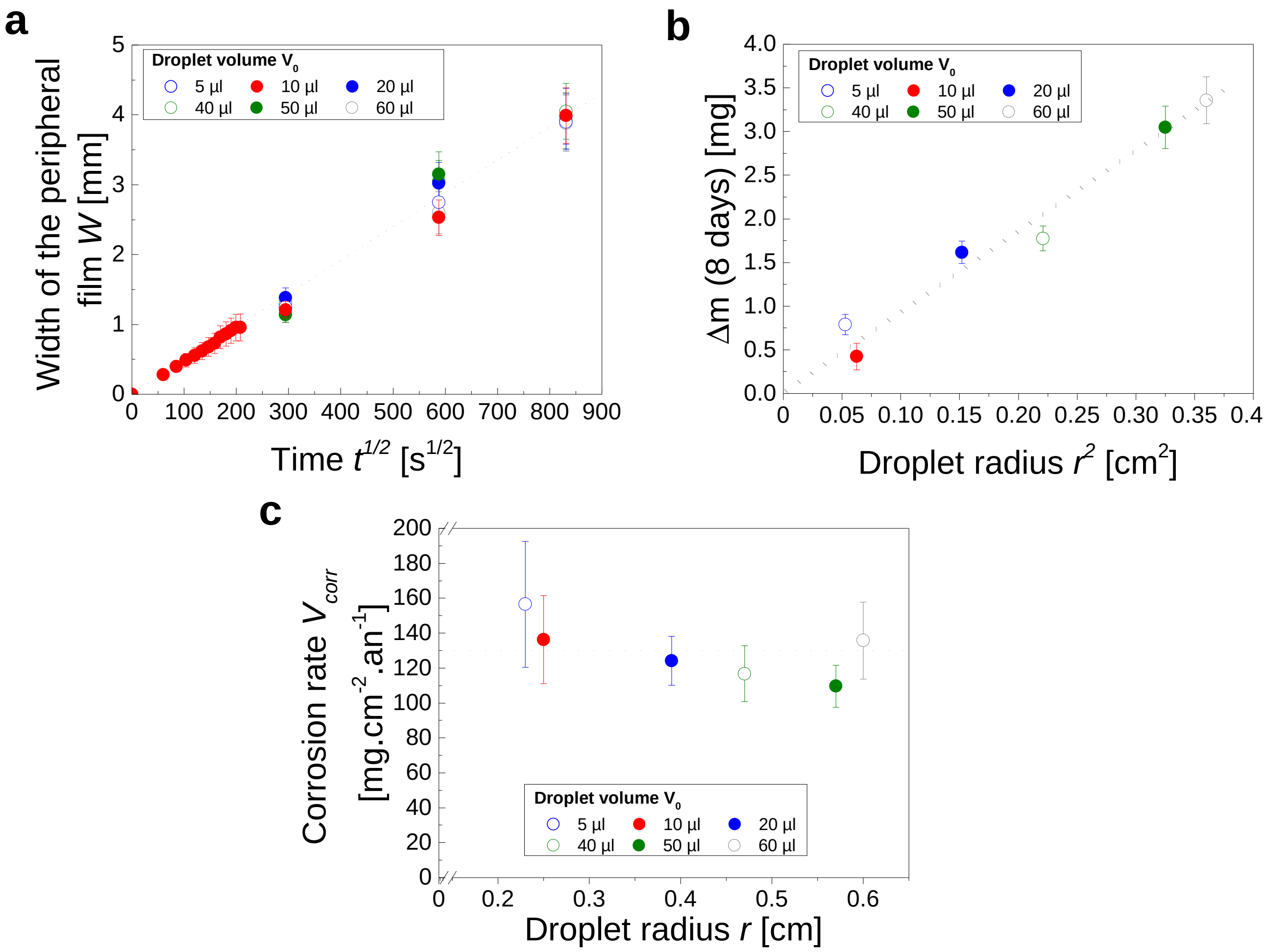

Figure 3.8 – ***a.*** *Evolution of the peripheral film width W (i.e., the distance from the droplet edge to the perimeter of the peripheral region) as function of the square root of the experimental time t. The corrosion experiments were performed with a sessile droplet from* 6.1*M NaCl deposited onto an iron surface, in humidified air with* RH_{eq} 75.4% *at* $T = 20°C$*, for different initial droplet volumes* V_0*:* 5, 10, 20, 40, 50 *and* 60 *µl.* ***b.*** *Weight loss of the iron substrate* Δm *(Equation 1.1) as function of the square of the droplet radius r.* Δm *was calculated after* 8 *days of exposure of the sessile droplets on the iron surface.* ***c.*** *The corrosion rate* V_{corr} *(Equation 3.1) is independent of the droplet radius r.*

corrosion process (i.e., at several exposure times ranging from 1 day to 1 month) is presented in Appendix B. Figure 3.8.b shows the measured Δm of iron samples after 8 days of exposure to a 6.1M-concentrated sessile droplet with different V_0 as function of the square of the droplet radius r. Δm at a given time linearly increases with r^2. A similar trend was observed, when we considered the weight loss of the iron substrate for shorter or longer exposure time periods. Therefore, the weight loss of the iron substrate, onto which differently sized-sessile droplets from 6.1M NaCl were deposited, depends on the droplet surface area S_{drop}. The corrosion rate V_{corr} was determined from the temporal weight loss of the iron substrate using Equation 3.1. As shown in Figure 3.8.c., the corrosion rate remains unchanged independent of the droplet radius: $V_{corr} \approx 130 \pm 30$ mg.cm^{-1}.an^{-1}. Neither of these trends is surprising, since in the studied range of initial droplet sizes, larger "Evans" droplets have a larger electrolyte-covered area on the iron substrate to induce more severe pitting corrosion in the metal [20, 25]. Once the footprint area of the initially deposited sessile droplet is accounted for as it is done in the determination of the corrosion rate (Equation 3.1), we confirmed that the droplet size had no influence on the overall corrosion kinetics. Therefore, as revealed in Figure 3.8, the corrosion process is not controlled by the anodic reaction itself occurring under the droplet diameter but rather depends on the cathodic reaction near the droplet edge region, where ion transport occurs towards the peripheral film induced by ionic composition (surface tension) changes at the three-phase contact line.

3.5 DISCUSSION AND OUTLOOK

Here we investigated the corrosion phenomenon induced when a sessile droplet from aqueous saline solutions was placed on a planar iron substrate. The bulk solution within the sessile droplet consisted of various aqueous chloride electrolytes of different counter-cations (sodium, potassium, lithium and magnesium) with initial chloride concentrations c_0 ranging from 0.5 to 11.4M, equilibrium relative humidities RH_{eq} between 10.5 and 99%, and surface tensions γ from 73.8 to 90.7 mN.m^{-1}. Within the limits of our parameter variations, we found the formation of a peripheral film ahead of the macroscopic contact line of the main sessile droplet deposited onto iron surfaces, a phenomenon explained in detail in the previous chapter (Figure 3.1). In the literature, the secondary spreading phenomenon [124] was not experimentally observed for $MgCl_2$ droplets at RH 90% [135]. The authors claimed that the precipitation of hydroxides prevented the formation of a micro-droplets'area at the droplet edge [135].

Quantitative analysis on the peripheral film phenomenon was performed by determining the dependence of the corrosion rate V_{corr} (i.e., the rate of weight loss of the iron substrate per droplet unit area) on various parameters. The experimental results prompt two questions: (1) Why does the diffusive ion transport occurring at the three-phase contact line govern the under-droplet corrosion process at RH_{eq}? (2) Why does the corrosion rate depend mainly on the initial chloride concentration and the surface tension, but only weakly on other parameters? According to the Bulter-Volmer model[151], the corrosion potential E_{corr}, at which the rate of oxygen reduction is equal to the rate of iron oxidation, is given by:

$$E_{corr} = K + \frac{2.3\ R\ T}{\alpha_A + \alpha_C}\ log\left(\frac{S_C\ k_C\ c_{O_2}}{S_A\ k_A}\right) \tag{3.2}$$

with R as the gas constant, T as the temperature, α_A and α_C as the transfer coefficient for the anodic and cathodic processes, S_A and S_C as the surface area of the anode and cathode, k_A and k_C as the standard rate constant of the anodic and cathodic reactions, c_{O_2} as the interfacial concentration of dioxygen and K as a constant involving the standard potentials and the number of electrons transferred for the anodic and cathodic reactions. Note that the rate of the cathodic reaction at E_{corr} is called corrosion current (density) I_{corr}, which corresponds to the corrosion rate V_{corr}. Therefore, any process that increases either the surface area of the cathodic reaction S_C or the interfacial concentration of oxygen c_{O_2}, or decreases the surface area of the anodic reaction S_A will lead to increased E_{corr} (Equation 3.2), resulting in an augmentation of V_{corr}. Thus, since S_A and S_C remained almost limited to the droplet footprint area and the three-phase contact line region, respectively, over the corrosion process (Figure 3.4), an increase in the interfacial concentration of oxygen for the most part at the droplet perimeter will induce a shift of E_{corr} to more positive values. This dependence is in agreement with the experimental observations regarding the effect of the initial chloride concentration c_0 within the deposited sessile droplet on the corrosion rate (Figure 3.6). The oxygen uptake influence or more generally the cathodic control nearby the droplet contact line region on the under-droplet corrosion process eliminates the dependence of the corrosion rate on the droplet (anodic) size (Figure 3.8), but points out the rate-determining influence of the diffusive ion transport occurring at this droplet peripheral part (Figure 3.4).

However, the corrosion rate is affected by the relative humidity RH in the surrounding environment (Figure 3.5) and a linear dependence has been measured between V_{corr} and the surface tension of the electrolyte solution γ (Figure 3.7). It appears most likely that Figure 3.5 reflects the formation of localised thicker micro-pools, observed in the course of the peripheral film (Figure 2.3). The hygroscopic cations concentrated along the ongoing peripheral film may adsorb water and create water clusters, which will increase locally the thickness of the film [144]. Therefore the vapour density may impact the thickness of the peripheral film by producing bulk-like localized aqueous conditions along the peripheral film. The film thickness may also be related to the disjoining pressure: a liquid thin film is subject to forces acting perpendicular to the plane of the film as introduced by Derjaguin [37]. As a consequence, the effect of restrictive diffusion of cations into the peripheral film may significantly decrease the diffusion coefficient D usually determined in bulk solution. As a result, an effective growth diffusion coefficient D_p in the peripheral film solution was measured (Figure 3.2).

Nevertheless the thickness of the resulting peripheral film e (estimated to less than 2 μm, Figure 2.5) is negligible compared to its millimeter width W, which suggests that the driving force for the corrosion process is related to some radial peripheral transport. Figure 3.7 demonstrates that V_{corr} is inversely proportional to the surface tension of the electrolyte solution within the initially deposited sessile droplet. Therefore, it can be assumed that the peripheral film phenomenon, as described in this thesis part, is predominantly caused by a peripheral surface tension gradient and the resulting Marangoni flow. The three-phase contact line is destabilized by the radial flow induced by ionic composition changes during the course of the cathodic reaction and migration of cations towards the droplet perimeter.

To conclude, we demonstrated in this chapter the origin of the peripheral film behaviour on the under-droplet corrosion process. As shown in this chapter, the dependence of the corrosion rate V_{corr} on various parameters is a powerful method for characterizing the rate-determining processes resulting in the peripheral film phenomenon. We found that the peripheral film behaviour barely depends on the droplet size. The dependence on the surface tension of the electrolyte solution and the initial chloride concentration within the deposited sessile droplet agrees with the scenario proposed in the previous chapter. As a result, the peripheral film phenomenon comes down to diffusion of cations from the droplet edge region into the thin film and diffusion of oxygen occurring essentially at the three-phase contact line.

To better elucidate the role of the environmental conditions, further experiments will include mixtures of oxygen and nitrogen gases. For a better understanding of the peripheral film formation, further experiments should include systematic studies of salt mixtures, which will have different surface tensions of the liquid-vapour interface. From a corrosion viewpoint, it will be interesting to transpose the under-droplet corrosion experiments to other metal substrates as stainless steel and also to investigate the possible influence of the roughness of the metal surface.

IV

Corrosion of Iron under Evaporating Sessile Droplets from Sodium Chloride Solutions

In marine atmospheres, the presence of natural chlorides deposited on metal surfaces as sprayed droplets carried by the wind from the sea, distinctly arises and supports corrosion cells. A prominent example is the so-called "Evans droplet" experiment [18], where the differential dissolved oxygen concentration along the air-electrolyte interface induces a spatial separation of the anodic and cathodic areas on the salty droplet surface (I.4.2). The Evans droplet experiment has been studied so far using different approaches: electrochemical methods (e.g., electrochemical impedance spectroscopy or scanning Kelvin probe) [19, 24, 25, 127], Raman spectroscopy [28, 102, 127], and microscopy characterization (e.g., SEM or AFM) [28–30]. In these experiments, the droplet characteristics such as its size and its composition, as well as the nature of the rust were investigated. Few studies have been extended to evaporating sessile droplets [20, 26, 152, 153]. None of them took into account the hydrodynamics inside droplets during the evaporation process, which is generic to drying sessile droplets [1].

As mentioned in I.2.2, for small contact angles ($\theta \ll 90^\circ$), the evaporative flux from the free surface of the liquid to the surrounding air diverges in the vicinity of the droplet edge [7, 8, 11]. As observed in the second part of this thesis, with the presence of non-volatile and soluble solutes such as salt within the sessile droplet, the spatially nonuniform evaporative flux leads to a flow field pattern resulting in inhomogeneous salt deposition/precipitation within the drying droplet [12, 83, 117, 118]. Therefore the evaporating version of the Evans droplet experiment illustrates factors not included in the classical model, i.e., the variation in electrolyte thickness, the impact of salt and its concentration increase over the evaporation exposure.

Although this has received little or no attention so far, corrosion has been observed under evaporating sessile droplets from aqueous saline solutions. In this last PhD part, we investigated the pitting corrosion phenomenon induced by the evaporation of sessile droplets from aqueous sodium chloride solutions on planar iron surfaces. We explored the influence of the salt initial concentration, its distribution and change within the evaporating sessile droplet and focused on the salt-induced mechanism and the subsequent anode/cathode localisation at the electrolyte-metal interface.

1 EVAPORATION OF SESSILE DROPLETS FROM SODIUM CHLORIDE ONTO IRON

We investigated the evaporation behaviour of sessile droplets from aqueous sodium chloride solutions on planar solid surfaces as function of the relative humidity. Most of this has been studied in detail for this naturally ubiquitous system on inert surfaces, i.e., silicon wafers, in the second part of this thesis. Henceforth, we focused essentially on *metallic* surfaces. We extended the experimental and theoretical description of the evaporation behaviour of salty sessile droplets on silicon wafers to pure iron surfaces. We examined particularly the surface influence and the impact of the gas environment. The gaseous phase surrounding the evaporating sessile droplets was a dry or wet mixture of high-purity nitrogen or synthetic air (standard gas mixture of N_2 (79.5% vol.) with O_2 (20.5% vol.), Air FID, Messer). This quantitative experimental study was performed in the setup for evaporation experiments presented in II.1.

Figure 5 presents the time evolution of the normalized droplet volume $\tilde{v}$ (Equation 2.1) during the evaporation of sessile droplets containing a 10^{-3}M NaCl-concentrated aqueous solution deposited either on silicon wafers or pure iron surfaces in two different gaseous environments: N_2 and air with a relative humidity RH 0% at $T = 23°\text{C}$. The initially deposited volume V_0, according to the readout of the syringe, was 10 μl.

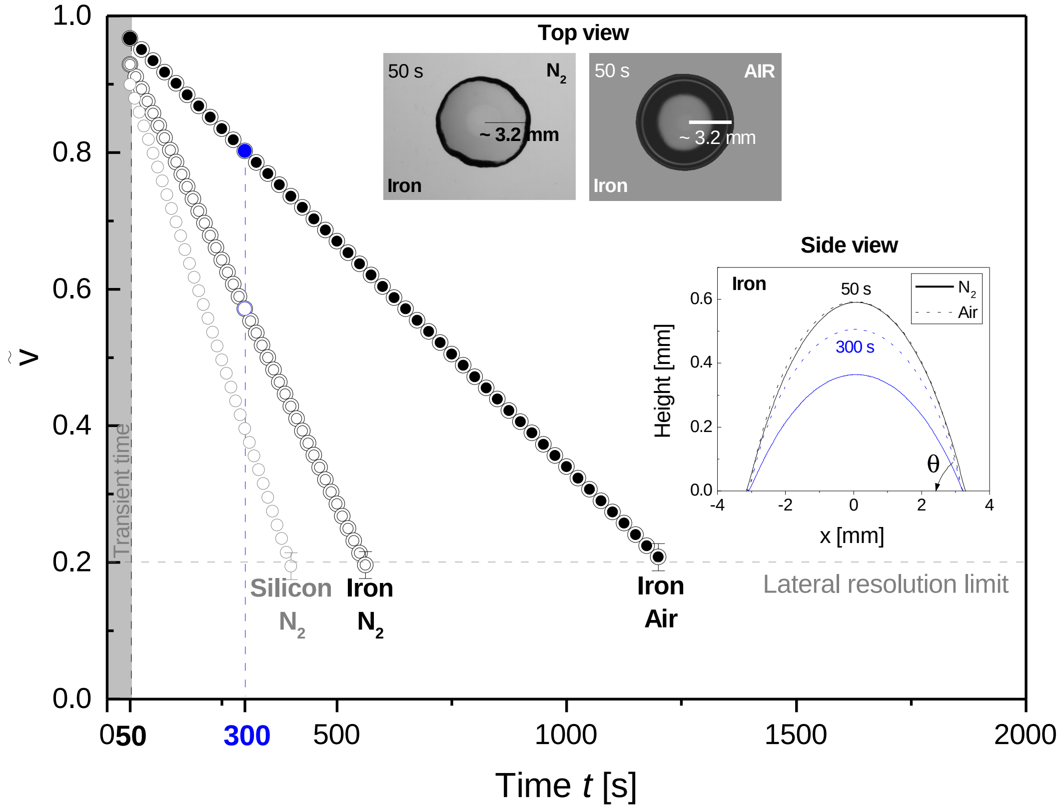

Figure 5 – *Evaporation of sessile droplets from* 10^{-3}*M NaCl deposited onto silicon wafers or iron substrates in a high-purity nitrogen or synthetic air environment with a relative humidity* RH *0% at* $T = 23°C$ ($V_0 = 10\ \mu l$)*. The inset plot shows the height profile at two different evaporation times: 50 and 300 s. The other inset shows top view imaging 50 s after droplet deposition.The two insets are only depicted for the sessile droplets deposited on iron surfaces under* N_2 *or air gaseous phases. The silicon wafers' case has been presented in detail in Figure 3.1.*

In all cases, Figure 5 shows a linear temporal decrease of the measured and normalized droplet volume (from top and side aspects) over the studied evaporation time range, i.e., from the transient to the lateral times (see II.3.1 for more detail information about the time window). Further, the height profiles depicted in Figures 5 (iron substrates) and 3.1 (silicon wafer) testify that the deposited salty sessile droplets evaporated in pinned, constant contact area mode. Since the three-phase contact line is anchored on the surface (see I.2.3) after sessile droplet deposition ($t = 0$ s) and spreading ($t < 50$ s), the radii remained constant ($r \sim 3.2$ mm for iron samples) while the contact angles θ decreased between $t = 50$ and 300 s as illustrated in the side aspects profiles. Therefore, there is no influence of the surrounding gaseous phase and no surface impact on the evaporation behaviour (i.e., the time evolution of the droplet shape) of sessile droplets from 10^{-3}M NaCl.

However, Figure 5 reveals a variation of the evaporation kinetics between the different studied droplet/substrate/gas systems. Under high-purity nitrogen environment, the metallic surface, onto which the sessile droplet is placed, induced a (expected) decrease in the evaporation rate $\frac{d\tilde{v}}{dt}$ (i.e., the normalized droplet volume per time unit) in comparison to silicon wafers. Although particular attention has been paid to obtain for these two substrates a quite similar surface condition, in particular surface roughness (1-2 nm, see II.1.2 and III.4.2), metals exhibit usually a less hydrophilic surface than silicon wafers, providing a lower wettability [31, 154–156]. Experimentally we noticed that the equilibrium contact angle θ_e at $t = 50$ s evolved from 2 ± 0.5 °to $10.3 \pm 1.5°$, if the silicon wafer turned into an iron sample. The question is whether the contact angle is the only differentiating parameter between silicon wafers and iron substrates relative to the evaporation rate measured when a sessile droplet from aqueous saline solution evaporates in high-purity nitrogen environment. We will answer this question by determining and analyzing in the following the normalized evaporation rates $\tilde{Q}_i$ (Equation 3.9).

Moreover, with iron samples, the surrounding gaseous phase has a significant influence on $\frac{d\tilde{v}}{dt}$ as presented in Figure 5. Note that experiments performed with salty sessile droplets deposited on silicon wafers in air (data not presented in Figure 5) matched quantitatively as well as qualitatively the evaporation under nitrogen environment as depicted in Figure 5. The large evaporation rate disparity observed for only iron substrates between the two different gaseous environments is surprising. Since the saturation vapour pressure P_{sat} at/above the sessile droplet surface (for a salt concentration c_0) can be assumed constant in all our cases, the evaporation should simply result in a single curve. This is not what we observed experimentally with iron samples.

The influence of the initial salt concentration and the relative humidity on the evaporation behaviour was investigated with droplets containing different (characteristic) NaCl concentrations from 10^{-6} to 6.1M (the saturation limit). For the various salt solutions RH varied between 0 and 60%. Within theses ranges of c_0 and RH, the evaporation on iron surfaces was not qualitatively different in N_2 environment or in air. The characteristic temporal patterns of pinned evaporating sessile droplets were observed: (a) $\tilde{v}$ decreased linearly with time within the "initial" evaporation range (we defined "initial" as covering the time span between $t = 50$ and 100 s) and for times much longer, (b) the contact area of the droplet remained constant and (c) the contact angle decreased over the lifetime of the drying droplet. An example of the time evolution of the normalized volume and shape (from top and side aspects) of the sessile droplet at 1M NaCl is shown in detail in Appendix C.1. In addition, with high-humidity environments for pinned sessile droplets deposited on iron substrates and containing initial salt concentration $\geq 10^{-6}$M, we found a decreasing evaporation kinetics. Equivalent results with lower $\frac{d\tilde{v}}{dt}$ with increasing RH were also obtained for silicon wafers (see II.3). Nevertheless, we demonstrated on silicon wafers that the environmental relative humidity had no quantitative influence on the evaporation of salty sessile droplets (Figure 3.7) insofar as the droplet volume V and the time t were correctly normalized (Equations 2.1 and 3.4). Because each parameter used in the volume or time scaling (i.e., the initially deposited volume V_0, the saturated vapour pressure of water $P_{sat}^{H_2O}$ and the droplet size factor $\tilde{r}$[1]) can be assumed constant in all cases, the result of the relative humidity on the scaled evaporation rate will remain the same with iron samples. This is the experimental case, directly confirmed by Figure C. 1 (see Appendix C.2) and demonstrated in the following (Figure 6).

The experimental study on the evaporation of sessile droplets from aqueous sodium chloride solutions described in this section resulted in a variety of different substrates, environmental gaseous phases, relative humidities and initial salt concentrations. The resulting, unit-free and universal normalized evaporation rate $\tilde{Q}_i$ (Equation 3.9) allows a convenient evaluation/comparison of the evaporation behaviour of such diversified systems. In all cases, the normalized evaporation rates experimentally determined from the linear decrease of the droplet normalized volume $\tilde{v}$ with the scaled time $\tilde{t}$ during the initial drying period should result in a value of 1. The main assumptions for the determination of $\tilde{Q}_i$ were the correct normalization of the volume (Equation 2.1) and time (Equation 3.4), and a homogeneous salt distribution within the droplet and in particular at the droplet surface (see II.3.4 for further explanation about $\tilde{Q}_i$).

Figure 6 shows the experimentally observed normalized evaporation rates $\tilde{Q}_i$ as function of the initial NaCl concentration c_0. The evaporation experiments were performed with 10-μl sessile droplets deposited either on silicon wafers or iron substrates. The gaseous phase in the environment chamber was high-purity nitrogen or synthetic air with RH varying from 0 to 60% at $T = 23°\text{C}$. The dashed line depicts the theoretically expected normalized evaporation rate, scaled to a value of 1 according to Equation 3.9.

With silicon wafers, the variation of the experimental $\tilde{Q}_i$ as function of c_0 and θ in comparison with the theory as well as the origin of its discrepancy with the latter for $c_0 \geq 0.5\text{M}$ NaCl and $\theta \leq 30°$ was fully described in the second part of this thesis. The main reason for the significant deviations between theory and experiment was explained by Marangoni flows that are (self-)induced by the peripheral salt enrichment, itself promoted by the locally nonuniform evaporative flux and the subsequent capillary flows, that are generic for sessile droplets. The data presented in Figure 6 indicate that the difference of contact angle values between naturally oxidized silicon wafers ($1° \leq \theta \leq 10°$) and pure iron substrates ($10° \leq \theta \leq 20°$) is the main parameter that governs the droplet evaporation profile in nitrogen environment. In this surrounding gaseous phase, the measured normalized evaporation rates $\tilde{Q}_i$ for iron substrates agreed quite well with the ones for thermally oxidized silicon wafers having a similar contact angle range values. As a consequence, the change of evaporation rate illustrated in Figure 5 is independent from the surface composition (silicon wafers or metallic substrates) but derives from wettability. Therefore, the general behaviour for drying sessile droplets from aqueous chloride solution on iron surfaces, e.g., the flow field and the deposit morphology as result of the evaporation process, will be identical to that on silicon wafers. This is confirmed by Figure 7. It shows top views of the deposition pattern obtained after complete evaporation of sessile droplets containing aqueous NaCl solutions at different initial concentrations ranging from 10^{-6} to 6.1M in high-purity nitrogen environment with RH 0%. Figure 7 presents the same three different NaCl concentration-dependent morphologies as identified on silicon

---

[1] Irrespective of the relative humidity and also the surrounding gaseous phase, the geometrical parameters (i.e., the droplet radius r and contact angle θ_e) values at $t = 50$ s can be assumed as constant for each substrate (as presented e.g., in Figure 5 for iron substrates). With Equation 3.3 this means $\tilde{r} \approx$ constant.

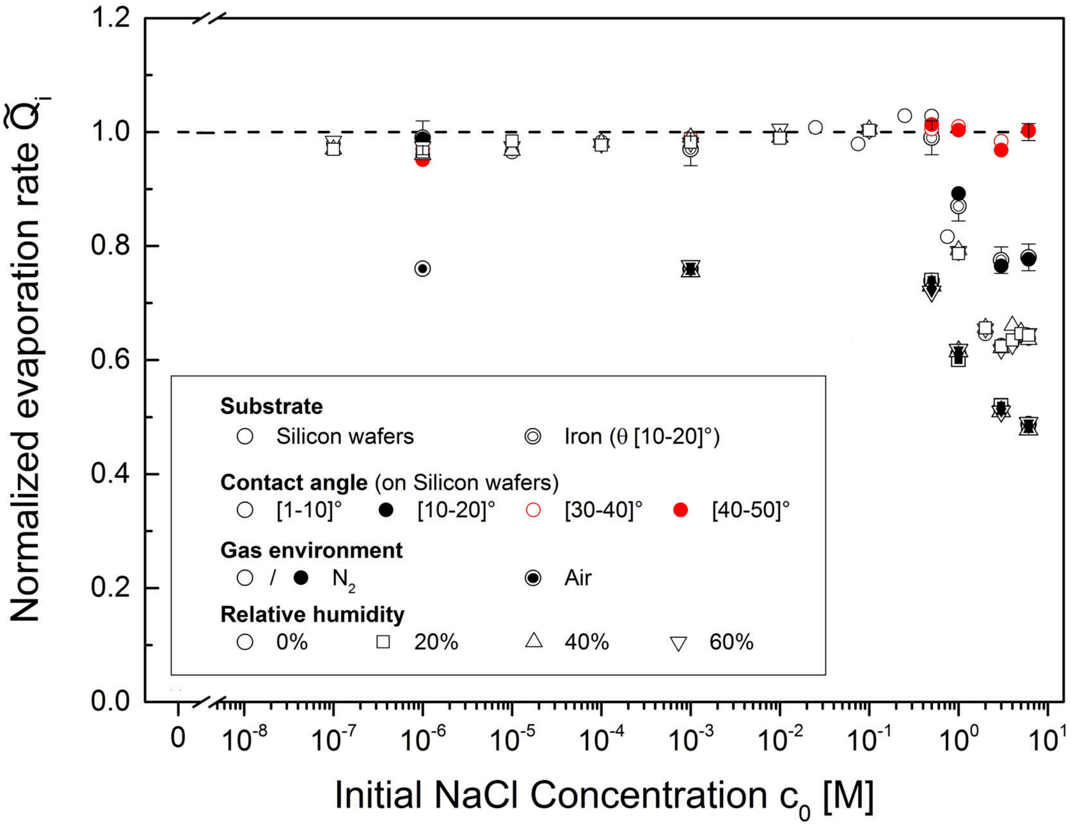

Figure 6 – *Experimentally observed normalized evaporation rates* $\tilde{Q}_i$ *as function of the initial NaCl concentration* c_0 *for sessile droplets deposited on silicon wafers or iron substrates. The contact angle* θ *was varied from* 1 *to* 50° *on silicon wafers whereas on iron samples its value range was between* 10 *and* 20°. *The evaporation experiments were performed with* 10 *μl-sessile droplets in high-purity nitrogen environment with RH* 0% *or in synthetic air at different RHs of* 0, 20, 40 *and* 60% *at* $T = 23°C$. *The dashed line depicts the theoretically expected normalized evaporation rate according to Equation* 3.9 *with the assumption of the (inweight) salt concentration distributed uniformly inside the droplet.*

wafers (Figure 3.2) for dried sessile droplets initially deposited on iron substrates in nitrogen environment. Up to a NaCl concentration of 10^{-3}M, the final dried structure exhibited the classic "coffee-ring" deposition mainly induced by outward capillary flows compensating from the local evaporative losses at the droplet edge region. Above a concentration of 10^{-3}M NaCl, a more uniform salt deposit or a wider salt-ring at the droplet periphery is observed since Marangoni and capillary flows led to circulating flows inside the drying sessile droplet.

The different gas environments, in which evaporate sessile salty droplets show similar but distinct normalized evaporation curves as presented in Figure 6. The measured normalized evaporation rates $\tilde{Q}_i$ remain constant with c_0 varying between 10^{-6} and 0.5M NaCl. This plateau is followed by a pronounced deviation of the experimental findings for higher initial salt concentrations. This holds for nitrogen and air environments. However, the synthetic air environment induces a shift of $\tilde{Q}_i$ to lower values for the entire studied range of c_0 as depicted in Figure 6. It is interesting to notice that the experimental measurements of $\tilde{Q}_i$ in air are independent of the relative humidity. The independence of the relative humidity from the normalized evaporation rate, initially demonstrated for silicon wafers, was theoretically predicted on iron surfaces above.

An analysis of the approach and assumptions for the determination/measurement of the normalized evaporation rates $\tilde{Q}_i$ suggested that during the droplet evaporation in air on iron samples there were most likely: (1) as in high-purity nitrogen environment, a peripheral salt enrichment (promoted by capillary and Marangoni flows), which will decrease in the droplet edge region, the water vapor pressure in the c-concentrated aqueous NaCl solution $P_{sat}(c)$ above/at the droplet surface and hence diminish the peripheral evaporative losses, and consequently, the overall evaporation rate, particularly for c_0 higher than 0.5M NaCl, and in addition, (2) local surface reactions at the solution-iron interface induced by the air environment in aqueous systems, which can lead to corrosion. If corrosion occurs, there will be local changes in the liquid composition within the sessile droplet (and also at the droplet surface): e.g. formation of hydroxide ions generated by oxygen reduction (Equation 2.3) and/or partial reaction of water with the oxidation and reduction products to form rust (Equation 2.5). Therefore the first assumption[2] that the evaporation of sessile droplets on metallic surfaces in synthetic air is described by Equation 3.2 [3] is not strictly valid. Thus, this scenario predicts that the corrosion process within the evaporating sessile droplet will alter (slow down) the evaporation profile, *in addition to* Marangoni flows at high salt concentrations. To a first approximation, the described scenario is validated by Figure 7. The three different characteristic final structures at the end of the evaporation of sessile droplets from aqueous sodium chloride solutions are preserved in air environment with RH 0%. This confirms the occurrence of Marangoni flow scenario in evaporating salty droplets deposited on iron substrates. Additionally the different morphologies developed reddish-yellowish patterns, which usually characterize the corrosion effect [18, 102, 127]. This assumption has been investigated experimentally by visual examination of the evaporating sessile droplets initially deposited onto iron substrates in air, as described in the following section.

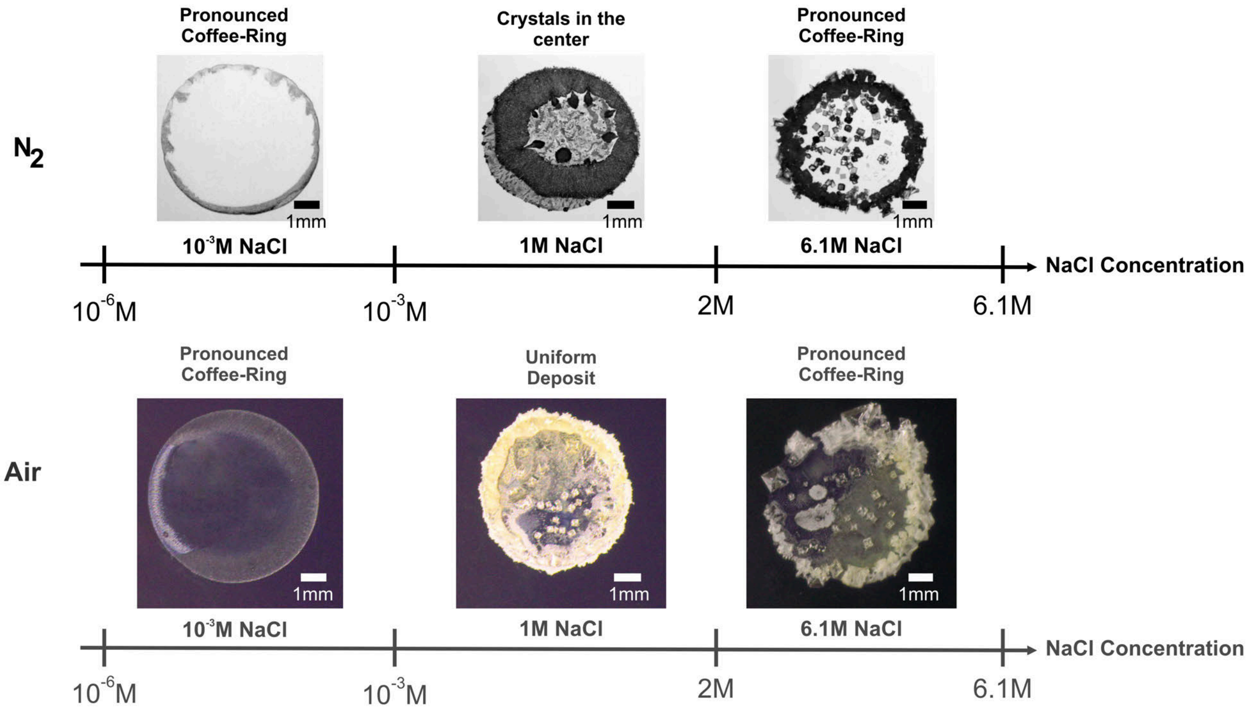

Figure 7 – *Morphologies of the deposit resulting from the evaporation of sessile droplets containing aqueous NaCl solutions at different initial salt concentrations from* 10^{-6} *to* 6.1*M. The evaporation experiments were performed with* 10*µl-sessile droplets placed on iron substrates in high-purity nitrogen or air environment with relative humidity RH of* 0%.

---

[2] The different assumptions used for the determination/measurement of $\tilde{Q}_i$ are presented in detail in the second part of this thesis, see II.3.4.

2 EVAPORATING SESSILE DROPLETS FROM NACL SOLUTIONS INDUCED IRON CORROSION

Iron samples, onto which aqueous sessile droplets from NaCl solutions were initially deposited, were exposed to air with a relative humidity RH of 40% at $T = 23°C$. Figures 8 and 9 show a microscopy image of an iron surface after complete evaporation of a sessile droplet from 10^{-3}M NaCl (Figure 8) and 1M NaCl (Figure 9) with an initial volume of 10 μl. We deliberately decided to focus the evaporation study on these two extreme salt concentrations representative of the two distinctive NaCl deposit regimes as depicted in Figure 7.

Figure 8 shows that the final deposit obtained after complete evaporation of an initially 10^{-3}M NaCl-concentrated sessile droplet exhibits the classic "coffee-ring" deposition. Most of the precipitates was concentrated close to the droplet edge region. In this peripheral droplet area we observed some yellowish/dark brown spots or areas (Figure 8), indicating the formation of rust phases through the corrosion process [18, 102, 127]. On contrary, at higher initial NaCl concentrations, the final pattern exhibited a more uniform deposition over the complete footprint droplet area, as illustrated in Figure 9. We observed a pronounced salt-ring at the droplet edge as well as many NaCl crystals in the droplet center. In addition, the entire footprint region of the initially deposited droplet appeared yellowish/dark brown (Figure 9), revealing the occurrence of corrosion under the evaporating salty sessile droplet. It is interesting to notice that increasing the relative humidity from 0 to 40% has a minor impact on the final structures obtained at the very last stage of evaporation (Figure 7). Even if from a droplet science viewpoint, the environmental relative humidity had no influence on the normalized evaporation rate (Figure 6), from a corrosion viewpoint, one must remember that a high-humidity environment leads to an increase of the exposure time of a sessile droplet on the iron substrate.

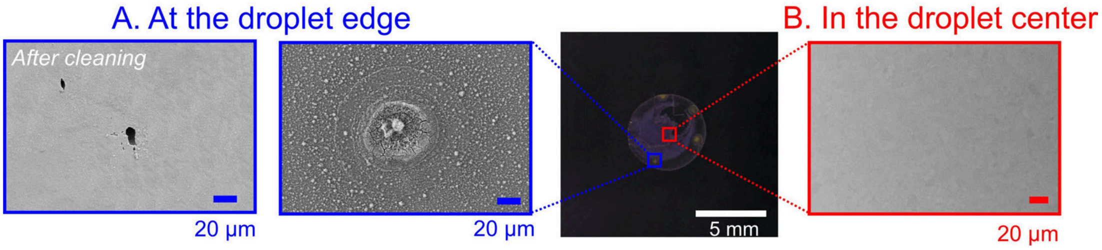

Figure 8 – *Microscopy image of an iron surface, onto which an aqueous sessile droplet from* 10^{-3}*M NaCl was deposited (*$V_0 = 10\mu l$*,* $\theta_0 = 10.5°$*), after complete evaporation with a relative humidity RH of* 40% *at* $T = 23°C$*. The two insets show SEM micrographs of two different locations on iron corroded under evaporating* 10^{-3}*M NaCl sessile droplets:* ***A.*** *at the droplet edge and* ***B.*** *in the droplet center. SEM analysis was carried out on dried iron surfaces after experiment and after removing of the products formed.*

Morphological analysis of the products formed on iron under evaporating sessile droplets from aqueous NaCl solutions was carried out through SEM for the different observed droplet areas. The two insets in Figures 8 and 9 show the resulting morphologies, after complete evaporation, before and after removal of the different products formed, at two different locations on the iron surface: at the droplet edge and in the droplet center. As presented in Figure 8.A, we observed at the droplet edge circular clusters made of a prolific flowery-like structure surrounded with similar patterned deposits. As mentioned in the third part of this thesis (see III.2.1), this is the characteristic morphology of lepidocrocite [130, 131], an iron hydroxide originating from the reaction between the ferrous ions and the dissolved oxygen [127, 132, 133].

After removal of the corrosion products, SEM analysis shows some pits with a diameter of at least 10-microns over the droplet edge region. In the central area of the droplet, no corrosion products or pits were observed.

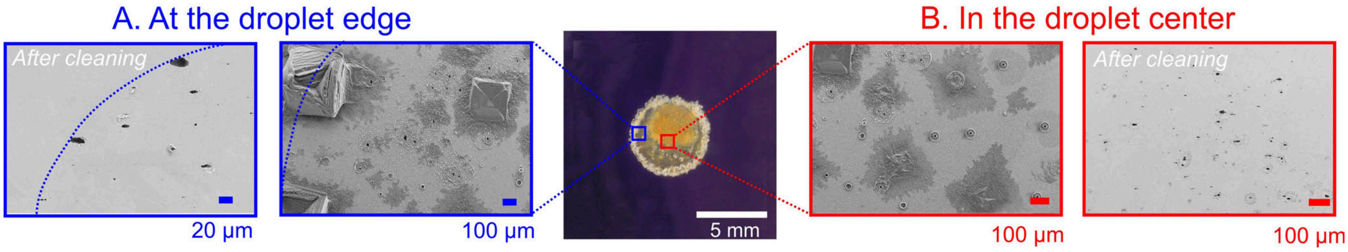

Figure 9 – *Microscopy image of an iron surface, onto which an aqueous sessile droplet from* 1M NaCl *was deposited* ($V_0 = 10 \mu l$, $\theta_0 = 15.2°$)*, after complete evaporation with a relative humidity RH of* 40% *at* $T = 23°C$. *The two insets show SEM micrographs of two different locations on iron corroded under evaporating* 1M NaCl *sessile droplets:* ***A.*** *at the droplet edge and* ***B.*** *in the droplet center. SEM analysis was carried out on dried iron surfaces after experiment and after removal of the products formed.*

Figure 9 reveals that the resulting morphologies after complete evaporation of a sessile droplet from 1M NaCl on an iron sample in air is the same over the complete footprint droplet area. SEM analysis shows NaCl crystals enclosed by rust phase, most likely lepidocrocite, as well as circular clusters of ferrous hydroxide, that we have already observed at low NaCl concentrations on iron surfaces (Figure 8.A). The edge of the footprint droplet area is depicted in Figure 9.A with a dotted line. After cleaning we observed the presence of several pits in the iron surface with a diameter of at least 20-microns over the entire footprint region of the initially deposited sessile droplet. It is interesting to note, that compared to the rounded pits formed under stationary sessile salty droplets, we observed elongated pits in the case of droplet evaporation. This may arise from the rolling of the iron surface or from the presence of a flow field inside the evaporating droplet (see IV.1) [18, 157, 158].

The evaporation of sessile droplets from aqueous NaCl solutions initially deposited onto iron surfaces in synthetic air environment induced pitting corrosion of the metal. The localisation of the pits strongly depends on the initial NaCl concentration within the sessile salty droplet. They were observed in the vicinity of the droplet edge at low salt concentrations, but over the entire footprint of the initially deposited droplet for higher salt concentrations. Experiments performed with droplets with different sizes (droplet radius ranging between 25 and 58 mm) or at different relative humidities *RHs* from 0 to 60% (Figure 7) in the surrounding air droplet environment confirmed the spatial distribution of the different corrosion and salt products as well as pits over the iron sample. Our observations indicate a strong influence of NaCl concentration on the observed corrosion phenomenon.

The initial (and visual) development of the corrosion phenomenon was investigated by observing the temporal evolution of the top and side aspects of a sessile droplet from aqueous saline solution during its evaporation on iron surface. Figures 10 and 11 show the (visual) initiation of the corrosion process induced, if a sessile droplet from 10^{-3}M NaCl (Figure 10) and 1M NaCl (Figure 11) is evaporated on iron samples, in humid air with *RH* 40% at $T = 23°C$.

A sequence of four frames are presented in each figure. Figure 10 shows a time span of 2000 s. It was recorded 50 s after the droplet deposition, i.e., long after the droplet had initially spread to its final perimeter and the three-phase contact line was pinned in this position. On contrary Figure 11 shows a time span of 1500 s. At the right of each sequence of Figures 10 and

11 is depicted the sessile droplet height profile as it was recorded from the side view camera (and also used for the determination of the droplet shape for its volume measurement). The main part of each image shows the simultaneous top view image of the evaporating sessile droplet. In the top view image, changes in the brightness between the droplet perimeter and its central parts occur inevitably according to ray optics, when the evaporation experiment is performed in the experimental setup (see II.1.1). The droplet perimeter appears dark, since the light is diffracted out of the optical path, whereas the central parts appear brighter due to the direct reflection off the liquid-vapour interface. These changes in brightness can be translated into local surface inclination. As the contact angle decreases during the pinned droplet evaporation, the changes in brightness in the top aspect over the footprint droplet area are reduced. In addition the dark dots or areas appearing within the evaporating sessile droplet in the top view imaging reflect the formed corrosion products. In each figure, the first observed corrosion phenomenon inside the drying droplet is marked with red circles.

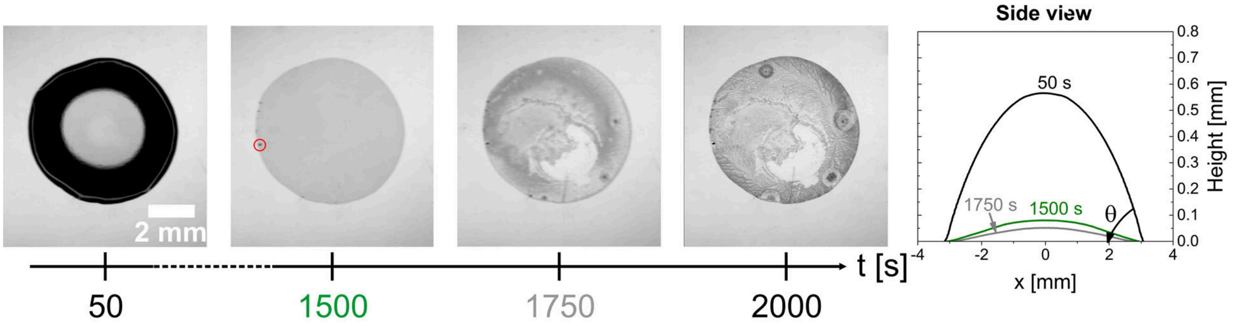

Figure 10 – *Visual observation of the corrosion process induced, when a sessile droplet from* 10^{-3}*M NaCl (with an initial volume of* $10\mu l$ *and contact angle of* $10.5°$*) evaporates on an iron surface, in humidified air with* 40% *RH at* $T = 23°C$*. The sequence of frames shows a time span of* 2000 s *starting* 50 s *after the droplet deposition. The main part of the images depicts a top view of the evaporating sessile droplet. The corrosion products show up as dark dots or areas within the drying droplet. The red circle identifies the first observed corrosion phenomenon. At the right of the sequence is illustrated the simultaneous droplet height profile.*

Figure 10 reveals the first formation of corrosion products and most likely visible and stable pits 1500 s after the deposition of the sessile droplet initially containing 10^{-3}M NaCl. As illustrated in the second image, at this given evaporation time, the corrosion products and hence the pits appeared at the three-phase contact line region. In the third image, i.e., $t = 1750$ s after droplet deposition, other dark dots show up in the vicinity of the droplet edge region and appear clearly at the end of the evaporation process, in the last image. Over the evaporation process, the droplet height, and by extrapolation its volume decrease as illustrated in the side view inset in Figure 10. This induces a global salt enrichment within the evaporating sessile droplet. We determined the critical global salt concentration c^* at which the first stable and visible pits appeared in the iron surface as follows:

$$c^* = \frac{c_0 \, V_0}{V*} \tag{1}$$

with V^* the sessile droplet volume at which a visible corrosion phenomenon starts under an evaporating sessile droplet containing an initial NaCl concentration c_0 and with an initial volume V_0. We found an unique value of the critical global salt concentration for all evaporations of sessile droplets from 10^{-3}M NaCl on iron samples in synthetic air environment at different relative humidities and for larger droplet sizes: $c^* = 7.5 \pm 0.2 \cdot 10^{-3}$M NaCl. The changes in brightness in the top aspect of the sessile droplet may alter the precise determination of c^*. Nevertheless, the c^* value that we determined is in good agreement with the literature where this parameter, well-known as critical chloride concentration, ranges from 10^{-4} to $3{\cdot}10^{-3}$M for pure iron in similar experimental conditions (i.e., $pH \approx$ 5-6 and $T = 20°$C) [159, 160]. In the end, when a sessile droplet initially containing 10^{-3}M NaCl evaporates, pitting corrosion starts near the contact line as soon as the critical global salt concentration c^* is reached (Figure 10.

When the initial NaCl concentration is higher, c_0 = 1M NaCl, the observed corrosion phenomenon appears within the evaporating sessile droplet deposited on iron samples about less than 1 minute after its deposition, as illustrated in the first frame in Figure 11. Because c_0 is higher than the experimental value of c^*, this prompt corrosion initiation is not surprising. Several control experiments have been performed with salt concentrations between 10^{-3} and 1M NaCl, they validated that pitting corrosion is initiated as soon as the initial global concentration is superior than c^*. The first visible dark dot showed up in the central area of the droplet. However, the local surface inclination of the droplet can alter the precise determination of the first location of the observed corrosion phenomenon. As the evaporation process occurred between t = 50 and 1500 s, the formation of corrosion products over the entire footprint droplet area is enhanced: the central parts of the droplet became darker with time. Thus stable and visible pits within the drying droplet are formed in the iron surface for a global salt concentration higher than c^*. As a consequence, salt concentration had an impact on the initiation of the observed pitting corrosion induced by the evaporation of sessile droplets from aqueous saline solution. This will be explained in the discussion section.

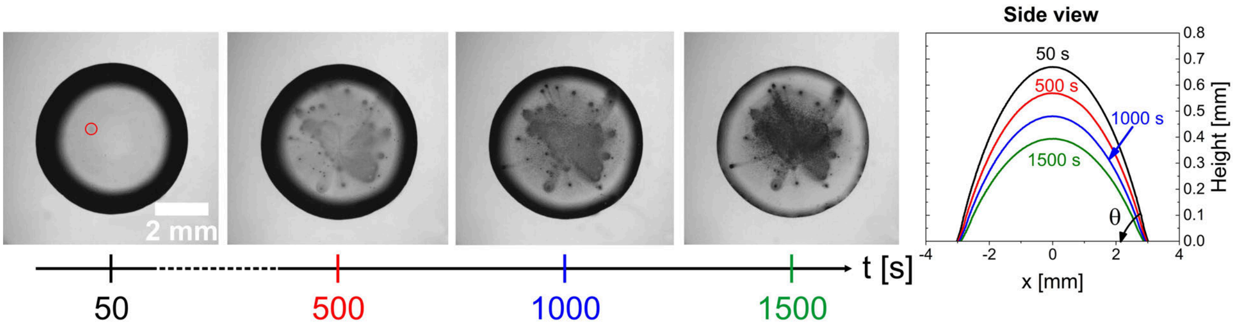

Figure 11 – *Visual observation of the corrosion process induced when a sessile droplet from* 1M NaCl *(with an initial volume of* 10μl *and contact angle of* 15.2°*) evaporates on an iron sample, in humidified air with* 40% *RH at* $T = 23°$C*. The sequence of frames shows a time span of* 1500 s *starting* 50 s *after the droplet deposition. The main part of the images depicts a top view of the evaporating sessile droplet. The corrosion products show up as dark dots or areas within the drying droplet. The red circle identifies the first observed corrosion phenomenon. At the right of the sequence is illustrated the simultaneous droplet height profile.*

3 DISCUSSION AND OUTLOOK

Here we investigated the evaporation of sessile droplets from aqueous sodium chloride solutions on planar and horizontal iron surfaces. The evaporation experiments were performed over six decades of initial NaCl concentrations, with various surrounding gaseous phase environments (high-purity nitrogen and air) and at different relative humidities varying from 0 to 60%. Within the limit of our parameters variations, we found that (oxygenated) air environment (Figure 7) and a quite low (global) salt concentration are the main ingredients to observe corrosion under evaporating sessile droplets from aqueous NaCl solutions. An oxygen free environment prevented the corrosion process (Figure 7). The environmental condition did not alter the occurrence of the corrosion process (Figures 7, 8 and 9) as well as the critical chloride concentration value c^*.

Quantitative and qualitative analysis on the evaporation experiments on iron samples was performed by determining the evaporation behaviour, the compositional evolution and the pinning behaviour of sessile salty droplets, and by characterizing the observed corrosion process. Our experimental results prompt one main question: how does the initial salt concentration influence the formation and distribution of the corrosion phenomenon induced on iron surfaces exposed to evaporating sessile droplets from aqueous NaCl solutions? In contrast to the simple, generally accepted Evans droplet model (Figure 12.a), the evaporation of pinned salty droplets (Figure 5) causes a local salt enrichment inside the drying droplet. The local NaCl enrichment/precipitation on the metal surface reduces the solubility of oxygen in the transient concentrated electrolyte solution, as an increase in NaCl concentration leads to a substantial decrease in oxygen solubility. The solubility of oxygen in saturated sodium chloride solution (6.1M NaCl) is about $0.3x10^{-3}$M compared to $1.4x10^{-3}$M for low concentration ($\geq$ 0.1M) NaCl solution at $T = 22°$C [149]. Therefore, as the sessile salty droplet evaporates, the transient and local salt enrichment enhances there the depletion of oxygen at the electrolyte-metal interface.

The local chloride ion (salt) enrichment within the evaporating sessile droplet will promote the initiation of corrosion. Figures 8 and 9 reveal that the location of the observed corrosion process (i.e., the observed corrosion products and pits formed) after complete evaporation is correlated to the structure of the drying stains as depicted in Figure 7. The compositional evolution inside the drying salty droplets as well as the properties of the deposits are the result of the evaporation-induced Marangoni and capillary flows inside the sessile salty droplet placed on iron samples (Figures 12.b and c.). The general evaporation behaviour, the resulting flow pattern and the subsequent local deposition/precipitation of salt for sessile salty droplets on iron surfaces, is identical to that on silicon wafers, fully described in the second part of this thesis (Figure 6). Therefore the spatial distribution of the salt within the drying sessile droplets from NaCl solutions governs the localisation of the anodic and cathodic activities over the initially footprint droplet area.

At low initial NaCl concentrations, $c_0 = 10^{-3}$M NaCl, pitting corrosion starts near the contact line as soon as the critical global chloride concentration is reached (Figure 8) The peripheral evaporative salt enrichment provides localisation of the anodic (pits) reactions and cathodic protection to the rest of the droplet surface and in particular, in the central part of the droplet over the evaporation process. As a consequence, during the evaporation exposure of sessile droplets from low concentrated NaCl solution, an inversion of the classical stationary Evans droplet scenario occurs as illustrated in Figure 12.c. On contrary, at high initial NaCl concentrations, $c_0 = 1$M NaCl, there is not a distinctive localisation of anode and cathode at the electrolyte-metal interface as promoted by the Evans droplet model [18], since c_0 is above the critical pitting chloride concentration and the evaporation leads a more uniform salt enrichment over the footprint area of the droplet on the iron surface (Figure 7). Thus, anodic dissolution and cathodic reduction occur regardless of where it is positioned within the evaporating sessile droplet. Principally, where local variations in chloride ions concentration occur inside the drying NaCl droplet, pitting dissolution is established, while cathodic reactions take place in areas surrounding this anodic activity as schematically illustrated in Figure 12.c. This suggests that in the case of evaporating sessile salty droplets, oxygen depletion is not the primary determining corrosion-step for the localisation of anodic and cathodic areas but for the initiation of the anodic process, when a critical chloride concentration is obtained to initiate iron corrosion. As a result, the spatial distribution of the salt inside the evaporating sessile droplet, which is influenced by the initial salt concentration in the droplet bulk, is correlated to the localisation of the anodic and cathodic reactions at the electrolyte-metal interface, over the footprint droplet area.

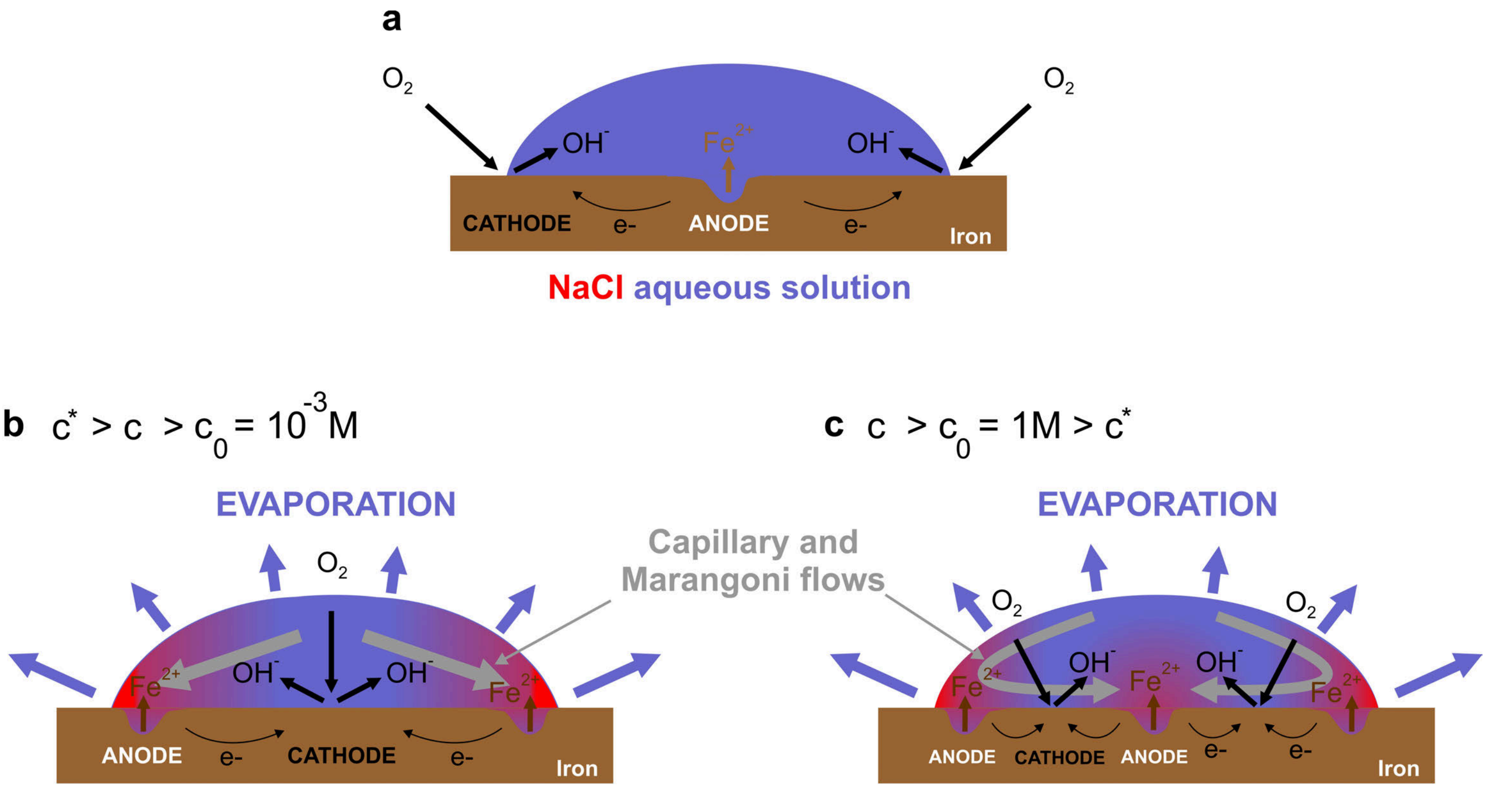

Figure 12 – *Schematic side views of the sessile droplet from NaCl aqueous solution deposited on an iron substrate in air. a. The classical Evans droplet model under a sessile droplet from NaCl solution: the oxygen is reduced at the droplet edge, acting as the cathode whereas the iron dissolution occurs in the droplet center acting as the anode.* ***b.*** *At a low initial salt concentration,* $c_0 = 10^{-3}$*M NaCl, the peripheral enrichment promoted by the evaporation-induced capillary and Marangoni flows causes an inversion of the Evans droplet model as soon as the critical global salt concentration* c^* *is reached: the anode is established near the contact line providing cathodic protection in the central part of the drying sessile droplet.* ***c.*** *On contrary, at a higher initial NaCl concentration,* $c_0 = 1$*M, which is by above to the experimental value of* c^**, the local variations in chloride ion concentration promoted by circulating evaporation-induced capillary and Marangoni flows, induces the occurrence of locally anodic and cathodic activities all over the iron surface at the metal-electrolyte interface.*

Another remarkable result of this experimental study of the corrosion process under evaporating sessile droplets from NaCl solutions is the observed critical global salt concentration c^*, at which visible and stable pits were formed. It is interesting though that the formation of visible and stable pits occurs already at quite low global salt concentration. This chloride threshold value indicates that the corrosion potential E_{corr}, at which the rate of oxygen reduction is equal to the rate of iron dissolution (see II.3.5), is higher than the pitting potential E_{pit} at which stable pits can form. E_{pit} is a linear function of the logarithm of the chloride ion concentration c: it decreases as c increases [44]. Therefore, assuming in first approximation that E_{corr} is almost constant in our studied case, when the salt concentration within the drying

NaCl droplet reaches c^*, stable pitting corrosion occurs. It is worth noting that E_{pit} is not only dependent on the chloride concentration but also on other factors such as pH or temperature.

To conclude, we demonstrated in this part that the evaporation behaviour of sessile droplets from aqueous NaCl solutions on iron samples is quite complex. It is less straightforward than with silicon wafers since in air corrosion alters in addition the overall evaporation profile. The spatial distribution of the salt over the footprint droplet area as well as its global concentration within the evaporating droplet have an impact on the location of the anodic and cathodic activities. These processes are independent of the relative humidity in the surrounding air environment.

To better elucidate the "necessary" conditions to induce corrosion of iron exposed to evaporating sessile droplets from aqueous saline solutions, further experiments should include a more detailed investigation on the influence of (initial) salt concentration inside the droplet, and particularly the spatial-temporal evolution of the localized NaCl concentration. This will allow to gain insight into the critical chloride concentration value. The role of the gaseous phase environment should be investigated with mixtures of oxygen and nitrogen. From an evaporation viewpoint, it will be interesting to figure out the (universal) evaporation equation for sessile salty droplets deposited on "reactive" surfaces.

SUMMARY AND CONCLUSION

When a sessile droplet from an aqueous saline solution evaporates on an inert surface, it leaves behind a stain of salt. In order to either prevent or to be able to control and use the patterns formed by such naturally ubiquitous drying droplets, one needs to understand the basic physics and chemistry of evaporating sessile salty droplets and their internal flow. In the second part of this thesis, we focused on the fundamentals of droplet evaporation, evaporation-driven flows inside the drying droplet, and the subsequent particle transport and deposition/precipitation.

In Chapter 2 we studied the evaporation of pure water droplets on silicon wafers. On these substrates, the pure water droplet retains a constant shape with a decreasing footprint area. Hence the evaporation can occur in the unpinned, constant contact angle mode. We found that the evolution of the rate of droplet (normalized) volume change is accurately described by a quasi-static, diffusion-driven evaporation model from Picknett and Bexon [3] for the entire range of relative humidities (0-80%), contact angles (1-40°) and initial droplet volumes (1-10 μl). Therefore, the evaporation of macroscopic droplets from pure water is controlled by the diffusion of the water vapour phase in the surrounding atmosphere.

In Chapter 3 we presented a detailed study on the evaporation behaviour of sessile droplets of aqueous sodium chloride (NaCl) solutions on inert surfaces. Quantitative evaporation experiments were performed over eight decades of initial NaCl concentrations, with various contact angles between nearly complete wetting and about 50°, with various initial droplet volumes ranging from 1 to 10 μl and at different relative environmental humidities varying from 0 to 60%. We have shown that already very low salt concentrations lead to a pinning of the three-phase contact line within the limits of our parameter variations. Whereas droplets with initial concentration $\geq 10^{-6}$M NaCl are pinned as soon as evaporation starts, droplets with lower salt concentration do evaporate in constant contact angle mode.

In addition, we analysed the influence of each experimental parameter on the evaporation rate following the well-accepted theoretical description of the diffusion-controlled evaporation of sessile droplets from pure water. To this end step-by-step the experimentally measured observed droplet geometries (volume, contact angle) and the liquid composition were scaled according to the theoretical approach such, that all the (normalized) data should result in a single, universal, unit-free initial volume evaporation rate. For the influence of the salt concentration on the vapour saturation pressure a uniform salt distribution within the droplet was assumed.

We have shown that at low salt concentrations or for high contact angles, the evaporation of sessile droplets from aqueous saline solutions occurs in a universal way based on the known scenario of a non-uniformity along the droplet surface of the evaporative flux diffusing from the free droplet surface into the surrounding environment. The singularity of the evaporative flux at the droplet edge drives an outward capillary (volume) flow towards the contact line [1] which leads to salt enrichment in this peripheral region.

For initial salt concentrations higher than 0.5M NaCl and contact angles smaller than 20°, the universal evaporation rate can no longer be applied and the flow structure becomes more complicated. We observed convection rolls near the droplet periphery. The evaporation-induced constitutional gradients resulting from the locally non-uniform evaporative flux from the droplet surface induces surface tension gradients on the liquid-air interface, generating Marangoni stresses. In the case of NaCl solutions the resulting Marangoni flow adds to the evaporation-driven flow and causes an additional salt enrichment near the contact line. Ultimately the capillary pressure increases near the contact line, provoking henceforth an additional compensating capillary flow from the droplet edge to its center. This means that the Marangoni effect significantly alters the flow field inside the drying droplet that in turn changes the evaporation behaviour of the sessile salty droplet.

The nature of the flow field inside the evaporating droplet also determined the patterns of the salty stains/deposits, that is formed during the drying and appear at the end of the water evaporation. We identified three different regimes of crystal depositions within the range of over six orders of magnitude of initial salt concentrations that were investigated.

In the particular case the sessile droplet of salt solution is deposited on planar iron surfaces under atmospheric conditions, the electrolyte solution within the droplet reacts with the surface, leading to differential aeration corrosion phenomenon. In the classical Evans droplet model [18], the cathodic reaction occurs at the droplet edge since there the diffusion path length of oxygen from the environmental vapour phase to the iron-saline solution interface is the shortest. The corresponding anode is established at the iron-electrolyte solution interface, close to the droplet center, where oxygen is deficient. In Part III we considered the spatial-temporal evolution of sessile droplets from aqueous saline solutions on iron surfaces, which were subjected to isohumidity exposure, at the equilibrium (deliquescence) relative humidity of the salt solution. In our experiments, in contrast to this simple, generally accepted Evans droplet model, we observed the formation and expansion of a peripheral film ahead of the macroscopic contact line.

Instead in Chapter 5 we found that the preferential oxygen reduction at the three-phase contact line gives rise to a cation displacement from the sessile salty droplet bulk through the "diffusive" peripheral film. The formation of this peripheral film and the corrosion behaviour have been investigated for various salt concentrations and ion species in Chapter 6. We found that the corrosion rate (i.e., the rate of weight loss of iron substrate per droplet area unit) strongly depends on the initial chloride concentration within the sessile droplet but barely on its size. However, we demonstrated that the corrosion behaviour is mainly governed by the surface tension of the electrolyte solution. This suggests that the simple Evans droplet model has to be modified significantly by taking into account a much more sophisticated contour of the droplet (liquid) surface in the droplet contact line region (peripheral film) and surface tension related transport processes. Most likely, the peripheral film phenomenon is predominantly caused by the peripheral surface tension gradient and the resulting Marangoni flow. The three-phase contact line should be destabilized by surface tension (salt) gradients induced by ionic composition changes during the course of the cathodic reaction and migration of cations towards the droplet perimeter. At present, the details of the dynamical process are not yet entirely understood.

In the fourth part of this thesis, we considered an evaporating droplet of sodium chloride solutions on iron. The evaporation experiments were performed over six decades of initial NaCl concentrations, with two different surrounding gaseous phase environments (i.e., inert high-purity nitrogen and synthetic air) and at different relative environmental humidities between 0 and 60%. A quite low (global) salt concentration within the drying droplet and (oxygenated) air environment are the main ingredients to observe the corrosion phenomenon under evaporating droplets of aqueous NaCl solutions. Similar to the evaporation on inert surfaces studied in Chapter 3, we found that the evaporation shows a strong dependence on initial salt concentration inside the drying droplet. By comparing our experimental evaporation study in inert gas to air environment, we identified and considered the salt-dependent evaporation-driven flow field within the drying sessile NaCl droplets.

We have shown that the observed corrosion phenomenon and in particular, the localisation of the anodic and cathodic activities over the initial footprint droplet area is correlated to the spatial distribution of the salt inside the evaporating sessile droplet. This process is independent of the relative humidity in the surrounding air environment. For a low initial NaCl concentration, the evaporative peripheral salt enrichment induces an inversion of the classical stationary Evans droplet experiment. As a critical chloride concentration is reached in the three-phase contact line region, the anode is established at the droplet edge whilst the cathodic reaction occurs away from the peripheral droplet area. On contrary, at higher initial NaCl concentration, the evaporative "uniform" salt enrichment leads to locally anodic and cathodic areas all over the iron surface under the drying droplet. Therefore by controlling the evaporation rate with the salt concentration but certainly also the droplet shape and size, and hence the internal flow, one can predict the localisation of the metal (pitting) corrosion under evaporating sessile salty droplets.

In the present work, we have shown that salt concentration gradients inside sessile droplets control the evaporation rate, the internal fluid flow, the subsequent deposition patterns formed at the end of the evaporation but also the corrosion behaviour under "stationary" and evaporating sessile salty droplets and the subsequent anode/cathode localisation at the saline solution-metal interface. In this thesis, we have mainly been concerned with evaporating sessile droplets. An interesting direction for future research is to study repetitive humidity cycles, i.e., evaporation-condensation, of the sessile droplet, distinctive feature of the atmospheric diurnal conditions (i.e., day/night alternating): hoes do evolve the salt concentration gradients within the sessile droplet subject to climatic changes?

BIBLIOGRAPHY

[1] R. D. Deegan, O. Bakajin, T. F. Dupont, G. Huber, S. R. Nagel, and T. A. Witten. Capillary flow as the cause of ring stains from dried liquid drops. *Nature*, **389**:827–829, 1997.

[2] J. C. Maxwell. Diffusion. In W.D. Niven, editor, *The Scientific Papers of James Clark Maxwell*. Cambridge University Press, 1980.

[3] R. G. Picknett and R. Bexon. The Evaporation of Sessile or Pendant Drops in Still Air. *Journal of Colloid and Interface Science*, **61**:336–350, 1977.

[4] S. M. Rowan, M. I. Newton, and G. McHale. Evaporation of Microdroplets and the Wetting of Solid Surfaces. *The Journal of Physical Chemistry*, **99**:13268–13271, 1995.

[5] J. Eggers and L. M. Pismen. Nonlocal description of evaporating drops. *Physics of Fluids*, **22**:112101, 2010.

[6] G. J. Dunn, S. K. Wilson, B. R. Duffy, S. David, and K. Sefiane. A mathematical model for the evaporation of a thin sessile liquid droplet: Comparison between experiment and theory. *Colloids and Surfaces A: Physicochemical and Engineering Aspects*, **323**:50–55, 2008.

[7] H. Hu and R. G. Larson. Evaporation of a sessile droplet on a substrate. *Journal of Physical Chemistry B*, **106**:1334–1344, 2002.

[8] H. Hu and R. G. Larson. Analysis of the Effects of Marangoni Stresses on the Microflow in an Evaporating Sessile Droplet. *Langmuir*, **21**:3972–3980, 2005.

[9] Y. O. Popov. Evaporative deposition patterns: Spatial dimensions of the deposit. *Physical Review E*, **71**:036313, 2005.

[10] R. D. Deegan, O. Bakajin, T. F. Dupont, G. Huber, S. R. Nagel, and T. A. Witten. Contact lines deposits in an evaporating drop. *Physical Review E*, **62**:756–765, 2000.

[11] H. Gelderblom, O. Bloemen, and J. H. Snoeijer. Stokes flow near the contact line of an evaporating drop. *Journal of the Fluid Mechanics*, **709**:69–84, 2012.

[12] E. Bormashenko, Y. Bormashenko, R. Pogreb, O. Stanevsky, and G. Whyman. Droplet behavior on flat and textured surfaces: Co-occurence of Deegan outward flow with Marangoni solute instability. *Journal of Colloid and Interface Science*, **306**:128–132, 2007.

[13] T. Still, P. J. Yunker, and A. G. Yodh. Surfactant-Induced Marangoni Eddies Alter the Coffee-Rings of Evaporating Colloidal Drops. *Langmuir*, **28**:4984–4988, 2012.

[14] W. Sempels, R. De Dier, H. Mizuno, J. Hofkens, and J. Vermant. Auto-production of biosurfactants reverses the coffee ring effect in a bacterial system. *Nature Communications*, **4**:1757, 2013.

[15] E. Senses, M. Black, T. Cunningham, S. A. Sukhishvili, and P. Akcora. Spatial Ordering of Colloids in a Drying Aqueous Polymer Droplet. *Langmuir*, **29**:2588–2594, 2013.

[16] T. A. H. Nguyen, M. A. Hampton, and A. V. Nguyen. Evaporation of Nanoparticle Droplets on Smooth Hydrophobic Surfaces: The Inner Coffee Ring Deposits. *The Journal of Physical Chemistry C*, **117**:4707–4716, 2013.

[17] S. Semenov, A. Trybala, H. Agogo, N. Kovalchuk, F. Ortega, R. G. Rubio, V. M. Starov, and Velarde M. G. Evaporation of Droplets of Surfactant Solutions. *Langmuir*, **29**:10028–10036, 2013.

[18] U. R. Evans. The Ferroxyl Indicator in Corrosion Research, With Special Reference to the Controversy Regarding the Cause of Pitting. *The Metal Industry*, **11**:481–508, 1926.

[19] C. Chen and F. Mansfeld. Potential Distribution in the Evans Drop Experiment. *Corrosion Science*, **39**:409–413, 1997.

[20] B. Maier and G. S. Frankel. Pitting Corrosion of Bare Stainless Steel 304 under Chloride Solution Droplets. *Journal of the Electrochemical Society*, **157**:C302–C312, 2010.

[21] Y. Tsutsumi, A. Nishikata, and T. Tsuru. Pitting corrosion mechanism of Type 304 stainless steel under a droplet of chloride solutions. *Corrosion Science*, **49**:1394–1407, 2007.

[22] I. S. Cole, T. H. Muster, S. A. Furman, N. Wright, and A. Bradbury. Products Formed during the Interaction of Seawater Droplets with Zinc Surfaces: I. Results from 1- and 2.5 Day Exposures. *Journal of the Electrochemical Society*, **155**:C244–C255, 2008.

[23] J. F. Li, B. Maier, and G. S. Frankel. Corrosion of an Al-Mg-Si alloy under $MgCl_2$ solution droplets. *Corrosion Science*, **53**:2142–2151, 2011.

[24] Y. Wang, W. Wang, Y. Liu, L. Zhong, and J. Wang. Study of localized corrosion of 304 stainless steel under chloride solution droplets using the wire beam electrode. *Corrosion Science*, **53**:2963–2968, 2011.

[25] T. H. Muster, A. Bradbury, A. Trinchi, I. S. Cole, D. Lau, S. Dligatch, A. Bendavid, and P. Martin. The atmospheric corrosion of zinc: The effects of salt concentration, droplet size and droplet shape. *Electrochimica Acta*, **56**:1866–1873, 2011.

[26] S. C. Morton and G. S. Frankel. Atmospheric pitting corrosion of AA7075-T6 under evaporating droplets with and without inhibitors. *Materials and Corrosion*, **65**:351–361, 2014.

[27] G. El-Mahdy, M. Abdel-Reheem, O. M. El-Roudi, A. M. Atta, Z. Issa, and H. A. Al-Lohedan. Assessment of Salt and Acid Droplets Evaporations on the Corrosion Mechanism of Aluminum. *International Journal of Electrochemical Science*, **10**:6392–6404, 2015.

[28] N. S. Azmat, K. D. Ralston, B. C. Muddle, and I. S. Cole. Corrosion of Zn under acidified marine droplets. *Corrosion Science*, **53**:1604–1615, 2011.

[29] R. Wang and M. Kido. Corrosion Behavior of Pure Iron by Different Droplet Volume of Sulfuric Acid Solution. *Materials Transactions*, **48**:1451–1457, 2007.

[30] S. Thomas, I. S. Cole, and N. Birbilis. Compact Oxides Formed on Zinc during Exposure to a Single Sea-Water Droplet. *Journal of the Electrochemical Society*, **160**:C59–C63, 2013.

[31] P.-G. De Gennes. Wetting: Statics and Dynamics. *Reviews of Modern Physics*, **57**:827–863, 1985.

[32] P.-G. De Gennes, F. Brochart-Wyart, and D. Quéré. *Capillary and Wetting Phenomrisena: Drops, Bubbles, Pearls, Waves*. Springer, 2003.

[33] T. Young. An essay on the Cohesion of Fluids. *Philosophical Transactions of the Royal Society of London*, **95**:65–86, 1805.

[34] A. M. Cazabat, N. Fraysse, and F. Heslot. Thin wetting films. *Colloids and Surfaces*, **52**:1–8, 1991.

[35] D. Bonn, J. Eggers, J. Indekeu, J. Meunier, and E. Rolley. Wetting and spreading. *Review of Modern Physics*, **81**:307–313, 2009.

[36] M. N. Popescu, G. Oshanin, S. Dietrich, and A.-M. Cazabat. Precursor films in wetting phenomena. *Journal of Physics: Condensed Matter*, **24**:243102, 2012.

[37] B. V. Derjaguin. Disjoining Pressure. In N. V. Churaev, B. V. Derjaguin, and V. M. Muller, editors, *Surface Forces*. Springer, 1987.

[38] J. N. Israelachvili. *Intermolecular and Surface Forces*. Academic Press, 2011.

[39] G. Jones and W. A. Ray. The Surface Tensions of Solutions of Electrolytes as a Function of the Concentration. I. A Differential Method for Measuring Relative Surface Tension. *Journal of the American Chemical Society*, **59**:187–198, 1937.

[40] G. Jones and W. A. Ray. The Surface Tensions of Solutions of Electrolytes as a Function of the Concentration. II. *Journal of the American Chemical Society*, **63**:288–294, 1941.

[41] K. D. Collins and M. W. Washabaugh. The Hofmeister effect and the behavior of water at interfaces. *Quaterly Reviews of Biophysics*, **18**:323–422, 1985.

[42] P. K. Weissenborn and R. J. Pugh. Surface Tension and Bubble Coalescence Phenomena of Aqueous Solutions of Electrolytes. *Langmuir*, **11**:1422–1426, 1995.

[43] W. Kunz. *Specific Ion Effects*. World Scientific Publishing, 2009.

[44] Y. Marcus. Surface Tension of Aqueous Electrolytes and Ions. *Journal of Chemical & Engineering Data*, **55**:3641–3644, 2010.

[45] R. L. Baldwin. How Hofmeister ion interactions affect protein stability. *Biophysical Journal*, **71**:2056–2063, 1996.

[46] T. Arakawa and S. N. Timasheff. Mechanism of protein salting in and salting out by divalent cation salts: balance between hydratation and salt binding. *Biochemistry*, **23**:5912–5923, 1984.

[47] T. Arakawa. Thermodynamic analysis of the effect of concentrated salts on protein interaction with hydrophobic and polysaccharide columns. *Archives of Biochemistry and Biophysics*, **248**:101–105, 1986.

[48] Ulrich J. Curtis, R. A., J. M. Prausnitz, and H. W. Blanch. Protein-Protein Interactions in Concentrated Electrolyte Solutions - Hofmeister Series Effects. *Biotechnology and Bioengineering*, **79**:367–380, 2002.

[49] W. M. Cox and J. H. Wolfenden. Viscosity of strong electrolytes measured by a differential method. *Proceedings of the Royal Society of London A.*, **145**:475–488, 1934.

[50] G. W. J. Stewart. The Variation in the Structure of Water in Ionic Solutions. *The Journal of Chemical Physics*, **7**:869–877, 1939.

[51] H. S. Franck and M. W. J. Evans. Free volume and entropy in condensed systems. *The Journal of Chemical Physics*, **13**:507–532, 1945.

[52] R. Zangi. Can Salting-In/Salting-Out Ions be Classified as Chaotropes/Kosmotropes? *The Journal of Physical Chemistry B*, **114**:643–650, 2010.

[53] A. M. Cazabat and G. Guéna. Evaporation of macroscopic sessile droplets. *Soft Matter*, **6**:2591–2612, 2010.

[54] N. Murisic and L. Kondic. On evaporation of sessile drops with moving contact lines. *Journal of Fluid Mechanics*, **679**:219–246, 2011.

[55] H. Hu and R. G. Larson. Drying a sessile droplet: Imaging and analysis of transport and deposition patterns. In Z. Lin, editor, *Evaporative Self-Assembly of Ordered Complex Structures*. World Scientific Publishing Company, 2012.

[56] N. A. Fuchs. *Evaporation and Droplet Growth in Gaseous Media*. Pergamon Press, 1959.

[57] C. Bourges-Monnier and M. E. R. Shanahan. Influence of evaporation on contact angle. *Langmuir*, **11**:2820–2829, 1995.

[58] G. McHale, S. M. Rowan, M. I. Newton, and M. K. Banerjee. Evaporation and the Wetting of a Low-Energy Solid Surface. *Journal of Physical Chemistry B*, **102**:1964–1967, 1998.

[59] H. Song, Y. Lee, S. Jin, H.-Y. Kim, and J. Y. Yoo. Prediction of sessile drop evaporation considering surface wettability. *Microelectronic Engineering*, **88**:3249–3255, 2011.

[60] K. S. Birdi, D. T. Vu, and A. A. Winter. A Study of the Evaporation Rates of Small Water Drops Placed on a Solid Surface. *The Journal of Physical Chemistry*, **93**:3702–3703, 1989.

[61] H. Y. Erbil. Determination of the Peripheral Contact Angle of Sessile Drops on Solids from the Rate of Drop Evaporation. *The Journal of Physical Chemistry B*, **102**:9234–9238, 1998.

[62] H.-Z. Yu, D. M. Soolaman, A. W. Rowe, and J. T. Banks. Evaporation of Water Microdroplets on Self-Assembled Monolayers: From Pinning to Shrinking. *A European Journal of Chemical Physics and Physical Chemistry*, **5**:1035–1038, 2004.

[63] X. Fang, B. Li, E. Petersen, Y. Ji, J. C. Sokolov, and M. H. Rafailovich. Factors Controlling the Drop Evaporation Constant. *The Journal of Physical Chemistry B*, **109**:20554–20557, 2005.

[64] R. W. Coutant and E. C. Penski. Experimental Evaluation of Mass Transfer from Sessile Drops. *Industrial & Engineering Chemistry Fundamentals*, **21**:250–254, 1982.

[65] H. Y. Erbil, G. McHale, and M. I. Newton. Drop Evaporation on Solid Surfaces: Constant Constant Angle Mode. *Langmuir*, **18**:2636–2641, 2002.

[66] C. Liu, E. Bonaccurso, and H.-J. Butt. Evaporation of sessile water/ethanol drops in a controlled environment. *Physical Chemistry Chemical Physics*, **10**:7150–7157, 2008.

[67] S. David, K. Sefiane, and L. Tardiest. Experimental investigation of the effect of thermal properties of the substrate in the wetting and evaporation of sessile drops. *Colloids and Surfaces A: Physicochemical and Engineering Aspects*, **298**:108–114, 2007.

[68] G. J. Dunn, S. K. Wilson, B. R. Duffy, S. David, and K. Sefiane. The strong influence of substrate conductivity on droplet evaporation. *Journal of Fluid Mechanics*, **623**:329–351, 2009.

[69] N. Shahidzadeh-Bonn, S. Rafai, A. Azouni, and D. Bonn. Evaporating droplets. *Journal of Fluid Mechanics*, **549**:307–313, 2006.

[70] G. Guéna, C. Poulard, and A. M. Cazabat. The leading edge of evaporating droplets. *Journal of Colloid and Interface Science*, **312**:164–171, 2007.

[71] V. A. Kaya, D.and Belyi and M. Muthukumar. Pattern formation in drying droplets of polyelectrolyte and salt. *The Journal of Chemical Physics*, **133**:114905, 2010.

[72] D. Brutin, B. Sobac, B. ans Loquet, and J. Sampol. Pattern formation in drying drops of blood. *Journal of Fluid Mechanics*, **667**:85–95, 2011.

[73] R. D. Deegan. Pattern formation in drying drops. *Physical Review E*, **61**:475–485, 2000.

[74] P. J. Yunker, T. Still, M. A. Lohr, and A. G. Yodh. Suppression of the coffee-ring effect by shape-dependent capillary interactions. *Nature*, **476**:308–311, 2011.

[75] H. B. Eral, D. M. Augustine, M. H. G. Duits, and F. Mugele. Suppressing the coffee stain effect: how to control colloidal self-assembly in evaporating drops using electrowetting. *Soft Matter*, **7**:1–5, 2011.

[76] L. E. Scriven and C. V. Sternling. The Marangoni Effects. *Nature*, **187**:186–188, 1960.

[77] J. Thomson. On certain curious Motions observable at the Surface of Wine and other Alcoholic liquors. *Philosophical Magazine*, **10**:330–333, 1855.

[78] H. Hu and R. G. Larson. Marangoni Effect Reverses Coffee-Ring Depositions. *The Journal of Physical Chemistry B*, **110**:7090–7094, 2006.

[79] W. D. Ristenpart, P. G. Kim, C. Domingues, J. Wan, and H. A. Stone. Influence of substrate conductivity on circulation reversal in evaporating drops. *Physical Review Letter*, **99**:234502, 2007.

[80] J. R. Trantum, Z. E. Eagleton, C. A. Patil, J. M. Tucker-Schwartz, M. L. Baglia, M. C. Skala, and F. R. Haselton. Cross-Sectional Tracking of Particle Motion in Evaporating Drops: Flow Fields and Interfacial Accumulation. *Langmuir*, **29**:6221–6231, 2013.

[81] M. Majumber, C. S. Rendall, J. A. Eukel, J. Y. L. Wang, N Behabtu, C. L. Pint, T.-Y Liu, A. W. Orbaek, F. Mirri, J. Nam, A. R. Barron, R. H. Hauge, H. K. Schmidt, and M. Pasquali. Overcoming the "Coffee-Stain" Effect by Compositional Marangoni-Flow-Assisted Drop-Drying. *The Journal of Physical Chemistry B*, **116**:6536–6542, 2012.

[82] F. Girard, M. Antoni, and K. Sefiane. On the Effect of Marangoni Flow on Evaporation Rates of Heated Water Drops. *Langmuir*, **24**:9207–9210, 2008.

[83] P. Takhistov and H.-C. Chang. Complex Stain Morphologies. *Industrial & Engineering Chemistry Research*, **41**:6256–6269, 2002.

[84] M. Cachile, O. Benichou, and A. M Cazabat. Evaporating Droplets of Completely Wetting Liquids. *Langmuir*, **18**:7985–7990, 2002.

[85] M. Cachile, O. Benichou, C. Poulard, and A. M Cazabat. Evaporating Droplets. *Langmuir*, **18**:8070–8078, 2002.

[86] H. Bodiguel and J. Leng. Imaging the drying of a colloidal suspension. *Soft Matter*, **6**:5451–5460, 2010.

[87] D. Landolt. *Corrosion et chimie de surfaces des métaux*. Presses Polytechniques et Universitaires Romandes, 1993.

[88] W. H. Ailor. *Atmospheric Corrosion*. John Wiley and Sons, 1982.

[89] P. A. Schweitzer. *Fundamentals of Corrosion: Mechanisms, Causes, and Preventative Methods*. CRC Press, 2010.

[90] Y. Tsutsumi, A. Nishikata, and T. Tsuru. Initial Stage of Pitting Corrosion of Type 304 Stainless Steel under Thin Electrolyte Layers Containing Chloride Ions. *Journal of The Electrochemical Society*, **152**:B358–B363, 2005.

[91] S. Hastuty, A. Nishikata, and T. Tsuru. Pitting corrosion of Type 430 stainless steel under chloride solution droplet. *Corrosion Science*, **52**:2035–2043, 2010.

[92] N. D. Tomashov. Development of the Electrochemical Theory of Metallic Corrosion. *Corrosion*, **76**:7t–14t, 1964.

[93] A. Nishikata, Y. Ichihara, Y. Hayashi, and T. Tsuru. Influence of Electrolyte Layer Thickness and pH on the Initial Stage of the Atmospheric Corrosion of Iron. *Journal of The Electrochemical Society*, **144**:1244–1252, 1997.

[94] P. B. Phipps and W. D. Rice. The Role of Water in Atmospheric Corrosion. In G. R. Brubaker and P. B. Phipps, editors, *Corrosion Chemistry*. American Chemical Society, 1979.

[95] L. Q. Guo, X. M. Zhao, Y. Bai, and L. J. Qiao. Water adsorption behavior on metal surface and its influence on surface potential study by *in situ* SPM. *Applied Surface Science*, **258**:9087–9091, 2012.

[96] W. H. J. Vernon. A laboratory study of the atmospheric corrosion of metals. Part I.-The Corrosion of copper in certain synthetic atmospheres, with particular reference to the influence of sulphur dioxide in air of various relative humidities. *Transactions of the Faraday Society*, **27**:255–277, 1931.

[97] W. H. J. Vernon. A laboratory study of the atmospheric corrosion of metals. Part II.-Iron: the primary oxide film. Part III.-The secondary product or rust (influence of sulphur dioxide, carbon dioxide, and suspended particles on the rusting of iron). *Transactions of the Faraday Society*, **31**:1668–1700, 1935.

[98] E. Schindelholz, B. E. Risteen, and R. G. Kelly. Effect of Relative Humidity on Corrosion of Steel under Sea Salt Aerosol Proxies. I. NaCl. *Journal of the Electrochemical Society*, **161**:C450–C459, 2014.

[99] E. Schindelholz, B. E. Risteen, and R. G. Kelly. Effect of Relative Humidity on Corrosion of Steel under Sea Salt Aerosol Proxies. II. $MgCl_2$, Artificial Seawater. *Journal of the Electrochemical Society*, **161**:C460–C470, 2014.

[100] R. P. V. Cruz, A. Nishikata, and T. Tsuru. Pitting corrosion mechanism of stainless steels under wet-dry exposure in chloride-containing environments. *Corrosion Science*, **40**:125–139, 1998.

[101] U. R. Evans. *An Introduction to Metallic Corrosion*. Edward Arnold, 1963.

[102] S. Li and L. H. Hihara. In situ Raman Spectroscopic Study of NaCl Particle-Induced Marine Atmospheric Corrosion of Carbon Steel. *Journal of The Electrochemical Society*, **159**:C147–C154, 2012.

[103] U. R. Evans and C. A. J. Taylor. Mechanism of atmospheric rusting. *Corrosion Science*, **12**:227–246, 1972.

[104] S. Karpitschka and H. Riegler. Quantitative Experimental Study on the Transition between Fast and Delayed Coalescence of Sessile Droplets with Different but Completely Miscible Liquids. *Langmuir*, **26**:11823–11829, 2010.

[105] S. Karpitschka and H. Riegler. Noncoalescence of droplets with different miscible liquids: Hydrodynamic analysis of the twin drop contour as self-stabilizing travelling wave. *Physical Review Letter*, **106**:066103, 2012.

[106] S. Karpitschka and H. Riegler. Sharp transition between coalescence and non-coalescence of sessile drops. *Journal of Fluid Mechanics*, **743**:R1, 2014.

[107] S. Karpitschka, C. Hanske, A. Fery, and H. Riegler. Coalescence and noncoalescence of sessile drops: impact of surface forces. *Langmuir*, **30**:6826–6830, 2014.

[108] S. P. Pinho and E. A. Macedo. Solubility of NaCl, NaBr, and KCl in Water, Methanol, Ethanol, and Their Mixed Solvents. *Journal of Chemical & Engineering Data*, **50**:29–32, 2005.

[109] E. B. Millard. *The Vapor Pressure of Water and of Aqueous Solutions of Magnesium Sulphate, Magnesium Chloride and Sodium Chloride*. Nabu Press, 2010.

[110] L. T. Zhuravlev. The surface chemistry of amorphous silica. Zhuravlev model. *Colloids and Surfaces A: Physicochemical and Engineering Aspects*, **173**:1–38, 2000.

[111] L. Greenspan. Humidity fixed points of binary saturated aqueous solutions. *Journal of Research of the National Bureau of Standards*, **81**:89–96, 1977.

[112] N. H. Chen and D. F. Othmer. New Generalized Equation for Gas Diffusion Coefficient. *Journal of Chemical & Engineering Data*, **7**:37–41, 1962.

[113] C. Bourgés-Monnier and M. E. R. Shanahan. Influence of Evaporation on Contact Angle. *Langmuir*, **18**:2820–2829, 1995.

[114] D. S. Golovko, H.-J. Butt, and E. Bonaccurso. Transition in the Evaporation Kinetics of Water Microdrops on Hydrophilic Surfaces. *Langmuir*, **18**:75–78, 2009.

[115] S. M. Rowan, M. I. Newton, and G. McHale. Evaporation of Pure Liquid Sessile and Spherical suspended drops: A review. *Advances in Colloid and Interface Science*, **170**:67–86, 2012.

[116] J. I. Partanen and A. K. Covington. Re-Evaluation of the Thermodynamic Activity Quantities in Aqueous Sodium and Potassium Chloride Solutions at 25°c. *Journal of Chemical Engineering Data*, **54**:208–219, 2009.

[117] N. Shahidzadeh-Bonn, S. Rafaï, D. Bonn, and G. Wegdam. Salt Crystallization during Evaporation: Impact of Interfacial Properties. *Langmuir*, **24**:8599–8605, 2008.

[118] J. Desarnaud and N. Shahidzadeh-Bonn. Salt crystal purification by deliquescence/crystallization cycling. *A Letters Journal Exploring the Frontiers of Physics*, **95**:48002, 2011.

[119] J. Kestin, E. Khalifa, and R. J. Correia. Tables of the Dynamic and Kinematic Viscosity of Aqueous NaCl Solutions in the Temperature Range 20-150°c and the Pressure Range 0.1-35 MPa. *Journal of Physical and Chemical Reference Data*, **10**:71–87, 1981.

[120] W. M. Haynes, editor. *Handbook of Chemistry and Physics 93rd Edition*. CRC Press, 2012.

[121] A. Apelblat. The vapour pressures of saturated aqueous lithium chloride, sodium bromide, sodium nitrate, ammonium nitrate, and ammonium chloride at temperatures from 283 K to 313 K. *The Journal of Chemical Thermodynamics*, **25**:63–71, 1993.

[122] R. Lindstrom, J.-E. Svensson, and L.-G. Johansson. The Atmospheric Corrosion of Zinc in the Presence of NaCl. the Influence of Carbon Dioxide and Temperature. *Journal of the Electrochemical Society*, **147**:1751–1757, 2000.

[123] R. Lindstrom, J.-E. Svensson, and L.-G. Johansson. The Influence of Salt Deposits on the Atmospheric Corrosion of Zinc. *Journal of the Electrochemical Society*, **149**:B57–B64, 2002.

[124] A. K. Neufeld, I. S. Cole, A. M. Bond, and S. A. Furman. The initiation mechanism of corrosion of zinc by sodium chloride particle deposition. *Corrosion Science*, **44**:555–572, 2002.

[125] Z. Y. Chen, S. Zakipour, D. Persson, and C. Leygraf. Effect of Sodium Chloride Particles on the Atmospheric Corrosion of Pure Copper. *Corrosion Science*, **60**:479–491, 2004.

[126] S. X. Li and L. H. Hihara. Atmospheric corrosion initiation on steel from predeposited NaCl salt particles in high humidity environment. *Corrosion Engineering, Science and Technology*, **45**:49–56, 2010.

[127] S. Li and L. H. Hihara. *In situ* Raman spectroscopic identification of rust formation in Evans' droplet experiments. *Electrochemistry Communications*, **18**:48–50, 2012.

[128] E. Schindelholz, B. E. Risteen, and R. G. Kelly. Effect of Relative Humidity on Corrosion of Steel under Sea Salt Aerosol Proxies. I. NaCl. *Journal of the Electrochemical Society*, **161**:C450–C459, 2014.

[129] E. Schindelholz and R. G. Kelly. Wetting phenomena and time of wetness in atmospheric corrosion: a review. *Corrosion Reviews*, **30**:135–170, 2012.

[130] R. M. Cornell and U. Schwertmann. *The Iron Oxides Structure, Properties, Reactions, Occurences and Uses*. Wiley-VCH, 2003.

[131] R. A. Antunes, I. Costa, and D. L. A. Faria. Characterization of corrosion products formed on steels in the first months of atmospheric exposure. *Materials Research*, **6**:403–408, 2003.

[132] M. Stratmann, K. Bohnenkamp, and H.-J. Engell. An electrochemical study of phase-transitions in rust layers. *Corrosion Science*, **23**:969–985, 1983.

[133] M. Stratmann and J. Muller. The mechanism of the oxygen reduction on rust-covered metal substrates. *Corrosion Science*, **36**:327–359, 1994.

[134] I. Newton. *Opticks: Or, A Treatise of the Reflexions, Refractions, Inflexions and Colours of Light. Also Two Treatises of the Species and Magnitude of Curvilinear Figures.* Royal Society of London, 1704.

[135] T. Tsuru, K.-I. Tamiya, and A. Nishikata. Formation and growth of micro-droplets during the initial stage of atmospheric corrosion. *Electrochimica Acta*, **149**:2709–2715, 2004.

[136] K. H. Raveesha, V. H. Doddamani, and B. K. Prasad. On a method to employ Newton's Rings concept to determine thickness of thin films. *International Letters of Chemistry, Physics and Astronomy*, **22**:1–7, 2014.

[137] J. K. Beattie, A. M. Djerdjev, A. Gray-Weale, N. Kallay, J. Lutzenkirchen, T. Preocanin, and A. Selmani. pH and the surface tension of water. *Journal of Colloid and Interface Science*, **422**:54–57, 2014.

[138] M. Pourbaix. *Atlas d'Equilibres Electrochimiques*. Gauthier-Villars, 1963.

[139] J. Zhang, J. Wang, and Y. Wang. Micro-Droplets Formation During the Deliquescence of Salt Particles in Atmosphere. *Corrosion Science*, **61**:1167–1172, 2005.

[140] J. Zhang, J. Wang, and Y. Wang. Electrochemical investigations of micro-droplets formed on metals during the deliquescence of salt particles in atmosphere. *Electrochemistry Communications*, **7**:443–448, 2005.

[141] R. Mills. A Remeasurement of the Self-diffusion Coefficients of Sodium Ion in Aqueous Sodium Chloride Solutions. *Journal of the American Chemical Society*, **77**:6116–6119, 1955.

[142] R. Mills and V. M. M. Lobo. *Self-diffusion in Electrolyte Solutions: A Critical Examination of Dat a Ccompiled from the Literature*. Wiley-Blackwell, 2000.

[143] C. Leygraf and T. Graedel. *Atmospheric Corrosion*. Wiley-Blackwell, 2000.

[144] G. S. Frankel and J. W. Braithwaite. Corrosion of Microelectronic and Magnetic Data-Storage Devices. In P. Marcus, editor, *Corrosion Mechanism in Theory and Practice*. CRC Press, 2012.

[145] W. H. J. Vernon. Adsorption of Water Vapour on Solid Surfaces. *Nature*, **167**:1037–1038, 1951.

[146] J. Kestin, E. Khalifa, and R. J. Correia. Tables of the Dynamic and Kinematic Viscosity of Aqueous KCl Solutions in the Temperature Range 20-150°c and the Pressure Range 0.1-35 MPa. *Journal of Physical and Chemical Reference Data*, **10**:57–70, 1981.

[147] J. M. Wimby and T. S. Berntsson. Viscosity and density of aqueous solutions of lithium bromide, lithium chloride, zinc bromide, calcium chloride and lithium nitrate. 1. Single salt solutions. *Journal of Chemical & Engineering Data*, **39**:68–72, 1994.

[148] S. E. Traubenberg and R. T. Foley. The Influence of Chloride and Sulfate Ions on the Corrosion of Iron in Sulfuric Acid. *Journal of the Electrochemical Society*, **118**:1066–1070, 1971.

[149] E. Janata, M. Kelm, and B. G. Ershov. Solubility of oxygen and nitrous oxide in aqueous solutions of NaCl: a pulse radiolysis study. *Radiation Physics and Chemistry*, **63**:157–160, 2002.

[150] F. J. Millero and F. Huang. Solubility of Oxygen in Aqueous Solutions of KCl, K_2SO_4, and $CaCl_2$ as a Function of Concentration and Temperature. *Journal of Chemical Engineering Data*, **48**:1050–1054, 2003.

[151] F. King. General corrosion in nuclear reactor components and nuclear water disposal systems. In D. Feron, editor, *Nuclear corrosion science and engineering*. Woodhead Publishing Limited, 2012.

[152] E. Dubuisson, P. Lavie, F. Dalard, J.-P. Caire, and S. Szunerits. Study of the atmopheric corrosion of galvanised steel in a micrometrical electrolytic droplet. *Electrochemistry Communications*, **8**:911–915, 2006.

[153] E. Dubuisson, P. Lavie, F. Dalard, J.-P. Caire, and S. Szunerits. Corrosion of galvanised steel under an electrolytic drop. *Corrosion Science*, **49**:910–919, 2007.

[154] M. Humenik and W. D. Kingery. Metal-Ceramic Interactions: III, Surface Tension and Wettability of Metal-Ceramic Systems. *Journal of The American Ceramic Society*, **37**:18–23, 1954.

[155] L. Boulange-Petermann, B. Baroux, and M.-N. Bellon-Fontaine. The influence of metallic surface wettability on bacterial adhesion. *Journal of Adhesion Science and Technology*, **7**:221–230, 1993.

[156] X. M. Yang, Z. W. Zhong, E. M. Diallo, Z. H. Wang, and W. S. Yue. Silicon wafer wettability ang aging behaviors: Impact on gold thin-film morphology. *Materials Science in Semiconductor Processing*, **26**:25–32, 2014.

[157] D. Landolt. *Corrosion and Surface Chemistry of Metals*. CRC Press, 2007.

[158] M.N. Illman. Analysis of internal corrosion in subsea oil pipeline. *Case Studies in Engineering Failure Analysis*, **2**:1–8, 2014.

[159] J. R. Galvele. Transport Processes and the Mechanism of Pitting of Metals. *Journal of the Electrochemical Society*, **123**:464–474, 1976.

[160] H.-H. Strehblow. Nucleation and Repassivation of Corrosion Pits for Pitting on Iron and Nnickel. *Werkstoffe und Korrosion*, **27**:792–799, 1976.

V

Appendix

EVAPORATION OF SESSILE DROPLETS

A

A. 1 EVAPORATION OF SESSILE DROPLETS FROM PURE WATER

The evaporation of sessile droplets from pure water was investigated at different relative humidities *RHs* (ranging from 0 to 80%), for different contact angles θ (ranging from 1 to 40°), and for different droplet volumes V_0 (ranging from 1 to 10 μl).

Sessile droplets from pure water evaporated in the unpinned, constant contact angle mode irrespective of the relative humidity, the contact angle or the droplet size. All the evaporation curves (i.e., the time evolution of the droplet volume during its evaporation) presented the characteristic patterns of an evaporating sessile droplet from pure liquids. Figure 2.1 illustrates as an example the typical evaporation behaviour of sessile droplets from pure water. At the initial stage of the evaporation, the loss of the droplet volume was linear with time and then deviated from its temporal linear change to a slower decrease with time until the sessile droplet totally evaporated. This characteristic evaporation behaviour was confirmed by the top and side view imagings of the sessile droplet at three different evaporation times. The footprint of the droplet contact area with the substrate decreased with time. Meanwhile the contact angle remained constant over the whole evaporation process.

In this appendix, we present only the evaporation curves of sessile droplets containing pure water at a higher relative humidity (*RH* of 40%, Figure 1), with a higher contact angle ($\theta \simeq 30°$, Figure 2) and with a smaller droplet volume ($V_0 \simeq 1$ μl, Figure 3). It is interesting to notice that the constant contact angle adopted by the sessile droplet containing pure water on the substrate was approximately identical ($\theta = 1 \pm 0.5°$) for all the evaporation experiments, i.e., with different relative humidities and various droplet sizes.

Effect of the Relative Humidity on the Evaporation Behaviour

Figure 1 shows the time evolution of the droplet volume and shape (from top and side aspects) during the evaporation of a sessile droplet containing pure water at a relative humidity *RH* of 40%.

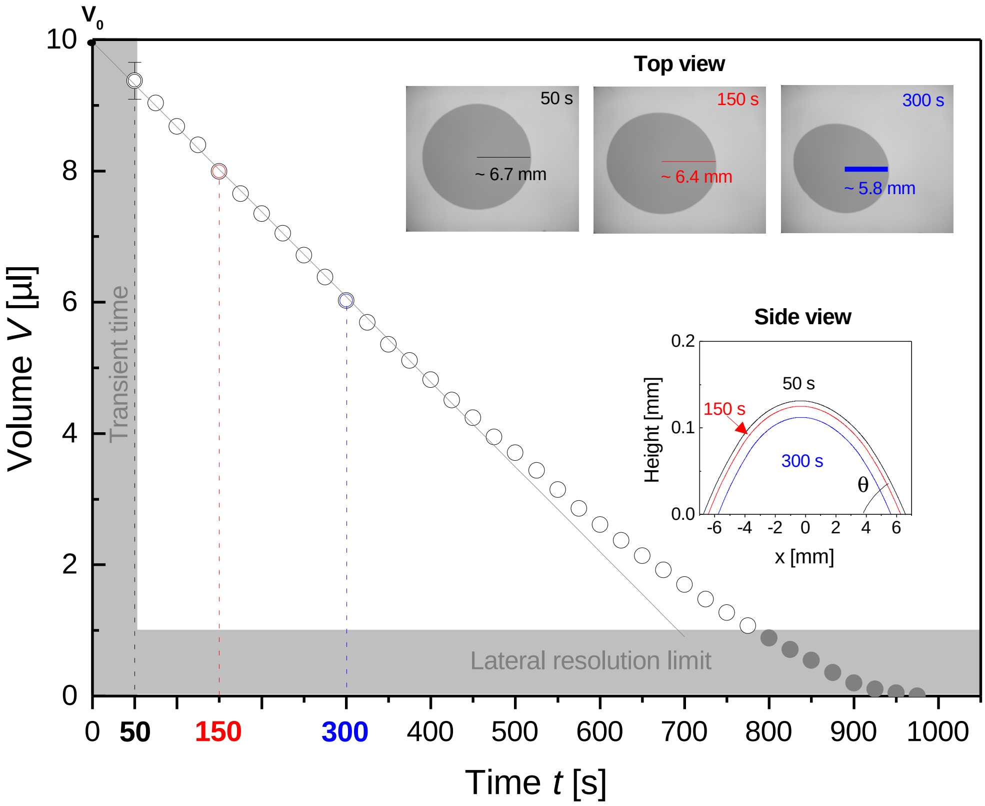

Figure 1 – *Evaporation of a sessile droplet from pure water at a relative humidity RH of* 40%. *The insets show the simultaneous height profile and top view images at three different evaporation times:* 50, 150 *and* 300 *s. The straight line depicts the linear decrease of the droplet volume with time experimentally observed at the initial stage of the evaporation (i.e., between* $t = 50$ *and* 400 *s). The extrapolation of this linear volume change yielded at* $t = 0$ *s the initially deposited volume* V_0.

Effect of the Contact Angle on the Evaporation Behaviour

Figure 2 shows the time evolution of the droplet volume and shape (from top and side aspects) during the evaporation of a sessile droplet containing pure water with a contact angle θ of 30° at a relative humidity RH of 0%.

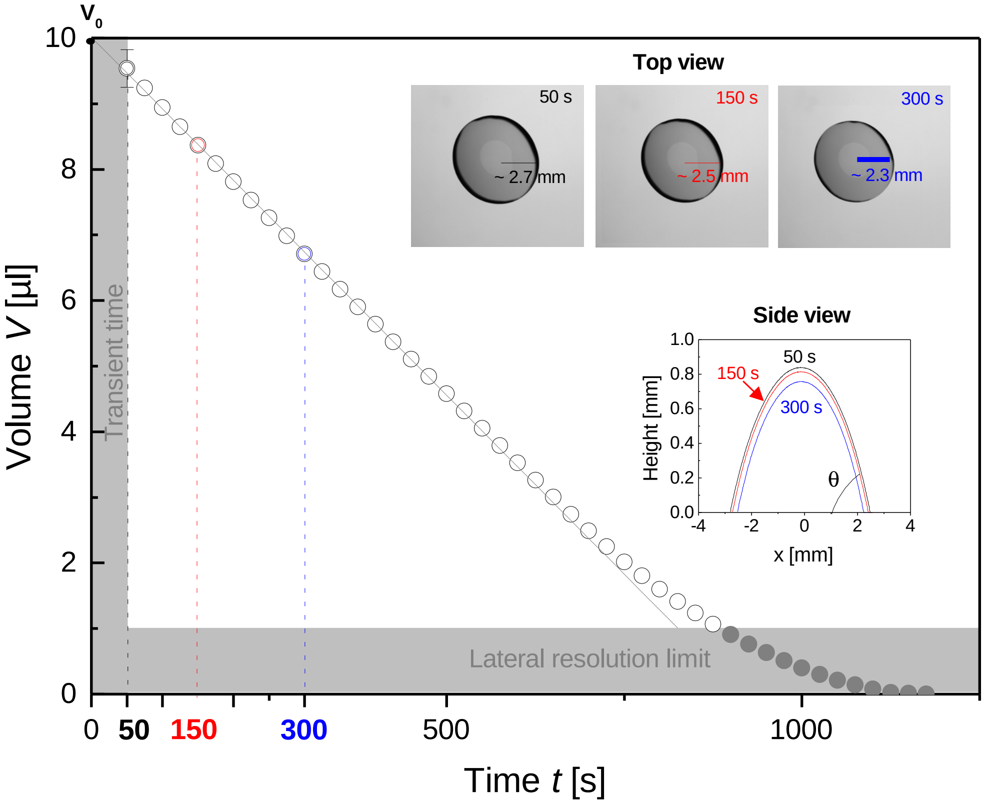

Figure 2 – *Evaporation of a sessile droplet from pure water with a contact angle* θ *of* 30° *at a relative humidity* RH *of* 0% *. The insets show the simultaneous height profile and top view images at three different evaporation times:* 50, 150 *and* 300 *s. The straight line depicts the linear decrease of the droplet volume with time experimentally observed at the initial stage of the evaporation (i.e., between* $t = 50$ *and* 600 *s). The extrapolation of this linear volume change yielded at* $t = 0$ *s the initially deposited volume* V_0.

Effect of the Droplet Volume on the Evaporation Behaviour

Figure 3 shows the time evolution of the droplet volume and shape (from top and side aspects) during the evaporation of a 1 μl-sessile droplet containing pure water at a relative humidity *RH* of 0%.

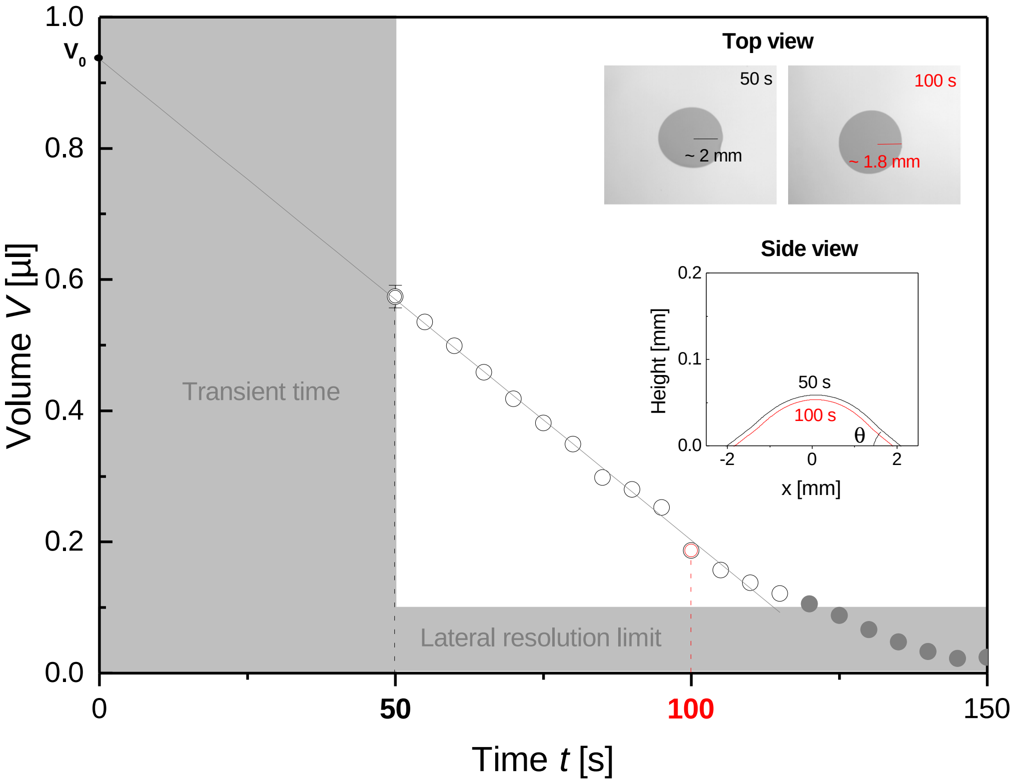

Figure 3 – *Evaporation of a* 1 *μl-sessile droplet from pure water at a relative humidity RH of* 0% *. The insets show the simultaneous height profile and top view images at two different evaporation times:* 50 *and* 100 *s. The straight line depicts the linear decrease of the droplet volume with time experimentally observed at the initial stage of the evaporation (i.e., between t =* 50 *and* 100 *s). The extrapolation of this linear volume change yielded at t =* 0 *s the initially deposited volume V_0.*

A. 2 EVAPORATION OF SESSILE DROPLETS FROM NACL SOLUTIONS

The evaporation of sessile droplets from aqueous saline solutions were performed over eight decades of initial sodium chloride concentrations from 10^{-8} to 6.1M NaCl, at different relative humidities from 0 to 60%, with various contact angles ranging from 2 to 50° and at different droplet volumes from 1 to 10 μl. Above a concentration of 10^{-6}M NaCl, the sessile droplets from NaCl solutions evaporated in pinned constant contact area mode irrespective of the relative humidity, the droplet contact angle and size. All the evaporation curves presented the same characteristics patterns. The droplet volume decreased linearly with time over the whole studied evaporation. This typical evaporation behaviour was confirmed by the top and side view imagings of the sessile droplet at three different evaporation times. The footprint of the droplet area with the substrate remained constant during the complete evaporation. Meanwhile the contact angle decreased with time.

In this appendix we present a selection of evaporation curves of sessile droplets containing NaCl solutions at different representatives sodium chloride concentrations: 10^{-6}M (in some cases), 10^{-3}M, 1M, 3M (in some cases) and 6.1M NaCl. Aqueous solutions containing 10^{-3}, 1 and 6.1M NaCl are illustrative of the three different regimes of pattern formation obtained after complete evaporation of the sessile droplet (Figure 3.2).

A. 2.1 Evaporation Behaviour of Sessile Droplets at different NaCl concentrations

Figure A. 4 shows the time evolution of the droplet volume and shape (from top and side aspects) during the evaporation of a sessile droplet containing different NaCl concentrations: (A) 10^{-6}M, (B) 1M, (C) 3M and (D) 6.1M NaCl at a relative humidity *RH* of 0%.

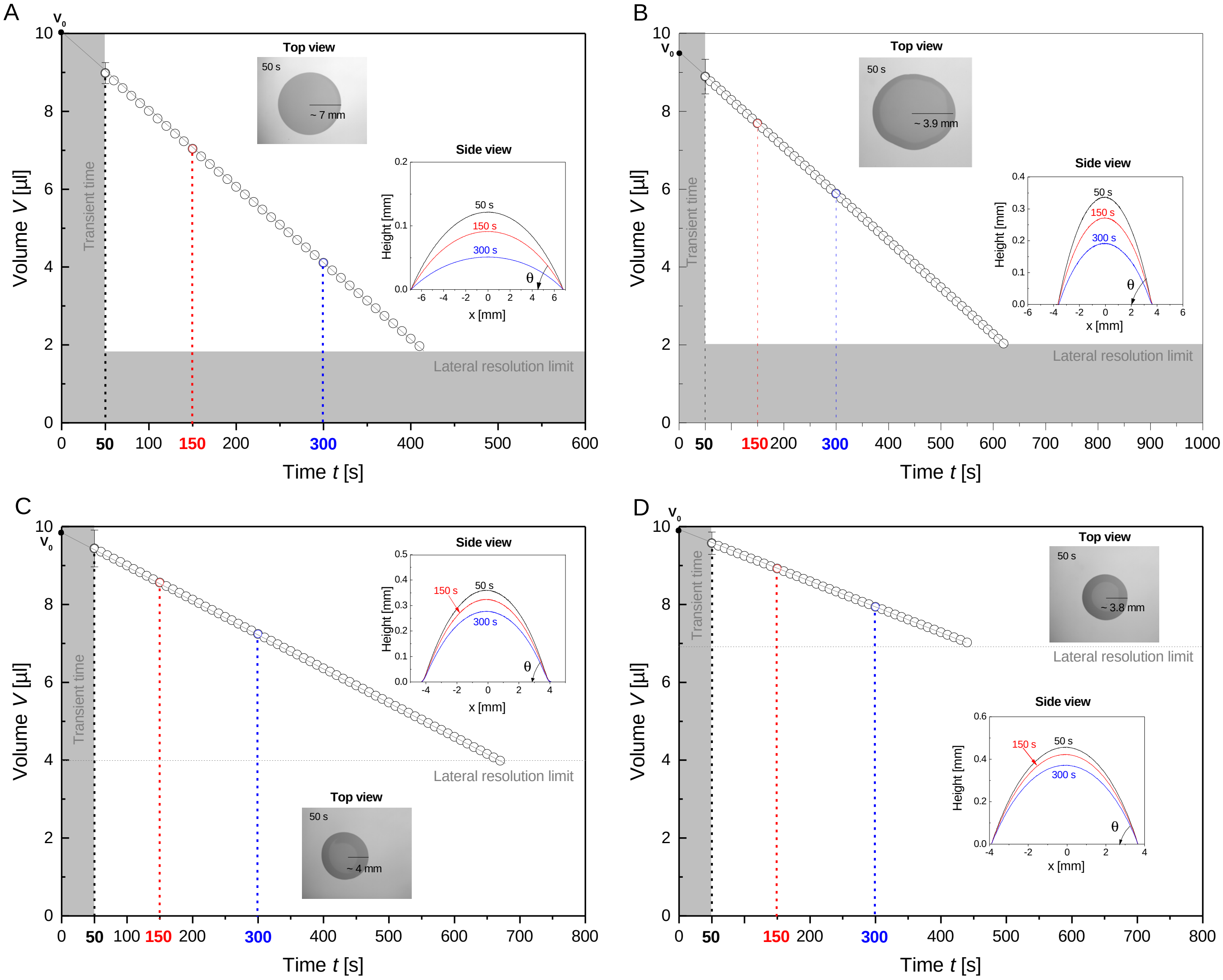

Figure A. 4 – *Evaporation of a sessile droplet from aqueous NaCl solutions at different representative NaCl concentrations:* ***A.*** 10^{-6}*M,* ***B.*** *1M,* ***C.*** *3M and* ***D.*** *6.1M NaCl at a relative humidity RH of 0%. The inset plot show the height profile at three different evaporation times: 50, 150 and 300 s. The other inset shows top view image 50 s after droplet deposition. The straight line depicts the linear decrease of the droplet volume with time experimentally observed. The extrapolation of this linear volume change yielded at t = 0 s the initially deposited volume* V_0.

A. 2.2 Impact of the Relative Humidity on Evaporation

A. 2.2.1 Evaporation Behaviour at Higher Relative Humidity

Figure A. 5 shows the time evolution of the droplet volume and shape (from top and side aspects) during the evaporation of a sessile droplet containing initially 10^{-3}M NaCl at a relative humidity *RH* of 40%.

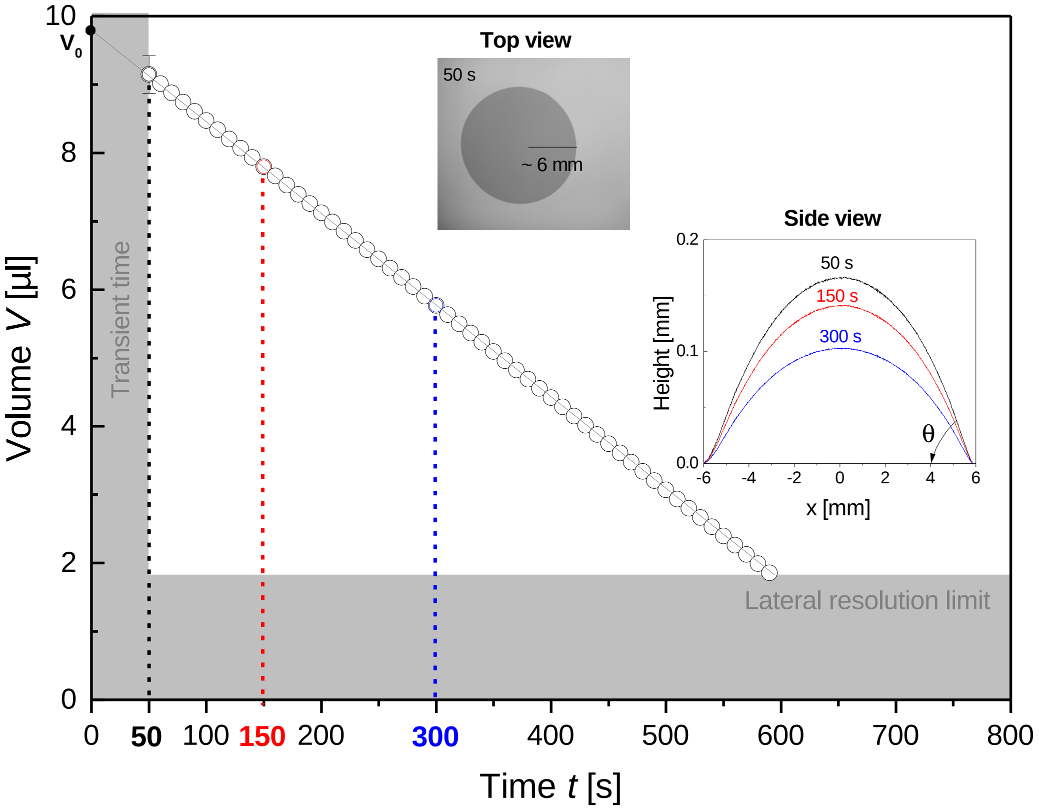

Figure A. 5 – *Evaporation of a sessile droplet from* 10^{-3}*M NaCl at a relative humidity RH of* 40%. *The inset plot show the height profile at three different evaporation times:* 50, 150 *and* 300 *s. The other inset shows top view image* 50 *s after droplet deposition. The straight line depicts the linear decrease of the droplet volume with time experimentally observed. The extrapolation of this linear volume change yielded at* $t = 0$ *s the initially deposited volume* V_0.

A. 2.2.2 Salt Concentration Influence

Figures A. 6 and A. 7 show the evolution of the normalized droplet volume $\tilde{v}$ (Equation 2.1) as a function of (A) the time t and (B) the scaled time with the normalized relative vapour pressure $\tilde{t}_{RH}$ (Equation 3.1). The experiments were performed with sessile droplets containing an initial NaCl concentration of 1M NaCl (Figure A. 6) and 6.1M NaCl (Figure A. 7) at different relative humidities of 0, 20, 40 and 60%.

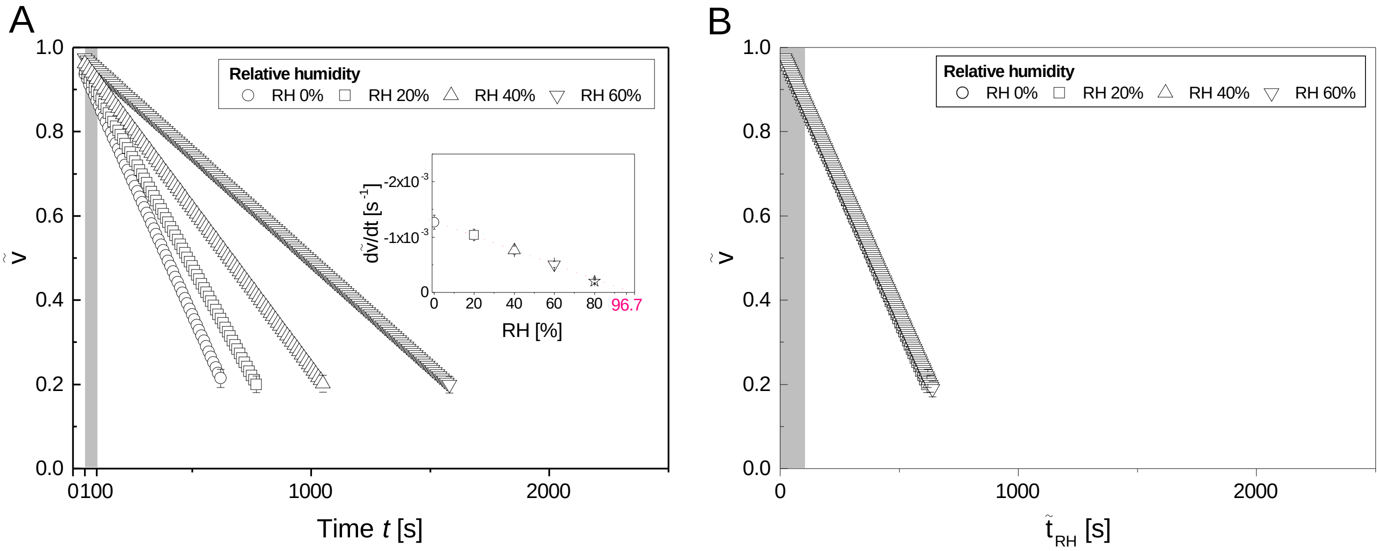

Figure A. 6 – *Normalized droplet volume* $\tilde{v}$ *(Equation 2.1) as a function of* **A.** *the time t and* **B.** *the scaled time with the normalized relative vapour pressure* $\tilde{t}_{RH}$ *(Equation 3.1). The experiments were performed with* 10 *µl-sessile droplets containing an initial NaCl concentration of* 1M *NaCl at different relative humidities of* 0, 20, 40 *and* 60%. *The decrease of the normalized volume between t* = 50 *and* 100 *s (marked in grey) was used to derive the evaporation rate. The inset shows the variation of the evaporation rate* $\frac{d\tilde{v}}{dt}$ *as a function of the relative humidity.*

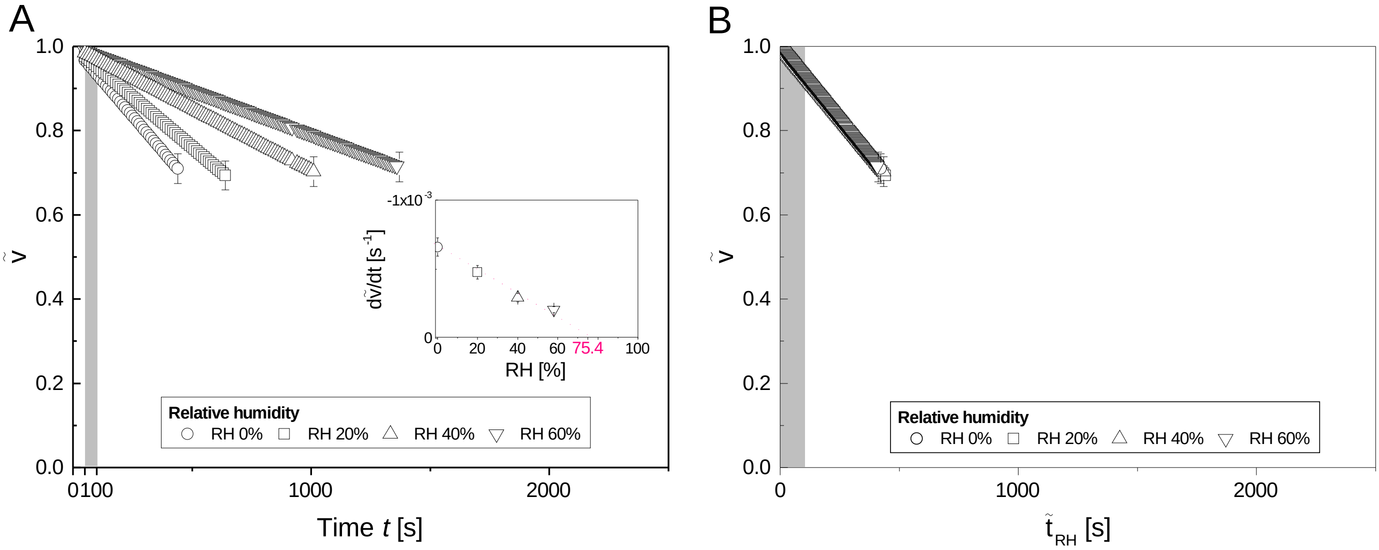

Figure A. 7 – *Normalized droplet volume* $\tilde{v}$ *(Equation 2.1) as a function of* **A.** *the time t and* **B.** *the scaled time with the normalized relative vapour pressure* $\tilde{t}_{RH}$ *(Equation 3.1). The experiments were performed with sessile droplets containing an initial NaCl concentration of* 6.1*M NaCl at different relative humidities of* 0, 20, 40 *and* 60%.*The decrease of the normalized volume between t* = 50 *and* 100 *s (marked in grey) was used to derive the evaporation rate. The inset shows the variation of the evaporation rate* $\frac{d\tilde{v}}{dt}$ *as a function of the relative humidity.*

A. 2.3 Impact of Droplet Size and Contact Angle on Evaporation

A. 2.3.1 Evaporation Behaviour at Higher Contact Angle and at Smaller Droplet Volume

Figure A. 8 shows the time evolution of the droplet volume and shape (from top and side aspects) during the evaporation of a sessile droplet containing initially 10^{-3}M NaCl (A) with a contact angle θ of 30° and (B) with an initial volume V_0 of 1 μl at a relative humidity RH of 0%.

A. 2.3.2 Salt Concentration Influence

Figure A. 9 and A. 10 shows the normalized droplet volume $\tilde{v}$ (Equation 2.1) as a function of (A) the time t and (B) the scaled time $\tilde{t}$ (Equation 3.4). The experiments were performed with sessile droplets containing an initial NaCl concentration of 1M NaCl (Figure A. 9) and 6.1M NaCl (Figure A. 10) with various contact angles θ and with different initial deposited volumes V_0 at a relative humidity RH of 0%.

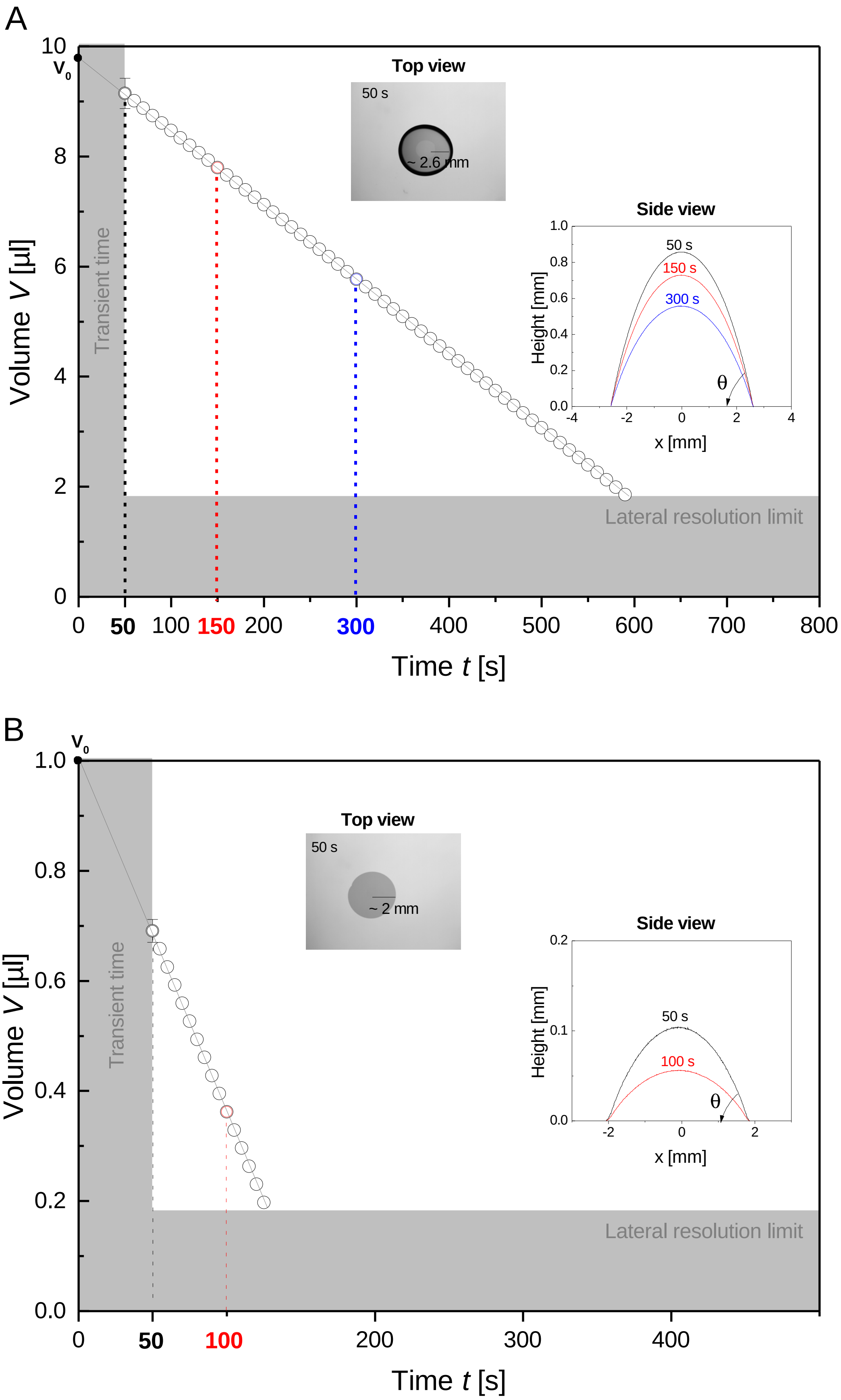

Figure A. 8 – *Evaporation of a sessile droplet from* 10^{-3}*M NaCl* ***A.*** *with a contact angle* θ *of* 30° *and* ***B.*** *with an initial volume* V_0 *of* 1 *µl at a relative humidity RH of* 0%*. The inset plot show the height profile at (A) three different evaporation times:* 50, 150 *and* 300 *s or (B) two different evaporation times :* 50 *and* 100 *s. The other inset shows top view image* 50 *s after droplet deposition. The straight line depicts the linear decrease of the droplet volume with time experimentally observed. The extrapolation of this linear volume change yielded at* $t = 0$ *s the initially deposited volume* V_0.

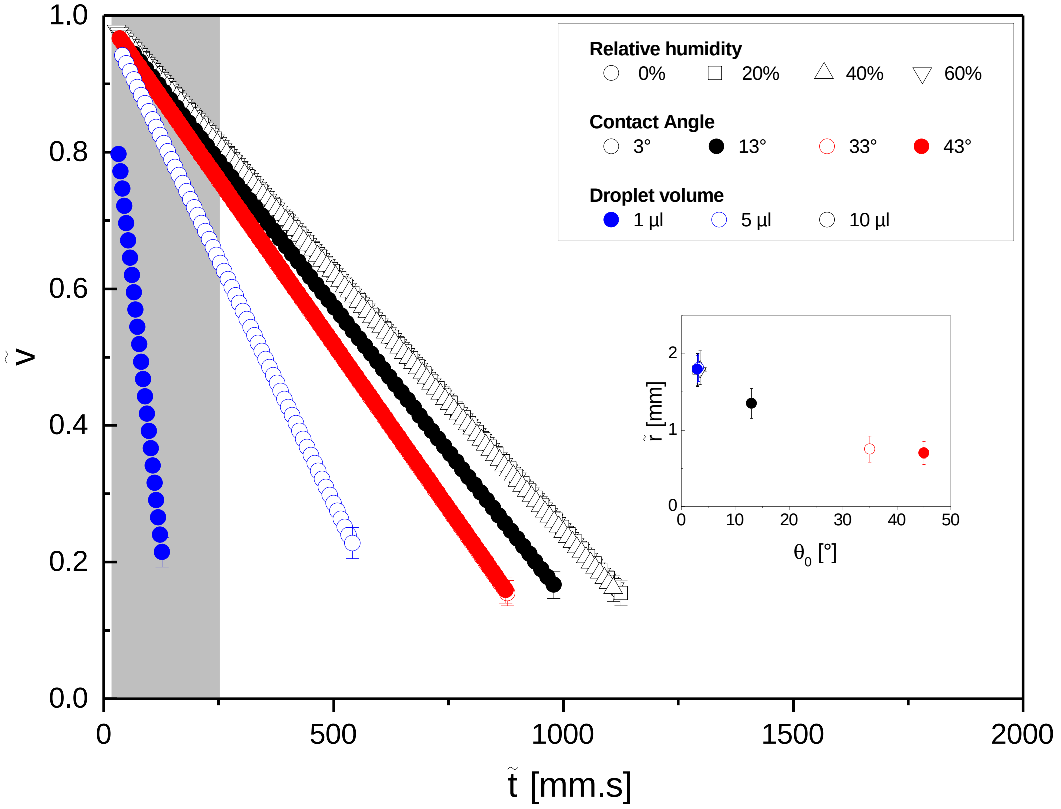

Figure A. 9 – *Normalized droplet volume $\tilde{v}$ (Equation 2.1) as a function of* ***A.*** *the time t and* ***B.*** *the scaled time $\tilde{t}$ (Equation 3.4). The experiments were performed with sessile droplets containing an initial NaCl concentration of* 1*M NaCl with various contact angles θ (*3, 13, 33 *and* 43°*) and with different initially deposited volumes V_0 (*1, 5 *and* 10 *µl) at a relative humidity RH of* 0%.

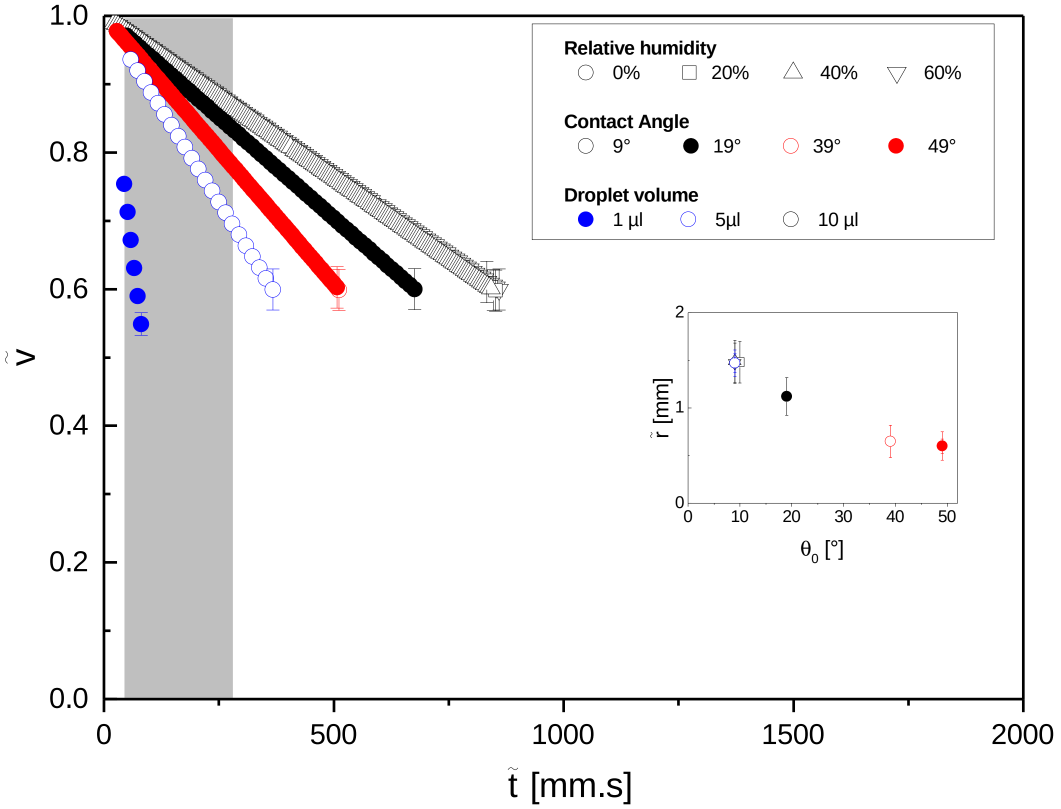

Figure A. 10 – *Normalized droplet volume $\tilde{v}$ (Equation 2.1) as a function of* ***A.*** *the time t and* ***B.*** *the scaled time $\tilde{t}$ (Equation 3.4). The experiments were performed with sessile droplets containing an initial NaCl concentration of* 6.1*M NaCl with various contact angles θ (*10, 20, 40 *and* 50°*) and with different initially deposited volumes V_0 (*1, 5 *and* 10 *µl) at a relative humidity RH of* 0%.

B

Size-Independent Peripheral Film Phenomenon

The corrosion phenomenon under sessile droplets from 6.1M NaCl in humid air with RH_{eq} 75.4% was investigated for different initial droplet volumes V_0 ranging from 5 to 60 μl. Irrespective of the droplet size, all the iron samples presented the characteristic pattern of the under-droplet corrosion experiments, i.e., the formation of a peripheral film ahead of the macroscopic contact line of the sessile droplet.

Figure B. 1 shows microscopy images of dried iron surfaces, on which sessile droplets from 6.1M NaCl with different V_0 were deposited, after 1 day of exposure to humid air with 75.4% at $T = 20°\text{C}$.

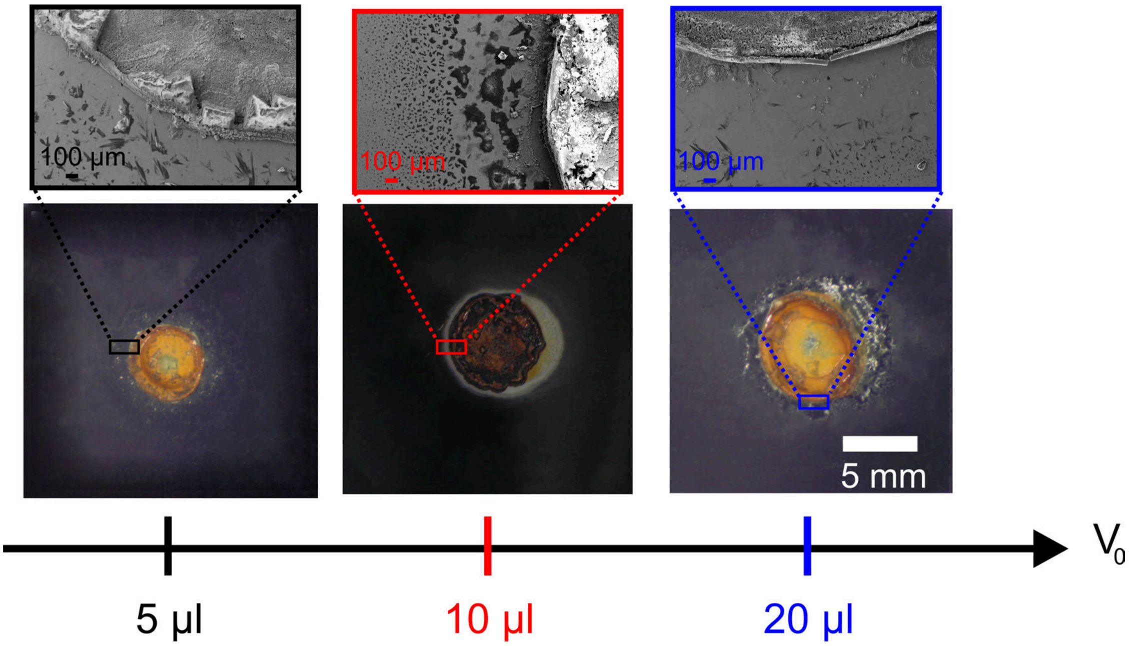

Figure B. 1 – *Microscopy images of dried iron surface, onto which an aqueous sessile droplet from* 6.1M *NaCl was deposited with an initial volume varying from* 5 *to* 20 μ*l, after* 1 *day of exposure to humid air with a relative humidity RH of* 75.4% *at* $T = 20°\text{C}$. *The insets in all three images show SEM micrographs of the droplet edge/peripheral region.*

Figure B. 2 presents the measured weight loss of iron substrates Δm (Equation 1.1), onto which sessile droplets from aqueous 6.1M NaCl solutions with different V_0 were deposited, over the corrosion process, at several exposure times ranging from 1 day to 1 month.

Figure B. 2 shows, that the weight loss of iron samples increases over the whole corrosion process. A temporal increase of Δm is observed for the different studied chloride solutions

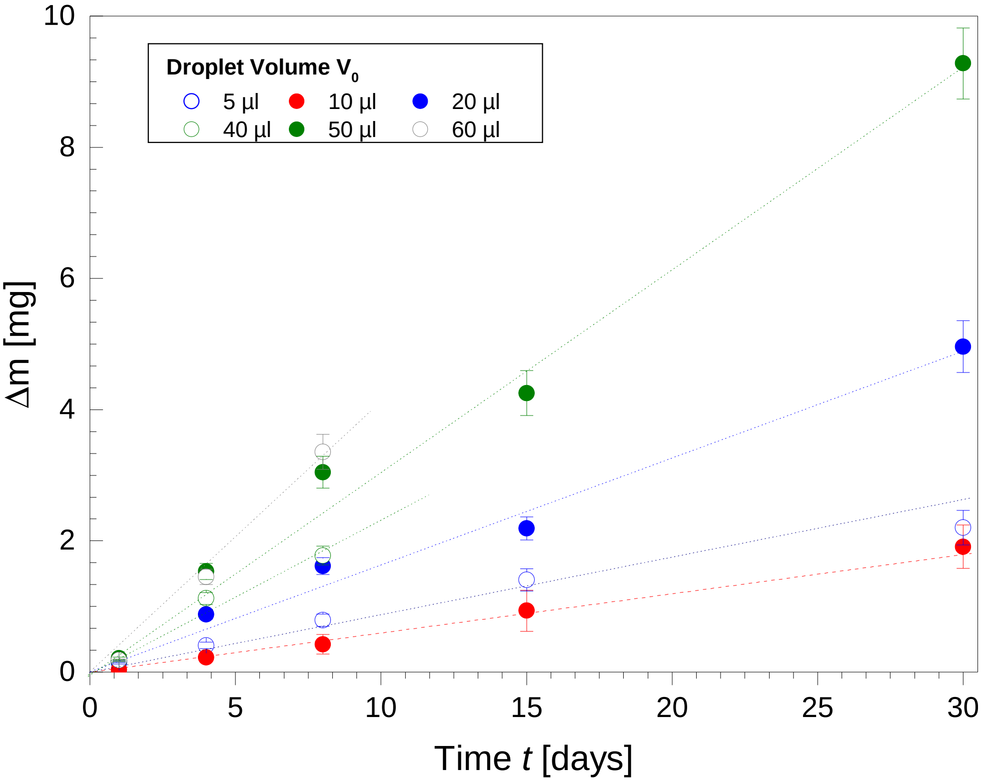

Figure B. 2 – *Weight loss of the iron substrate* Δm*, onto which sessile droplets containing aqueous solutions of* 6.1*M NaCl with different initial volumes* V_0 *from* 5 *to* 60 *µl were deposited, as function of the exposure time* t*. Over the corrosion process,* $\Delta m(t)$ *was calculated from the measured initial weight* m_0 *and the final weight* m_F *using Equation 1.1. The linear increase of* Δm *between* $t = 1$ *day and* 1 *month was used to determine the corrosion rate* V_{corr}.

within the initially sessile droplets deposited onto iron substrates. Between $t = 1$ and 30 days, the weight loss increase is nearly linear with time, as depicted by the dotted lines in Figure 3.3. Thus a corrosion rate (Equation 3.1) is rather well defined and can be determined in this exposure time interval.

C

Evaporation of Sessile Droplets on Iron

C. 1 ... with an Higher NaCl Concentration

Figure C. 1 presents the time evolution of the normalized droplet volume $\tilde{v}$ (Equation 2.1) during the evaporation of sessile droplets containing a 1M NaCl-concentrated aqueous solution deposited either on silicon wafers or pure iron surfaces in two different gaseous environments: N_2 and air with a relative humidity RH 0% at $T = 23°C$. The initially deposited volume V_0, according to the readout of the syringe, was 10 μl.

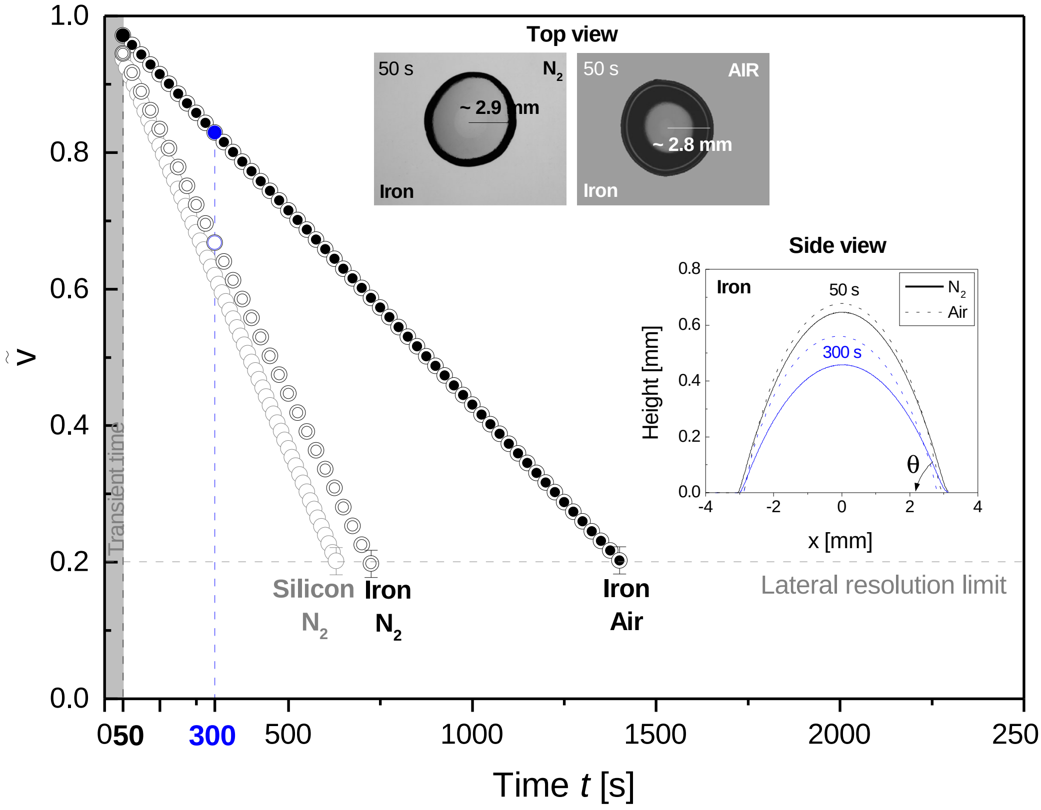

Figure C. 1 – *Evaporation of sessile droplets from 1M NaCl deposited onto silicon wafers or iron substrates in a high-purity nitrogen or synthetic air environment with a relative humidity RH 0% at $T = 23°C$ (V_0 10 μl). The inset plot shows the height profile at two different evaporation times: 50 and 300 s. The other inset shows top view imaging 50 s after droplet deposition.The two insets are only depicted for the sessile droplets deposited on iron surfaces under N_2 or air gaseous phases. The silicon wafers' case has ever been presented in detail in Figure A. 4.*

C. 2 ... AT AN HIGHER RELATIVE HUMIDITY IN AIR

Figure C. 2.a shows the temporal change of the normalized volume $\tilde{v}$ (Equation 2.1) during the evaporation of sessile droplets placed down on iron substrates and containing 10^{-3}M NaCl at different relative humidities *RHs* of 0, 20, 40 and 60%. Figure C. 2.b presents the measured normalized droplet volume $\tilde{v}$ (Equation 2.1) as a function of the scaled time $\tilde{t}$ (Equation 3.4) for sessile droplets containing initially a concentration of 10^{-3}M NaCl at different *RHs* from 0 to 60%.

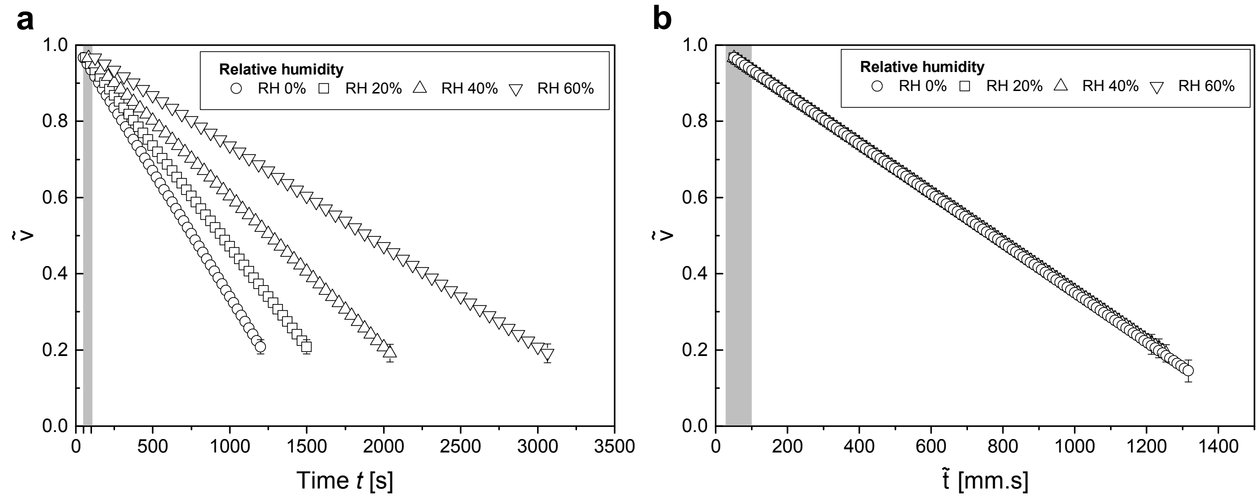

Figure C. 2 – *Normalized droplet volume $\tilde{v}$ (Equation 2.1) as a function of* ***a.*** *the experimental time t and* ***b.*** *the scaled time $\tilde{t}$ (Equation 3.4). The evaporation experiments were performed with* 10 *µl-sessile droplets deposited onto iron substrates and containing an initial NaCl concentration of* 10^{-3}*M NaCl at different relative humidities RHs of* 0, 20, 40 *and* 60%. *The decrease of the normalized volume $\tilde{v}$ between $t = 50$ and* 100 *s after the sessile droplets deposition (marked in grey) was used to derive the initial evaporation rate.*

Title Sessile Droplets of Salt Solutions on Inert and Metallic Surfaces: Influence of Salt Concentration Gradients on Evaporation and Corrosion Behaviour

Abstract In this thesis we investigate the evaporation behaviour of sessile droplets of aqueous saline solutions on planar inert and metallic surfaces and characterise the corrosion phenomenon for iron surfaces. First we study the evaporation behaviour of sessile salty droplets on inert surfaces for a wide range of salt concentrations, relative humidities, droplet sizes and contact angles. Our study reveals the range of validity of the well-accepted diffusion-controlled evaporation model and highlights the impact of salt concentration (surface tension) gradients driven Marangoni flows on the evaporation behaviour and the subsequent salty deposit patterns. Furthermore we study the spatial-temporal evolution of sessile droplets from saline solutions on metallic surfaces. In contrast to the simple, generally accepted Evans droplet model, we show that the corrosion spreads ahead of the macroscopic contact line with a peripheral film. The three-phase contact line is destabilized by surface tension gradients induced by ionic composition changes during the course of the corrosion process and migration of cations towards the droplet perimeter. Finally we investigate the corrosion behaviour under drying salty sessile droplets on metallic surfaces. The corrosion process, in particular the location of anodic and cathodic activities over the footprint droplet area is correlated to the spatial distribution of the salt inside the drying droplet.

Keywords Sessile droplet, Salt, Evaporation, Corrosion

Titre Gouttes Sessiles de Solutions Salines sur des Surfaces Inertes et Métalliques : Influence des Gradients de Concentration en Sel sur la Dynamique d'Evaporation et le Processus de Corrosion

Résumé Dans cette thèse, la dynamique d'évaporation de gouttes sessiles de solutions salines sur des surfaces planes inertes et métalliques a été étudiée et le phénomène de corrosion pour les surfaces ferriques caractérisé. En premier lieu, nous nous sommes intéressés à la dynamique d'évaporation de gouttes sessiles salées sur des surfaces inertes pour une large gamme de concentrations en sel, d'humidité relatives, de tailles de goutte et d'angles de contact. Notre étude révèle les domaines de validité du modèle classique d'évaporation, processus contrôlé par la diffusion de la vapeur dans l'air et met en évidence l'impact de flux (de Marangoni) induits par des gradients de concentration (tension de surface) en sel sur la dynamique d'évaporation et les dépôts salins obtenus après évaporation de la goutte. De plus, nous nous sommes consacrés à l'évolution spatio-temporelle de gouttes sessiles de solutions salines sur des surfaces métalliques. Contrairement au modèle simplifié de la goutte d'Evans, nous avons montré que le processus de corrosion s'étend aux abords de la ligne de contact, avec la formation d'un film périphérique. La ligne triple est déstabilisée par des gradients de tension de surface induits par des variations de composition ionique au cours du processus de corrosion et la migration des cations vers la périphérie de la goutte. Enfin nous avons étudié le phénomène de corrosion du métal induit par l'évaporation de gouttes sessiles salées. Le processus de corrosion, en particulier la localisation des réactions anodiques et cathodiques sur la surface métallique en contact avec la goutte est corrélée à la distribution spatiale du sel au sein de la goutte s'évaporant.

Mots-Clés Gouttes sessiles, Sel, Evaporation, Corrosion